Studies of a Digital SiPM and MAPS Prototypes as Key Technologies for Future High-Energy Physics Experiments

Dissertation
zur
Erlangung des Doktorgrades (Dr. rer. nat.)
der
Mathematisch-Naturwissenschaftlichen Fakultät
der
Rheinischen Friedrich-Wilhelms-Universität Bonn

vorgelegt von
Gianpiero Vignola
aus
Cisternino, Italy

Bonn 2025

Angefertigt mit Genehmigung der Mathematisch-Naturwissenschaftlichen Fakultät der Rheinischen Friedrich-Wilhelms-Universität Bonn

Gutachterin/Betreuerin:	Prof. Dr. Ingrid-Maria Gregor
Gutachter:	Prof. Dr. Klaus Desch
Tag der Promotion:	21.03.2025
Erscheinungsjahr:	2025

Abstract

Digital Silicon Photomultipliers (dSiPMs) and Monolithic Active Pixel Sensors (MAPS) are technologies, fabricated using commercial Complementary Metal-Oxide-Semiconductor (CMOS) processes. These detectors have the potential to become key components in High-Energy Physics (HEP), with the ability to meet the demanding requirements of future experiments, which aim to push the boundary of current knowledge of the world of particles and fundamental interactions.
The first part of the thesis analyzes the DESY dSiPM prototype as an example of the technology potential. Extensive laboratory characterizations confirm the functionality of the sensor and of all integrated CMOS circuitry. Sensor calibrations ensure stable and controlled operation of the prototype. The performance of the DESY dSiPM in Minimum Ionising Particles (MIP) detection is evaluated through beam tests at the DESY II test-beam facility. The bare DESY dSiPM in MIP detection shows a spatial resolution of 20 µm, a time resolution of 50 ps with an efficiency of about 30 %, limited by the fill-factor characteristic of the technology. A novel detector-concept is therefore introduced that combines dSiPM with thin Cerium-doped Lutetium Yttrium OxyorthoSilicate (LYSO(Ce)) radiators to overcome these efficiency limitations. This approach improves detection efficiency over 99 %, and enables better discrimination of signal events. The results presented support the potential use of dSiPM in MIPs 4D-tracking applications, where temporal resolutions of less than 100 ps and spatial resolutions on the order of 10 µm are required in MIP detection.
The second part of this thesis focuses on MAPS technology, analyzing two prototypes developed using a 65 nm CMOS imaging process. The first sensor, DESY Chip V1, is designed to verify the performance of a fast Charge Sensitive Amplifier (CSA), characterized in laboratory and test-beam. The studies confirm the functionality of the circuits while highlighting some limitations that contributed to design improvements in later versions. Several Analog Pixel Test Structure (APTS) prototypes are also studied in collaboration with CERN and the ALICE ITS3 group. The operational parameters of the sensors are optimized and charge calibrations are performed. The study of the performance in MIP detection of an APTS prototype with a pixel pitch of 15 µm demonstrates spatial resolutions of less than 3.5 µm and detection efficiencies higher than 99 % with low noise occupancy in a wide operational window. The results presented support the potential of MAPS technology in meeting the stringent requirements of future experiments, particularly for vertex detectors in future lepton colliders.

Contents

Introduction 1

1 Status and Perspective of High-Energy Physics 3
1.1 Standard Model of Particle Physics . . . 3
1.1.1 Open Questions of the Standard Model . . . 4
1.2 The Large Hadron Collider . . . 5
1.3 High Luminosity LHC Upgrades . . . 6
1.3.1 ATLAS . . . 7
1.3.2 CMS . . . 8
1.3.3 LHCb . . . 9
1.3.4 ALICE . . . 10
1.4 Beyond LHC: Future Lepton Colliders . . . 11
1.4.1 Physics Program . . . 11
1.4.2 Lepton Colliders Proposals . . . 12
1.5 Key Technologies Research and Development . . . 13
1.5.1 CMOS MAPS Sensors . . . 13
1.5.2 Sensor for 4D-Tracking . . . 14
1.5.3 Semiconductor Photo-Detectors . . . 14

2 Physics of Solid-State Detectors 15
2.1 Semiconductors Basics . . . 15
2.1.1 Doping . . . 17
2.1.2 The pn-Junction . . . 17
2.1.3 Junction Depletion . . . 18
2.2 Energy Loss of Charged Particles . . . 19
2.3 Interaction of Photons with Matter . . . 20
2.3.1 Attenuation of Photon Intensity . . . 22
2.4 Particle Detection with Solid State Detectors . . . 22
2.4.1 Charge Generation . . . 22
2.4.2 Charge Transport . . . 24
2.4.3 Charge Multiplication . . . 25
2.4.4 Signal Formation . . . 26

2.4.5 Detector Readout . . . 27
2.4.6 Hybrid and Monolithic Detectors . . . 27
2.5 Solid State Detectors Properties . . . 28
2.5.1 Spatial Resolution . . . 28
2.5.2 Time Resolution . . . 29

3 Beam Tests of Pixel Sensors 31
3.1 The DESY II Synchrotron Test-Beam Facility . . . 31
3.2 Beam Telescopes . . . 32
3.3 Telescope Configuration and Track Resolution . . . 33
3.3.1 Track Resolution Estimations . . . 34
3.4 Data Acquisition and Synchronization . . . 35
3.4.1 Caribou DAQ System . . . 35
3.4.2 The Trigger Logic Unit . . . 36
3.4.3 EUDAQ2 Framework . . . 37
3.5 Analysis of Test-Beam Data with the Corryvreckan Framework . . . 37
3.5.1 Data Decoding and Event Definition . . . 38
3.5.2 Clustering . . . 38
3.5.3 Tracking and Telescope Alignment . . . 39
3.5.4 DUT Alignment and Analysis . . . 39

I Studies on a Digital Silicon Photomultiplier Prototype 41

4 Silicon Photomultipliers Principles and the DESY Prototype 43
4.1 Silicon Photomultipliers . . . 43
4.1.1 Single Photon Avalanche Diodes . . . 43
4.1.2 Analogue SPAD Arrays . . . 44
4.1.3 Digital SPAD Arrays . . . 45
4.1.4 Current-Voltage and Breakdown . . . 46
4.1.5 Photo Detection Efficiency . . . 47
4.1.6 Uncorrelated Noise: Dark Counts . . . 48
4.1.7 Correlated Noise: Afterpulsing and Crosstalk . . . 48
4.1.8 Spatial Resolution . . . 49
4.1.9 Timing Resolution . . . 50
4.2 The DESY dSiPM . . . 50
4.2.1 Pixel Electronics . . . 52
4.2.2 Timestamping and 12-bit TDC . . . 53
4.2.3 Validation Logic . . . 53
4.2.4 Test Structures . . . 54

5 Laboratory Characterization of the DESY dSiPM 57
5.1 Temperature Diode Calibration . . . 57
5.2 Current-Voltage and Dark Count Rate Measurements . . . 58
5.2.1 Measurements Setup . . . 59

5.2.2 Breakdown Voltage and Pixel Dark Count Rate . . . 59
5.3 Masking . . . 61
5.4 Crosstalk Measurement . . . 65
5.4.1 Single Pixel Crosstalk . . . 65
5.4.2 Overvoltage and Crosstalk Probability . . . 66
5.4.3 Crosstalk Probability and Defect Position . . . 66
5.5 Timing Measurements with a Picosecond-Pulsed Laser . . . 67
5.5.1 Laser Setup . . . 69
5.5.2 SPAD and Pixel Analogue Signals . . . 69
5.5.3 SPAD and Pixel Time Resolution . . . 70
5.5.4 Propagation Delays . . . 72
5.5.5 TDC resolution . . . 72
5.6 Summary of Results . . . 73

6 Test-Beam Characterization of the DESY dSiPM 75
6.1 dSiPM in direct MIP detection . . . 75
6.2 Test-Beam Setup . . . 75
6.2.1 Trigger Systems . . . 76
6.3 Test-Beam Campaigns . . . 77
6.4 Alignment of the DUT and Trigger System . . . 79
6.5 Analysis Procedure . . . 80
6.5.1 Data Structure and Decoding . . . 81
6.5.2 Clustering, Software Alignment and Association . . . 81
6.5.3 Observables . . . 81
6.6 Bare dSiPM in MIP Detection . . . 84
6.6.1 Cluster Size . . . 84
6.6.2 Spatial Resolution . . . 85
6.6.3 Time Resolution . . . 86
6.6.4 Efficiency . . . 87
6.7 Summary of Results . . . 89

7 dSiPM coupled with Thin LYSO 91
7.1 Overcome SiPM Intrinsic Limits in MIP Detection . . . 91
7.1.1 A new Detector Concept: Coupling with Thin Radiator . . . 92
7.1.2 Multipurpose Detector for Single Photons and MIPs . . . 92
7.2 Radiators for MIP detection . . . 94
7.2.1 The Scintillation Process . . . 94
7.2.2 The Cerenkov Effect . . . 96
7.3 Geant4 Simulation . . . 96
7.3.1 Simulation Model . . . 97
7.3.2 Simulation Results . . . 98
7.4 DESY dSiPM and Thin LYSO Coupling . . . 101
7.4.1 Laboratory characterization with Sr-90 . . . 102
7.5 Test-Beam Characterization . . . 102
7.5.1 Clustering and Cluster Size . . . 102

7.5.2 Spatial Resolution . . . 105
7.5.3 Efficiency . . . 106
7.5.4 Time Resolution . . . 106
7.5.5 Independent LYSO Characterization Using Commercial SiPMs . . . 107
7.6 Summary of Results . . . 109

II Studies on Monolithic Active Pixel Sensors Prototypes 111

8 MAPS in a 65 nm CMOS Imaging Technology 113
8.1 Monolithic Active Pixel Sensors . . . 113
8.2 MAPS Layouts . . . 114
8.3 MAPS R&D Activities at DESY . . . 114
8.4 Multi-Project Production using a 65 nm CMOS Imaging Process . . . 116
8.4.1 DESY Chip V1 Prototype . . . 116
8.4.2 The Analogue Pixel Test Structure Prototype . . . 118

9 Laboratory & Test-Beam Characterization of MAPS Prototypes 121
9.1 DESY Chip V1 Laboratory Studies . . . 121
9.2 Test-Beam in MAMI . . . 122
9.2.1 Waveform Analysis . . . 123
9.3 APTS Laboratory Studies . . . 125
9.3.1 Charge Injection & Parameters Optimization . . . 125
9.3.2 Gain Characterization . . . 126
9.3.3 Charge Calibration Using Fe-55 Source . . . 127
9.4 APTS Test-Beam Studies on a 15 µm Prototype . . . 128
9.4.1 Test-Beam Setup and Data Analysis . . . 128
9.4.2 Clustering, Cluster Size and Cluster Charge . . . 130
9.4.3 Efficiency . . . 131
9.4.4 Spatial Resolution . . . 134
9.5 Summary of Results . . . 135

10 Summary and Prospect 137

List of Figures 141

List of Tables 145

Bibliography 151

Introduction

Science arises from the innate desire to understand and answer fundamental questions about existence and evolves into an extraordinary tool for progress. Therefore, scientific research does not represent the mere satisfaction of human curiosity, but offers the possibility of transforming what surrounds us; a power that comes with the responsibility of using this knowledge to promote collective well-being, respecting the balance of nature, aware that we are part of it and not its owners.

High-Energy Physics (HEP) represents one of the test beds for this concept. The study of fundamental particles and interactions expands the boundaries of our knowledge of nature, fostering innovations that extend far beyond scientific research. Particle accelerators such as the Large Hadron Collider (LHC) and its future evolutions, as well as next-generation colliders, play a fundamental role in the understanding of particle physics, with their development driven by continuous technological progress. These large experiments demonstrate how the sharing of knowledge, resources, and values is of paramount importance in achieving ambitious goals. Goals that are not reachable by single individuals or entities but that require the contribution of the entire scientific community.

Thanks to these collective efforts, the current description of matter and fundamental forces in our universe has been defined piece by piece: the Standard Model (SM) of particle physics. Although this theory has proven to be extraordinarily successful, there are still numerous open questions and unaddressed aspects. These limits in our current knowledge represent a stimulating opportunity to pursue research. The goal, perhaps utopian, of a complete and precise understanding of the mechanisms that govern our universe, drives research toward the development of new tools and techniques that often have important impacts on society.

Research and Development (R&D) activities in the context of particle physics are constantly stimulated by an increasing demand in terms of performance and precision. Cutting-edge research is often associated with cutting-edge technologies, and that is the context in which this thesis is developed. In this work, two silicon detector technologies that are emerging in HEP are being studied: digital Silicon Photomultipliers (dSiPMs) and Monolithic Active Pixel Sensors (MAPS). The dSiPMs represent the digital evolution of conventional SiPMs developed originally for single photon detection and with possible applications in Minimum Ionising Particles (MIP) detection. MAPS are a MIP detection technology already in use for several years in HEP experiments that is expected to play a significant role in the vertex and tracker detectors of the next generation HEP experiments. MAPS and dSiPM investigated in this thesis are produced using commercial Complementary Metal-Oxide-Semiconductor

(CMOS) processes, where the synergy between fundamental science and industry fosters a continuous exchange of innovation and is a tangible example of how scientific research can have a direct impact in other fields.

This thesis is structured as follows. Chapter 1 presents an introduction to the SM and its open questions, and then describes the future prospects of HEP experiments focusing on some of the key R&D technologies topics. Chapter 2 introduces semiconductor physics, describes the interaction of charged particles and photons, detection mechanisms, and the main properties of solid-state detectors. Chapter 3 describes instrumentation and methodologies used for beam tests of pixel sensors: the main method of investigation used in this work for the studies presented in subsequent Parts I and II of the thesis.

Part I focuses on the study of dSiPM and in particular the characterizations performed on the DESY dSiPM prototype. In Chapter 4 (d)SiPM technology is introduced followed by a description of the DESY dSiPM prototype. Chapter 5 reports the main characterizations and calibrations performed in the laboratory on the DESY dSiPM. Chapter 6 illustrates the setup and performance of DESY dSiPM in MIP detection studied at DESY II test-beam facility by evaluating its performance in terms of 4D-tracking of MIP. Chapter 7 extends these characterizations by evaluating the 4D-tracking performance of DESY dSiPM coupled with a thin radiator.

Part II analyzes the MAPS technology and presents the results of characterizations performed on two different prototypes: DESY Chip V1 and Analog Pixel Test Structure (APTS) developed using a 65 nm CMOS technology. Chapter 8 describes MAPS technology, presents research activities in this context at DESY, and describes the two prototypes investigated. Chapter 9 reports the laboratory characterizations and test-beams studies on the DESY Chip V1. This is followed by a description of the calibrations of APTS prototypes and the presentation of test-beams studies performed on one of the samples.

The last chapter of the thesis summarizes the key findings from both parts and provides a brief outlook on potential future developments.

CHAPTER 1

Status and Perspective of High-Energy Physics

The constant drive for precision in High-Energy Physics (HEP) experiments requires continuous advances in particle detection technologies. To contextualize the technological developments analyzed in this thesis, this chapter provides an overview of the current status and future perspectives of HEP. Section 1.1 introduces the Standard Model (SM) of particle physics, highlighting its successes and open questions driving frontier research. Section 1.2 describes the fundamental role played by the Large Hadron Collider (LHC) in this context, followed, in Section 1.3, by insights into the ongoing and future upgrades planned for the High-Luminosity LHC (HL-LHC). Looking forward, Section 1.4 discusses some of the proposals for future experiments focusing on Lepton Collider (LC), analyzing their main scientific goals and design. Section 1.5 presents some of the research and development areas identified as essential to meet the research goals of future HEP experiments, context in which this thesis develop.

1.1 Standard Model of Particle Physics

The SM of Particle Physics [1], Figure 1.1, represents our current understanding of particles and their fundamental interactions. All ordinary matter is composed of elementary particles divided into two main categories: quarks and leptons, with their respective anti-particles, classified as fermions with a spin of $1/2$. Fermions are organized into three generations, each generation including quarks with charge $+2/3$ and $-1/3$, a lepton with charge -1, and the corresponding neutrino which is electrically neutral. Among the quarks, the first generation includes the up quark and the down quark, followed by the charm-strange pair and the top-bottom (or beauty) pair. Leptons are electron, muon, and tau, each with its respective neutrino. The lightest and most stable particles belong to the first generation, while the heaviest and most unstable particles are in the second and third generations. Stable matter in the universe consists exclusively of first-generation particles, as higher-generation particles rapidly decay into more stable particles, except for neutrinos, which are described as massless and intrinsically stable by the SM.

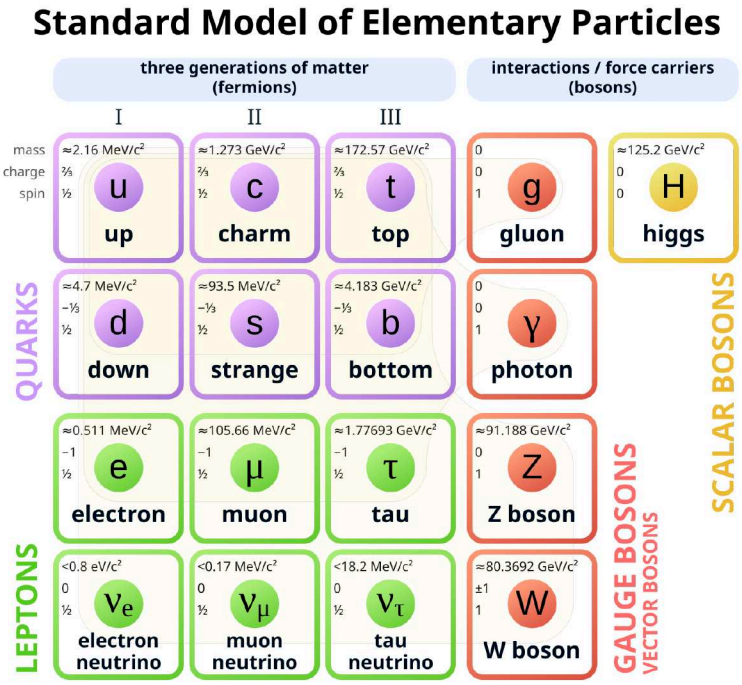

Figure 1.1: Standard Model of particle physics. From [2].

The SM also describes three fundamental forces: electromagnetic force, strong force, and weak force. The electromagnetic force acts on charged particles and has an infinite interaction range. The strong force, which has a range of approximately 1 fm, is the most powerful of the three and holds quarks together within hadrons[1]. The weak force, with an even shorter interaction range of about 10^{-3} fm, is the weakest of the three and governs processes such as radioactive decay.

Fundamental interactions are mediated by particles called gauge bosons, which transfer discrete energy between particles. The photon mediates the electromagnetic force, the gluon the strong force, and the W and Z bosons the weak force. An additional fundamental boson is the Higgs boson, associated with the Higgs field, which gives mass to leptons (except neutrinos), quarks, W and Z bosons, and itself. A comprehensive description of the SM can be found, e.g., in [1].

This theoretical framework explains the structure and dynamics of matter and its interactions in the universe with high precision while leaving fundamental questions open.

1.1.1 Open Questions of the Standard Model

Despite the great success of the SM in describing physical phenomena with very high accuracy and its agreement with numerous experimental measurements, several evidences demonstrate its

[1] Hadrons are composite particles made of two or more quarks

incompleteness. Below, some of the major indications for the need of physics Beyond Standard Model (BSM) are summarized:

- **Fundamental Interactions:** The SM includes three of the four fundamental forces: electromagnetic, weak, and strong, but does not consistently integrate gravity [3].
- **Matter-Antimatter Asymmetry:** The observed asymmetry between matter and antimatter in the universe remains unexplained [4].
- **Dark Matter:** The rotational behavior of some galaxies [5], including the Milky Way, and the phenomenon of gravitational lensing [6] indicate the existence of dark matter.
- **Dark Energy:** The accelerated expansion of the Universe, detected through observations of supernovae or the cosmic microwave background, suggests the presence of dark energy [7].
- **Neutrino Properties:** Observations of neutrino oscillations in various experiments require that they have a mass, a property not predicted by the SM [8].
- **Number of Particle Generations:** The SM does not provide an explanation for why exactly three generations of fermions exist [9].
- **Particle Masses:** The masses of elementary particles are not predicted by the SM and must be determined experimentally, suggesting the existence of a more fundamental theory [1].

To address these and other observables not described by the SM, several BSM theories have been proposed, such as supersymmetry [10] and grand unified theories [11]. Despite theoretical and experimental advances, so far, none of the BSM proposals have led to the discovery of evident new physics phenomena, keeping the search open for a more complete understanding of the Universe.

1.2 The Large Hadron Collider

LHC is currently the largest and most powerful particle accelerator in the world, probing the SM and searching for BSM physics evidence. It broke its own record during Run-3, achieving proton collisions at an energy in the center of mass of 13.6 TeV [12]. The LHC is located at the European Organization for Nuclear Research (CERN) in a 26.7 km-long underground circular tunnel under the Geneva area, which stretches between Switzerland and France. This tunnel previously housed the Large Electron-Positron collider (LEP) [13], which held the title of the most powerful LC, with an energy in the center of mass of up to 209 GeV.

A schematic diagram of the accelerator complex is shown in Figure 1.2. Proton beams are obtained from hydrogen gas and accelerated to 50 MeV in the LINear ACcelerator 2 (LINAC2). Then, the protons are further accelerated in stages in the Proton Synchrotron Booster (PSB), Proton Synchrotron (PS) and Super Proton Synchrotron (SPS), until they reach an energy of 450 GeV before being injected into the LHC. In the LHC, protons are injected in bunches of about 10^{11} particles, spaced 25 ns (or 7.5 m) apart. Two proton beams rotate in opposite directions, contained in two separate rings within the same double-hole magnet. The oppositely rotating beams cross at four main interaction points,

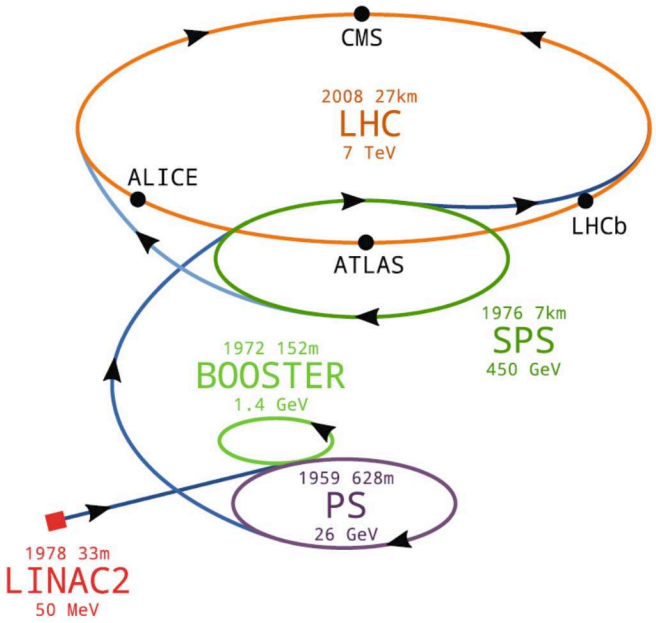

Figure 1.2: CERN accelerator complex. From [20].

where protons-protons, protons-ions, or ions-ions collisions occur[2]. These points are where the four major LHC experiments are located. A Toroidal LHC ApparatuS (ATLAS) [14] and Compact Muon Solenoid (CMS) [15] experiments, both general-purpose detectors designed to detect the Higgs boson, a goal achieved in 2012 [16, 17], and to search for potential BSM physics. The A Large Ion Collider Experiment (ALICE) experiment [18] focuses on studying the deconfinement of quarks and gluons in the hot plasma produced by heavy-ion collisions. Lastly, Large Hadron Collider beauty (LHCb) [19] experiment dedicated to the study of hadron decays involving bottom or charm quarks.

1.3 High Luminosity LHC Upgrades

The potential of a particle collider to produce a statistically significant sample of rare processes, needed for precision measurements of SM or BSM physics research, depends on its luminosity $\mathcal{L}$ and the duration of its operation.

The luminosity $\mathcal{L}$ of a particle collider is defined as the number of particle interactions per unit area and time. This, multiplied by the cross-section σ of a given process, defines its interaction rate:

$$\frac{\mathrm{d}N}{\mathrm{d}t} = \sigma\mathcal{L}. \tag{1.1}$$

The LHC is designed for a luminosity on the order of $\mathcal{L} = 1 \times 10^{34}\,\mathrm{cm}^{-2}\mathrm{s}^{-1}$ with a peak luminosity reached during Run-2 of $\mathcal{L} = 2.0 \times 10^{34}\,\mathrm{cm}^{-2}\mathrm{s}^{-1}$. The integrated luminosity is obtained by integrating

[2] Ions beams can also be accelerated in the LHC complex

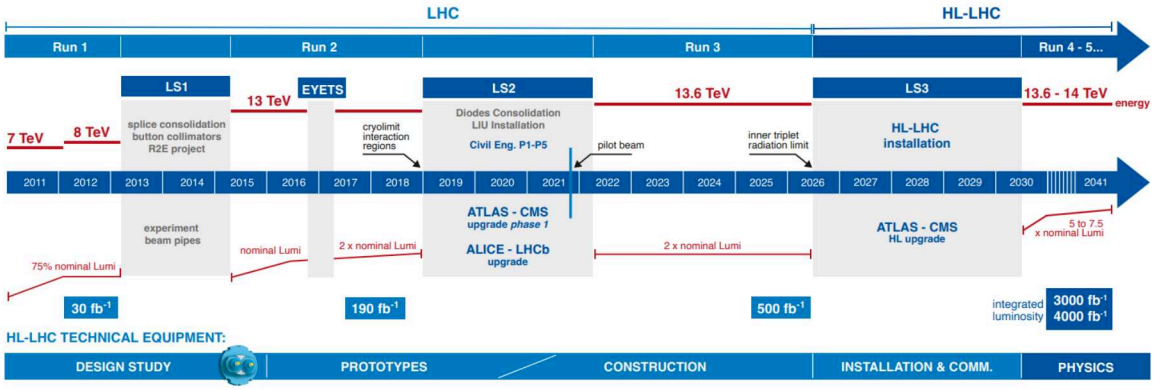

Figure 1.3: Schedule of the LHC and HL-LHC with measured/expected integrated luminosity. From [21].

the instantaneous luminosity $\mathcal{L}$ over time, representing the total number of accumulated collisions. In practical applications, it is often expressed in inverse femtobarns (fb^{-1}), where $1\ \text{fb}^{-1} = 1 \times 10^{43}\ \text{m}^{-2}$.

To increase the rate of rare interactions, the luminosity of the LHC will be boosted to values between $\mathcal{L} = 5.0 \times 10^{34}\ \text{cm}^{-2}\text{s}^{-1}$ and $\mathcal{L} = 7.5 \times 10^{34}\ \text{cm}^{-2}\text{s}^{-1}$ during the third scheduled shutdown period between 2026 and 2030. Figure 1.3 illustrates the current schedule, at the time of writing, of the LHC and HL-LHC and the measured/expected luminosity.

Although the increase in luminosity primarily concerns acceleration technologies and beam optics [22], all major experiments at the LHC will undergo significant detector upgrades. Among other reasons, these upgrades aim to adapt the experiments to the increased number of simultaneous collisions, called *pile-up*, expected for Run-4 and beyond, as well as to improve accuracy in event reconstruction. A simulation of a bunch crossing in the ATLAS experiment is shown in Figure 1.4 and indicates the increase in pile-up/track multiplicity comparing the LHC and HL-LHC scenarios.

Listed below are the main upgrade activities planned for the four major experiments in the HL-LHC phase, focusing on solid-state detector technologies relevant in the context of this work.

1.3.1 ATLAS

For HL-LHC, the current mixed configuration of the ATLAS tracker (silicon and transition radiation detectors) will be replaced with an all-silicon detector called ITk, extending the pseudorapidity coverage[3] up to $|\eta| < 4$ [24]. This new tracker will include $165\ \text{m}^2$ of strip sensors distributed over four barrel layers and six end-cap disks, as well as $13\ \text{m}^2$ of pixels over five barrel layers and end-cap disks. Compared with the current system, the new tracker will have a significantly reduced material budget and improved tracking performance. The ITk-Pixel subsystem will use hybrid pixel modules with pixel sizes of 50×50 µm and 25×100 µm and thicknesses between 100 µm and 150 µm. The inner layers will be equipped with radiation-resistant 3D-sensors, while planar sensors will be used for the

[3] Pseudorapidity coverage is defined as the range of pseudorapidity $\eta = -\ln(\tan(\theta/2))$ values measurable by a detector, indicating the angular extent of particle detection relative to the beam axis

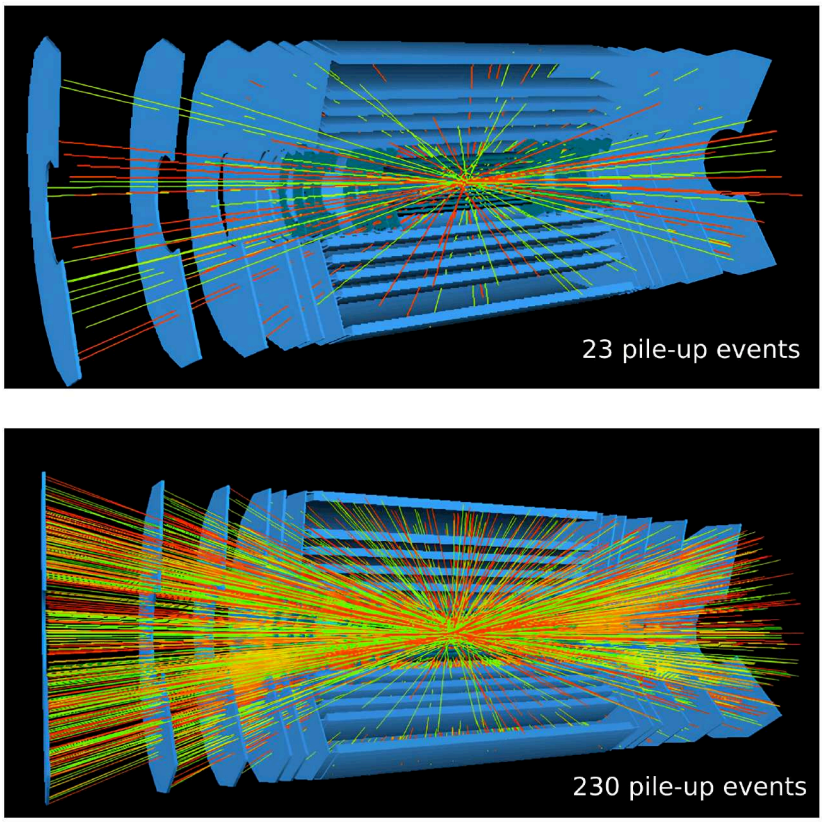

Figure 1.4: Baseline layout of ATLAS HL-LHC Inner Tracking system (ITk) detector traversed by the tracks from 23 pile-up events in the LHC scenario (top) and 230 pile-up events in the HL-LHC scenario (bottom). Adapted from [23].

outer areas. For the ITk-Strip subsystem, silicon strip sensors with a pitch between 70 µm and 80 µm will be used.

Another significant upgrade for ATLAS HL-LHC is the introduction of a new High Granularity Timing Detector (HGTD), designed to mitigate the pile-up problem and to measure bunch-by-bunch luminosity. This detector will use the Low Gain Avalanche Diode (LGAD) technology, providing a time resolution of 30 to 50 ps per track. The HGTD will consist of four layers of silicon modules with coverage in the $2.4 < |\eta| < 4.0$, totaling 3.6 MP. These combined improvements will provide greater precision in tracking and timing, optimizing ATLAS's ability to analyze events produced in the HL-LHC's regime. Precise temporal information will be added to the tracks, allowing them to be assigned to the corresponding vertex and realizing the so-called *4D-Tracking*. A summary of the main ATLAS upgrades for HL-LHC can be found in [24].

1.3.2 CMS

For the HL-LHC program, the CMS detector will undergo a radical upgrade of the tracking system [25]. The new Inner Tracker (IT) will extend to pseudorapidity $|\eta| < 4$ and will consist of approximately

3900 hybrid pixel modules for a total surface area of 4.9 m^2 and 2 billion readout channels. To increase granularity, the IT will have a new pixel pitch of 25×100 μm^2, the thickness will be reduced to 150 µm silicon, and n-in-n silicon will be used instead of the current n-in-p. CMS will also use a combination of 3D and planar pixels for the IT system. The Outer Tracker (OT) will maintain coverage up to $|\eta| < 2.4$ and will integrate an innovative tracking system using double layers of silicon sensors arranged to provide information not only on position but also on transverse momentum (p_T). The system will have sufficient resolution to discriminate particles with p_T above or below about 2 GeV c^{-1}, information that will be used for the trigger decision. Two types of modules are employed in the OT: Pixel-Strip (PS) modules, used at radii less than 60 cm from the interaction point, and Strip-Strip (2S) modules for longer radii, both with pitches of about 100 µm.

A new MIP Timing Detector (MTD) will also be introduced during the upgrade. This system will provide precise time information with a resolution on the order of 30 ps for charged particle tracks, allowing the 4D-Tracking presented in the previous section and decreasing pile-up effects. The MTD is divided into two main components: the Barrel Timing Layer (BTL) and the Endcap Timing Layer (ETL). The BTL uses Cerium-doped Lutetium Yttrium OxyorthoSilicate (LYSO(Ce)) crystals coupled with Silicon PhotoMultiplier (SiPM) sensors to achieve precise time resolution over a large area (∼38 m^2) while maintaining high performance even at moderate neutron equivalent fluence (∼2 × 10^{14} n_{eq}/cm^2). To address radiation damage, thermoelectric cooling systems will be installed to lower the operating temperature and optimize the performance of SiPMs. For the endcap regions, where fluence reaches higher values (∼2 × 10^{15} n_{eq}/cm^2), CMS will also adopt the LGAD technology. These sensors will allow a time resolution of 30 to 50 ps.

CMS's new High Granularity Calorimeter (HGCAL) calorimeter also uses advanced silicon technologies to address the high radiation tolerance and precision requirements of the HL-LHC program. The new calorimeter will be instrumented with silicon sensors for the electromagnetic section and for the areas of the hadronic calorimeter exposed to the highest levels of radiation. In the less irradiated areas of the hadronic calorimeter, plastic scintillating tiles with direct readout via integrated SiPMs will be used. The system involves nearly 600 m^2 of silicon sensors with about 6 million readout channels and about 370 m^2 of scintillating tiles with SiPMs using 240,000 readout channels. A summary of the main CMS upgrades for HL-LHC is given in [25].

1.3.3 LHCb

The LHCb detector upgrade aims to take full advantage of the opportunities offered by the HL-LHC program through two main phases: Upgrade I and II [26]. During Upgrade I, which was completed in Long Shutdown 2 (LS2), all detector subsystems were upgraded or replaced to operate at an increased luminosity of 2 × 10^{33} $cm^{-2}s^{-1}$ and handle more pile-up. The tracking system has been completely redesigned: the VErtex LOcator (VELO) is now installed and consists of a hybrid pixel detector comprising 52 modules with four sensors each. Each sensor comprises 256×256 pixel with a pitch of 55×55 μm^2 and improves spatial and time resolution compared with the previous detector. The new Upstream Tracker (UT) includes four layers of silicon strips, offering greater granularity to handle the increased particle density. The downstream taker system has been replaced by the Scintillating Fiber Tracker (SciFi), a detector based on 2.5 m long scintillating fibers with a diameter of 250 µm and read by SiPM; the system provides higher resolution and radiation resistance.

The Upgrade II, planned for LS4[4], is designed to operate at a maximum luminosity of $1.5\times10^{34}\text{cm}^{-2}\text{s}^{-1}$, corresponding to an average pileup of 40 collisions per bunch crossing in LHCb. To handle this challenge, a further increase of the granularity and radiation tolerance of all sub-detectors is planned. The tracking system will include the VELO and UT upstream of the magnet made with 3D silicon pixels, with a time resolution of ~50 ps, and Monolithic Active Pixel Sensors (MAPS), respectively. Downstream of the magnet, the new Mighty Tracker will consist of MAPS for the inner region and scintillating fiber for the outer region. The Particle IDentification (PID) system will include Ring Imaging CHerenkov (RICH) detectors with SiPMs for higher granularity and better timing. The Time Of internally Reflected CHerenkov light system (TORCH) will be introduced with SiPM/MCPs readout for time-of-flight measurements. With track time resolution on the order of tens of picoseconds, the new LHCb will be able to associate charged tracks with the correct interaction vertices even under high pile-up conditions [26].

1.3.4 ALICE

The ALICE experiment also planned a multi-stage upgrade [27]. The upgrade of the Inner Tracking System 2 (ITS2) during LS2 introduced significant improvements in the ALICE tracking system, particularly improving the pointing resolution. The new ITS2 is lighter than the previous detector, with an active area of about $10\,\text{m}^2$, and is currently the largest tracker based on MAPS sensors, the ALICE PIxel DEtector (ALPIDE) [28]. The structure of the new ITS2 includes three inner layers, with radii of 23 mm, 31 mm and 39 mm, each corresponding to 0.35 percent of a radiation length. These layers form the inner barrel detector, which helps improve the pointing resolution by a factor of 3 compared with the previous version. The outer barrel consists of two pairs of layers that cover the radii up to the inner radius of the Time Projection Chamber (TPC). The muon system has also been further extended with the introduction of the Muon Forward Tracker (MFT), a set of 5 tracking disks. This new tracker uses the same ALPIDE sensor developed for ITS2, allowing muon tracks to be associated to a primary vertex.

The next ALICE detector upgrade, ITS3, during LS3 will significantly improve the ITS to optimize vertex reconstruction accuracy and tracking by bringing the inner barrel layer closer to the interaction point while minimizing the material budget. MAPS in a 65 nm Complementary Metal-Oxide-Semiconductor (CMOS) process are identified as the optimal candidate thanks to the low power consumption and the possibility of integrating power and data lines into the sensors. Wafer-scale sensors will be produced by exploiting the CMOS stitching technique [29]. The sensors thinned to 20 to 40 µm will be bent to form rigid half cylinders, significantly reducing structural material. This system will improve pointing resolution by a factor two and increase tracking efficiency for low p_T particles.

Looking ahead, ALICE 3 installation planned for LS4, represents a radical step forward. An entirely new detector will be installed, consisting of 11 barrel layers and 24 endcap disks, capable of measuring secondary vertices with a resolution of 2.5 µm and offering broad PID capabilities with acceptance in pseudorapidity up to $|\eta| < 4$. It will integrate a Time Of Flight (TOF) system with a time resolution of 20 ps to identify low-energy particles, a RICH detector to separate electrons, pions, protons, and

[4] LS4 at HL-LHC expected for 2034-35 at the time of writing

kaons up to 14 GeV c^{-1}, an electromagnetic calorimeter, a 2 T solenoidal field, and a muon detector. Most of the detectors for ALICE 3 will be silicon-based and focus on technologies with excellent spatial and time resolutions, such as MAPS, LGADs, and SiPMs [27].

1.4 Beyond LHC: Future Lepton Colliders

The future generation of accelerators and experiments are already under consideration Although, as shown in Figure 1.3, several years of HL-LHC operation are planned.

The latest European Particle Physics Strategy Update (EPPSU) in 2020 [30] identified that *"an electron-positron Higgs factory is the highest-priority next collider"*. Such colliders will offer a unique capability to investigate the Higgs boson, top quarks and possible new particles and phenomena BSM. By enabling high-precision measurements in very clean environments, the new accelerators and experiments will aim to address unresolved questions within the SM, continue precision measurements, or explore potential BSM phenomena that persist after the operation of the HL-LHC.

1.4.1 Physics Program

LC collide fundamental and point-like particles, unlike protons, which have a complex structure composed of partons. In LC, the total center of mass energy is available to produce high-energy reactions, making them more efficient than proton colliders, at the same energy and luminosity. LC allow physical phenomena to be explored with greater precision, making experiments much more effective in the study of fundamental interactions. An overview of the physics accessible to future LC is given in [31] and includes:

Precision Probes of SM physics

- High statistics study of the Higgs boson production and decay mechanism
- Precision measurements of the mass, width, and quantum numbers of the Higgs boson, a free parameter of the SM
- Precision measurements on the SM with a focus on Z, W, and top quark properties
- Precision measurements of the ElectroWeak (EW) symmetry-breaking processes

Direct Searches for BSM physics

- Search for new particles produced via the EW interaction with masses up to several TeV
- Search for new force-carrying vector bosons predicted by different BSM theories
- Search for deviations from SM predictions, and new particles probing BSM theories
- Testing of composite Higgs theories, which suggest that the Higgs boson is composed of other elementary particles

Table 1.1: Main parameters of future lepton colliders. $\sqrt{s}$ is the center of mass energy, $\mathcal{L}$ refers to instantaneous luminosity per detector and $\mathcal{L}_{\text{int}}$ is the total integrated luminosity. Adapted from [31]

Collider	**Geometry**	$\sqrt{s}$ [GeV]	$\mathcal{L}$ [10^{34} cm^{-2}s^{-1}]	**Time** [years]	$\mathcal{L}_{\text{int}}$ [ab^{-1}]
ILC	Linear	250	1.35–2.7	11.5	2
		350	1.6	1	0.2
		500	1.8–3.6	8.5	4
CLIC	Linear	380	1.5	8	1
		1500	3.7	7	2.5
		3000	6	8	5
FCC-ee	Circular	91	100–200	4	150
		161	25	1–2	10
		240	7	3	5
		365	0.8–1.4	5	1.5

- Search for dark matter and weakly interacting particles

1.4.2 Lepton Colliders Proposals

Several proposals for future LC have been made in recent years. The main design parameters of the three most mature proposals at the time of writing are shown in Table 1.1.

The International Linear Collider (ILC) [32] is a 31 km LC based on 1.3 GHz superconducting radio frequency acceleration technology. Designed to operate at center-of-mass energies between 250 GeV and 500 GeV, it also envisions future upgrades to 1 TeV. The machine plans a phased schedule, starting with collisions at 500 GeV, then moving to energies of 250 GeV and 350 GeV. The ILC, with minor modifications, could also operate at lower energies, such as 91 GeV, improving EW parameter measurements.

The Compact Linear Collider (CLIC) [33] is an ambitious project based on an innovative acceleration technology with electric-field gradients up to 100 MV m^{-1}. This approach allows CLIC to achieve high-energy collisions, with a schedule starting at 380 GeV and extending up to 3 TeV. The project is developed in three phases, each with specific integrated luminosity goals, and the entire program will be completed in about two decades. The first phase focuses on 380 GeV collisions for precision physics, followed by subsequent phases at 1.5 TeV and 3 TeV, allowing for exploration of higher energy scenarios and adapting to any new experimental discoveries.

The Future Circular Collider electron-positron (FCC-ee) [34] is also designed to operate at multiple energy levels. It will focus on collisions at the Z pole (91 GeV), at the W^+W^- threshold (161 GeV), at the maximum production energy of the Higgs boson associated with a Z boson (240 GeV), and collisions up to 365 GeV to study top quark pairs. This collider stands out for its ability to achieve extremely high luminosities, up to $\sim 2 \times 10^{36}$ cm^{-2}s^{-1} at 91 GeV. However, the luminosity of circular colliders decreases rapidly with increasing energy due to synchrotron radiation losses. This feature contrasts with LCs, whose luminosity is planned to increase with the collision energy.

1.5 Key Technologies Research and Development

In June 2020, the EPPSU [30], which is reviewed and updated every five years, adopted a set of recommendations outlining an ambitious vision for the HEP experimental program, with a perspective spanning on several decades. Among these recommendations, a key requirement was the creation of a roadmap for detector Research and Development (R&D) with the goal of: *"identify and describe a diversified detector R&D portfolio that has the largest potential to enhance the performance of the particle physics program in the near and long term"*. In line with these recommendations, in October 2021, the European Committee for Future Accelerators (ECFA) defined a roadmap [35]. This roadmap highlights the essential detector R&D activities necessary to fully leverage: the HL-LHC, long-baseline neutrino detectors, future e^+e^- Higgs-EW-Top factories, future hadron and muon colliders as well as accelerator-based studies of rare processes. Additionally, it addresses detector R&D for non-accelerator-based experiments, considering neutrino observatories and other areas intersecting with astroparticle physics.

This work develops in this context. The following sections provide a brief description of some key R&D activities identified by ECFA that align with the research described in this thesis.

1.5.1 CMOS MAPS Sensors

MAPS produced using standard CMOS imaging technologies allow achieving exceptional spatial resolution in Minimum Ionising Particles (MIP) detection in the order of a few micrometers [36]. By integrating the signal readout circuitry directly into the sensing element, MAPS reduce the material budget of a detector system, hence multiple scattering, further improving track and momentum resolution in practical tracking and vertexing applications. Recent advances have also made MAPS able to tolerate significant radiation exposures through innovations in engineering and manufacturing processes [37].

Advances in CMOS technology, particularly with technologies smaller than 100-180 nm, allow even smaller pixels, hence better spatial resolution, and the integration of the circuitry needed to handle high particle rates in various applications. Reduced feature size also implies lower power consumption and reduced cooling requirements[5], as well as significant improvement in radiation tolerance. In addition, stitching techniques [29] enables the production of large CMOS MAPS sensors, which are essential for building wide-area trackers. These properties make MAPS one of the ideal candidates for some of the HL-LHC trackers (Section 1.3) as well as one of the key technologies for future LC detectors (Section 1.4).

To meet the growing needs, research on MAPS is focused on several aspects: development of MAPS in sub-micrometers nodes, studying of stitching processes for large sensors, optimization of sensor and electronics design for precise timing, low granularity and low power MAPS for large-scale tracking and calorimetry detectors [35].

[5] Resulting in less materials in tracking systems

1.5.2 Sensor for 4D-Tracking

In recent years, silicon sensors have been increasingly used in high-precision timing systems. In future detectors, such as TOF systems or large 4D-trackers, requiring simultaneous tracking and timing accuracy, further advancement in performance is needed. There is also growing interest in improving the temporal performance of calorimeters by introducing fast silicon detectors in these systems. Thus, 4D-tracking will help not only to mitigate collision pile-up and beam-induced background but also to improve tracking accuracy and detailed reconstruction of particle showers. The required temporal accuracy is about 30 to 50 ps for the HL-LHC detectors, and up to 10 to 20 ps for the TOF/tracking systems for future Higgs-EW-top factories. The spatial resolution required for 4D-tracking sensors varies, ranging from the millimeter scale to less than 10 µm for the most demanding applications [38].

The main specifications of 4D-Trackers are generally defined in terms of spatial and temporal accuracy. However, other key parameters determine the overall architecture, including detection efficiency, material budget, power consumption, area, and, in some cases, radiation hardness. ECFA identifies planar LGADs, 3D sensors and BiCMOS MAPS as major technology candidates for future 4D-trackers [35]. This work expands the list of candidates by exploring the potential of CMOS Single-Photon Avalanche Diode (SPAD) arrays, as discussed in Part I of this thesis.

1.5.3 Semiconductor Photo-Detectors

SiPMs are nowadays considered the leading solid-state photo-detector devices, with wide applications in particle physics experiments, and other research and industrial fields [39]. A detailed overview of this technology is provided in Section 4.1. Currently, most SiPM-based systems use an analog design. These sensors have achieved a highly efficient production with low cost, high Photon Detection Efficiency (PDE), and effective control of major noise sources. On the other hand, Digital Silicon PhotoMultiplier (dSiPM), represent an attractive alternative, promising better performance and unique advantages in some applications.

To meet the challenges of future experiments, both SiPMs and dSiPMs require further development. Major areas for improvement include PDE, radiation tolerance, fast timing capabilities, further noise reduction, cell size optimization, dynamic range, operability at cryogenic temperatures, and the development of dedicated fast and low-power readout electronics. The effectiveness of (d)SiPM in light detection is related to the context of the specific experiment, as the optimal performance characteristics vary depending on the intended application. For example, the ability to achieve fast timing with SiPMs when coupled with radiators depends not only on the sensors but also on input characteristics, such as the light output of the radiator, and the spectral and temporal properties of the emitted photons. Other factors to consider include light collection efficiency and optical coupling techniques. In addition, readout electronics for fast timing with (d)SiPMs must balance the needs for low power consumption, reduced noise, and compatibility with cooling systems, particularly in cryogenic and large-scale applications.

The increasing use of SiPM in industrial applications ensures that R&D activities for future HEP detectors will benefit from advances in this field, emphasizing the importance of collaboration between science and industry [35].

CHAPTER 2

Physics of Solid-State Detectors

Chapter 1 showed how solid-state detectors, particularly silicon-based technologies, are essential components of current and future High-Energy Physics (HEP) detector systems. Solid-state detectors operate similarly to ionization chambers, exploiting the generation and movement of charge carriers in semiconductors to produce detectable signals [40]. This chapter summarizes the principles governing the operation of solid-state detectors, which are the subject of study in this thesis. Section 2.1 describes the fundamentals of semiconductors, from doping to pn-junctions and their depletion, which enable the creation of a charge-sensitive volume. Section 2.2 discusses the mechanisms of energy loss by charged particles, while Section 2.3 focuses on the main interactions of photons. In Section 2.4, the mechanisms of charge generation, transport, multiplication, signal formation, and read-out in solid-state detectors are elaborated. Finally, Section 2.5 presents some of the properties of interest in this work of solid-state detectors.

2.1 Semiconductors Basics

Common semiconductor materials include group-IV elements. Of these, silicon is the most widely used in the semiconductor industry and HEP detectors. Although other semiconductor materials are used for specialized applications, silicon remains the material of choice in many applications due to its optimal electrical characteristics, practical advantages, and the widespread diffusion of silicon in industry. A comprehensive discussion of concepts related to the physics of semiconductor devices and the relevant properties of silicon is given in [40], serving as a basis for the brief summary here reported.

In semiconductor crystals, overlapping atomic orbitals lead to a shift in energy levels and the formation of distinct energy bands: valence band and conduction band. Electrons are arranged in free energy states according to the Pauli principle. The Fermi-Dirac distribution $f(E)$ describes the probability

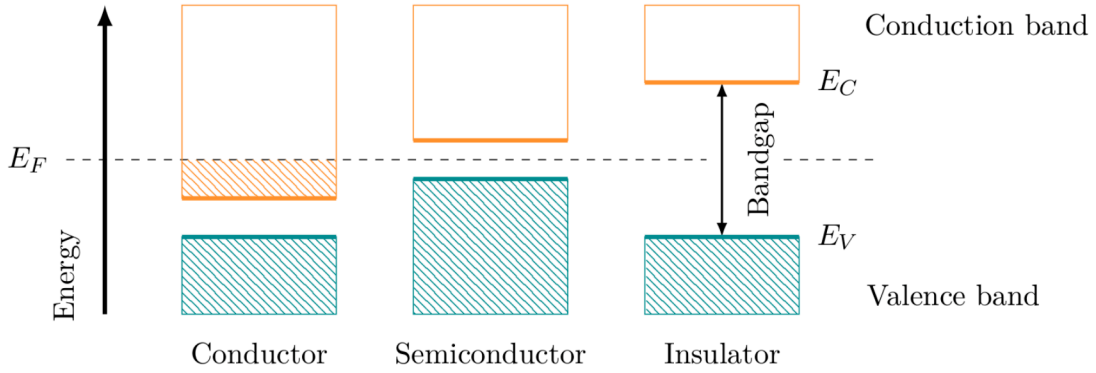

Figure 2.1: Band structure for conductor, semiconductor and insulator materials. From [42].

that a given energy state is occupied by an electron and is defined as:

$$f(E) = \frac{1}{e^{(E-E_F)/(k_B T)} + 1}, \tag{2.1}$$

where E is the energy of the state, k_B is the Boltzmann constant, T is the absolute temperature, E_F is the Fermi energy. E_F is defined as the energy level at which the probability that an electron occupies the energy state is exactly 0.5. In conductor materials, E_F is in the conduction band and the electrons are free to move. In insulator or semiconductor materials, on the contrary, E_F lies above the valence energy E_V and below the conduction energy E_C as shown in Figure 2.1. At very low temperatures (near 0 K), semiconductor materials behave as insulators since their valence bands are completely occupied, thus leaving no electrons available for conduction in the conduction band. However, as these materials are characterized by a narrow energy gap $E_G = E_C - E_V$. With increasing temperature, thermal energy might excite electrons with sufficient energy to reach the conduction band. When an electron is excited in the conduction band, it leaves a vacancy in the valence band, referred to as a hole. The balance between the electron concentration n and the hole concentration p is expressed by:

$$n \cdot p = n_i^2, \tag{2.2}$$

where n_i is the intrinsic carrier concentration. For a pure (intrinsic) semiconductor, this carrier concentration is given by:

$$n_i = \sqrt{N_c N_v} e^{-\frac{E_g}{2k_B T}}, \tag{2.3}$$

where N_c and N_v represent the effective density of states in the conduction and valence band, respectively. For example, at room temperature (300 K), silicon has a $E_G = 1.12\,\text{eV}$ and an intrinsic electron-hole (e-h) density of approximately $n_i \approx 1 \times 10^{10}\,\text{cm}^{-3}$, which corresponds to an intrinsic resistivity of approximately $350\,\text{k}\Omega \cdot \text{cm}$ [41].

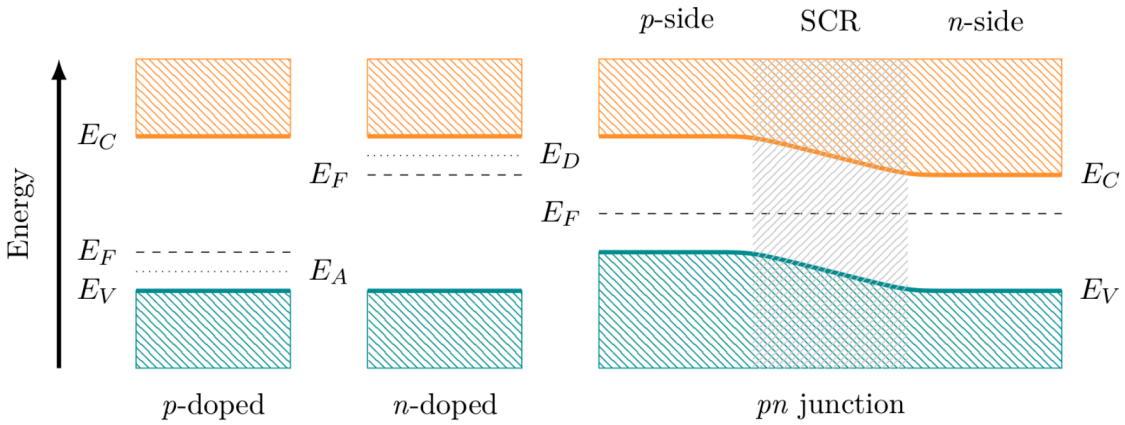

Figure 2.2: Band structure for p-doped (left) and n-doped (center) semiconductors. The band structure representation for a pn-junction (right), the Space Charge Region (SCR) is marked in gray. From [42].

2.1.1 Doping

An *intrinsic semiconductor* does not contain impurities. Doping is a process that consists of introducing impurity atoms into a semiconductor crystal. Impurities can be group-V elements (such as phosphorus or arsenic) or group-III elements (such as boron, aluminum, and gallium). A doped semiconductor is called *extrinsic semiconductor*. When group-V elements, such as phosphorus, are introduced, causing an excess of electrons that act as negative charge carriers. These impurity atoms, known as donors, introduce energy levels E_D close to the conduction band. Extrinsic semiconductors of this type are known as n-type. When group-III elements, such as boron, are introduced, *holes* (the absence of an electron) that act as positive charge carriers are introduced. These impurity atoms, known as acceptors, introduce energy levels E_A near the valence band. Extrinsic semiconductors of this type are known as p-type. In extrinsic semiconductors, most of the charge carriers usually come from the impurities themselves. Doping alters the electrical properties of a semiconductor material but does not change the net charge of the material, as both the silicon and doping atoms are neutral. Doping shifts E_F towards higher values (for n-type) or lower values (for p-type) due to the introduction of new filled energy levels E_D and empty levels E_A. The effect of doping on the Fermi energy is shown in Figure 2.2 left and center. This shift affects the electrical conductivity of the material, which becomes more conductive than intrinsic semiconductor.

2.1.2 The pn-Junction

The pn-junction, a fundamental element in semiconductor devices, is formed by joining p-type and n-type materials. At the interface of the junction, electrons on the n side recombine with the holes on the p side, balancing the different Fermi energies and creating a SCR emptied of charge carriers, gray part in Figure 2.2 right. Within the SCR, the positively charged donor and negatively charged acceptor, bound in the n and p regions, generate an electric field, and a built-in potential V_{bi} is created

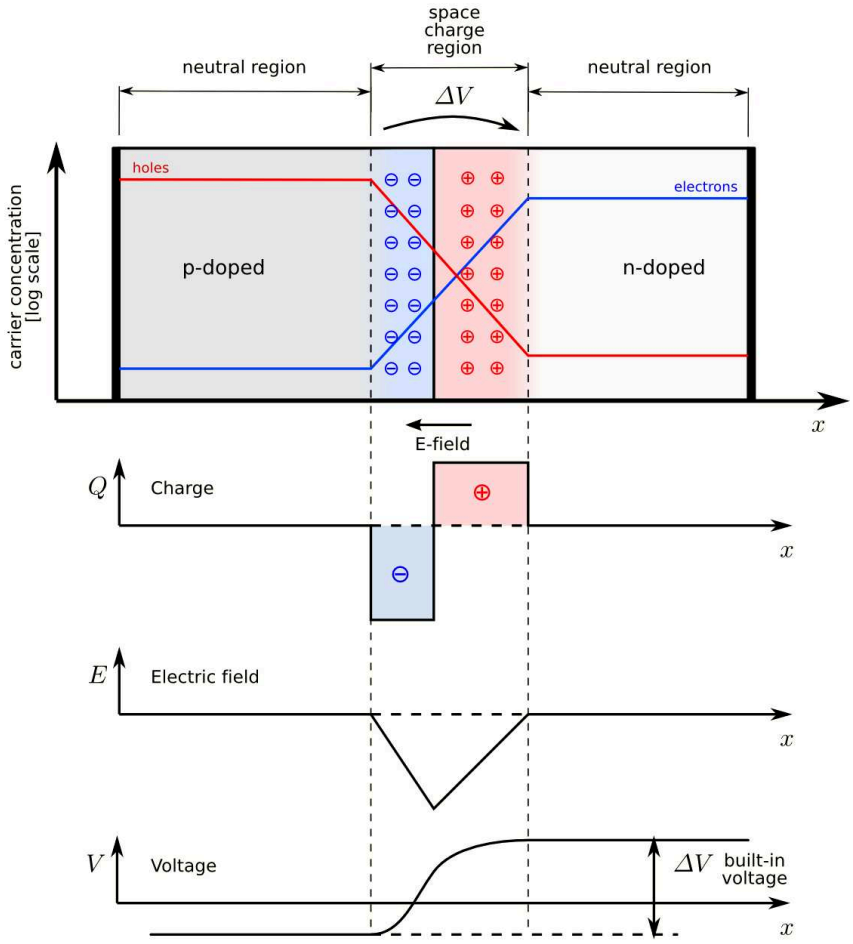

Figure 2.3: Pn-junction structure (a), charge density (b), electric field (c) and built-in potential (d). From [43].

in the junction [40]:

$$V_{\text{bi}} = \frac{k_B T}{e} \ln\left(\frac{N_D N_A}{n_i^2}\right), \tag{2.4}$$

where e is the elementary charge, N_D and N_A are the doping concentrations of donors and acceptors, respectively. For typical doping concentrations in silicon pn-junctions $V_{\text{bi}} \approx 0.4$ to $0.8\,\text{V}$. The structure and properties of a pn-junction are schematically shown in Figure 2.3.

2.1.3 Junction Depletion

By highly doping one side of the junction with respect to the other ($N_D >> N_A$ or $N_A >> N_D$), the depletion region mainly extends into the less-doped side. The depletion region can further be extended by applying an external inverse bias voltage V_{ext} with the same sign as V_{bi}. The width of the depleted

region $d_{n,p}$ can be approximated by the expression [40]:

$$d_{n,p} \approx \sqrt{\frac{2\epsilon\epsilon_0}{e}\frac{1}{N_{D,A}}\left(V_{bi}+V_{ext}\right)}, \tag{2.5}$$

where $d_{n,p}$ represents the depth of the depletion region in the least-doped side of type n or p, ϵ is the permittivity of the semiconductor material, ϵ_0 is the permittivity of the vacuum. Therefore, large regions of depletion can be achieved by using either a high resistivity bulk (low-doped) or a high reverse bias voltage. However, if the reverse bias voltage becomes too high, breakdown will occur, causing a large current flow across the p-n junction. The breakdown voltage depends on both the doping concentration and the geometric layout of the junction.

Thermally generated e-h pairs are created in the depleted region. This effect is strongly influenced by the presence of impurities acting as generation/recombination centers. These carriers generate a constant leakage current I_L, which is proportional to the depleted volume $A \cdot d$, and can be expressed as:

$$I_{\mathrm{L}} = eAd\frac{n_i}{\tau_g}, \tag{2.6}$$

where τ_g is the charge carrier generation lifetime, and n_i is the intrinsic carrier concentration, which depends strongly on temperature, following approximately the law $n_i \propto T^{3/2}\exp\left(-\frac{E_G}{2kT}\right)$. Consequently, the leakage current I_L is also influenced by temperature; it can be demonstrated that:

$$I_L \propto T^2 \exp\left(-\frac{E_a}{2kT}\right), \tag{2.7}$$

where E_a is called the activation energy. For silicon, E_a has a best-fit value of 1.21 eV. At room temperature, typical I_L is in the range of (nA/cm^2). More details in [40].

2.2 Energy Loss of Charged Particles

When a charged particle passes through a medium, it loses energy mainly via ionization, atomic excitation, and bremsstrahlung radiation.

The loss of energy in a material with atomic number Z and mass number A by a charged massive particle with charge z and relativistic parameter[1] β due to ionization and atomic excitation can be described using the Bethe-Bloch formula [44]:

$$-\frac{dE}{dx} = K\frac{Z}{A}z^2\beta^2\left(\ln\left(\frac{2m_e\gamma^2v^2W_{\max}}{I^2}\right) - 2\beta^2 - \delta - 2\frac{C}{Z}\right), \tag{2.8}$$

where K has a value of 0.1535 MeV, m_e is the mass of the electron, $\gamma = \frac{1}{\sqrt{1-\beta^2}}$ is the relativistic factor of the incident particle, $W_{\max}$ is the maximum energy that can be transferred to an electron in the medium in a single collision, and I denotes the average ionization potential of the material. The

[1] Velocity of the particle v relative to the speed of light c, $\beta = v/c$

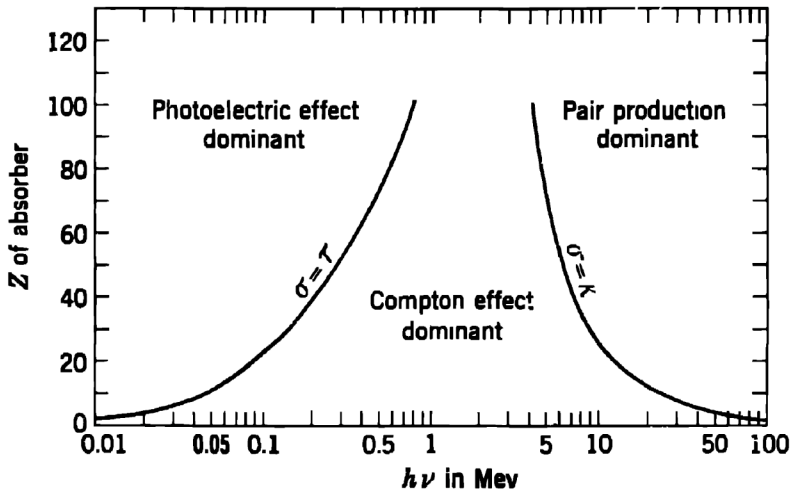

Figure 2.4: Relative significance of the three main types of photon interactions. The lines indicate the values of Z and $h\nu$ where two adjacent effects are equivalent. From [45].

factors δ and C correspond to the density and shell corrections, respectively. This formula provides an accurate description of the average energy loss due to relativistic charged particles in the range of $0.1 < \beta\gamma < 1000$. Additional corrections are necessary for low-energy interactions, while radiative processes become the dominant factor for higher energies.

The minimum energy loss occurs around a value of $\beta\gamma \approx 3 - 3.5$, known as the Minimum Ionising Particles (MIP) region. The Bethe-Bloch formula describes the average energy loss, but since energy loss is a stochastic process, fluctuations occur in both the number of ionization events and the energy transferred in each event [40].

2.3 Interaction of Photons with Matter

When photons pass through a material, they interact mainly through three processes: the photoelectric effect, the Compton effect, and pair production. Figure 2.4 shows the relative weight of these interactions as a function of the photon energy (expressed in terms of Planck's constant multiplied by the photon frequency $h\nu$) and the atomic number of the material (Z). Figure 2.5 shows the cross-section in silicon of the three main interaction processes. A comprehensive discussion of concepts related to the interaction of photons with matter is given in [45], serving as a basis for the brief summary here reported.

Photoelectric Effect

In the photoelectric effect, a photon with energy E_γ is absorbed by an atom, ejecting an electron from one of its bound shells. The kinetic energy of the ejected electron E_e is given by:

$$E_e = E_\gamma - E_b, \tag{2.9}$$

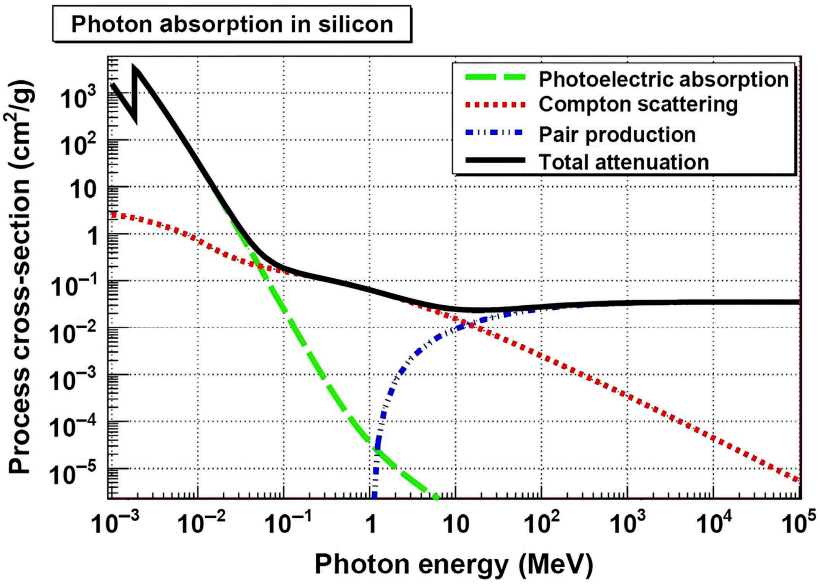

Figure 2.5: Photon absorption cross section in silicon. From [46].

where E_b is the binding energy of the ejected electron. The probability of the photoelectric effect occurring is proportional to Z^4 up to Z^5 and decreases rapidly with increasing photon energy, as shown in the example for silicon in Figure 2.5.

Compton Effect

The Compton effect involves the inelastic scattering of photons by weakly-bound or free electrons. In this process, an incident photon with energy $E_\gamma = h\nu$ is scattered by an electron, resulting in a photon with lower energy E'_γ and an electron recoiled with kinetic energy E_e. The energy transfer to the electron is given by:

$$E_e = \frac{E_\gamma \epsilon(1 - \cos\theta)}{\epsilon(1 - \cos\theta) + 1}, \tag{2.10}$$

where $\epsilon = E_\gamma/(m_e c^2)$ is the ratio of the photon's energy to the electron's rest energy, and θ is the photon's scattering angle. The maximum energy transfer occurs when the photon is scattered backward ($\theta = 180^\circ$).

Pair Production

Pair production occurs when a photon with energy greater than 1.022 MeV (the sum of the rest masses of an electron and positron) interacts with a nucleus, producing an electron-positron pair. This process conserves energy and momentum, with the excess energy of the photon going into the kinetic energy of the particles produced.

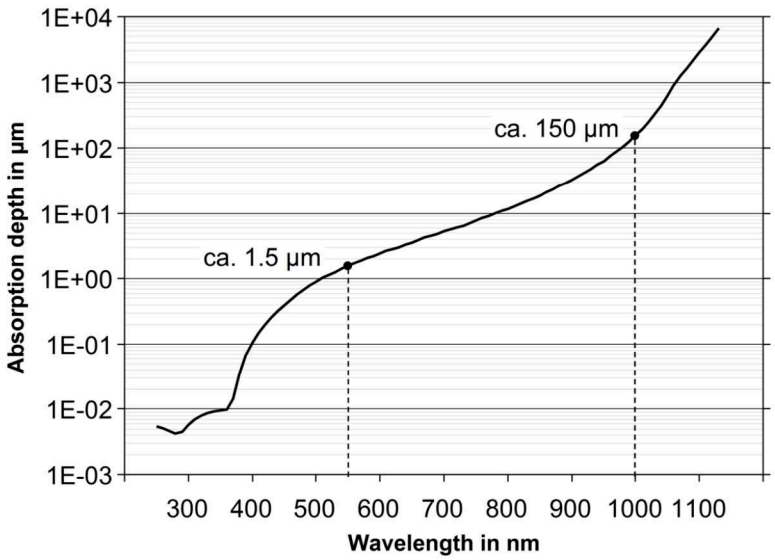

Figure 2.6: Photon absorption depth in silicon at 300 K. From [47].

2.3.1 Attenuation of Photon Intensity

The attenuation of the photon intensity as it passes through a material is given by:

$$I(x) = I_0 e^{-\mu_0 x}, \tag{2.11}$$

where I_0 is the initial intensity, $I(x)$ is the intensity after passing through a thickness x of material, and $\mu_0 = \sigma + \tau + \kappa$ is the total linear attenuation coefficient. The individual coefficients σ, τ, and κ correspond to the processes of Compton scattering, photoelectric absorption, and pair production, respectively.

The absorption depth is the distance at which the intensity I_0 of the light falls to $1/e$ ($\sim$ 37 %) of its initial value due to interactions in the absorbing material. Figure 2.6 shows an example of the average absorption depth in silicon for visible and Near InfraRed (NIR) light.

2.4 Particle Detection with Solid State Detectors

Solid-state detectors exploit the depleted region formed with pn-junctions to detect the energy loss by interacting particles. The mechanisms of charge generation, transport, multiplication, and signal formation are presented in the following sections. The key elements of the typical readout chain are also discussed.

2.4.1 Charge Generation

When charged particles lose energy through ionization, or when a photon is absorbed in a semiconductor detector, a portion of the energy goes into the excitation of charge carriers, creating e-h pairs. To form

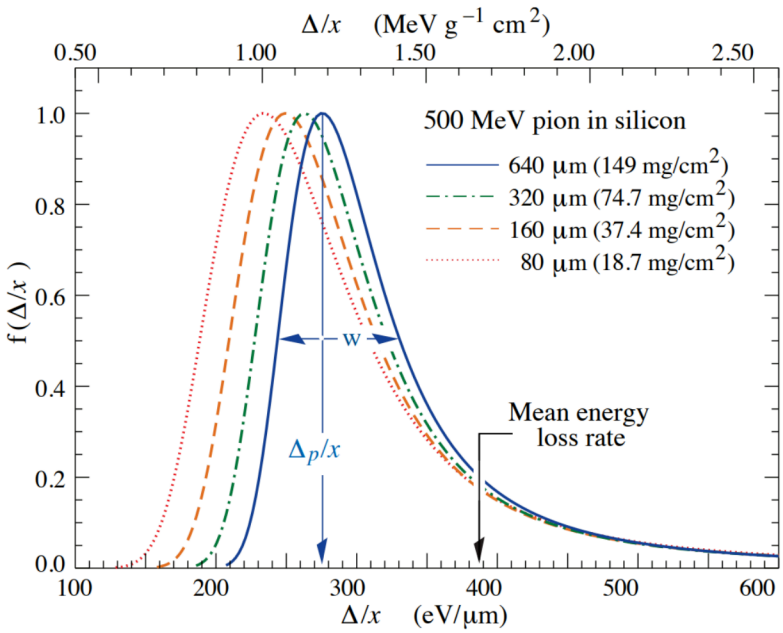

Figure 2.7: Straggling functions in silicon of different thickness for 500 MeV pions, normalized to unity at the maximum. From [48].

an e-h pair, it is necessary to provide an amount of energy at least equal to the band-gap (for silicon $E_G = 1.12\,\text{eV}$). However, part of the energy is dissipated in lattice excitations (phonons), so the average ionization energy w_i to generate an e-h pair is higher and depends on temperature. For silicon at 300 K, $w_i = 3.65\,\text{eV}$, about three times the energy gap between valence and conduction band [40].

The energy loss by particles is subject to fluctuations with occasional significant energy depositions far from the mean energy loss value [48]. The associated energy-loss distributions are referred to as *straggling functions*. Figure 2.7 illustrates the straggling functions for 500 MeV pions in silicon of different thicknesses. In this work, silicon sensors with sensitive layers of 10 µm or thinner are investigated. As described in [49], energy loss distributions in thin silicon sensors can be used to estimate the number of primary e-h pairs generated. The Most Probable Value (MPV) of the energy loss distribution Δ_p in keV is derived as function of the thickness d of the silicon absorber in µm:

$$\Delta_p = d \cdot (190 + 16.3 \ln(d)). \tag{2.12}$$

According to [49], the absolute uncertainty of Δ_p is below 1 % for electrons, pions, and protons with $\beta\gamma > 100$.

Evaluating Δ_p with a thickness of 10 µm results in a energy loss MPV of 2.3 keV. Considering the mean ionization energy in silicon at room temperature of 3.65 eV [40], this corresponds to an expected MPV of 630 e-h pairs. In this work, the energy loss distributions obtained from measurements are fitted using a convolution of a Landau and a Gaussian function.

The number of intrinsic or extrinsic charge carriers in a semiconductor is significantly greater than the charge generated by the interaction of particles. Depleted pn-junctions, described in Section 2.1.3, are

therefore used in particle detection as they are emptied of free charge carriers. In this configuration, applying an external electric field accelerates the generated charges, allowing the particle signal to be detected.

2.4.2 Charge Transport

The generated e-h pairs move inducing a signal at the junction electrodes. In a semiconductor, there are two main mechanisms for charge transport: diffusion and drift. Diffusion is caused by thermal motion here briefly described. This section is based on [40], which provides a comprehensive discussion on the topic.

The gradient in carrier concentration ∇n, p generates a diffusion current $\vec{j}_{diff}$, which for the density of electrons n and holes p is expressed as:

$$\vec{j}_{n,\text{diff}} = -eD_n \nabla n, \quad \vec{j}_{p,\text{diff}} = -eD_p \nabla p, \tag{2.13}$$

where $D_{n,p}$ represents the diffusion coefficient for electrons and holes, respectively, and is specific to the semiconductor material. Diffusion occurs without the influence of an electric field and is characterized by slow transport and stochastic dispersion of the charge.

When an electric field $\vec{E}$ is present, charges are accelerated in the direction of the field, scattering with phonons and lattice defects. The drift velocity of the carrier is given by:

$$\vec{v}_{Dn} = -\mu_n \vec{E}, \quad \vec{v}_{Dp} = -\mu_p \vec{E}, \tag{2.14}$$

where μ_n and μ_p are the mobilities of electrons and holes, respectively. At low electric fields, the mobilities remain relatively constant, while at higher fields (above about $1 \times 10^5\,\text{V}\,\text{cm}^{-1}$) the mobilities decrease, resulting in saturation of the drift velocity (v_{sat}). For silicon, typical values for the mobilities are $\mu_n(\text{Si}) = 1\,450\,\text{cm}^2\,\text{V}^{-1}\,\text{s}^{-1}$ and $\mu_p(\text{Si}) = 500\,\text{cm}^2\,\text{V}^{-1}\,\text{s}^{-1}$, while the saturation velocity is approximately $v_{\text{sat}} \approx 1 \times 10^7\,\text{cm}\,\text{s}^{-1}$. The drift motion leads to a drift current described as:

$$\vec{j}_{\text{drift}} = \frac{1}{\rho}\vec{E}, \tag{2.15}$$

where ρ is the electrical resistivity, which is defined as:

$$\rho = \frac{1}{e(n\mu_n + p\mu_p)}, \tag{2.16}$$

In a doped semiconductor, the density of charge carriers n and p is generally determined by the doping concentration N_A and N_D (Defined in Equation 2.4), which is usually much higher than the intrinsic carrier density.

Table 2.1: Impact ionization phenomenological parameter in silicon from [51].

Parameter	**Electrons (e)**	**Holes (h)**
A	$4.43 \times 10^5\,\mathrm{cm}^{-1}$	$1.13 \times 10^6\,\mathrm{cm}^{-1}$
C	$9.66 \times 10^5\,\mathrm{V\,cm}^{-1}$	$1.71 \times 10^6\,\mathrm{V\,cm}^{-1}$
D	$4.99 \times 10^2\,\mathrm{V\,cm}^{-1}\,\mathrm{K}^{-1}$	$1.09 \times 10^3\,\mathrm{V\,cm}^{-1}\,\mathrm{K}^{-1}$

2.4.3 Charge Multiplication

Charge multiplication in semiconductors happens when charge carriers encounter an electric field $\vec{E}$ exceeding approximately $300\,\mathrm{kV\,cm}^{-1}$. In this high-field region, primary charge carriers $N_{0\,e,h}$, gain enough kinetic energy to create, via impact ionization, secondary e-h pairs, amplifying the signal [50]. The number of $N_{e,h}(d)$ of e-h produced by the avalanche effect depends exponentially on the impact ionization coefficient $\alpha_{e,h}$ and the distance d traveled in the high electric field region:

$$N_{e,h}(d) = N_{0\,e,h} e^{\alpha_{e,h} d}. \tag{2.17}$$

The inverse of the ionization coefficients $\alpha_{e,h}$ represents the average free path between two consecutive ionization events generating secondary charges, defined as $\lambda = \frac{1}{\alpha}$. For the same electric field, this distance is smaller for electrons (λ_e) than for holes (λ_h). Impact ionization occurs on average when a charge carrier travels a sufficient distance ($\sim \lambda$) to acquire a kinetic energy equal to or greater than the average ionization energy w_i.

The ionization coefficients $\alpha_{e,h}(\vec{E}, T)$ can be defined using a simplified model of avalanche multiplication, the Massey model [51]:

$$\alpha_{e,h}(\vec{E}, T) = \frac{1}{\lambda_{e,h}(\vec{E}, T)} = A_{e,h} e^{-B_{e,h}(T)/\vec{E}}, \tag{2.18}$$

where $A_{e,h}$ and $B_{e,h}(T)$ are phenomenological parameters, distinct for electrons and holes. The dependence of the $B_{e,h}$ parameters on temperature T introduces a relationship between the ionization coefficients $\alpha_{e,h}(\vec{E}, T)$ and temperature: at lower temperatures (smaller phonon population), the average distance required for multiplication is shorter, which leads to an increase in gain [52]. $B_{e,h}(T)$ can be expressed as:

$$B_{e,h}(T) = C_{e,h} + D_{e,h} \cdot T. \tag{2.19}$$

Typical values of A, C, and D for silicon are given in Table 2.1. Other commonly used impact ionization models include the Van Overstraeten-De Man model [53], the Okuto-Crowell model [54], and the Bologna model [55].

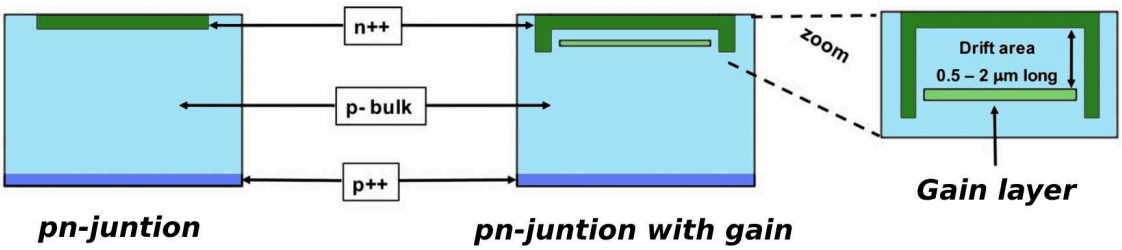

Figure 2.8: Sketch of n-in-p junction with additional gain layer. Adapted from [52].

The gain G of the avalanche process is defined as the ratio of the total number of e-h pairs generated $N_{e,h}$ to the number of primaries e-h pairs $N_{0\,e,h}$:

$$G = \frac{N_{e,h}}{N_{0\,e,h}}. \tag{2.20}$$

The avalanche process can be achieved in semiconductor pn-junctions in very localized regions by implanting an additional heavily doped gain layer, as shown schematically in Figure 2.8. Heavy doping results in to a large space charge after depletion generating an electric field $\vec{E}$ high enough to activate the avalanche process described. The intensity of the electric field, which also depends on the reverse bias applied to the junction, determines the gain G of the avalanche processes. For moderate gains (10-1000), the proportionality between $N_{0\,e,h}$ and $N_{e,h}$ is maintained. If the junction is, instead, operated in Geiger mode [56], gains larger than 10^6 can be achieved. In this regime, the proportionality between the primary charge and the charge produced via impact ionization is no longer maintained. The generated charges begin to neutralize in the inner regions of the avalanche due to a high recombination probability caused by the high charge density [40].

2.4.4 Signal Formation

The movement of the generated charge carriers in the sensor's electric field induces a signal on the electrodes, as described by the Shockley-Ramo theorem [40]. The instantaneous current generated by a single charge carrier $q = e$ moving with a velocity v is expressed by:

$$i_{e/h} = -\frac{dQ}{dt} = e\,\vec{\mathcal{E}}_w \cdot \vec{v}, \tag{2.21}$$

where the weighted field $\vec{\mathcal{E}}_w$ represents the property that determines how the movement of charges couples to a given electrode, depending on the spatial arrangement of the electrodes. The total charge Q induced on an electrode is:

$$Q = \int_{t_1}^{t_2} i_{e/h}(t)\,dt, \tag{2.22}$$

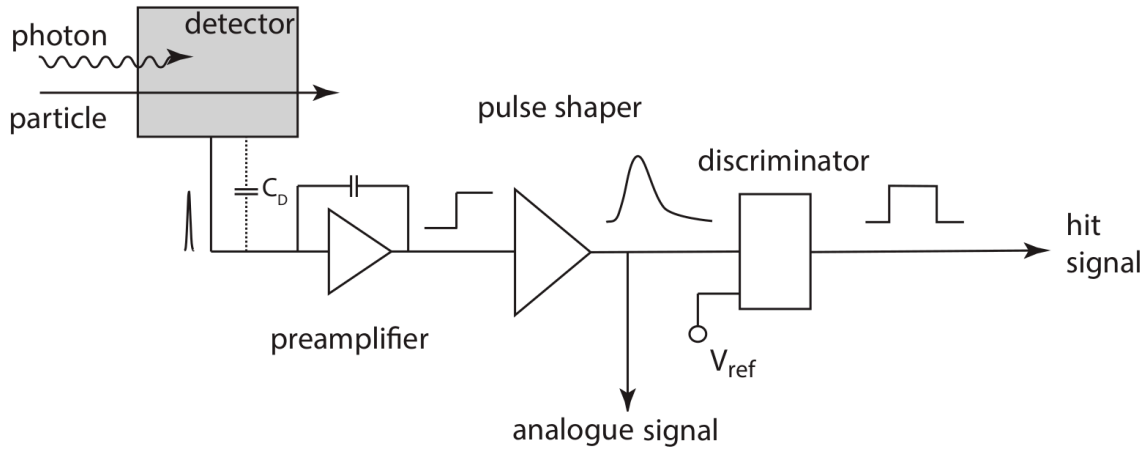

Figure 2.9: Typical detector signal readout chain. Adapted from [40].

where $t_2 - t_1$ is the integration time interval. Due to the diffusion of the charge cloud (or inclined tracks), the total charge can be distributed among several electrodes in segmented detectors (described in Section 2.5). This process is usually called *charge sharing*.

2.4.5 Detector Readout

The charge collected from individual electrodes in a solid-state detector is processed by the front-end electronics in order to extract the hit information. A typical signal readout chain is illustrated in Figure 2.9. The current induced in the collection electrode is delivered to the input of a preamplifier. This represents the first, or only, amplification stage of the readout chain. Typically, the preamplifier acts as an integrator of the input current producing a voltage at the output that is proportional to the signal charge. This can be realized by implementing a capacitive feedback circuit. A shaper is usually used as the next stage to obtain a pulse returning to the baseline level, ideally producing an output signal proportional, in amplitude and/or duration, to the signal induced in the electrode. At this stage, the amplified analog pulse is available for subsequent signal processing stages that depend on the specific application. The analog signal can, for example, be digitized using an Analog to Digital Converter (ADC). A discriminator can be employed for the digitization of the signal. In the simplest version, the discriminator compares the voltage of the input signal with a reference voltage V_{ref}, and each time the signal exceeds V_{ref}, a digital signal of fixed width is generated as output, hit signal in figure 2.9. The signal thus processed is then transmitted to the back-end electronics, which collects information from different electrodes for further signal processing and/or final storage [40].

2.4.6 Hybrid and Monolithic Detectors

Solid-state detectors can be classified as hybrid or monolithic, depending on the method of integration of the readout electronics [40].

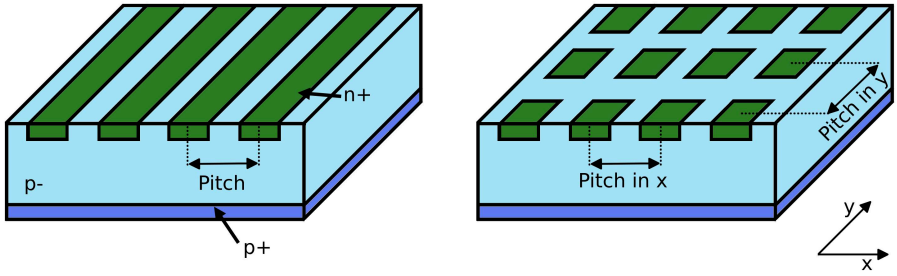

Figure 2.10: Sketch of n-in-p strip (left) and pixel (right) detector segmentation.

Hybrid detectors consist of two parts: a sensitive sensor and an Application Specific Integrated Circuit (ASIC) containing the front-end electronics. These two elements are thus connected by solder or wire bonding techniques. The main advantage of this technology is the ability to separately optimize the sensor and readout chip, allowing advanced industrial processes or innovative concepts to be adopted in the optimization of the sensor and/or the electronics. The main disadvantages of this technology include an increase in overall material, higher fabrication costs, and electrode granularity potentially limited by the bonding technology used.

In monolithic detectors, the readout electronic is integrated directly into the same silicon, eliminating the need for connections between the sensor and the ASIC. These sensors can be manufactured using standard Complementary Metal-Oxide-Semiconductor (CMOS) processes, leading to a reduction in material required and production costs. The main challenge in monolithic detectors is the simultaneous integration and optimization of the active sensor and integrated electronics, which can be located either at the periphery of the sensor or in electrode proximity.

2.5 Solid State Detectors Properties

Solid state detectors are generally segmented to achieve higher position resolution and reduce the input capacitance to the front-end electronics. There are two main segmentation approaches: strip and pixel detectors with segmentation in one or two dimensions, respectively. A sketch of n-in-p strip and pixel detectors is shown in Figure 2.10. The distance between units in one dimension, pixel or strip, is usually called *pitch* and, in current HEP applications, is on the order of tens of micrometers.

2.5.1 Spatial Resolution

The error on the position measurement that a sensor provides is called *spatial resolution*. An interaction in a segmented solid-state Device Under Test (DUT) can generate a signal in one or more electrodes, i.e. pixels or strips. To simplify the nomenclature, the case of segmented pixel detectors is analyzed from now on. A group of pixels sharing the charge deposited by the same particle interaction is called *cluster*. The cluster is used to determine the particle interaction position, exploiting the information available in the pixels involved. The more information available, the better the accuracy with which the particle interaction position can be determined. A DUT with a binary response (hit/no-hit) and the

charge collected in a single pixel with pitch p will have a spatial resolution σ_{DUT} given by [40]:

$$\sigma_{DUT} = \frac{p}{\sqrt{12}}. \tag{2.23}$$

Better spatial resolutions can be obtained by exploiting charge sharing between pixels. If the charge information is available, the cluster's center is usually calculated as the charge-weighted average of the position of the pixels in the cluster; this clustering technique is known as the center of gravity algorithm.

The spatial resolution of a DUT σ_{DUT} in particle detection can be extracted from the width of unbiased spatial residual distribution $\sigma_{redisuals}$. The unbiased spatial residual is defined as the difference between the position of the particle interaction on the DUT, reconstructed independently using a reference system with pointing resolution σ_{ref}, and the particle interaction position reconstructed by the DUT, i.e. the center of the cluster. The spatial resolution of the DUT can be obtained by subtracting quadratically the reference system pointing resolution from the measured unbiased residuals width:

$$\sigma^2_{DUT} = \sigma^2_{residuals} - \sigma^2_{ref}. \tag{2.24}$$

2.5.2 Time Resolution

The temporal performance of a solid-state detector is the result of a complex interplay between sensor and read-out electronics properties, discussed in [57] and here summarized. The overall time resolution σ_t arises from various components that are quadratically summed:

$$\sigma^2_t = \sigma^2_{TS} + \sigma^2_{Landau} + \sigma^2_{Dist.} + \sigma^2_{Jitter} + \sigma^2_{TDC}, \tag{2.25}$$

the components are:

- The time slewing term σ_{TS} (or time walk) is typical for sensors where the signal is proportional to the deposited charge and a fixed discrimination threshold is used. The deposited charge is distributed according to straggling functions described in Section 2.4.1. This generates signals of different amplitudes that cross the threshold with different delays, causing fluctuations in the Time Of Arrival (TOA). This contribution is generally reduced by using sensor layouts that generate large and short signals and setting the discrimination thresholds at the maximum slope of the signal. The contribution can be minimized using Constant Fraction Discrimination (CFD) circuits or corrected if the amplitude of the signal is known.

- The Landau term σ_{Landau} is dominated by the non-uniformity in the deposition of charge within the sensor, resulting in non-uniformity in the induced signal. Signal shape variations cannot be corrected; however, it is possible to minimize their effect by design.

- The Distortion term $\sigma_{Dist.}$ is related to the non-uniformity of the weighting field and drift velocities within the sensor. It can be minimized by design by striving for uniform drift velocity (possibly saturated) and ensuring uniformity of the weighting field, e.g. by using parallel plate geometries for the collection electrode with $width \sim pitch >> thickness$

- The Jitter term σ_{Jitter} is due to the presence of electronic noise superimposed to the signal, leading to fluctuations of the crossing time at the chosen discrimination threshold. This contribution is directly proportional to the electronic noise and inversely proportional to the slope of the signal at the threshold. It can be minimized by using low-noise technologies and selecting threshold values where the signal slope is maximum.
- The term σ_{TDC} is related to the accuracy of the Time to Digital Converter (TDC) used in the TOA measurement. This term is directly related to the binning of the TDC by the relation: $TDC_{bin}/\sqrt{12}$. Although this term can be minimized by choosing the appropriate TDC, it is certainly not obvious that this contribution is negligible. The performance of TDCs in detectors may be limited by available space, technology, power consumption, and costs.

Similar to what was shown in the previous section for spatial resolution, the time resolution of a DUT can be measured using a reference detector. The difference between the TOA measured by the reference system and the TOA of the DUT is called *time residual*. The time resolution of the DUT $\sigma_{t_{DUT}}$ can be obtained by subtracting quadratically the reference system time resolution $\sigma_{t_{ref}}$ from the measured unbiased residuals width $\sigma_{t_{residuals}}$:

$$\sigma^2_{t_{DUT}} = \sigma^2_{t_{residuals}} - \sigma^2_{t_{ref}}. \tag{2.26}$$

If a detector identical to the DUT is used as a reference (i.e. same time resolution), it is possible to extract the time resolution of the DUT directly from the measurement of the time residuals:

$$\sigma_{t_{DUT}} = \frac{\sigma_{t_{residuals}}}{\sqrt{2}}. \tag{2.27}$$

CHAPTER 3

Beam Tests of Pixel Sensors

Pixel sensor prototypes are studied in this work as Minimum Ionising Particles (MIP) detectors. Performance validation of new sensors requires testing under controlled conditions. This chapter describes the experimental configurations and analysis frameworks used for test-beam characterization of pixel sensors. Most of the test-beam measurements described in the following chapters are carried out in the DESY II test-beam facility [58], which is therefore introduced in Section 3.1. Precise reference systems are essential for determining Device Under Test (DUT) properties; Section 3.2 describes the beam telescopes used to track particles, while Section 3.3 explores their estimated tracking resolution. Section 3.4 discusses the data acquisition and synchronization systems used for the studies in this thesis, while Section 3.5 describes the Corryvreckan framework [59] used for test-beam data analysis. The methodologies reported are essential for the evaluation of the performance of the Digital Silicon PhotoMultiplier (dSiPM) and Monolithic Active Pixel Sensors (MAPS) prototypes, which are described in the following chapters.

3.1 The DESY II Synchrotron Test-Beam Facility

The DESY II Test-Beam facility [58], located at the Deutsches Elektronen SYnchrotron (DESY) in Hamburg, Germany, provides electron and positron beams with energies ranging from 1 to 6.3 GeV. The facility is part of the DESY II complex, a synchrotron with a circumference of about 293 m, which serves as a pre-accelerator for the PETRA III synchrotron light source. The primary beam, originating from electron bunches injected by the LINAC II linear accelerator at 450 MeV, is accelerated inside DESY II to an energy of 6.3 GeV, extendable up to 7 GeV. Each acceleration cycle lasts about 80 ms, and the beam circulates at a frequency of 1.024 MHz. Test-beams are generated through a double conversion process. Initially, a carbon fiber target inserted into the primary beam of DESY II creates bremsstrahlung photons. These photons then interact with a secondary target, usually copper or aluminum, creating electron and positron pairs. The facility uses a dipolar spectrometer magnet: by changing the polarity and intensity of this magnetic field, it is possible to choose the particle type (electron or positron) and fine-tune the beam momentum. The DESY II Test-Beam facility has three

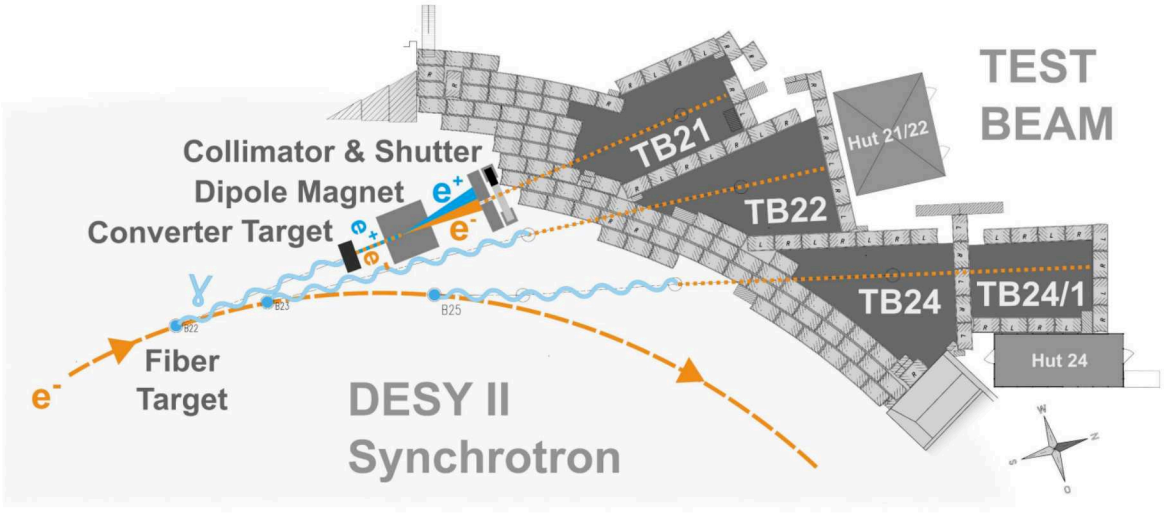

Figure 3.1: DESY II test-beam facility. Adapted from [58]

separate beamlines, each with its own primary target and particle/momentum selection system. This configuration allows for independent extraction and configuration of the beams, which are collimated to reduce particle rates and adjust the beam spot size and angular spread. Typical rates available in test areas reach a few kHz per cm^2. An illustration of the test-beam facility is shown in Figure 3.1. More details on the facility can be found in [58].

3.2 Beam Telescopes

A beam telescope is a crucial tool used in test-beam environments to characterize the performance of new detector technologies, such as tracking efficiency and intrinsic spatial resolution. The main purpose of a beam telescope is to provide highly accurate and unbiased reference measurements of particle trajectories, which are essential for comparing and validating the performance of a DUT. Beam telescopes are typically built with several well-characterized pixel or strip silicon detector planes.

In silicon detector characterization, the telescope setup is generally divided into two sections: an upstream arm, consisting of the telescope planes placed before the DUT, and a downstream arm, consisting of the planes after the DUT with respect to the beam direction. The beam telescope typically includes mechanical structures, trigger systems and logic, data acquisition systems, and, if necessary, cooling equipment. In this work, referring to beam telescopes, a right-handed Cartesian coordinate system is used, in which the z axis is aligned with the beam direction and the y axis points upward. Each beamline at the DESY II test-beam facility is equipped with a beam telescope that is available to users. The test-beam data analyzed in this work are acquired in test-beam lines 21 and 22 equipped with an EUDET-type [60] and the ADENIUM [61] beam telescopes, respectively, at the time of data taking.

EUDET-type telescopes

The EUDET telescopes consist of six monolithic MIMOSA 26 active pixel sensors [62], each with a pixel size of 18.4 µm × 18.4 µm. MIMOSA 26 sensors have a binary readout with an intrinsic spatial resolution of 3.24 µm and is read using a rolling-shutter method with an integration time of 115.2 µs. Each plane has a material budget of 0.00076 radiation length X_0 and is supported by water-cooled aluminum frames maintained at 18 °C [60].

ADENIUM Telescope

The ADENIUM telescope is a new-generation beam-tracking system using ALICE PIxel DEtector (ALPIDE) sensors [28]: MAPS fabricated in a 180 nm Complementary Metal-Oxide-Semiconductor (CMOS) imaging process. These sensors have a slightly larger pixel pitch than MIMOSA sensors: 26.88 µm × 29.24 µm with a resolution of ∼ 5 µm. Although worse in spatial resolution, the ADENIUM telescope offers a faster readout time of only 10 µs, significantly reducing the dead time during data taking and track multiplicity due to pile-up. ALPIDE sensors have a high detection efficiency exceeding 99 % and a very low noise rate ($< 1 \times 10^{-6}$ per pixel per event). Unlike EUDET telescopes, ADENIUM uses passive cooling due to its power-efficient design, simplifying the telescope mechanics.

3.3 Telescope Configuration and Track Resolution

One of the most important properties of a beam telescope is its track resolution, which defines the precision in determining a particle's trajectory. Track resolution is not constant throughout the trajectory and depends on several factors: sensor properties, material budget, particle momentum, geometry, and system alignment. The spatial resolution of the sensor used for the telescope planes directly improves accuracy by reducing the position uncertainty of the hits. The material budget in the telescope and DUT affects the resolution due to uncertainties caused by multiple scattering of the tracks [63]. This phenomenon is more pronounced for beams with lower momentum, as charged particles are affected more by interactions with the atoms in the material, leading to larger deflections and, consequently, lower track resolution. Optimized detector geometry, with careful spacing between sensor planes, improves trajectory reconstruction, while precise alignment of these planes is crucial to minimize systematic uncertainties. By managing these factors, beam telescopes can achieve accurate particle tracking, essential for high-precision measurements on the DUT.

Track resolution can be estimated using the General Broken Lines (GBL) formalism: an initial simple trajectory (i.e. straight line) is re-fitted, taking scattering uncertainties into account. A global χ^2-fit is carried out, including all hits and their resolution and the width of the scattering angle distribution along the trajectory. This leads to a trajectory formed by straight lines with scattering angles at the positions corresponding to the crossing of scattering materials (i.e. telescope planes or DUTs), as illustrated in Figure 3.2 where a GBL track is shown in blue. The track resolution is derived from the covariance matrix, which is computed for each track parameter. More details on the method, as well as the estimated EUDET-type telescope performance, can be found in [60].

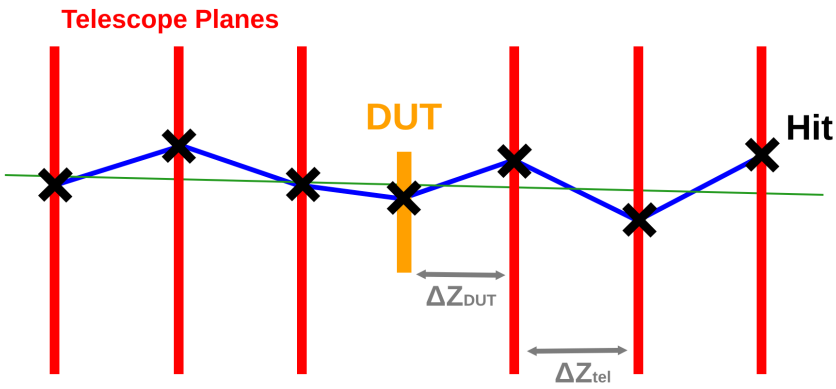

Figure 3.2: Illustration of particle track reconstruction using a test-beam telescope. Hit (black cross) in the telescope planes (in red) and in the DUT (orange) are used to reconstruct tracks using the straight line (green) and the GBL (blue) model.

3.3.1 Track Resolution Estimations

Figure 3.3 shows examples of track resolution estimations at the DUT position, obtained using an EUDET-telescope-like configuration and the software in [64]. Six MIMOSA 26 planes with a spatial resolution of 3.24 µm are arranged as in Figure 3.2. In the estimation, the distance of the DUT from the closest telescope plane Δz_{DUT}, the distance between telescope planes Δz_{Tel}, DUT material budget, and beam momentum are configurable. The material budget of the scattering medium is defined as the material thickness normalized by its radiation length X_0. A thickness of 55 µm of silicon and 50 µm of Kapton material are fixed in the estimation for the telescope planes, while the DUT is modeled as a layer of silicon with adjustable thickness. An electron beam is used in the estimation.

Figure 3.3(a) shows the spatial resolution of the telescope at the DUT level as a function of the geometric arrangement of the telescope planes and the DUT along the z-axis (beam direction). In this example, the material budget of the DUT is set at 50 µm silicon equivalent. The electron beam energy is set to 4 GeV. For simplicity, a symmetrical configuration as shown in Figure 3.2 is used. Analyzing the results, it can be seen that by bringing the telescope arms closer to the DUT, i.e., small Δz_{DUT}, the spatial resolution of the track improves considerably. For low Δz_{DUT}, performance improves further by maintaining a compact telescope geometry, i.e., small Δz_{Tel}. On the other hand, if Δz_{DUT} is constrained to larger values (e.g., due to the DUT mechanics), larger Δz_{Tel} values result in better spatial resolution of the reconstructed track.

Figure 3.3(b) shows the spatial resolution of the telescope at the DUT level as a function of the material budget of the DUT and the particle momentum. In this example, a specific geometric configuration is used with Δz_{DUT} and Δz_{Tel} both fixed at 30 mm. It can be seen that the material budget of the DUT, as well as the beam momentum, are both factors that considerably influence the track resolution at the DUT position.

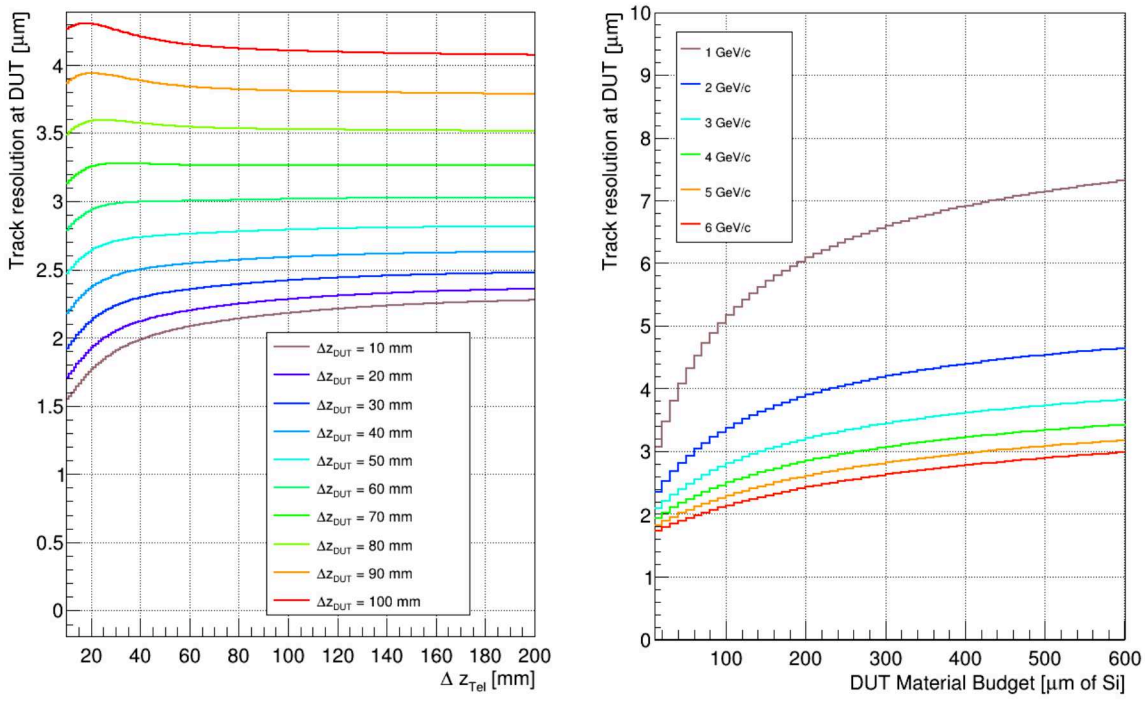

(a) (b)

Figure 3.3: Track resolution estimated ad the DUT level using the GBL model and the software in [64]. In (a), track resolution is shown as a function of Δz_{Tel}; different Δz_{DUT} used are displayed with different colors. In (b), track resolution is shown as a function of DUT material budget; different beam momentum selected are displayed with different colors.

3.4 Data Acquisition and Synchronization

The different devices involved in a test-beam setup (beam telescopes, DUTs, trigger systems, etc.) produce data that must be digitized and saved for subsequent analysis. Each device has its own specific data acquisition system and devices and frameworks capable of communicating and synchronizing all devices are required for test-beam experiment. In Section 3.4.1, the Caribou Data AcQuisition (DAQ) system is introduced as it is used with the DUTs studied in this work. Sections 3.4.2 and 3.4.3 present the AIDA Trigger Logic Unit and the EUDAQ2 software framework used for the synchronous operation of the devices in the test-beam experiments presented in this work.

3.4.1 Caribou DAQ System

Caribou is a flexible data acquisition system optimized for prototyping solid-state detectors or Application Specific Integrated Circuits (ASICs) [65, 66]. Caribou's modular design includes a Zynq System-on-Chip (SoC) board, a Control and Readout (CaR) board, and a prototype-specific chipboard. Figure 3.4 shows the Caribou DAQ system.

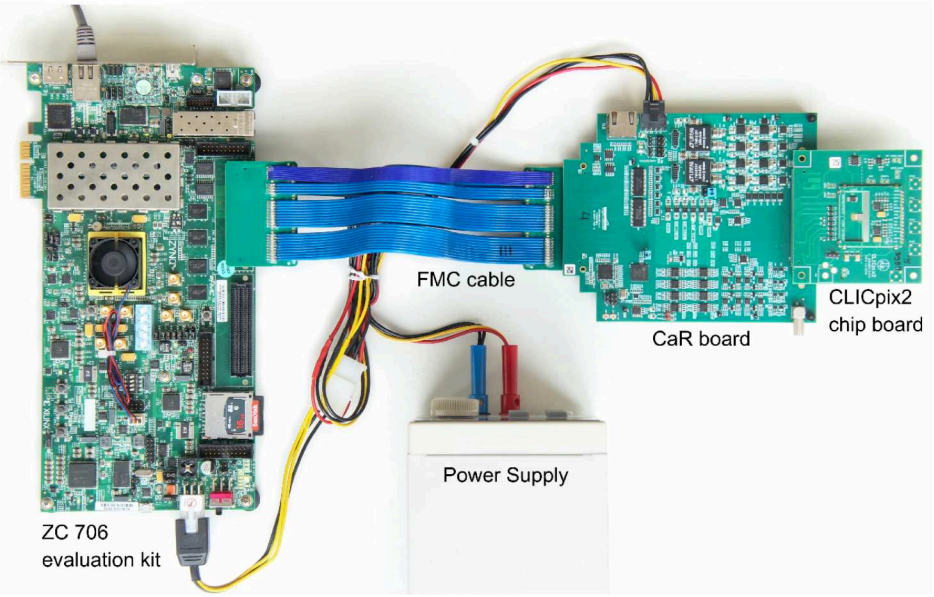

Figure 3.4: Picture of the Caribou DAQ system. From [65].

The main hardware architecture in the version used in this work exploits Xilinx's Zynq SoC platform, specifically the Zynq 7000 series. The system uses a Linux distribution based on Yocto (Poky) and the Peary software for interfacing with the hardware [67].

The CaR board connects to the SoC board via an FPGA Mezzanine Card (FMC) interface, which can be further extended via a cable to reduce mechanical constraints in complex setups. The CaR board provides the hardware components required to operate the prototype: adjustable power supplies, two types of Analog to Digital Converters (ADCs), programmable voltage and current references, bidirectional LVDS connections, a low-noise clock generator, etc.

The prototype-specific chip board interfaces with the CaR board via a 320-pin SEARAY connector and contains only passive components or detector-specific circuits not present on the CaR board.

Caribou is used as a DAQ system for the prototypes investigated in this work, enabling their rapid and low-cost implementation in laboratory and test-beam setups.

3.4.2 The Trigger Logic Unit

The AIDA-2020 Trigger Logic Unit (TLU) is a system designed to generate and manage trigger and control signals for devices used in particle beam experiments. Developed as part of the AIDA-2020 project, and the TLU is compatible with the data acquisition systems EUDAQ2 (presented in Section 3.4.3).

The TLU is used as the hardware control unit in all test-beam experiments performed in the context of this work. The TLU is highly configurable, allowing trigger signals to be generated based on customizable logic combinations of input signals. In addition, the TLU provides 12 V power supply

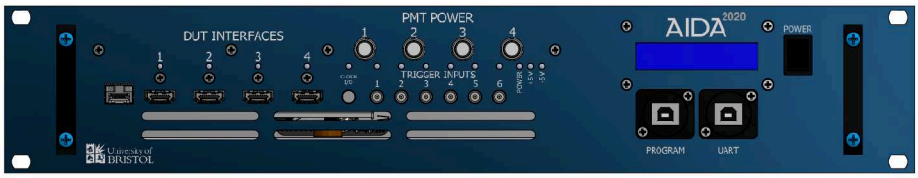

Figure 3.5: Sketch representation of the front view of AIDA-2020 Trigger Logic Unit. from [68].

and adjustable control voltage for up to four PhotoMulTipliers (PMTs), which can be used as triggers when coupled with scintillators. The TLU can generate timestamps with a time resolution of 1.56 ns for the input trigger signals; timestamps are recorded separately for each input, ensuring precise time sampling of the different signals. Another important function of the TLU is the generation of a global clock signal, a trigger ID number, and a time reset signal, which can be distributed to all systems of the experiment, e.g. telescope and DUTs, and used for device synchronization. The TLU also handles busy signals, preventing the release of new triggers while a system component is still processing a previous event. Communication with the DUTs occurs using four standard HDMI connectors. Control signals, such as clock, trigger and busy signals, use LVDS logic and can be configured bi-directionally, allowing signals to be transferred from the DUT to the TLU and vice versa.

More details on the operation of the AIDA TLU can be found in [68]. Figure 3.5 shows the front control panel, where the described inputs and outputs are visible.

3.4.3 EUDAQ2 Framework

The EUDAQ2 framework manages the data acquisition during the test-beam measurements shown in this work. Its main function is to centralize the control, synchronization, and data acquisition of the various devices interfaced with it.

The architecture of EUDAQ2 is shown in Figure 3.6. A central control, *RunControl*, oversees all connected hardware components and framework units. Each device in the system is connected to the central control and operates via a dedicated local *Producer*, which is responsible for performing tasks such as starting or stopping data collection and system configuration. Producers send event data to a central *DataCollector*, which organizes and stores the data. The system also enables real-time monitoring of all components and collects status and error messages by storing them in a *LogCollector*. More details on the EUDAQ2 software framework can be found in [69].

3.5 Analysis of Test-Beam Data with the Corryvreckan Framework

Corryvreckan is a modular and versatile framework designed for the reconstruction and analysis of data from test-beam experiments using beam telescopes. This tool allows a complete reconstruction of events by combining data from different devices, enabling track reconstruction and investigation of the DUT performance. Users interact with Corryvreckan through two main configuration files: one describes the specific geometry of the setup (detector properties, position, orientation), and the

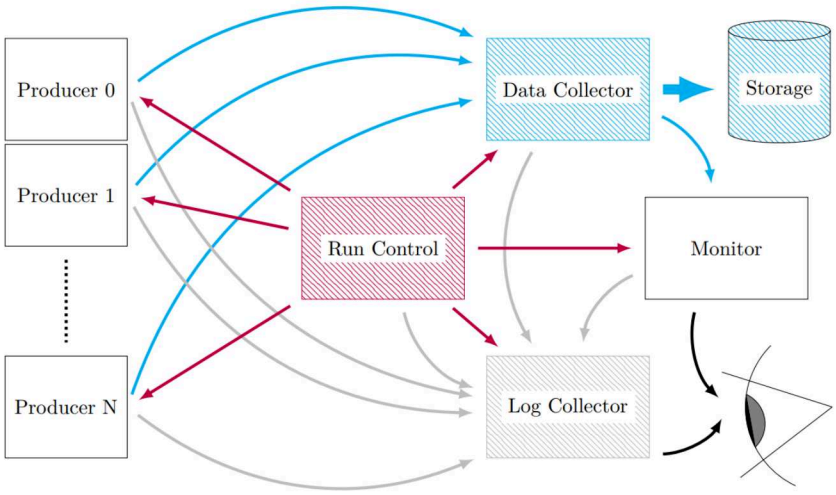

Figure 3.6: Architecture of EUDAQ2 Framework. From [42].

second sets the global framework as well as the configurable set of software modules needed for the reconstruction process.

The reconstruction process with Corryvreckan is comprised of several steps. The modular structure of the software enables customization, allowing users to add or remove modules according to the specific needs of the analysis. The order of modules in the configuration file defines the sequence of tasks, ensuring that data is processed in the right flow. In the following sections, the typical reconstruction process in Corryvreckan used for the test-beam data analysis presented in this work is summarized. More details can be found in [59, 70]. The code is open source and available in [71].

3.5.1 Data Decoding and Event Definition

In the early processing stages, Corryvreckan decodes the raw data from the various detectors or systems. It includes user-defined data reading modules to interpret the specific data structure, facilitating interoperability between devices of different types. Individual events are defined by timestamp or trigger number. For each event, detector data, such as hitmaps, hit-charge information or hit-timestamps, are placed on a central clipboard, making them available for further software reconstruction and analysis steps. The software has been extended, integrating specific decoders, to allow the conversion of raw data from the prototypes investigated in this work by enabling their analysis in Corryvreckan.

3.5.2 Clustering

Clustering is grouping adjacent hits that are likely to originate from the same particle interaction. In the Corryvreckan analysis presented, a touching-neighbors method is used to define the clusters; each of the eight touching pixels is considered a neighbor. In this work, the Corryvreckan modules *[ClusteringSpatial]*, *[Cluseting4D]*, and *[ClusteringAnalog]* are used depending on whether the

temporal information and/or the full analog waveform of the hit are available or not. If charge information is available, the cluster position is defined using a charge-weighted center-of-gravity algorithm; in contrast, on binary hit data, a cluster center calculation based on the arithmetic mean is used.

3.5.3 Tracking and Telescope Alignment

Tracking in Corryvreckan is used to reconstruct particle trajectories by associating clusters in telescope detectors (usually DUT is excluded) while applying spatial and temporal cuts. Corryvreckan supports various track models: straight lines, multiplets, and GBL. The straight line track model ignores multiple scattering effects and describes the particle trajectory as a straight line taking into account only hit uncertainties. The multiplets track model involves two distinct track segments, which correspond to fits of detector hits in upstream and downstream subsets. These segments are joined at a specific position along the z-axis, permitting a discontinuity or 'kink' to account for potential scattering effects. The GBL track model includes hit and scattering uncertainties, reconstructing particle trajectories more realistically. The *[Tracking4D]* module with the GBL track model is used in the analysis presented in this work, the DUT is excluded from the tracking in all the analyses.

Offline telescope alignment is performed for fine-tuned correction of detector positions necessary for accurate track reconstruction. A multi-stage process is usually employed. In a preliminary step, the detectors are aligned using a reference plane and exploiting correlations between the clusters in the various planes; the *[Prealignment]* module is used for this scope. The resulting tracks are then used for the second alignment step, performed with the *[AlignmentTrackChi2]* module, where an iterative process adjusts the telescope planes by shifting and/or rotating them. The best configuration is determined by minimizing the global χ^2 of the fits.

3.5.4 DUT Alignment and Analysis

The DUT is also aligned in the software through the use of the *[AlignmentDUTResidual]* module. The DUT cluster centers are compared with the position of the reconstructed tracks intercepted with the DUT plane. Clusters in the DUT are then associated with reconstructed tracks by applying spatial and temporal cuts. The distance between the DUT cluster center and track intercept is defined as a spatial residual. The alignment of the DUT is carried out through translations and/or rotations of the DUT, minimizing the overall spatial residual width.

During data acquisition, especially for long runs without control over environmental conditions, thermal expansions of the mechanics or undesired setup movements lead to misalignment of the setup over time. A time-dependent alignment function can be used in Corryvreckan to compensate for slight variations and improve analysis accuracy. Figure 3.7 shows the effect of the correction on a dataset with a duration of more than 14 hours. The figure shows the sum in quadrature of the spatial residuals in the x and y directions ($sqrt(D_x^2 + D_y^2)$) before and after correction.

The last step in the Corryvreckan chain is the analysis of the DUT performance. Specific modules, such as *[AnalysisDUT]* or *[AnalysisEfficiency]*, are used in the context of this work to evaluate detector

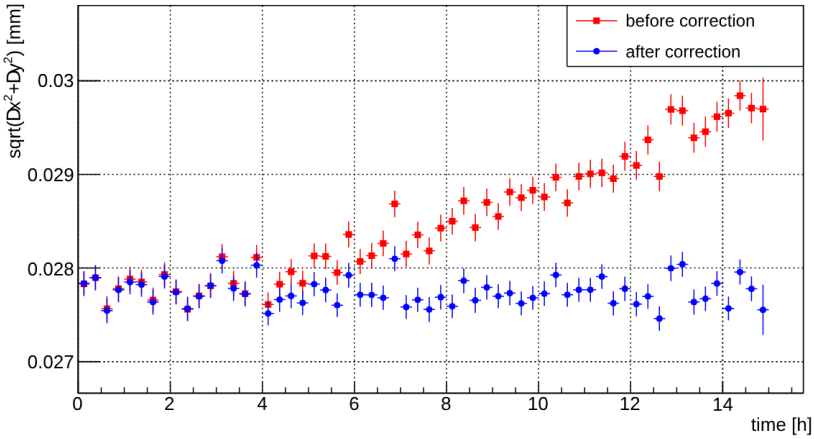

Figure 3.7: Example of time-dependent alignment correction in Corryvreckan.

performance, such as particle detection spatial resolution, associated cluster size, fake hit rate, and efficiency. All outputs of the used modules are saved in ROOT [72] format.

Part I

Studies on a Digital Silicon Photomultiplier Prototype

CHAPTER 4

Silicon Photomultipliers Principles and the DESY Prototype

Silicon PhotoMultiplier (SiPM) and Digital Silicon PhotoMultiplier (dSiPM) represent an essential research and development topic for future High-Energy Physics (HEP) experiments, as introduced in Section 1.5. This chapter introduces (d)SiPMs and describes the digital prototype developed at Deutsches Elektronen SYnchrotron (DESY) under study in this work. Section 4.1 describes the fundamental concepts of SiPMs and their core elements: Single-Photon Avalanche Diode (SPAD). The differences between analogue and digital SPAD arrays are then presented, followed by a discussion of some (d)SiPMs properties such as operating conditions, Photon Detection Efficiency (PDE), main noise sources, and spatial and time resolution. Section 4.2 focuses on the DESY dSiPM prototype description, providing details on the sensor properties and functionality.

4.1 Silicon Photomultipliers

SiPMs are the solid-state version of conventional PhotoMulTipliers (PMTs) and are widely used as photodetectors in HEP, medical and industrial applications. SiPMs are characterized by low-voltage operation, insensitivity to magnetic fields, excellent timing resolution, robustness and high PDE. These characteristics make SiPMs one of the most widely used technologies in light detection in contexts where high photon sensitivity and timing resolution on the order of a few tens of picoseconds are required [39].

4.1.1 Single Photon Avalanche Diodes

The SPAD is the key element in SiPMs. The SPAD is an Avalanche PhotoDiode (APD) operated in Geiger mode [56]. The structure of a p-in-nwell SPAD is illustrated in Figure 4.1. In the example shown, a deep n-well is implanted on a p-substrate. The deep n-well hosts an additional p-n junction that is highly doped. In this region, when reverse biased, a localized high electric field region is

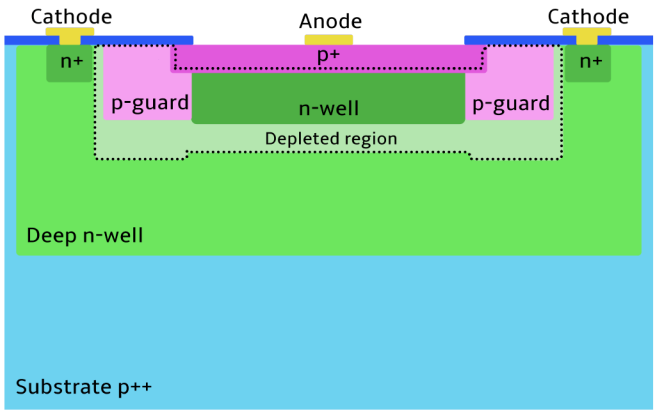

Figure 4.1: P-in-nwell SPAD structure on a p substrate. The depleted region is marked with a dotted line. Not to scale.

created (in the order of few 10×10^5 V cm^{-1} [73]). SPADs are typically operated 10-20 % above the breakdown voltage. In this regime, the primary charges created in the depleted region gain sufficient energy in the high-field region to generate new charges via impact ionization, starting an avalanche process (as described in Section 2.4.3). The SPAD discharges and amplifies the single primary charge into a macroscopic current (typical gain > 10^5). The avalanche is interrupted by a quenching component, usually a resistor in series. The quenching lowers the voltage seen by the SPAD, terminating the avalanche process. The diode then recharges and returns to its original bias. The high gain amplification process makes the SPAD sensitive to single photons that only produce a single primary electron-hole (e-h) pair. The characteristics of the SPAD discharge depend on design, overvoltage, quenching circuit, and operating conditions. The rise time of SPAD signals is less than 1 ns, and the typical quenching time is in the order of a few tens of nanoseconds [74]. In the recent SPAD designs, a guard ring (p-guard in Figure 4.1) is used to lower and smooth the high electric field in the edge regions, improving SPAD response uniformity and reducing noise.

4.1.2 Analogue SPAD Arrays

SPAD dimensions are limited to a few tens of micrometers to preserve timing and power consumption. Furthermore, given the binary nature of SPAD signals, proportionality can not be preserved in multi-photon light detection using a single SPAD (usually possible with PMTs). To overcome this, SPADs are usually arranged in arrays to form a SiPM. Each SPAD has its resistor in series to form an independent *microcell*, connected in parallel with the other, which shares the same bias. Essential in this structure is the use of trench or junction terminations to contain the avalanche within the cell where the primary ionization takes place and shield from secondary photons produced during the avalanche that may induce crosstalk (see Section 4.1.7). No complex electronics are included in this type of design, which is characterized by an analog signal output with amplitude proportional to the number of firing SPADs, hence the name *analog SiPM*. Figure 4.2 shows an example of an analog SiPM structure.

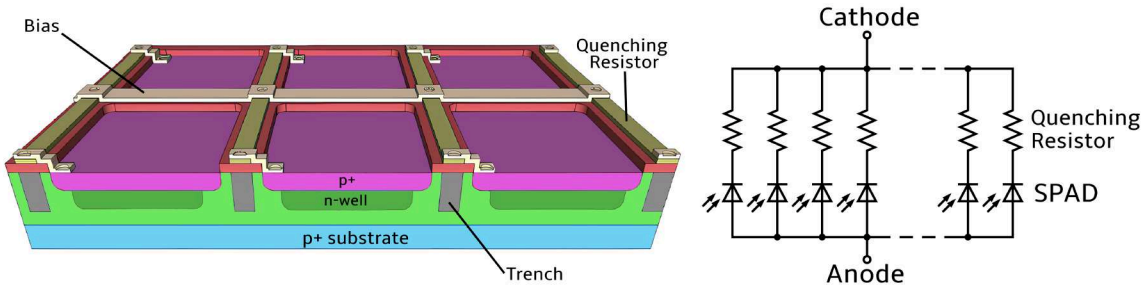

Figure 4.2: Typical p-in-nwell analogue SiPM structure (left), adapted From [75]. Equivalent electric circuit (right).

In standard applications, SiPMs are used as light detectors. By appropriately choosing the granularity and number of SPADs in the SiPM, a signal that scales with the number of incident photons in a given dynamic range can be obtained. Being connected in parallel, the SPADs create an additive signal in the sensing node.

4.1.3 Digital SPAD Arrays

APDs and SPADs produced in Complementary Metal-Oxide-Semiconductor (CMOS) nodes, introduced in the 1990s [76], developed rapidly in recent years [77]. This allows to extend the performance of SiPMs integrating CMOS circuitry in the same die. Signal digitization can occur at the level of the individual SPAD, directly connected to the front-end electronics. The sensor provides a digital output, hence the name *digital SiPM*. Pixel masking, active quenching, full hit-map readout, timestamping, and photo-counting are some of the functionalities that can be introduced on-chip in digital SPADs arrays. Hybrid and monolithic solutions can be used for dSiPMs (see Section 2.4.6).

In monolithic SiPMs, SPAD diodes and CMOS components are implemented in the same silicon die. CMOS electronics can be placed at the level of the single SPAD or in the chip periphery. These monolithic SiPMs are produced in conventional CMOS fabrication process. Figure 4.3 shows an example of a monolithic digital SPAD structure. The image also shows the use of Shallow Trench Isolation (STI), a technology that allows for improved SPAD surface leakage current and isolation [78]. Despite the advantages offered by conventional CMOS processes, monolithic SPAD arrays suffer from problems related to detection efficiency and SPAD quality. The need to separate the electronics wells from the sensing volume reduces the overall sensitive area (see Section 4.1.5). This becomes even more restrictive when increasing the granularity of the microcells and the complexity of the in-pixel electronics. Furthermore, the several production steps needed for the CMOS electronics can influence the quality of the SPAD. These limitations can be solved by exploiting technologies developed in the CMOS imaging commercial context. For example, microlenses, charge focusing systems [79], or advanced light trapping techniques [80] can be used to improve SPADs fill-factor.

Hybrid solutions can be used to further increase active volume and SPAD quality. SPADs are produced in dedicated nodes and then bonded to wafers containing only CMOS electronics (possibly produced using a different technology). In this configuration, the sensitive wafer is thinned to a few micrometers to enable SPAD BackSide Illumination (BSI), a technique where the photodiode is illuminated from

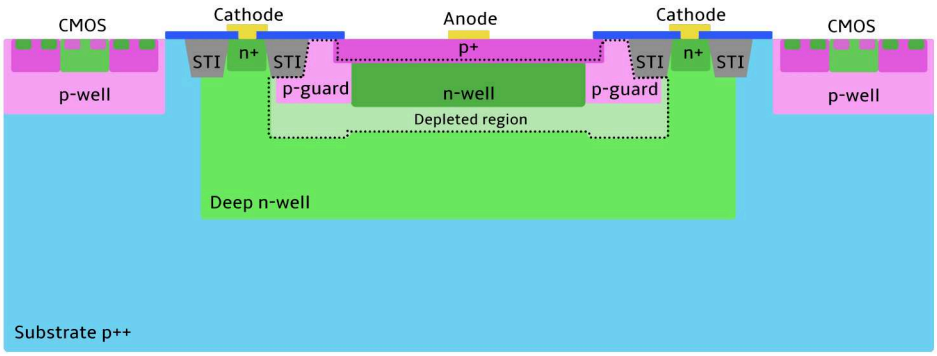

Figure 4.3: Monolithic digital p-in-nwell SPAD structure with in-pixel electronics. The depleted region is marked with a dotted line. Not to scale.

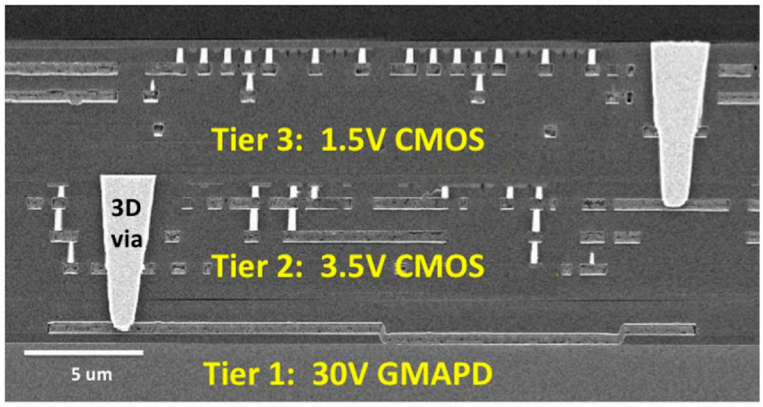

Figure 4.4: 3D integrated LIDAR image sensor from [83]. BSI SPADs in tier 1, signal conditioning circuits in tier 2 and high-speed logic for timestamping in tier 3.

the back side of the wafer [81]. Optimizing active part design without interfering with the electronics also allows further improvement of the SPAD characteristics. The coupling can be achieved using conventional bump bonding or more advanced technologies such as hybrid-bonding [82] that enables micrometers scale bonding pitch. Figure 4.4 shows an example of a 3D stacked Geiger mode LIght Detection And Ranging (LIDAR) imager [83]. The latest prototypes of stacked-SiPMs count millions of digital pixels with a few micrometers pitch and sensor performance competitive with the most advanced analog SiPMs [84].

4.1.4 Current-Voltage and Breakdown

Current-Voltage (IV) characterization is an essential measurement in most detector technologies. It allows identification of the operating point and gives immediate feedback on sensor functionality.

When reverse-biased, the SiPMs show the leakage current typical for pn-junctions (see Section 2.1.2). When the breakdown voltage (V_{BD}) is reached, the current increases exponentially. In this regime, avalanche multiplication can occur, and the SPADs are sensitive to single photons [73]. The current I after the BD is proportional to the Dark Count Rate (DCR) (described in Section 4.1.6) and the gain

G of the SPAD, both functions of the overvoltage bias V_{OV} above V_{BD}:

$$I \propto DCR(V_{OV}) \cdot G(V_{OV}). \tag{4.1}$$

The identification of the V_{BD} is required in order to operate the SiPM properly and needs to be repeated for every environmental condition (V_{BD} is, for example, strongly temperature dependent). Various techniques can be used to determine the breakdown of SiPM. This work uses the logarithmic derivative method described in [85]. The breakdown voltage is defined as the maximum of the logarithmic derivative LD of the current I measured with a fine IV scan in the region of interest:

$$LD = \frac{dln(I)}{dV}. \tag{4.2}$$

4.1.5 Photo Detection Efficiency

The PDE is one of the main characteristics of a photo-detector. It is defined as the ratio of incident photons to detected ones. In SiPMs, the PDE can be defined as (adapted from [73]):

$$PDE = FF(\lambda, V_{OV}) \cdot QE(\lambda) \cdot P_{av}(\lambda, V_{OV}), \tag{4.3}$$

here, the intrinsic Fill-Factor $FF(\lambda, V_{OV})$ is closely related to the layout and structure of the SPAD. Larger pitches generally correspond to a higher FF but, at the same time, reduce the dynamic range in photon counting. The presence of inactive areas in the SiPM also determines the FF, e.g., the size and shape of metal layers, quenching resistors and possible in-pixel electronics in monolithic sensors. The FF in a SPAD can be different at different depths in the silicon and is, therefore, wavelength-dependent.

$QE(\lambda)$ is the quantum efficiency, i.e. the probability that a photon entering the sensitive part of the device is then absorbed, generating an e-h pair. As described in Section 2.3 in silicon detector, this is related to the wavelength of the interacting photon λ.

$P_{av}(\lambda, V_{OV})$ is the probability of triggering the avalanche before the primary e-h pair recombines. This depends on the strength of the electric field, i.e. doping and overvoltage, and the position where the primary charges are generated. Photons of different wavelengths interact on average at different depths in the SPAD (see Figure 2.6) and will, therefore, have different distances from the high gain region, resulting in different probabilities of triggering the avalanche.

The uniformity of electric fields and edge effects in SPADs negatively influence PT and FF. In the peripheral regions of the active area, trenches or termination wells are introduced to contain avalanches in SPADs. In these regions, the electric field is lower and non-uniform, as seen in Figure 4.5. The dimensions of these containment areas do not scale with the size of the SPADs; uniformity effects are, therefore, much more important for small SPADs.

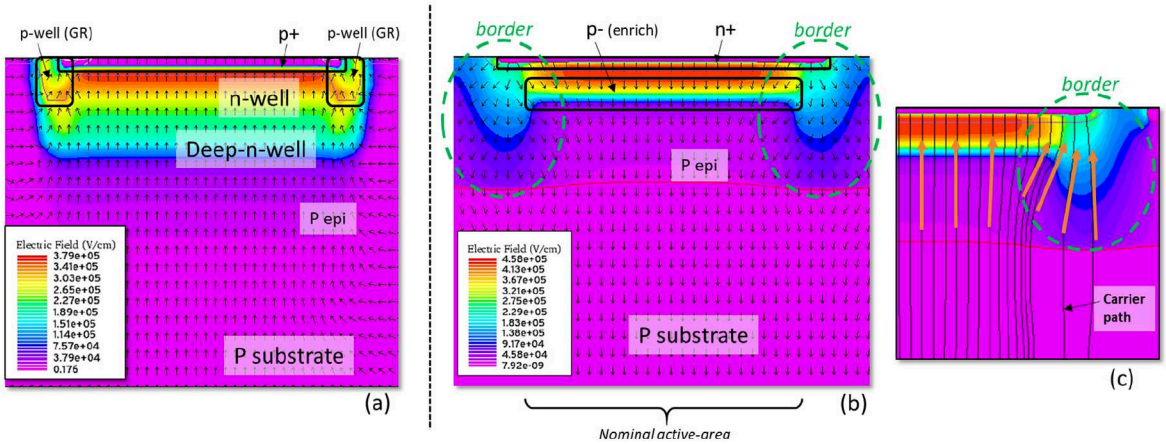

Figure 4.5: Simulation of SPAD electric field from [73]. Examples of CMOS SPAD (a) and custom process SPAD (b-c) are shown.

4.1.6 Uncorrelated Noise: Dark Counts

Uncorrelated noise, better known as DCR, refers to avalanche pulses triggered in the SiPM under dark conditions.

Thermal crystal excitation and tunneling effect are the main sources of DCR in SiPMs. While thermal DCR is strongly correlated with temperature, tunneling is strongly dependent on the doping of the junction and electric field strength; it becomes the main source of DCR at low temperatures [73]. These processes can be trap-assisted according to the Shockley-Read-Hall Model [86]. The higher the concentration of crystal defects, the higher the number of levels in the middle of the band-gap, thus, the probability of trap-assisted thermal excitation and tunneling. The strong electric field in the avalanche region also influences the DCR through the Pole-Frenkel effect [87], according to which strong electric fields significantly decrease the activation energy of traps.

Crystal quality, optimization of production processes, cooling, and reduction of the volume of the high field region are all strategies adopted to reduce the DCR in SiPMs.

4.1.7 Correlated Noise: Afterpulsing and Crosstalk

The term *correlated noise* denotes noise events generated as a consequence of a previous discharge. So-called *afterpulse* and *crosstalk* events fall into this category [88]. The different types of crosstalk, as well as afterpulsing, are schematically illustrated in Figure 4.6.

An afterpulse event is a SPAD discharge generated by a residual charge, which was trapped during a previous avalanche and is subsequently released. The probability of afterpulse depends on the number of traps in the high electric field region and their release time. Afterpulsing can be mitigated by adjusting the recharge time constant of the SPAD (i.e. the quenching resistor) so that most of the trapped charges are released before the cell is fully recharged. The recharge time is a compromise between the afterpulse probability and the dead time of the detector. The use of a quenching transistor

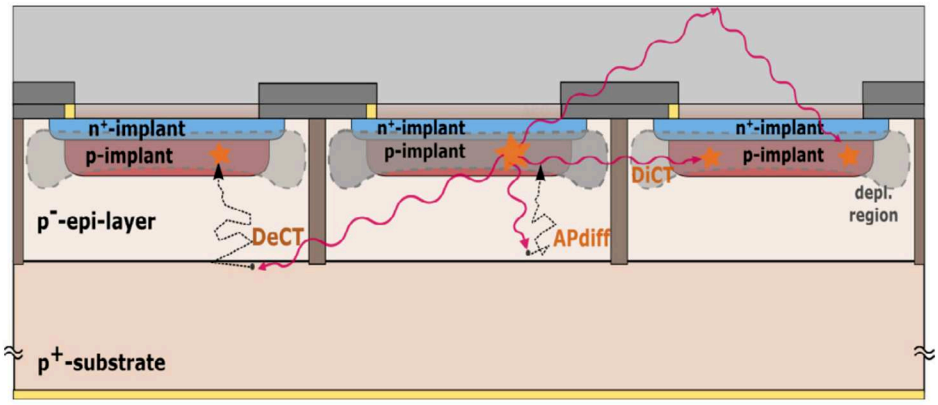

Figure 4.6: Correlated noise in SiPM schematic representation from [73]. Prompt (DiCT) and delayed (DeCT) crosstalk are shown, as well as crosstalk induced by reflections and afterpulse events (APdiff).

instead of a resistor, which is possible in dSiPMs, allows the quenching time to be adapted to the needs of the specific application.

A large number of secondary photons are produced during an avalanche process [89, 90]. These photons are emitted isotropically and can, directly or by reflection, reach adjacent SPADs where they can trigger another avalanche. This correlated noise is called *optical crosstalk*. When the secondary avalanche is immediately triggered, this is called *prompt crosstalk*. If, on the other hand, the photon generates an e-h pair in a low electric field region of the adjacent SPAD, diffusion or slow drift of charges before the start of the new avalanche causes so-called *delayed crosstalk*. Crosstalk probability is dependent on overvoltage as it is directly proportional to the gain of the SPAD (i.e. the number of charges generated per avalanche). Geometrical and optical factors also influence crosstalk. Separation distances between SPADs and avalanche containment technologies, such as trenches, can strongly suppress the effect [91, 92]. Optical coupling of SiPMs with reflective materials can also cause crosstalk events: photons emitted in the avalanche escape from the silicon of the primary SPAD and reach adjacent cells by reflection in the coupled material.

4.1.8 Spatial Resolution

The spatial resolution of SiPMs is not an essential parameter in applications involving only photon counting. Instead, when spatial resolution is needed, the choice of technology and sensor size are crucial. For example, in modern Positron Emission Tomography (PET) scanners, arrays of SiPMs are coupled to segmented scintillators and used to detect scintillation light [93]. Here, the size of the individual SiPMs, combined with their dynamic range and segmentation of scintillators, impacts the resolution of the image reconstructed by the device. As a further example, the spatial resolution of SPAD arrays is crucial when they are used as imaging sensors. An important distinction must be made in this context between analog and digital SiPMs. In analog SPAD arrays, the spatial resolution is determined by the size of the array. As SPADs are connected in parallel, no information on the position of firing cells is available in standard designs. In dSiPM, on the other hand, the possibility of integrating read-out electronics at the level of the individual SPAD opens the possibility of achieving spatial resolutions of the order of the binary resolution of segmented detectors: $SPAD_{pitch}/\sqrt{12}$.

4.1.9 Timing Resolution

SiPMs are known to reach excellent time resolution, down to a few tens of ps [39]. The excellent timing response is linked to the structure and operating principle of SPADs. In the high field regions, the primary charges immediately reach saturation velocity in silicon and typically drift for a few micrometers in high electric field regions before generating the Geiger discharge, which is also an immediate process. This leads to an intrinsic time response of the SPAD σ_{SPAD} on the order of picoseconds. However, the definition of the time resolution of a SiPM σ_{SiPM} in a system is not trivial and application-dependent. In the context of this work, the time resolution can be expressed as the squared sum of four terms:

$$\sigma^2_{SIPM} = \sigma^2_{SPAD} + \sigma^2_{Delay} + \sigma^2_{Noise} + \sigma^2_{TDC}, \tag{4.4}$$

σ_{SPAD} includes all the intrinsic characteristics of SPADs as well as the physics of the interaction and avalanche process. The geometry of the SPAD, uniformity and intensity of the electric field, position and energy of the interacting photon as well as environmental conditions, such as temperature, are included in this term. This contribution is usually not constant. The timing resolution of the SPAD may change depending on the operating conditions, signal source, and interaction position within the SPAD.

σ_{Delay} is related to the actual distance of the individual SPAD firing from the electronic front-end. This factor can be dominant in large analog sensors, as differences of tens of millimeters occur. Design strategies can be adopted to minimize or correct the effect. In dSiPM, for example, this contribution can be evaluated and corrected since the position of the firing SPAD is usually known.

The term σ_{Noise} refers to the temporal uncertainty introduced by the early or delayed activation of the comparator, which is attributable to the presence of noise [57]. The noise contribution can be minimized by shielding the sensor, minimizing the distance between SPAD and front-end electronics, or by choosing an optimal comparator threshold on analog signals. dSiPM are usually a better choice in this context, as the digitization of the signal can take place at the level of the individual SPAD.

Finally, the term σ_{TDC} is determined by the temporal resolution of the Time to Digital Converter (TDC) used to define the timestamp. This contribution is defined by the technology and the component design used for timestamping. It is important to emphasize that TDC resolutions of the order of picoseconds are very difficult to achieve if there are limitations in space and available power for the readout electronics.

4.2 The DESY dSiPM

A prototype of monolithic dSiPM has been developed at DESY using LFondry CMOS 150 nm technology [94]. This chip is one of the main objects of study in this work.

The Application Specific Integrated Circuit (ASIC) schematic of the chip and a microscope picture of a bonded prototype are shown in Figure 4.7. The prototype features a main array consisting of 32 $\times$ 32 pixels with an active area of $\sim 2.2 \times 2.4\,\mathrm{mm}^2$ and additional test structures in the periphery for the characterization of the individual components. A temperature diode is integrated into the chip

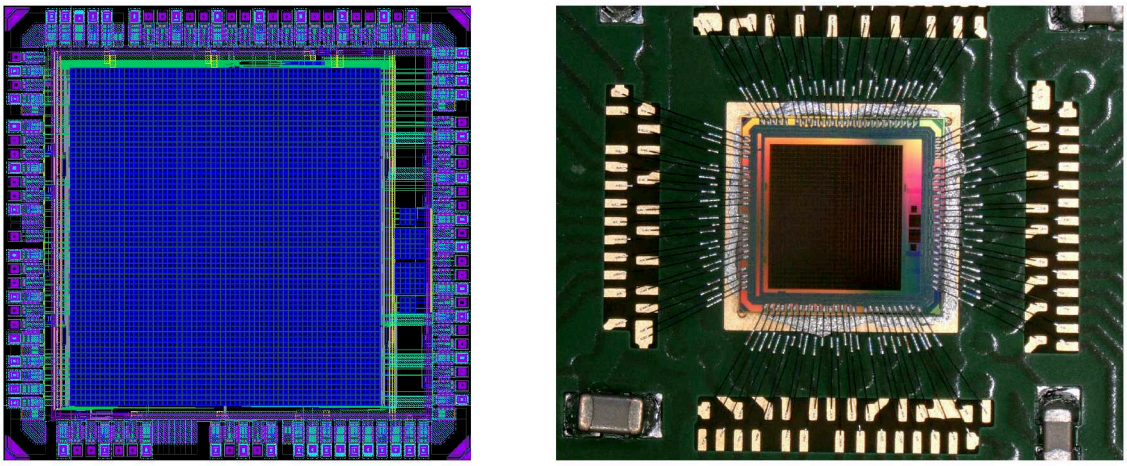

(a) (b)

Figure 4.7: ASIC design of DESY dSiPM (a). Microscope picture of a bonded sample (b).

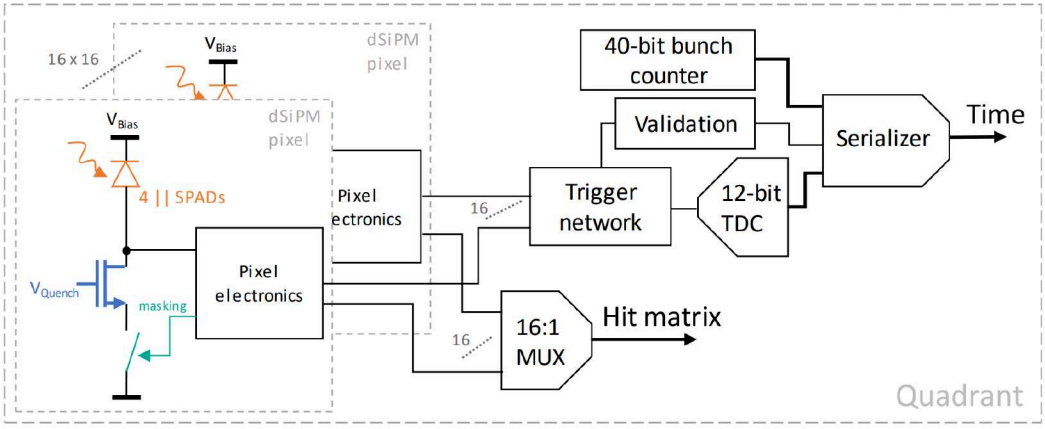

Figure 4.8: Quadrant Structure. From [95].

to monitor the operating temperature. SPADs are placed alongside CMOS electronics in the same silicon die, following the monolithic approach described in Section 4.1.3. Several digital components are implemented at pixel level, while others are located in the chip periphery. A detailed description of the chip design can be found in [94].

The Caribou setup described in Section 3.4.1 is used as Data AcQuisition (DAQ) system. It provides the clocks, control signals, and power supply for chip operation. Only the main SPADs bias is provided with an external power supply. The data readout is frame-based with a readout frequency of 3 MHz (i.e. 333 ns long frames). The integrated circuit of the main matrix is subdivided into four quadrants. Each consisting of 16×16 pixels, a trigger network, a 40-bit bunch counter, a 12-bit TDC, a validation logic and a serializer circuit followed by data links for fast data readout (up to 1 Gbit s^{-1}). A schematic representation of the quadrant structure is shown in Figure 4.8.

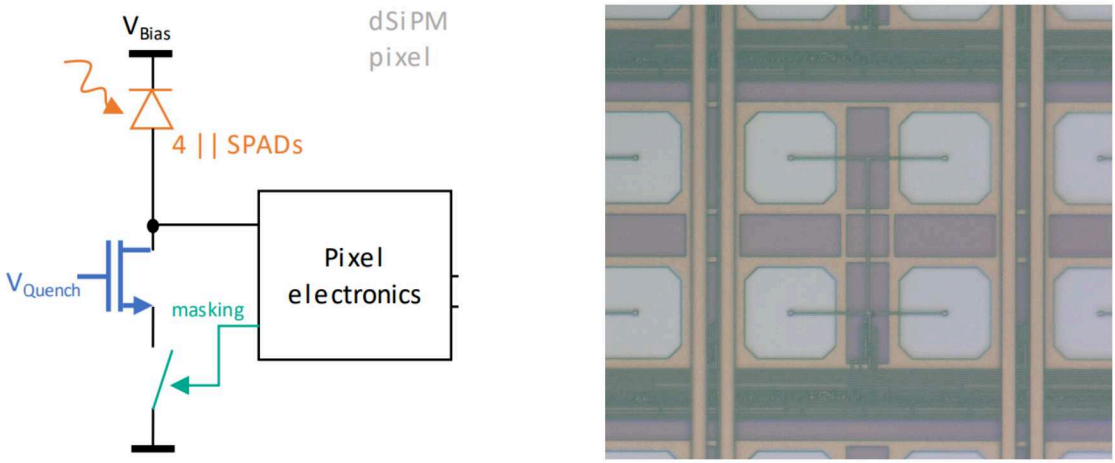

(a) (b)

Figure 4.9: Schematic representation of a dSiPM pixel (a). Microscope picture of a pixel(b).

The digital output coming from the pixel electronics (Section 4.2.1) in the array are connected via a wired-OR trigger network to the TDC (Section 4.2.2) and the validation logic (Section 4.2.3). The fastest pixel within the frame defines the time stamp that is serialized and read, together with the bunch count and the validation outcome, by the DAQ. The frame hitmap of the entire quadrant is also digitized using a 16-to-1 multiplexer. Operating the chip in *2-bit mode* is also possible: a 2-bit counter is included within each pixel to count multiple threshold crossings within the same frame. This allows the storing of hitmaps with more information on the detected event. Two consecutive frames must be read out to include this additional information.

4.2.1 Pixel Electronics

A schematic representation and a microscope picture of a DESY dSiPM pixel are shown in Figure 4.9. Each pixel contains four p-in-nwell SPADs sharing the same front-end electronics. Each SPAD has a nominal active area of $20 \times 20\,\mu m^2$, a cathode ring is used for top-side biasing and pwell rings surround the SPADs to minimize the crosstalk and contain the avalanche in the firing SPAD. NMOS transistors are placed in the pwell ring, while an additional nwell is added in the pixel periphery to host the PMOS transistors. Using this configuration, the total fill-factor of the pixel is estimated to be 30 %. The pixel has an area of $\sim 69.6 \times 76\,\mu m^2$. Each pixel contains a transistor which acts as a quenching circuit. This replaces the resistors used in analog SiPMs with the advantage that its equivalent resistance (i.e. the avalanche quenching duration) can be adjusted by changing the gate bias V_{Quench}. Another feature implemented at the pixel level is the possibility of masking via an SRAM cell, whose state is set during the configuration of the chip. This allows the disabling of pixels that are unused or contain a noisy SPAD. The pixel electronics also host an inverter used for the immediate digitization of the analog signal. The digital pulse is then connected to the chip periphery and processed by further digital components.

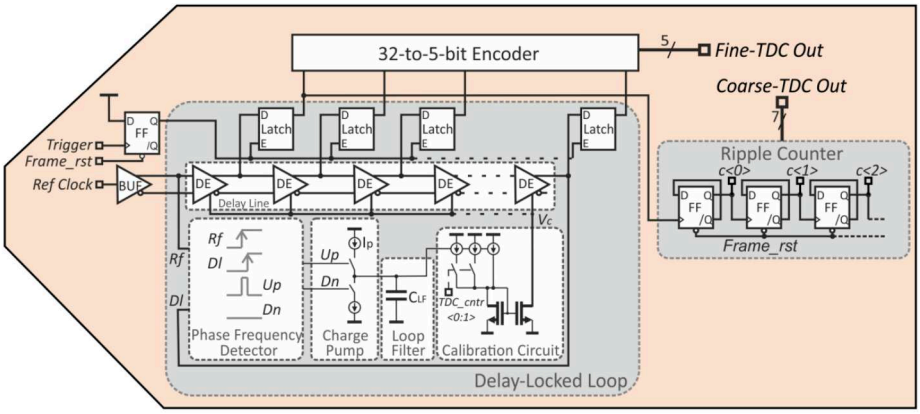

Figure 4.10: TDC structure of the DESY dSiPM. From [94].

4.2.2 Timestamping and 12-bit TDC

For each frame, the circuit of the discharged pixels draws a current to the chip periphery. Here, the fastest signal in the quadrant (if any) triggers the TDC. The converter includes three separate units to achieve precise time measurements.

The primary component is a 40-bit counter, which counts the number of frames since the start signal sent by the DAQ system at the beginning of data acquisition. This allows for a continuous measurement duration of approximately 100 hours.

A *coarse TDC* then provides timestamps within each frame. This coarse TDC is a 7-bit ripple counter operating on a 408 MHz system clock, yielding a coarse bin width of 2.45 ns.

For finer time resolution, the system also includes a *fine TDC* consisting of a Delay Locked Loop (DLL) with 32 differential delay elements. This configuration operates on the 408 MHz system clock, dividing each coarse clock cycle into 32 fine bins, achieving a theoretical bin width of 76.6 ps. A phase-frequency detector compares the incoming signal with the delayed one, adjusting the delay of the differential elements. The outputs of the delay elements are latched until the next frame starts and are encoded by storing the last delay element reached. After each DLL cycle, the counter is incremented in the coarse TDC. Figure 4.10 shows the schematic structure of the dSiPM TDC.

4.2.3 Validation Logic

In each quadrant, the wired-OR of the 16 pixels in each row is processed using a four-step validation logic. This provides a validation bit as the output of a pattern recognition algorithm on the hits of a frame. In the first step the rows are compared in pairs: the outputs are connected to a configurable AND/OR gate. The eight outputs of the first validation step are then compared by a new AND/OR gate step. The operation is repeated for four validation levels, as shown in Figure 4.11. Although configurable (in AND or OR), all gates in the same level must be the same type. The validation logic generates a validation bit for each frame, the value of which will depend on the logic sequence used and the result of the validations performed at each level (thus dependent on the position of the hits).

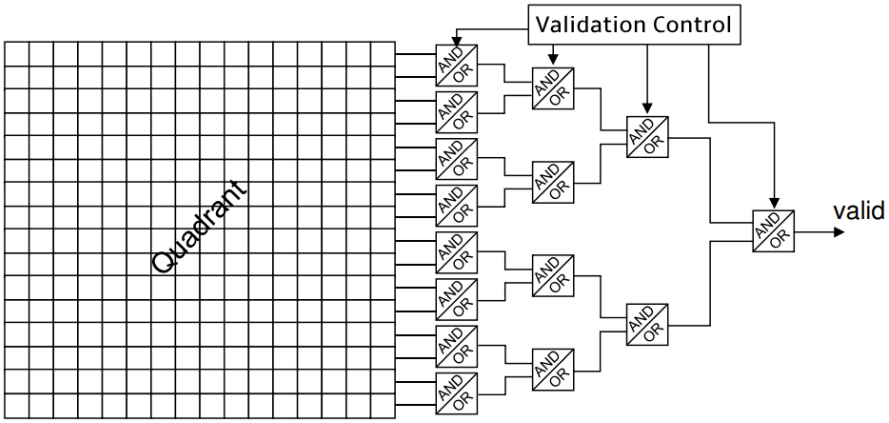

Figure 4.11: Validation logic circuit. From [95].

For example, by design, the validation bit is always valid if there is at least one hit in the array and all gates are set to OR. If, on the other hand, the gate at the last validation level is set to AND and all others are set to OR, the validation bit will be valid if there is at least one pixel firing in the first eight rows and one in the last eight rows of the quadrant. The validation logic is implemented to allow fast discrimination of events based on hit patterns.

4.2.4 Test Structures

Various test circuits are included at the sensor periphery to evaluate the performance of individual components independently of other upstream or downstream circuits that cannot be disconnected in the main array.

An independent TDC using the same clocks and input signals as the matrix is implemented and triggered with an external stop signal. It can be used to evaluate effective resolution for the fine and coarse TDC components [94]. A single pixel with front-end, surrounded by eight other pixels (to avoid edge-effects), is implemented to evaluate single pixel behavior, as shown in Figure 4.12(a). Only the central pixel provides a differential output terminated by a 20 kΩ quenching resistor, which can be probed on the chipboard. Surrounding pixels can be masked, and bias and quench voltage are configurable. For single SPAD measurements with front-end, a similar structure with single SPADs is present as shown in Figure 4.12(b). The operation and read-out are similar to the previously described pixel structure.

The other two test structures shown in Figure 4.12(c) and Figure 4.12(d) represent single pixel and single SPAD test structures without front-end electronics. These structures provide direct access to the analog signal produced by pixel/SPAD. The masking of surrounding pixels and bias are as described above; however, the central unit can not be disabled here.

The last test structure implemented in the ASIC's pad ring is a set of Low-Voltage Differential Signal links (LVDS) receivers and transmitters that can be used to determine the performance of the data links.

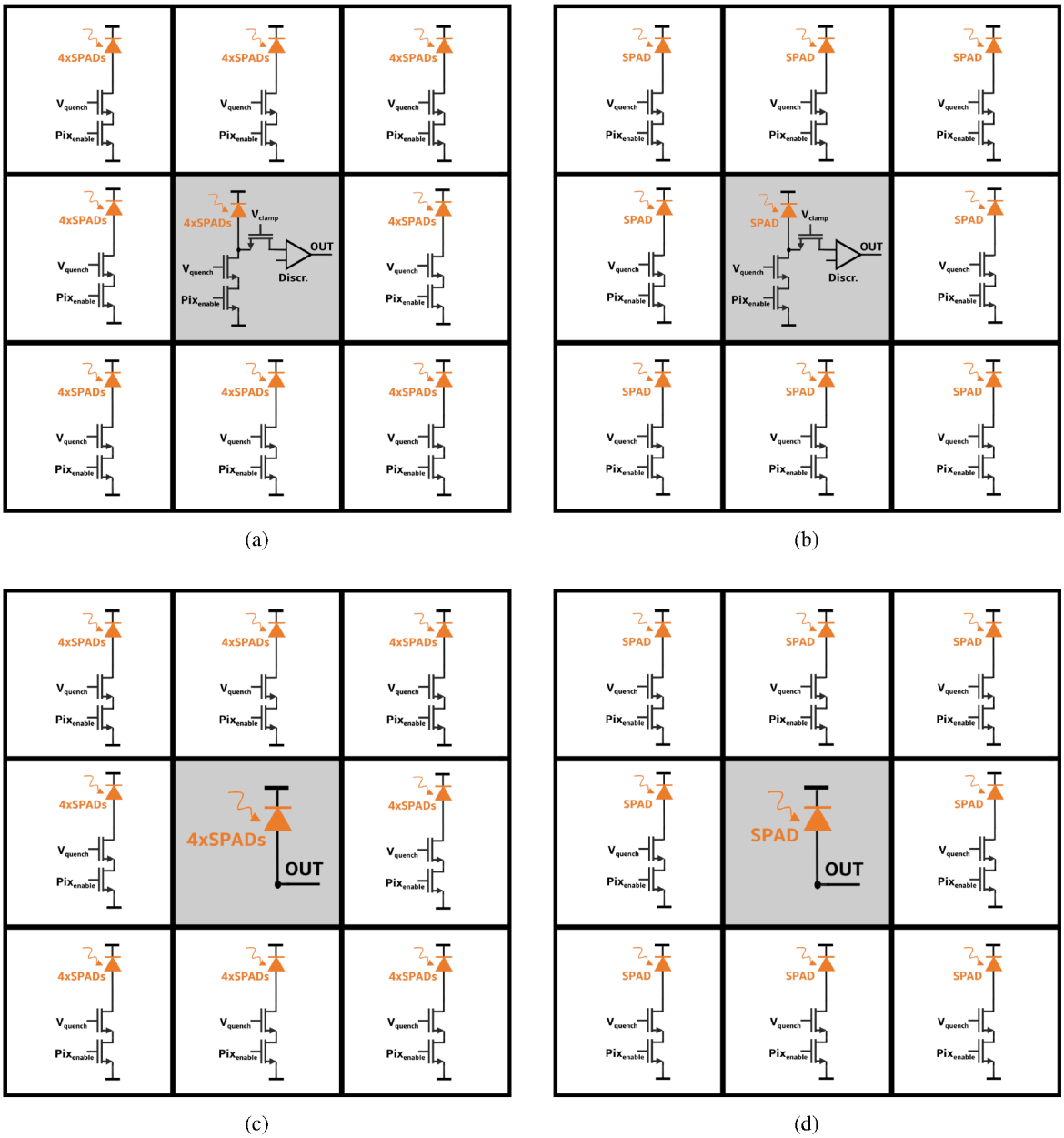

Figure 4.12: Schematic representation of the test structures. Digital pixel (a), digital SPAD (b), analog pixel (c) and analog SPAD (d).

CHAPTER 5

Laboratory Characterization of the DESY dSiPM

This chapter reports the results of detailed laboratory characterizations carried out on the DESY Digital Silicon PhotoMultiplier (dSiPM) prototype described in Section 4.2. Several samples of the DESY dSiPM prototype are characterized to compare the measured and expected performance of the dSiPM and to verify the functionality of the integrated Complementary Metal-Oxide-Semiconductor (CMOS) circuits. A selection of these studies is here reported, complementing the results published in [94]. Parts of the presented results are published in [96]. Section 5.1 summarizes the calibration procedure of the dSiPM temperature diode, which is crucial to maintain stable operation of the dSiPM. Section 5.2 presents measurements of Current-Voltage (IV) and Dark Count Rate (DCR), describing the experimental setup and results obtained on one of the prototypes tested. Section 5.3 reports the results of measurements obtained by exploiting the pixel-masking capability introduced in the DESY dSiPM design. Section 5.4 focuses on detailed studies of crosstalk, a typical noise source in Silicon PhotoMultipliers (SiPMs), correlating the probability of crosstalk with the location of noisy Single-Photon Avalanche Diodes (SPADs). Finally, Section 5.5 describes and analyzes the timing performance of the prototype studied using a fast pulsed laser setup.

5.1 Temperature Diode Calibration

Most of the SiPM properties and noise sources are temperature-dependent, as described in Section 4.1. Therefore, it is necessary to monitor the temperature of DESY dSiPM and keep it stable for the proper operation of the sensor. Several heat sources can be found in the Data AcQuisition (DAQ) system and on the chipboard of the dSiPM during standard operation, as shown in Figure 5.1. In this regard, the ambient temperature of the setup is not a proper estimate of the actual sensor temperature. The chip is equipped with a temperature diode integrated into the periphery; the current through the diode is sampled using the acquisition system. This allows the measurement of the actual operation temperature. The design of this diode makes it particularly prone to chip-to-chip variations. Therefore, all tested sensors must be calibrated to estimate the effective operation temperature.

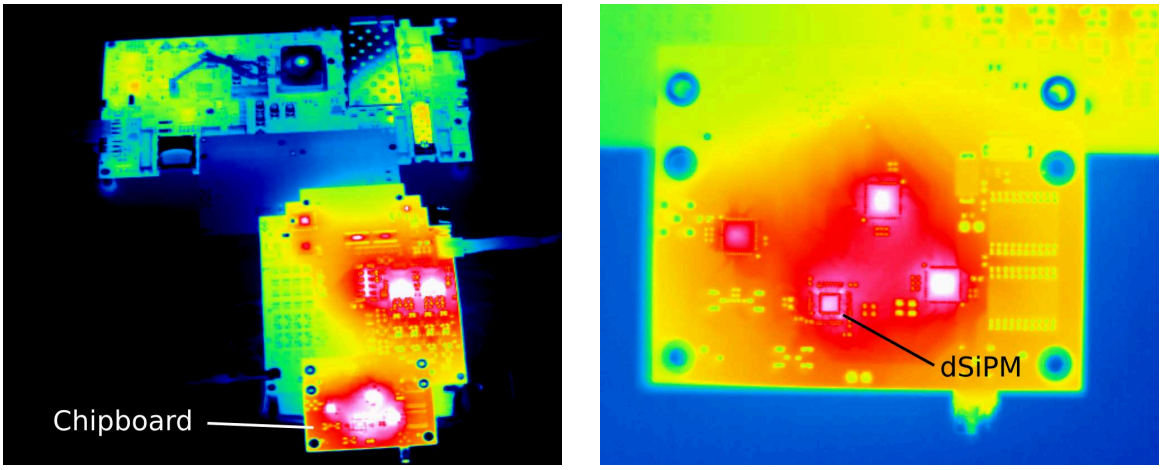

(a) (b)

Figure 5.1: Heath source of Caribou (a) system and chipboard (b). Image acquired at room temperature with the Jenoptik Variocam-IR [97] thermal camera. The color scale is not calibrated and, therefore, not shown. As a general indication, the peak temperature (white in the figure) is estimated to be ~40 °C in the shown example.

The ACS-DY200 [98] climatic chamber is used for this calibration, which allows the setup to be operated in a stable temperature and humidity environment. An active ventilation system also allows efficient heat transfer by minimizing thermal gradients between the tested systems and the climate chamber set point. The diode is set to be the only active element on the sensor during the calibration being independent of any other sensor components. All the main heat sources visible in Figure 5.1(b) are turned off, ensuring a minimum temperature difference between the climate chamber and the chipboard when the system's thermal equilibrium is reached. The difference between the two values is less than one degree Celsius according to measurements made with two different calibrated PT100 temperature sensors (one coupled to the climate chamber and the other to the chipboard). A calibration of the temperature diodes of the dSiPMs is possible under these conditions, with systematic uncertainties estimated to be of the order of one degree Celsius. Figure 5.2 shows the results of this calibration performed on seven different sensors. The uncalibrated chip temperature, T_{Chip}, obtained through the current measurement on the temperature diode, is shown as a function of the temperature of the climate chamber T_{CC}. Each point shows the average of 60 measurements, and the standard deviation is used as measurement uncertainty. The measurements are performed in the temperature range between ~15 °C and ~25 °C. Several minutes are waited before taking a new measurement to allow the system to reach thermal equilibrium. A linear fit of the data is performed to obtain a calibration function. The behavior of the diode is expected to be linear for all temperatures reported in this work. The values measured are used to calibrate the subsequent temperature measurements reported.

5.2 Current-Voltage and Dark Count Rate Measurements

IV measurements are essential to verify sensor functionality and to determine the breakdown voltage required to define a working point, as described in section 4.1.4. The DCR of a SiPM described in

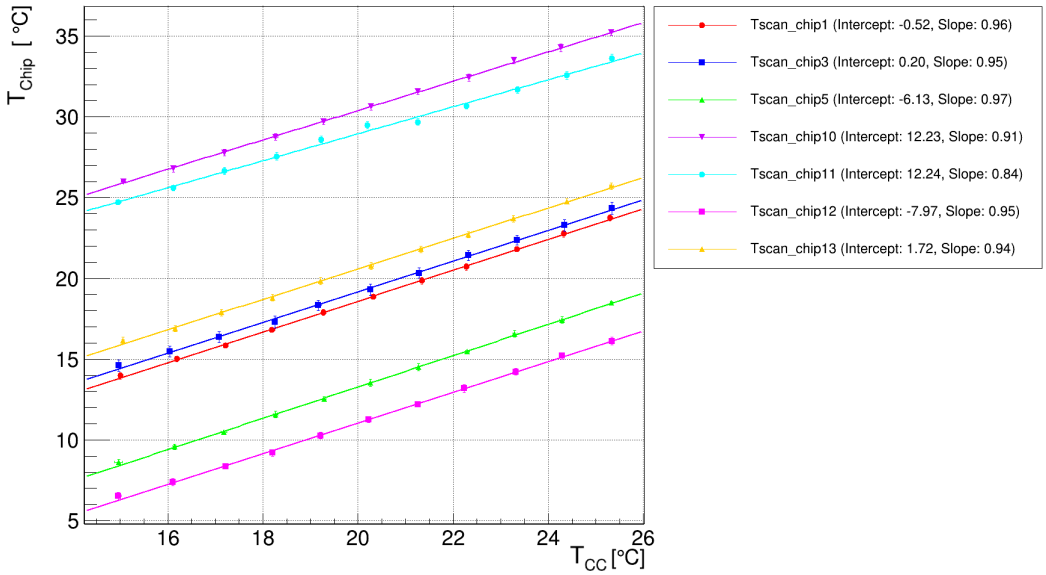

Figure 5.2: Temperature diodes calibration results. Calibration is performed on seven different prototypes.

Section 4.1.6 is also an important property that determines possibilities and limitations in sensor applications. IV and DCR measurements are carried out on tested dSiPMs for different sensor temperatures. An example is shown in this section.

5.2.1 Measurements Setup

IVs and DCR scans are performed in dark conditions using the ACS-DY200 [98] climatic chamber, which allows stable temperatures and relative humidity of ~0 %. The sensor circuitry is configured and biased using the Caribou DAQ system. Only the SPADs bias V_{Bias} is provided externally by a Keithley 2410 [99] source meter, which is also used for current measurement. All pixels in the main array of the dSiPM are enabled, while the pixels in the test circuits are disabled. A temperature and V_{Bias} scan is performed to determine dSiPM performance. The automated measurement includes waiting for thermal equilibrium to be reached for each new temperature value tested. With a stable temperature, an IV measurement is made using the source meter in the selected V_{Bias} range. The measurement is repeated multiple times for each voltage to reduce the uncertainty. Constant pauses between voltage values are set. For each configuration, a given number of data frames are saved using the DAQ system to evaluate the sensor's DCR. The frames are chosen randomly, without zero suppression.

5.2.2 Breakdown Voltage and Pixel Dark Count Rate

Figure 5.3 shows examples of IV curves taken with the same sensor, operated with climate-chamber set temperatures in the range $-25\,°C < T_{CC} < 20\,°C$. It can be noted that the current as a function of voltage is almost constant on the left part, analyzing the IV curves. The value here is dominated

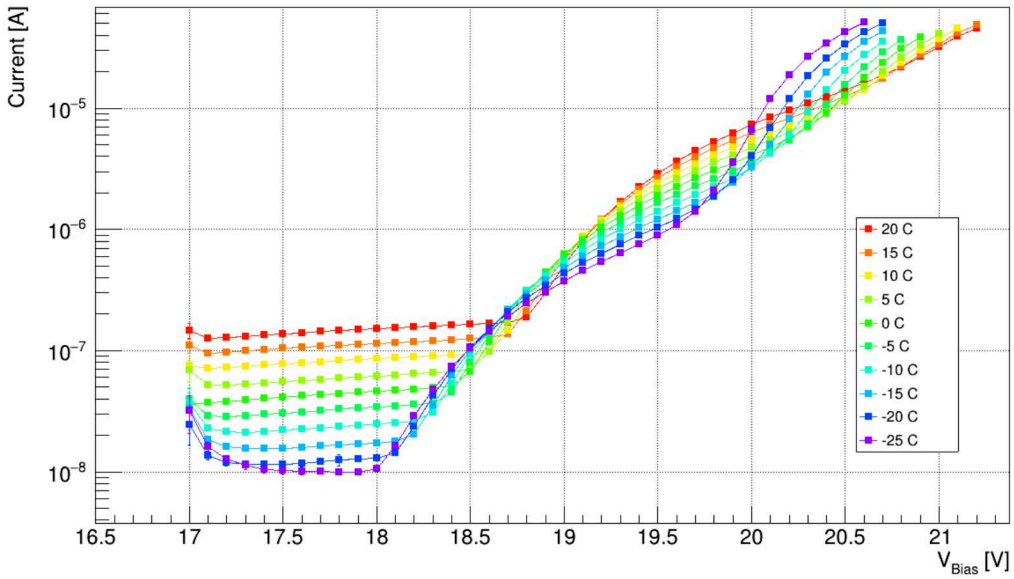

Figure 5.3: IV scan of a prototype. Measurements are performed in a climate chamber at different T_{CC} temperatures and with humidity control.

by the leakage current, which has an important temperature dependence[1], changing by more than an order of magnitude over the studied temperature range.

The breakdown voltage is qualitatively recognizable as a rapid slope change in the central part of the curves, between ~18 V and ~19 V, depending on temperature. A quantitative measure of the breakdown voltage is obtained as the position of the peak in the logarithmic derivative described by Equation 4.2. Figure 5.4 shows the logarithmic derivative of the current obtained with steps of 0.01 V in the breakdown region. The estimated breakdown voltages are 18.1 V and 18.9 V, at −25 °C, and 20 °C, respectively. The dV used for this evaluation is 0.08 V. This choice allows an accurate and robust validation of the breakdown voltage by sufficiently smoothing the measurements subject to noise. It introduces a systematic effect on the evaluation, which is assumed to be constant in all breakdown values reported in this work. The systematic uncertainty in the evaluation of the breakdown voltage is estimated to be less than 0.1 V.

Further changes in the slope of the IV curves for high overvoltage values are also evident in Figure 5.3 between ~19.2 V and ~19.8 V depending on temperature. For these values of bias, the probability of secondary avalanches due to charge trapping or crosstalk is expected to be so high that it leads to an increase in the dark current of the chip [100]. Overvoltages higher than those reported are not tested to protect front-end CMOS electronics directly connected to the SPAD (3.3V transistors).

The average DCR of the pixels is calculated by counting dark hits in the random frames saved during the IV measurements. This evaluation does not consider multiple hits of the same pixel in a single frame. Although the approximation is generally valid, in extremely noisy pixels this leads to an underestimation of the DCR. This effect affects a small percentage of the pixels (<1 %) and is therefore

[1] Described in Section 2.1.3

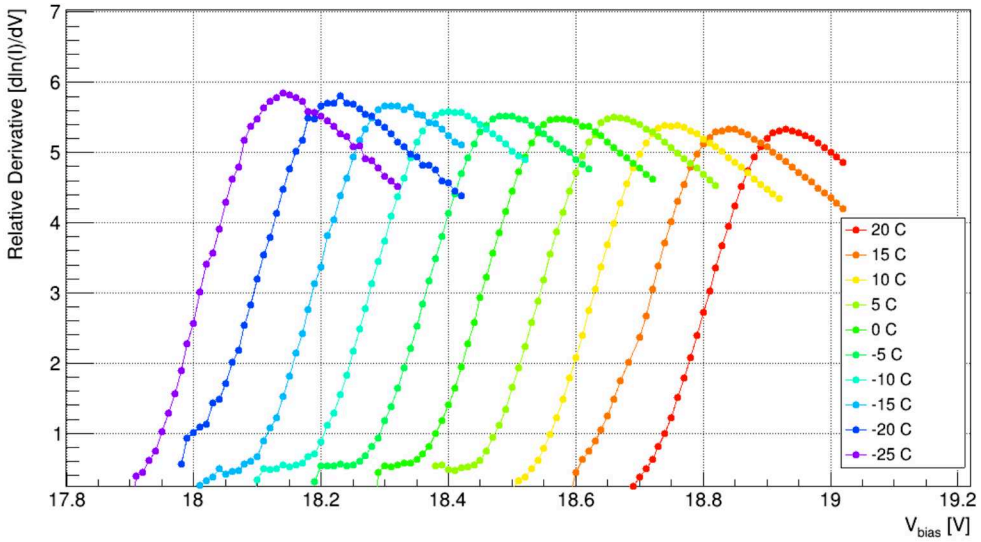

Figure 5.4: Breakdown evaluation using the logarithmic derivative technique. Measurements are performed in a climate chamber at different T_{CC} temperatures and with humidity control.

negligible in the results presented here. Figure 5.5 shows an example of the average DCR per pixel as a function of temperature and overvoltage V_{OV}. Sensor, temperature range and voltage steps are the same as in Figure 5.3 (simultaneous measurements). The DCR is strongly temperature-dependent and correlated with the overvoltage. It should also be noted that direct measurement of the DCR on the digital matrix is only possible from V_{OV} ≥0.6 V. This is the minimum overvoltage required for the avalanche-induced signal to be sufficiently large to exceed the threshold of the pixel discriminator. The DCR should be kept as low as possible in all possible applications to minimize the probability of DCR. The best way to keep the DCR low is to operate the sensor at low temperatures, as demonstrated by these measurements, or to decrease the overvoltage if possible. Timing and Photon Detection Efficiency (PDE) are negatively affected by lower overvoltage.

5.3 Masking

in DESY dSiPM, it is possible to mask individual pixels, as described in Section 4.2.1. Masking can be used to disable unused parts of the sensor or to deactivate noisy pixels. This can lead to a significant reduction in DCR and chip power consumption. Any masking pattern can be applied. Figure 5.6 shows a DCR hitmap taken with a mask reproducing the DESY logo, confirming the masking circuit functionality and the correct pixel mapping.

The possibility of masking individual pixels allows further studies of SPADs array properties that are not easily accessible with analog SiPMs. The influence on the DCR and IV curves of individual pixels is investigated. The measurements in this section are taken using the setup and analysis procedure described in Section 5.2.

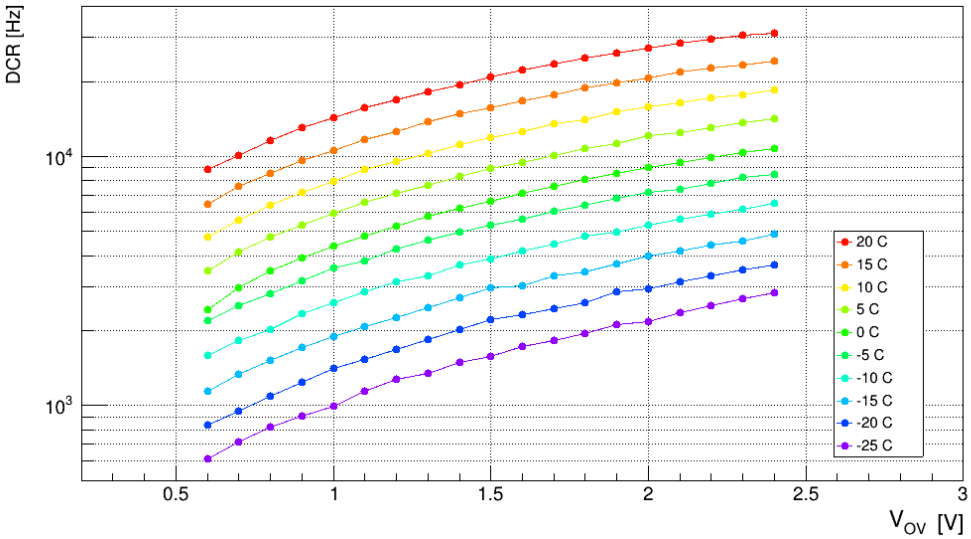

Figure 5.5: Average pixel Dark Count Rate evaluation as a function of the overvoltage for a prototype. Measurements are performed in a climate chamber at different T_{CC} temperatures and with humidity control.

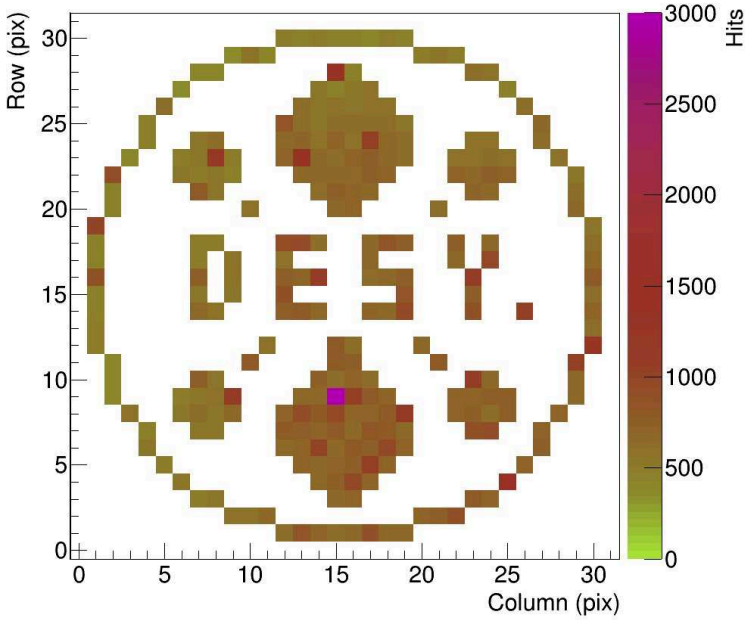

Figure 5.6: DESY logo DCR hitmap obtained via pixel masking on a prototype.

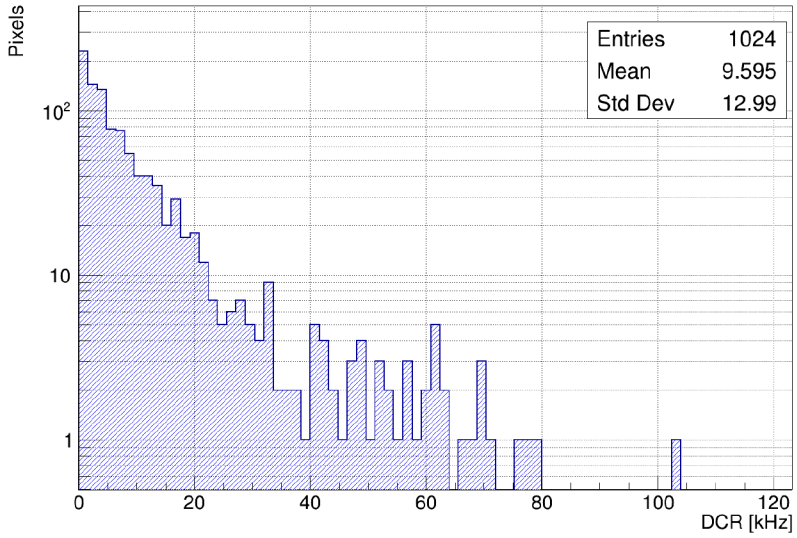

Figure 5.7: Pixels DCR of a prototype operated at $V_{OV} = 2\,\mathrm{V}$ and $T_{Chip} = 0\,^{\circ}\mathrm{C}$.

The histogram in Figure 5.7 shows the DCR of all pixels of a prototype operated at $V_{OV} = 2\,\mathrm{V}$ and $T_{Chip} = 0\,^{\circ}\mathrm{C}$. Most of the pixels show a DCR value of a few kHz, while some pixels show counts of one order of magnitude higher than average. Therefore, the average sensor DCR can be reduced considerably by masking a small percentage of noisy pixels. Figure 5.8 shows the effect of masking on the average DCR as a function of temperature. Masking 10 % of the noisiest pixels reduces the average DCR by about a factor of two. Due to design choices, masking one pixel simultaneously deactivates four SPADs. In Section 5.4, it is shown that the DCR of a pixel usually arises from a single SPAD. A minor design modification that allows the masking of individual SPADs would, therefore, lead to DCR reductions compatible with a much smaller reduction in the active area of the sensor.

Masking also allows accurate characterization of the IV curve properties (and thus power consumption) of SPAD arrays. As described in Section 5.2, the IV of a SiPM is highly correlated to the currents generated by DCR. Different masking patterns will, therefore, lead to different sensor IV responses. An example is shown in Figure 5.9: the IV of a sensor with different masks applied is measured. The largest currents and the most significant slope of the IV curve after the breakdown point are observed when the entire array is active (red curve) or when characterizing the IV of individual noisy pixels (pink curve, obtained by deactivating all other pixels in the array). By characterizing only 50 % of the least noisy pixels (green curve), the breakdown point seems to shift to higher values, and the current values, as well as the slope of the curve, change considerably. Looking instead at the IV of a pixel with little DCR (blue curve), the breakdown point is almost imperceptible, and although the pixel is perfectly functional, it no longer shows the typical exponential increase due to a low probability of DCR.

A quantitative interpretation of these effects is beyond the scope of this work. However, it is intended to show how masking and the behavior of single pixels/SPADs can considerably improve some of the main properties of a SiPM, such as DCR and power consumption.

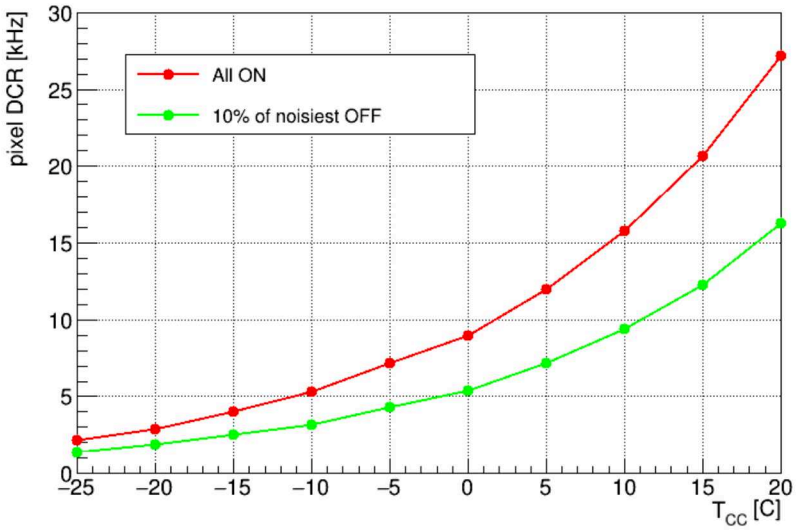

Figure 5.8: DCR characterization with different masks applied on a prototype. Measurements are performed in a climate chamber with temperature and humidity control at $V_{OV} = 2$ V and $T_{Chip} = 0\,^{\circ}$C.

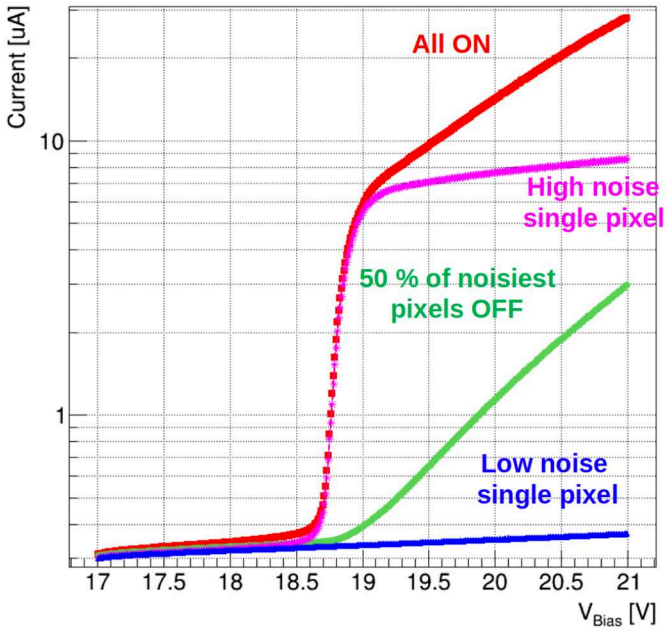

Figure 5.9: Effect of masking on the IV. Measures performed on the same prototype at the same temperature.

5.4 Crosstalk Measurement

Optical crosstalk is due to secondary photons generated during avalanche processes of SPADs that reach adjacent SPADs and trigger secondary events, as described in Section 4.1.7. The crosstalk probability is influenced by several factors, such as the design of the SPAD, the trench technology used, the quenching circuit, operation temperature, or overvoltage. This section reports procedures and results of crosstalk characterizations of individual DESY dSiPM pixels.

5.4.1 Single Pixel Crosstalk

The digital nature of the sensor allows crosstalk probability to be measured on individual pixels using an approach similar to the one described in [101]. A particularly noisy pixel surrounded by non-noisy pixels is chosen.

The DCR probability p_A for the central pixel and the eight neighbors are evaluated. The entire dSiPM is masked except for the investigated pixel for this measurement. This eliminates any crosstalk contribution from other pixels, as the masked pixels are not biased. p_A is then defined by counting the number of frames with dark counts of the investigated pixel, N_A, over the total number of analyzed frames N_{Frames}:

$$p_A = \frac{N_A}{N_{Frames}}. \tag{5.1}$$

Analyzed frames are chosen with a few milliseconds time gaps to minimize delayed crosstalk and afterpulse contamination. To simplify the notation p_c and p_n are defined, indicating the p_A of central and neighbor pixels respectively.

The DCR measurement is repeated for the eight pixels adjacent to the noisy one. This time, the central pixel is always active in addition to the investigated neighbor. The probability of central and neighbor pixel firing simultaneously $p_{c\cap n}$ is then computed:

$$p_{c\cap n} = \frac{N_{c\cap n}}{N_{Frames}}, \tag{5.2}$$

where $N_{c\cap n}$ is the number of frames containing an avalanche in both unmasked pixels.

Assuming p_c significantly larger than p_n, the crosstalk probability p_{CT} from the central pixel to a given neighbor n can be derived as:

$$p_{CT} = \frac{p_{c\cap n} - p_c p_n}{p_c(1 - p_n)}. \tag{5.3}$$

An example evaluation is shown in Figure 5.10, where the computed probability of crosstalk in the neighbors of the investigated pixel is shown. An overvoltage of 2 V and a temperature of 0 °C are set in a dark environment with temperature and humidity control. It can be seen that the probability of crosstalk is not uniform in the surrounding pixels.

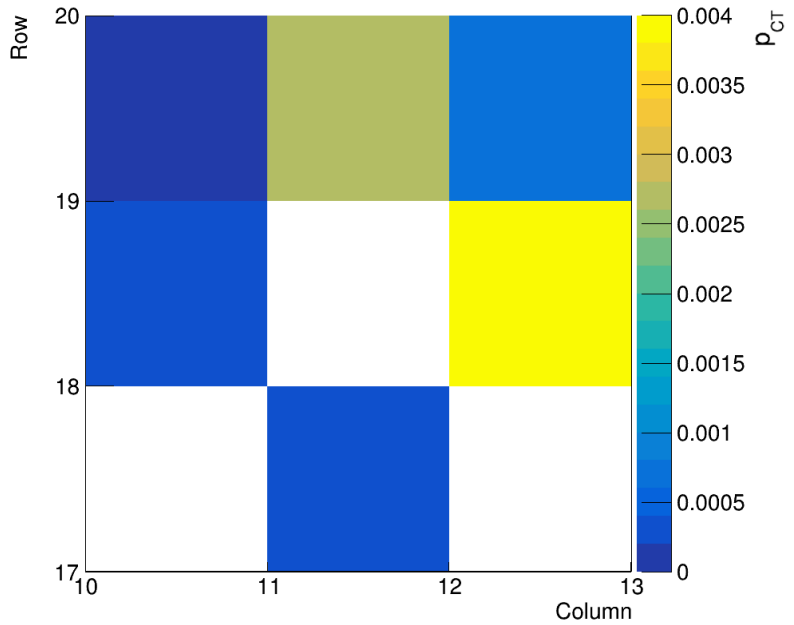

Figure 5.10: Crosstalk to neighbor (noisy pixel in the center). Measured with $V_{OV} = 2\,\mathrm{V}$ and $T_{Chip} = 0\,^{\circ}\mathrm{C}$.

5.4.2 Overvoltage and Crosstalk Probability

The correlation between overvoltage and crosstalk probability is also investigated. The measurement described above is repeated by changing the overvoltage of the SPADs. Figure 5.11 shows the results of this measurement. For better visualization, the reported value p_{CT} represents the sum of the probability of crosstalk in all eight pixels surrounding the noisy pixel. The SPAD has a higher gain at higher overvoltage, so more charges are created in the avalanche. This leads to a greater number of recombined charges and, thus, more photons emitted from the avalanche, increasing the crosstalk events.

5.4.3 Crosstalk Probability and Defect Position

Measurements taken on different pixels show that the probability of crosstalk and the position of the most involved adjacent pixels vary, as shown in Section 5.4.1. This can be deduced to be related to the exact position of the Geiger avalanche within the pixel, which, in noisy pixels, is assumed to be mostly limited to a specific SPAD where a crystal defect is localized. Pixels closer to the defect will have a higher probability of crosstalk due to the higher flux of photons from the primary avalanche.

To confirm this hypothesis, the light emitted during avalanches in noisy pixels can be directly detected using the method described in [102]. The chip is operated in darkness under a Zeiss Axioscope equipped with a Charge Coupled Device (CCD) camera[2]. Long-exposure measurements with dark frame subtraction allow light emission images from noisy pixels to be obtained. In Figure 5.12, the

[2] Jenoptik, model ProgRes SpeedXT core5 [103]

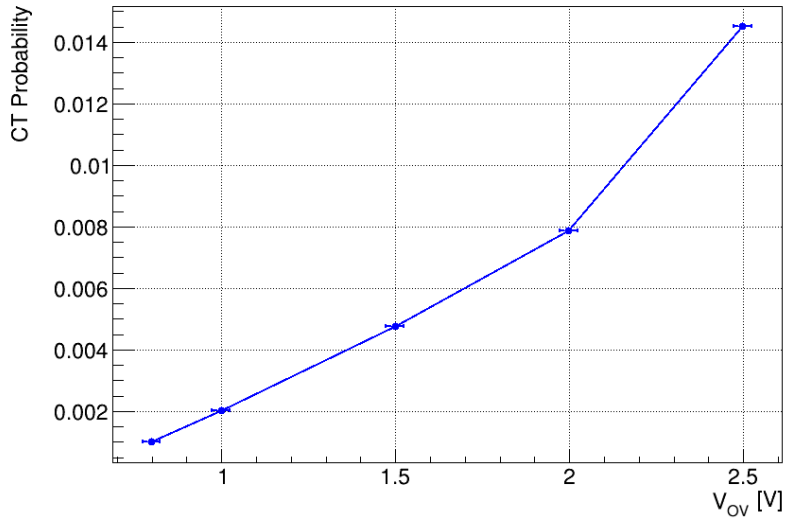

Figure 5.11: Crosstalk probability as a function of V_{OV}. Measured with $T_{Chip} = 0\,^{\circ}\mathrm{C}$.

example of two noisy pixels of light emissions superimposed on a pixel picture is compared to the relative crosstalk measurement in adjacent pixels. It can be seen that a single SPAD mainly emits light and that the probability of crosstalk is consistent with the above hypothesis. Furthermore, the crosstalk probability is higher in the x-direction because the distance between pixels in the y-direction is larger due to the presence of in-pixel electronics. In order to maximize the intensity of the emitted light, particularly noisy pixels are chosen in the shown examples, and the chip is operated under non-standard conditions: the use of maximum allowed overvoltage and an atypical quenching value make avalanches in the noisy pixel much more frequent and longer, thus generating more detectable photons. The p_{CT} in equation 5.3, although proportional to the actual value, is no longer a reasonable estimate of the probability of crosstalk. Under these conditions, overlapping avalanches in the same frame are no longer negligible, in Figure 5.12 the probability of crosstalk is therefore expressed in arbitrary units. It can also be seen that the detected light is mainly emitted near the collection electrode (in the center of the SPAD). This is probably due to the sensitivity of the CCD sensor limited to visible light. According to what is presented in Section 2.3, visible light travels less than one micrometer in the silicon before being absorbed. Only light emitted near the surface can, therefore, escape from the silicon and be detected. A Near InfraRed (NIR) light-sensitive camera could represent a more effective tool for a detailed investigation of the exact position of avalanches within the SPAD [102].

5.5 Timing Measurements with a Picosecond-Pulsed Laser

The timing performance of SiPMs is one of the main characteristics of the sensors, as described in Section 4.1.9. The temporal properties of the DESY dSiPM are investigated with a fast laser setup. The σ_{SPAD}, σ_{Delay} and σ_{TDC} components of the Equation 4.4 are evaluated by exploiting the digital nature of the sensor and the test structures implemented in the chip periphery.

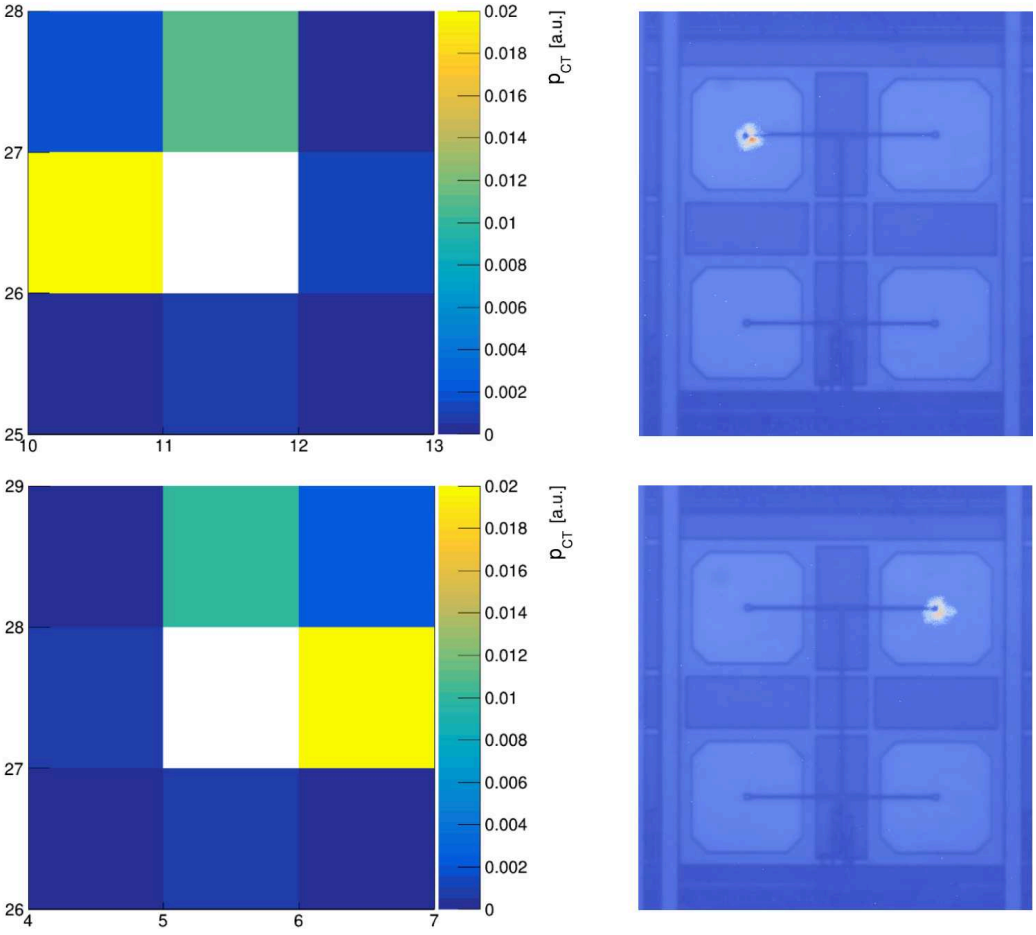

Figure 5.12: On the left, crosstalk to neighbors of two noisy pixels (noisy pixel in the center). Light emitted by the corresponding noisy SPAD is measured and shown on the right. Measured at room temperature with $V_{OV} \sim 3\,\mathrm{V}$ and minimum quenching resistance to maximize light emission. Crosstalk pattern and emitted light position are correlated.

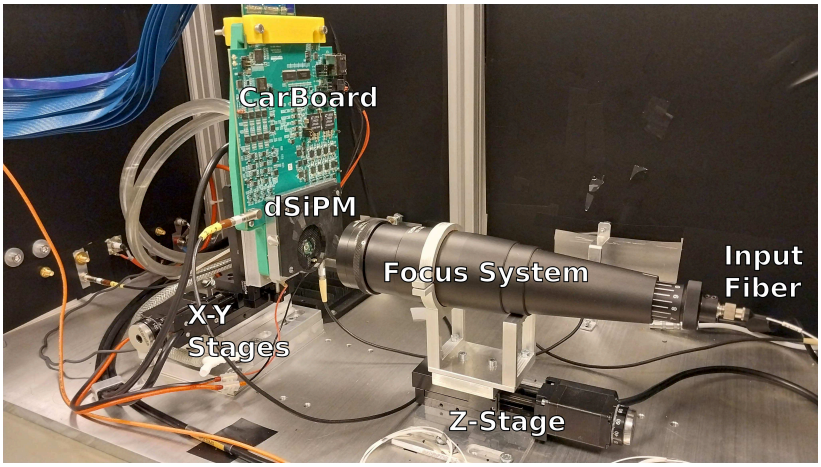

Figure 5.13: Laser Setup used for dSiPM timing studies.

5.5.1 Laser Setup

The laser setup used is shown in Figure 5.13. The ALS Laser Systems EIG1000D with 672 nm laser head [104] is used. It produces a tunable pulse with a duration of ~50 ps and a rise time of a few picoseconds. The system is operated with an external trigger with a nominal input jitter in the laser driver of ~4 ps. The laser is collimated and focused by an optical system and can achieve a minimum spot size of ~6 µm. The SiPM is mounted on a remotely controlled double axes stage, which enables the positioning of the Device Under Test (DUT) with micrometer accuracy. The optical system is also mounted on a remotely controlled stage that allows the distance to the dSiPM to be set and the laser focus adjusted. The entire system is enclosed in an aluminum dark box to ensure operation in dark conditions. The measurements presented in this section are taken at room temperature.

5.5.2 SPAD and Pixel Analogue Signals

The analogue test structures described in Section 4.2.4 and shown in Figure 4.12, are used for the characterization of the intrinsic time resolution of the SPAD and pixel of the dSiPM. All SPADs/pixels of the test structures are active during the measurement to ensure uniformity in the fields of the investigated structures (central unit). A high laser pulse intensity is used for this measurement, and the laser spot is deliberately enlarged to illuminate the test structures uniformly. The analog and digital pulses of the SPAD/pixel are sampled directly on the chipboard using Waverunner 640Zi [105] oscilloscope equipped with a ZS1000 1GHz active probe. A fast trigger signal is generated by the Keithley 3390 [106] pulse generator and split to trigger the laser driving system and oscilloscope readout simultaneously. Trigger system jitter is measured to be <5 ps. Structures are investigated in the $-0.1\,\mathrm{V} < V_{OV} < 2.6\,\mathrm{V}$ range. 2000 waveforms are recorded for each bias tested. Figure 5.14 shows the amplitude of the signals defined as the average of the maximum waveform amplitudes. The standard deviation of the mean is shown as uncertainty (within the marker in most cases). The structures, providing direct access to the SPAD/pixel signal, show an increasing amplitude with overvoltage over the entire test range. This is consistent with the increase in gain. No particular difference is visible in amplitude between SPAD and pixel output. Sharing the same quenching circuit,

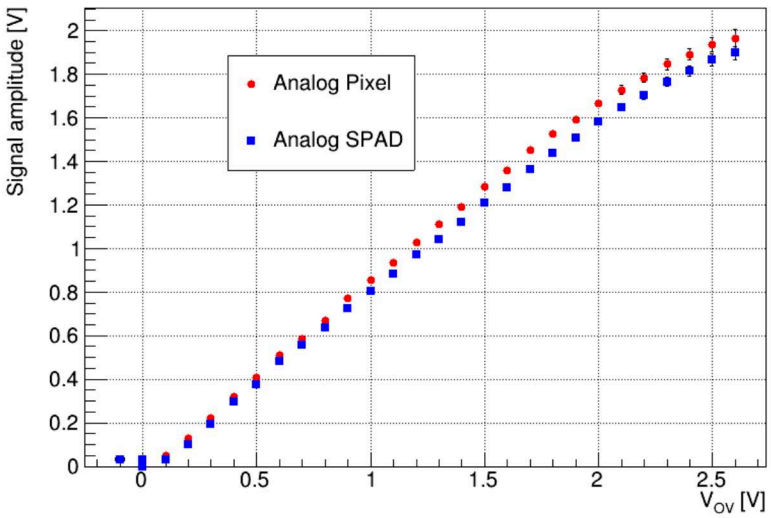

Figure 5.14: Analogue signal output measured on the pixel/SPAD test structures as a function of the overvoltage. Measurement is performed at room temperature.

the pixel behaves like a larger SPAD. The only appreciable difference is probably due to the different systematics due to the non-simultaneous measurement procedure.

5.5.3 SPAD and Pixel Time Resolution

The Time Of Arrival (TOA) of the analog signal, with respect to the pulse generator trigger, is defined using a Constant Fraction Discrimination (CFD) method at 50 % of the signal amplitude. An example of TOA distribution is shown in Figure 5.15 for the sensor operated at 2 V overvoltage. The distribution is fitted with a Gaussian, and the extracted σ_{Fit} is used as an estimate of the temporal resolution of the SPAD/pixel and can be expressed as:

$$\sigma^2_{FIT} = \sigma^2_{SPAD/Pixel} + \sigma^2_{Trigger} + \sigma^2_{DAQ} + \sigma^2_{Laser} + \sigma^2_{Noise}, \tag{5.4}$$

where $\sigma_{SPAD/Pixel}$ is the intrinsic resolution of the central unit investigated, $\sigma_{Trigger}$ is the contribution of the trigger system, σ_{DAQ} the resolution of the acquisition system (active probe and oscilloscope), σ_{Laser} the laser pulse jitter and σ_{Noise} the noise contribution.

Figure 5.16 shows σ_{FIT} obtained with the different analog test structures. Only statistical uncertainties are shown. The timing performance improves as a function of overvoltage, reaching ~12 ps in the analog pixel structure. The trend is in line with expectations; in fact, higher overvoltage corresponds to a stronger electric field, higher gain values, higher PDE, and better signal-to-noise ratio. These factors reduce the contribution of $\sigma_{SPAD/Pixel}$ and σ_{Noise}, i.e. improve timing with overvoltage. It is also observed that the timing of the analog pixel is considerably better than the single analog SPAD. In this measurement, the entire test structure is illuminated with several photons per pulse. The four SPADs of the pixel are, therefore, with high probability, all active with simultaneous avalanches in the entire pixel, resulting in a better timing performance of the pixel.

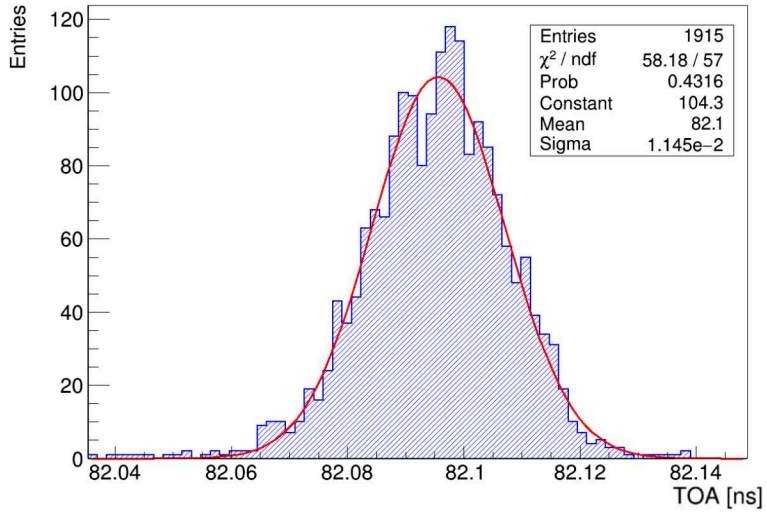

Figure 5.15: Example of TOA distributions for the analog pulses of the pixel test structure operated at $V_{OV} = 2$ V.

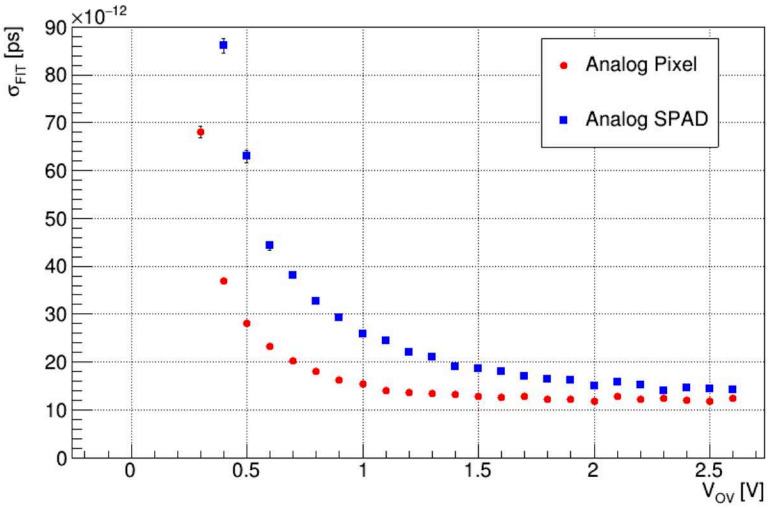

Figure 5.16: Signal TOA as a function of the overvoltage for analogue pixel/SPAD test structures.

Although the measurements shown in this example are a good estimate of actual timing performance, the type of primary charge source used also determines them. Light with a different wavelength or intensity, as well as the interaction of charged particles instead of photons, can result in a different intrinsic time response of the SPAD/Pixel, as described in Section 4.1.9.

5.5.4 Propagation Delays

The laser setup is also used to characterize σ_{Delay} in Equation 4.4. The main array is used for this measurement, uniformly illuminated by the pulsed laser with high light intensity. A dedicated acquisition mode has been developed for this measurement: the Caribou FPGA generates a fast trigger output coincidentally with frames marked for storage. The trigger signal has a configurable delay from the start of the frame and is used to trigger the laser control unit. This allows the synchronization of laser pulses to the dSiPM Time to Digital Converter (TDC) clock. The entire matrix is masked except for one pixel per quadrant in turn, which ensures that the timestamp saved by the respective TDC corresponds to the signal generated by the unmasked pixel. The laser pulse TOA of individual pixels can thus be defined as the timestamp recorded by the respective TDC (reset at the beginning of the frame). The measurement is repeated 500 times for each pixel to minimize statistical uncertainties. An example of such a measurement is shown in Figure 5.17. It can be seen that different TOA values are recorded from different pixels despite the constant delay of the laser pulse with respect to the start of the frame. Signals from more distant pixels will take longer to propagate, resulting in a delayed timestamp. The measured values and the pattern are consistent with the chip design and TDCs positions. The standard deviation of all measured values represents a reasonable estimate of σ_{Delay} for these operational conditions and is measured to be ~80 ps. Note that in low occupancy conditions, where no more than one pixel per quadrant has a hit, this contribution can be corrected in order to improve the temporal resolution of the sensor[3].

5.5.5 TDC resolution

Another essential component in the time response of the dSiPM is the intrinsic resolution of the TDC σ_{TDC} in Equation 4.4. Although its nominal value is directly related to the design bin width of the TDC (76.6 ps), the laser setup is used to determine its actual value. A fast trigger signal is generated by the Keithley 3390 [106] pulse generator, which is used in 'noise' mode to trigger the laser with randomly distributed pulses within frames. Random frames are saved and analyzed. With sufficiently high statistics, a uniform distribution covering the entire dynamic range of the timestamps within the frame is expected. However, the measurements show that the fine TDC dynamic range cannot be fully exploited due to a discrepancy between the actual and nominal values of the delay elements used. This results in a resolution of the fine TDC of ~4.8 bit instead of 5 bit. Furthermore, the delay elements used, due to fluctuations in the production process, produce slightly different delays and thus a non-constant bin width. This effect, known as Differential Differential Non-Linearity (DNL), can be characterized on individual TDCs and corrected using high statistic measurements of uniformly distributed hits within the frame. More details on the actual time resolution of the DESY dSiPM TDC and the DNL correction performed on DCR events can be found in [107]. The average effective bin

[3] If more than one pixel per quadrant is active in the same frame, it is not possible to determine which pixel determined the timestamp of the corresponding TDC.

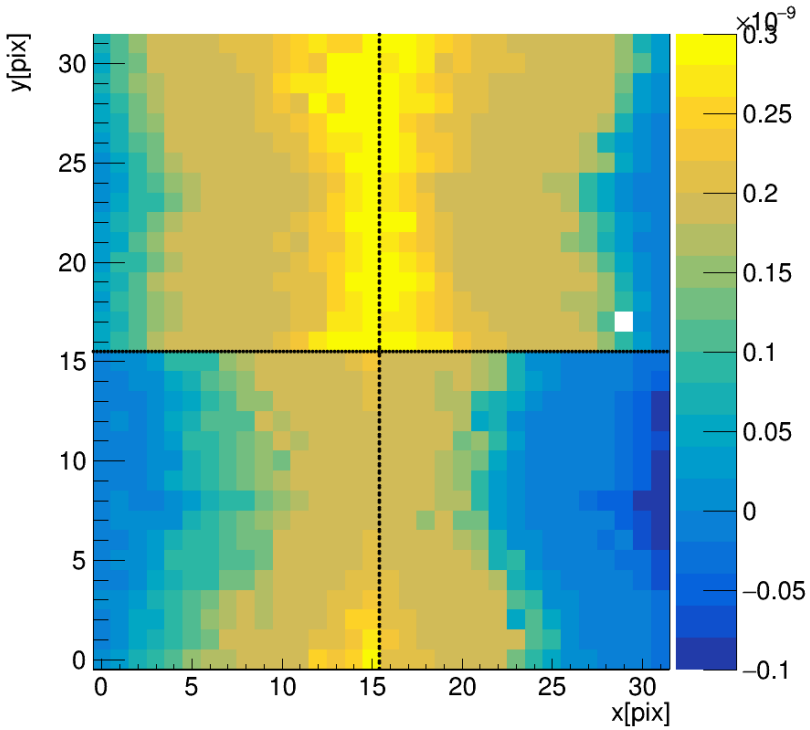

Figure 5.17: Example of pixels delays measured at V_{OV} = 1.5 V. Quadrant separations are marked with a dashed line. The white pixel is not functional in the prototype tested. The measurement is performed at room temperature.

width of the TDC (with slight variations in different TDCs) is found to be ~95 ps, which corresponds to a binary resolution σ_{TDC} of ~27 ps.

5.6 Summary of Results

Extensive laboratory characterizations are presented in this chapter confirming the functionality of the DESY dSiPM SPAD array and all integrated CMOS circuits.

Calibration of the integrated temperature diode is performed on all investigated samples, allowing the operation under stable and controlled conditions, since many of the sensor performances are temperature-dependent.

IV curves and DCR are measured to identify the optimal working points of the samples and to evaluate noise. The measurements show uniformity among the studied samples and are compatible with the nominal values provided by the foundry with a breakdown voltage in the range of 18.1 to 18.9 V depending on the operation temperature, and average DCR value per pixel in the range of 0.5 kHz to 3 MHz depending on temperature and overvoltage used. Masking of noisy pixels affects sensor power consumption and results in a reduction of DCR up to 50 % by masking 10 % of the noisiest pixels.

A detailed study of crosstalk is carried out by taking advantage of the digital nature of the sensor and the possibility of masking individual pixels. The probability of crosstalk is thus correlated with the location of noisy SPADs.

The temporal performance of the sensor is studied using a picoseconds pulsed laser. The main contributions to the temporal resolution of the DESY dSiPM are evaluated using masking and exploiting the test structures embedded in the periphery of the chip. The intrinsic pixel/SPAD resolution reaches values of $\sim$ 12 ps for higher overvoltage, the contribution of delays stemming from the relative position of the pixel with respect to the TDC is measured to be $\sim$ 80 ps, and the contribution caused by the TDC binning is measured to be $\sim$ 27 ps.

The characterizations described in this chapter are repeated on multiple samples. These measurements and calibrations allow the sensors to operate under known and controlled conditions allowing accurate characterization of DESY dSiPM performances.

CHAPTER 6

Test-Beam Characterization of the DESY dSiPM

One of the main objectives of this work is to verify the feasibility of using Digital Silicon PhotoMultiplier (dSiPM) in 4D-Tracking applications, an essential research and development topic for future High-Energy Physics (HEP) experiments as described in Section 1.5.2. The 4D-Tracking capabilities of the DESY dSiPM described in Section 4.2 are verified in test-beam experiments by using the infrastructure and methodologies discussed in Chapter 3. The setups used in the different test-beam campaigns are described in Sections 6.2 and 6.3. Sections 6.4 and 6.5 elaborate on the specific alignment procedures used and give details on the analysis. The results of the measurements, including spatial resolution, timing resolution, and efficiency in direct Minimum Ionising Particles (MIP) detection, are then presented in Section 6.6. Parts of the presented results are published in [96, 108].

6.1 dSiPM in direct MIP detection

Single-Photon Avalanche Diodes (SPADs) and Silicon PhotoMultipliers (SiPMs) are widely used for single-photon detection and photon counting applications. Given the timing and spatial resolution achievable with dSiPMs, these sensors could also be promising candidates for 4D-tracking in MIP detection. Differently from single photons, the passage of MIP in the SPAD generates hundreds of primary electron-hole (e-h) pairs, as sketched in 6.1, SPAD (i.e. SiPM) response in MIP detection is then expected to be different from the photo-detection case.

6.2 Test-Beam Setup

The 4D-tracking performances of DESY dSiPM are investigated in several test-beam campaigns at the DESY II test-beam facility with a 4 GeV electron beam. The test-beam setup of dSiPM studies uses the hardware and frameworks described in Chapter 3. The specific configuration used is schematized in Figure 6.2. The core of the system is the AIDA Trigger Logic Unit (TLU) [68]. The TLU interfaces with all the devices involved and enables their synchronous operation. It accepts trigger input ($Trigger\ IN$) from the $scintillators$ or $Telepix$ described in the next section; the latter also receives

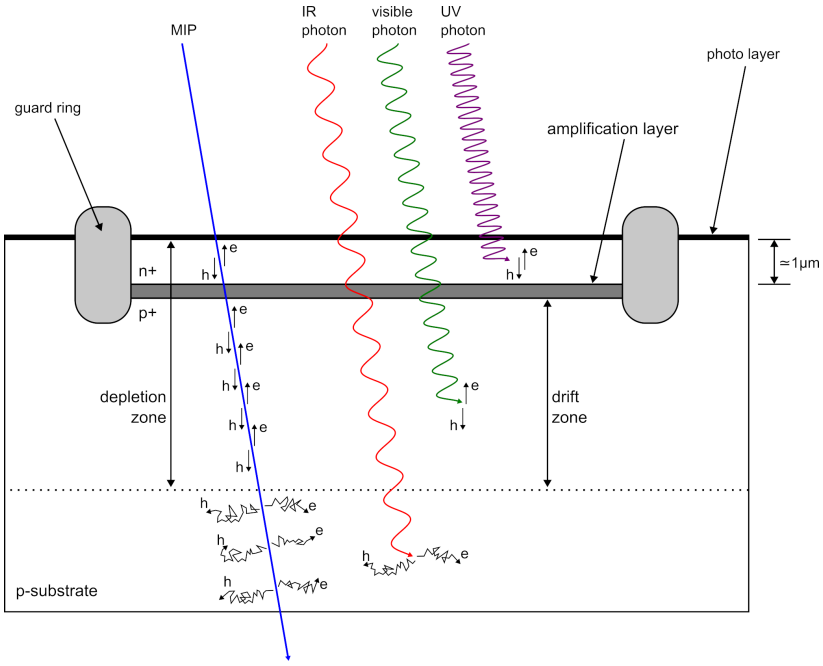

Figure 6.1: Schematic representation of MIP and photons Interactions in a SPAD. From [107].

a *Clock* and a *t*0 synchronization signal from the TLU. When interfacing with the six planes of the telescope used to reconstruct the tracks, the TLU sends *Trigger IDs* and accepts a *BUSY* signal; i.e. it will not issue any further triggers until all planes are ready for a new acquisition. The dSiPM interfaces with the *Caribou DAQ* system [65] via *LVDS* links and also receives *Clock* signals and biasing. The Caribou system gets a reference *Clock*, *t*0, and *Trigger OUT* from the TLU. When the trigger is received, data storage for the selected frames starts, and the system returns a *BUSY* long enough to ensure that no new triggers are issued during data readout and storage. The storing of the data from all devices, as well as their simultaneous configuration and management, is handled by the EUDAQ2 software [69]. The software also saves the *Telescope Hitmaps*, *TLU Timestamps & Trigger IDs*, *dSiPMHitmap & Timestamp* to disk for later analysis, performed with the Corryvreckan framework described in Section 3.5.

6.2.1 Trigger Systems

A trigger plane or configuration is used in dSiPM test-beam studies to determine the track acceptance region. The aim is to maximize the acceptance of tracks passing through the Device Under Test (DUT) while minimizing unnecessary event storage and dead time needed by the Data AcQuisition (DAQ) system each time a trigger is issued. Therefore, triggers with dimensions similar to those of the DUT are employed. Two trigger systems are used in the test-beam campaign here presented:

- The first system includes scintillators and a veto scheme. Three different scintillators read by PhotoMulTipliers (PMTs) are aligned and positioned before and after the telescope planes to ensure that the tracks pass the entire telescope. A fourth scintillator is instead positioned close

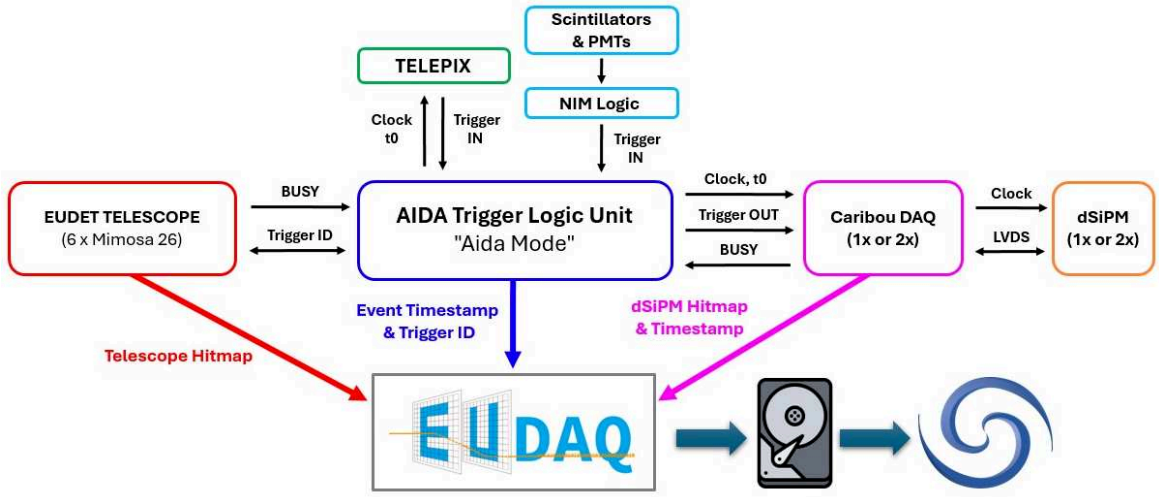

Figure 6.2: Schematic representation of the dSiPM test-beam DAQ system.

to the DUT; this scintillator has a hole with a diameter of about 2 mm. The coincidence of the three outer scintillators is used in anti-coincidence with the scintillator with a hole. The logic is performed using conventional NIM modules. This results in a trigger pattern that only selects tracks that pass through the hole of the veto scintillator, i.e. a fast analog trigger that only selects an area of approximately 2 mm diameter. Figure 6.3(a) shows a hitmap of one of the telescope planes when this trigger configuration is used.

- The second trigger system allows the selection of tracks in the entire active area of the dSiPM and is used to confirm the functionality of the whole matrix. A pixel detector prototype called TelePix [109], currently under development at DESY and available in the beam line for internal users, is used as a trigger system. This device has an active area of $\sim 3 \times 4\,\mathrm{mm}^2$ and consists of an array of 29×124 pixels that can be individually masked. It also has a fast output that can be used as a trigger signal. By masking a few pixels, a trigger area of $\sim 3 \times 3.4\,\mathrm{mm}^2$ is selected, sufficient to cover the entire DUT while still maintaining a small trigger window relative to the size of the beam spot, Figure 6.3(b) shows a hitmap of one of the telescope planes when this trigger is used.

6.3 Test-Beam Campaigns

Three different test-beam campaigns have been carried out on bare prototypes at DESY II test-beam facility [58]. Pictures and a schematic of the setups are illustrated in Figure 6.4. The setups were progressively adapted and improved over the three measurement periods. In details:

- May 2022: The main objective of this first test-beam was to implement and test the DESY dSiPM in the test-beam setup. The dSiPM, DUT, was mounted on a dual-axis stage to allow its positioning with micrometric accuracy. As a reference for track reconstruction, the EUDET-type telescope [60] available in the facility was used, consisting of 6 planes of MIMOSA 26 pixel

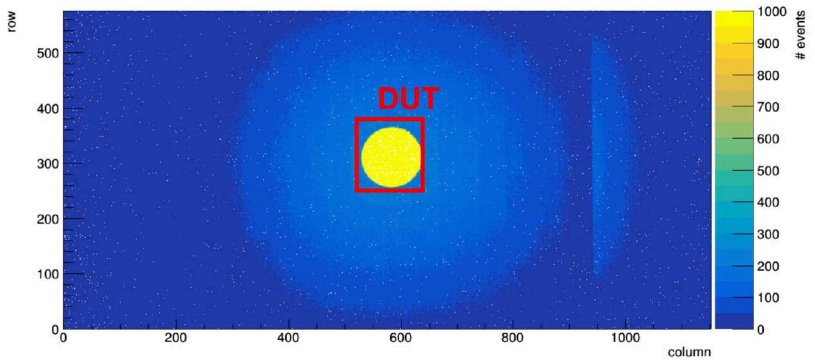

(a)

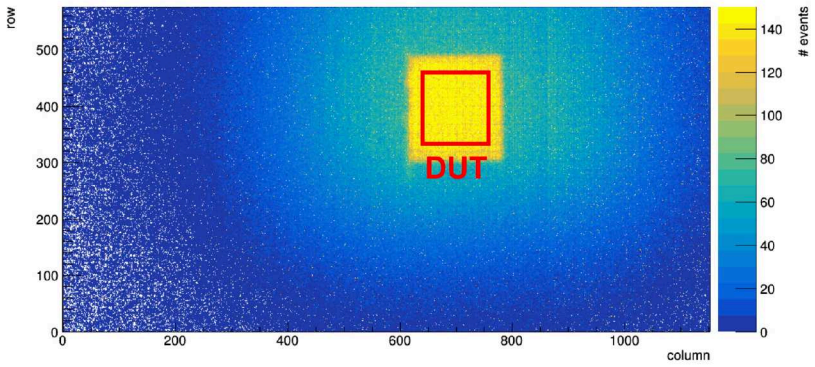

(b)

Figure 6.3: Hitmap on the reference telescope plane using the two trigger systems: scintillators+veto (a) and TelePix (b). In red is shown the relative position of the dSiPM of May 22 test-beam (a), October 22 test-beam (b).

detectors [62]. The combination of scintillators and a veto described in the previous section was used as trigger. An active cooling system enabled stable temperature operation at $\sim 20^{\circ}C$ on the chip. The dSiPMs chipboards were placed inside an aluminum case, which acted as a light shield and provided thermal contact to the cooling element. Hardware and software were developed and tested to include DESY dSiPM in the test-beam setup, and the DESY dSiPM performances in direct MIP detection were evaluated for the first time.

- October 2022: In this test-beam, the mechanic of the setup was improved, and a better cooling system was installed, using nitrogen to avoid condensation, which enabled stable temperatures of $\sim 0^{\circ}C$ on the chip. The aluminum casings and outer plastic housing used were designed with holes to reduce the amount of material, positively affecting the tracking precision. Thin layers of aluminum or Kapton foil were applied to ensure the casings remained both light and airtight. Telepix system, described in the previous section, was here used as trigger. Several bias and temperature scans were carried out in this campaign to evaluate the chip's performances under different environmental and overvoltage conditions.

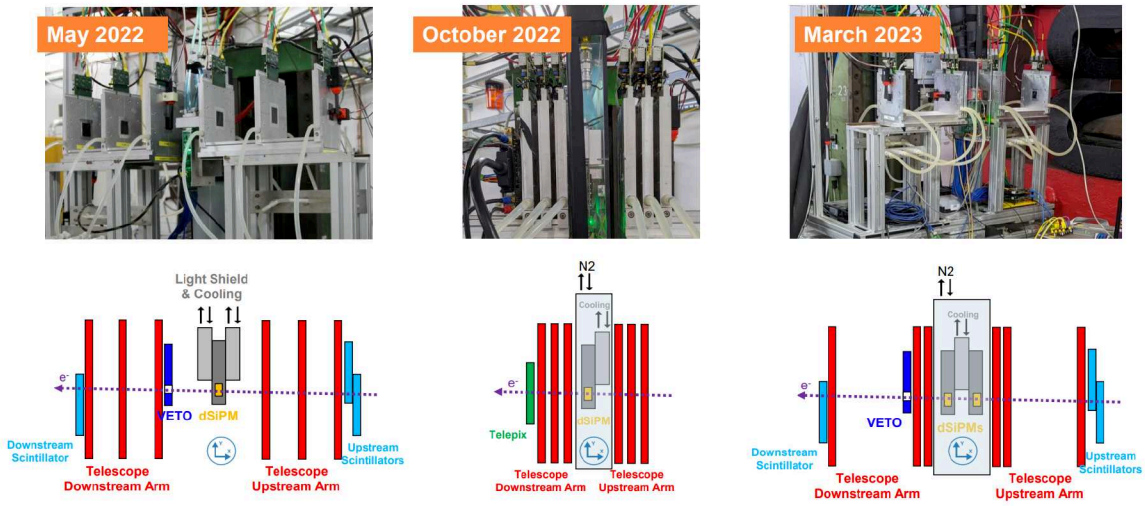

Figure 6.4: Setups used in the three test-beams at DESY II test-beam facility.

- March 2023: In this test-beam, the spatial and time performance of the dSiPM in MIP detection were investigated, and the mechanics of the setup and the DAQ system were adapted to allow the simultaneous study of two DUTs. Scintillators and veto trigger system was here used. The aim was to use the timestamps of coincident events to determine the temporal performance of the DUTs. Again, bias and temperature scans were performed.

To avoid unnecessary repetition, most of the results reported in the remaining sections of this chapter refer to the March 2023 test-beam (unless otherwise indicated). Comparable dSIPMs performances are measured in MIP detection in the early test-beam campaigns.

6.4 Alignment of the DUT and Trigger System

DUT, reference telescope, and beam spot must be aligned to get and reconstruct tracks through the DUT. The beam spot is first aligned to the telescope by moving the entire setup and monitoring the hitmaps of the telescope planes. Subsequently, a first coarse alignment of the DUT is carried out using position markers on the dSiPM cooling box and the telescope structure, which guarantees an alignment accuracy of a few millimeters.

The trigger systems used, described in Section 6.2.1, guarantee trigger acceptance in very small areas. Small trigger areas allows to minimize data storage and dead time, however, a perfect alignment between DUT and the selected trigger area (Figure 6.3) is now crucial. Due to the high Dark Count Rate (DCR) of the dSiPM and the efficiency limited by the fill-factor to ~30 %, the Material Budget Imaging (MBI) technique [110] is used to identify the position of the DUT precisely. The material budget at the DUT can be determined by measuring the electron scattering angles using the Corryvreckan framework, reference telescope data, and a low-momentum electron beam to maximize Coulomb scattering. Here, straight-line reconstruction is used separately for particle tracking in the upstream and downstream arms of the telescope. A matching cut in the two tracks intercept of 200 µm is used

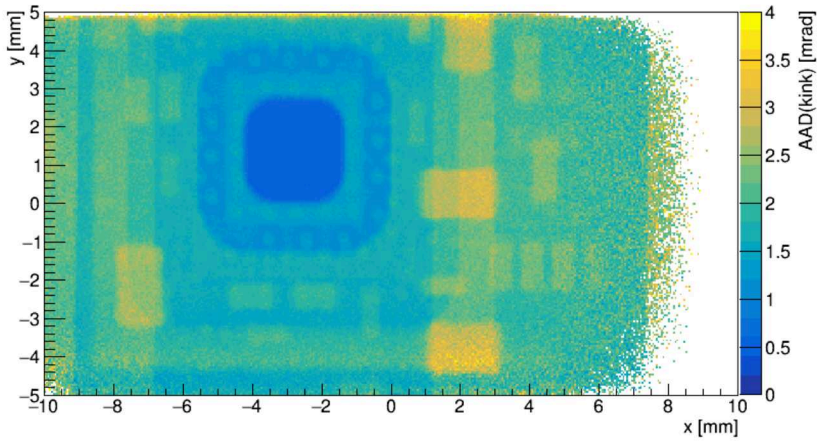

(a)

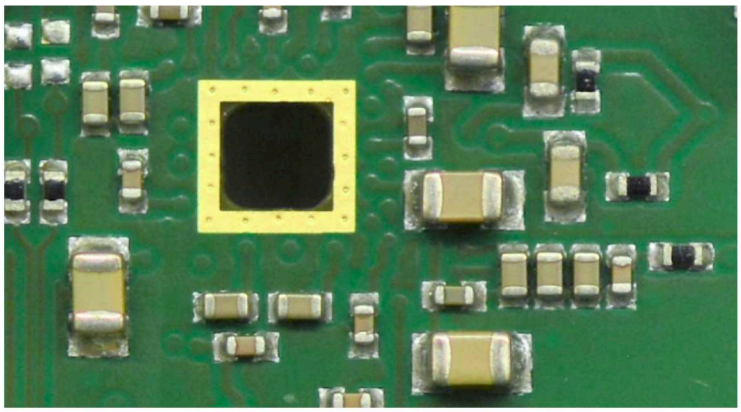

(b)

Figure 6.5: Material Budget Image obtained using a 2 GeV electron beam and Corryvreckan reconstruction Framework (a). Microscope image of the PCB (from the backside) where the dSiPM is glued and bonded (b).

on the DUT plane. The Average Absolute Deviation (AAD) of the scattering angle is then calculated as a function of the position as shown in Figure 6.5(a), and is used to determine the exact position of the DUT. Figure 6.5(b) shows a microscope picture of the Printed Circuit Board (PCB) on which the dSiPM is bonded and glued (the backside of the PCB is shown). It can be seen that the material budget is limited to silicon only at the DUT; this, consequently, corresponds to the lowest AAD.

Knowing the exact position of the dSiPM (DUT), this is then moved using a dual-axis stage with micrometric precision and aligned to the area selected by the trigger. The relative position of the DUT after alignment is marked in Figure 6.3 in red.

6.5 Analysis Procedure

Test-beam data analysis is performed using the Corryvreckan framework (described Section 3.5). Details on the analysis are provided in this section. The investigated observables are also described.

6.5.1 Data Structure and Decoding

Raw data from the reference telescope, TLUs, and dSiPMs are saved by EUDAQ2 software, as described in Section 6.2. The data are decoded (see Section 3.5.1) and an event-structure is defined as an initial step in the reconstruction. Events are defined by TLU trigger IDs (i.e. triggers issued by the TLU during acquisition). Telescope-data contain the hitmaps of the six MIMOSA26 planes, TLU-data the trigger IDs and corresponding timestamps and Caribou-data the hitmaps and timestamps of the dSiPMs (DUTs).

Three DUTs frames are saved for each trigger. The firmware running on Caribou continuously buffers the frames from the dSiPMs; when a trigger signal is issued by the TLU, it arrives on Caribou with a certain delay and is asynchronous to the frame clock. The corresponding hit could, therefore, have been recorded recorded in the current or previous frame. Both frames are then saved and combined for subsequent analysis. The third, subsequent, frame is also saved to allow DCR studies under test-beam conditions.

6.5.2 Clustering, Software Alignment and Association

For each event, clusters of hits are reconstructed in telescope and DUTs planes as described in Section 3.5.2. In the DUT, only clusters within a Region Of Interest (ROI) are reconstructed. This is chosen by selecting the region of the DUT within the trigger acceptance area described in Section 6.2.1.

Tracks are reconstructed using telescope data and the General Broken Lines (GBL) track model [64] as described in Section 3.3. Only tracks with an associated cluster in all telescope planes are analyzed. After Telescope alignment (see Section 3.5.3) only tracks with $\chi^2 < 5$ are accepted.

The DUTs are aligned as described in Section 3.5.4. Time-dependent alignment has also been necessary in some analyses to compensate for movements due to the thermal expansion of the mechanical components.

After the telescope and DUT alignment, DUTs clusters are associated with the reconstructed tracks when these are within 70 µm at the DUT level. The timestamps of the dSiPM hits are also required to be within 230 µs than the TLU timestamps (event timestamps) in order to account for the integration time of telescope sensors described in Section 3.2.

6.5.3 Observables

Cluster Size

One of the observables in the investigation of pixel detector spatial resolution is the cluster size, which is defined as the number of pixels contributing to the clusters associated with a track. For certain sensor types and conditions it exceeds unity, mainly due to charge sharing in MIP detection. This can be related to the angle of incidence of the particle or the diffusion of the generated charge carriers. Charge sharing, in combination with a charge measurement itself, allows for interpolation between pixel centers within a cluster and can contribute to improved spatial resolution. For the digital DESY dSiPM, the cluster size is expected to be mostly unitary due to the geometry of the pixels and the

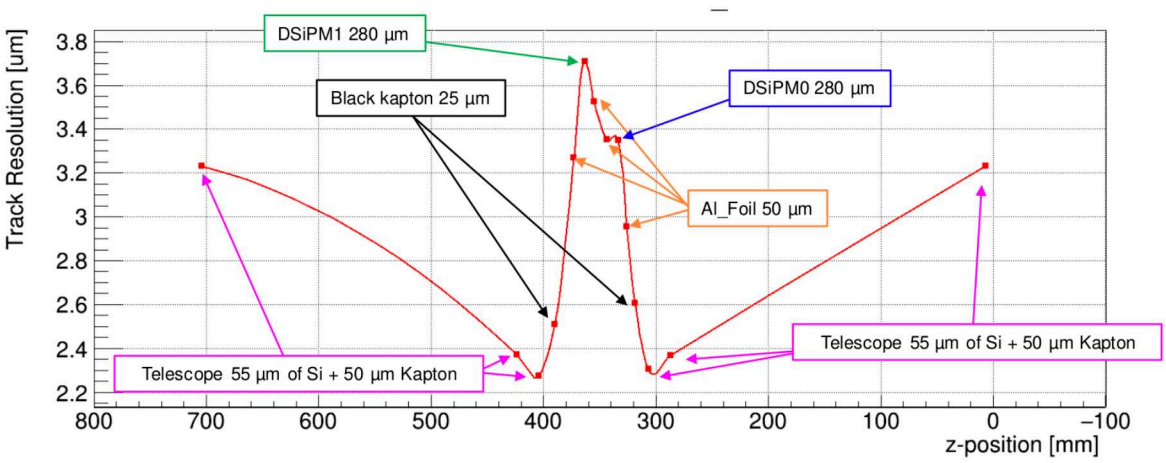

Figure 6.6: Track resolution estimated using GBL formalism for March 23 dSiPM test-beam. All materials in the particle trajectory are marked at the corresponding z position (beam along the z-axis, orthogonal to the dSiPM sensor plane).

angle of incidence of the particles. Larger cluster sizes are expected to be governed by the optical crosstalk described in Section 4.1.7.

Spatial Residuals

The spatial resolution of dSiPM is estimated from the spatial residuals $\Delta\vec{x}$:

$$\Delta\vec{x} = \vec{x}_{track} - \vec{x}_{cluster}, \tag{6.1}$$

where $\vec{x}_{cluster}$ is the position of the associated cluster on the DUT and $\vec{x}_{track}$ is the position of the reconstructed track on the DUT plane. The width of the $\Delta\vec{x}$ distribution depends on the tracking uncertainty and the properties of the dSiPM as described in Section 2.5.1.

Tracking uncertainty depends on the setup configuration, electron momentum, material budget, and telescope sensors' spatial resolution. This is estimated in the specific setup using the GBL formalism described in Section 3.3 and the software in [64]. Figure 6.6 shows the track resolutions calculated for the March 2023 setup in Figure 6.4.

The shape of the Δx distribution, in the x or y coordinate, consists of the signal $S(\Delta x)$ and background $B(\Delta x)$ contribution of the four SPADs in the pixel (see Figure 4.9).

The position and size of the SPADs within the pixel are parameterized and used to define $S(\Delta x)$:

$$S(\Delta x) = N_S \cdot \frac{f_1 - f_2 + f_3 - f_4}{2}, \tag{6.2}$$

where

$$f_{1,2}(x) = \mathrm{erf}\left(\frac{x - C \pm \frac{W}{2}}{\sqrt{2}\sigma}\right) \text{ , and } f_{3,4}(x) = \mathrm{erf}\left(\frac{x + C \pm \frac{W}{2}}{\sqrt{2}\sigma}\right).$$

The parameters C and W represent the position of the SPAD center with respect to the pixel center and the nominal active width of the SPAD; those are fixed to be at 17.4 µm and 19.93 µm, respectively. The free parameters N_S and σ, are a normalization factor and the width of a Gaussian, which includes the tracking uncertainty and the efficiency profile at the boundaries of the SPADs.

The DCR contribution $B(\Delta x)$, on the other hand, identifies tracks erroneously associated with dSiPM DCR events. This contribution is minimized via online and offline masking of noisy pixels but cannot be eliminated due to the intrinsic properties of SPADs. The contribution is modeled by integrating the acceptance of the cluster-association cut:

$$B(\Delta x) = N_B \cdot 2 \cdot \left(\sqrt{\left| D^2 - x^2 \right|} \right), \tag{6.3}$$

where D is the radial cut used (70 µm) and N_B a normalization factor.

By fitting the combination of signal and DCR on residual distribution Δx it is possible to define the spatial resolution of dSiPM as illustrated in Section 6.6.2. Difficulties were encountered in data analysis, particularly in offline alignment, because of the complex shape of the spatial residuals. The Corryvreckan framework (described in Section 3.5) has been extended to support arbitrary residual shapes for alignment in the context of this thesis.

Time Residuals

Similarly to spatial residuals, time residuals can be used to define the time resolution of the dSiPM in MIP detection. Time residuals Δt can be defined as:

$$\Delta t = t_{ref} - t_{cluster}, \tag{6.4}$$

where t_{ref} is the time stamp defined by a reference detector and $t_{cluster}$ the timestamp of the dSiPM associated cluster. The timestamp provided by the TLU can be used as t_{ref}. However, the time resolution of the trigger system (consisting of scintillators, photomultipliers, NIM logic, and TLU electronics) is expected to dominate the time residual not allowing an accurate definition of the time resolution of the DUT.

This is the main reason driving the choice of using two aligned dSiPMs in the most recent test-beam campaigns. By doing so, events where tracks are detected by both dSiPMs are selected and it is possible to use the time stamp of one of them as t_{ref}. The resulting distribution Δt will only contain time contributions from the dSiPMs and can be used to estimate the time resolution of the sensor in MIP detection as shown in Section 6.6.3. A detailed study of these time residuals is given in [107],

Detection Efficiency

Using the dSiPM as MIP detector, due to the high number of primary e-h pairs created, a higher MIP detection efficiency is expected compared to the Photon Detection Efficiency (PDE)[1]. To confirm this hypothesis, efficiency measurements can be performed on test-beam data. Efficiency ϵ_{rec} is defined

[1] Of the order of 15 % at the peak wavelength

as:

$$\epsilon_{rec} = \frac{N_{hits}}{N_{tracks}}, \tag{6.5}$$

where N_{tracks} is the number of selected tracks, and N_{hits} is the subset of tracks with an associated cluster on the DUT. For this study, tracks interpolated near noisy or masked pixels are excluded from the analysis to avoid biasing the efficiency measurement.

The measured efficiency ϵ_{rec} is corrected by considering the non-negligible probability of associating DCR with the reconstructed track in the two frames f_{F1} and f_{F2}, evaluated using the same data. The density of DCR events is measured in regions of the DUT far from reconstructed tracks. Multiplying this value by the area used in track association yielded f_{F1} and f_{F2}. The effective efficiency ϵ is then calculated using the equation:

$$\epsilon = c_{dt} \cdot \frac{\epsilon_{rec} - (f_{F1} + f_{F2} - f_{F1} f_{F2})}{1 - (f_{F1} + f_{F2} - f_{F1} f_{F2})}, \tag{6.6}$$

here the factor $c_{dt} = 1.0342$ is added to compensate for the selected frames dead-time. Each frame is 136 cycles of the 408 MHz clock long (i.e. 333 ns). However, due to the readout scheme described in [94] MIP or DCR events within a frame dead-time window of 11 ns cannot be detected. Due to the triggering scheme used, the trigger can also arrive during this dead time. The efficiency is therefore corrected using the factor c_{dt} corresponding to the ratio of total frame length and the efficient fraction (333/322).

Noise event contamination is also evaluated using the third frame following the two containing the signal events. In this case, the probability of associating fake hits f_{F3} is directly evaluated under the same experimental conditions with an 'efficiency' measurement in this frame containing only DCR hits. Considering the trigger rate, the probability of MIP events on the DUT in this frame is found to be negligible. The same equation 6.6 is used, replacing f_{F1} and f_{F2} with the value f_{F3}, assuming uniform DCR contamination in the three frames. The two methods used are found to be compatible within the uncertainties.

Results of efficiency measurements performed in test-beams are given in Section 6.6.4

6.6 Bare dSiPM in MIP Detection

6.6.1 Cluster Size

Cluster size is measured on the clusters associated with reconstructed tracks. As mentioned in Section 6.5.3, the cluster size is found to be mainly unitary. This is due to the layout of the pixel and SPADs, with wide separation structure and thickness of the active area of a few µm, which makes charge sharing unlikely. Only a few clusters show a size greater than one, mainly due to crosstalk. Figure 6.7 shows an example of cluster size distribution. The figure compares the cluster size of signal events associated with tracks in red with the cluster size of DCR events acquired under the same experimental conditions in blue. It can be seen that the two distributions are compatible within the uncertainties and that only a small percentage of events have a cluster size larger than one. This shows

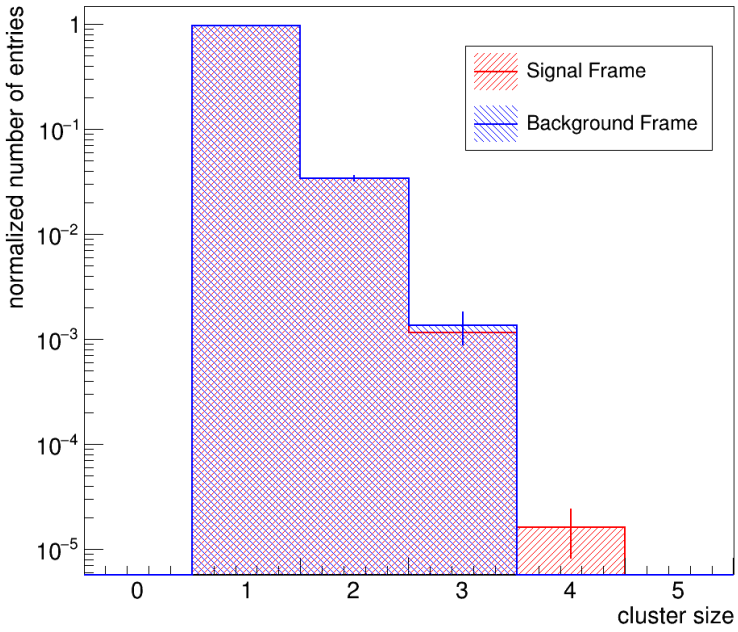

Figure 6.7: Cluster size distribution for signal (in red) and background (in blue) frames. In the example shown the sensor is operated at $V_{OV} = 2\,\mathrm{V}$ and $T_{Chip} = -2\,^{\circ}\mathrm{C}$.

that clusters tagging of MIP and DCR events is the same when bare dSiPM are used for detection. The signal cannot, therefore, be distinguished from DCR without prior tracking information.

The cluster size of associated events is studied as a function of overvoltage for all sensors and for the different temperatures investigated in the March 2023 test-beam. Figure 6.8 shows the fraction of clusters with a size greater than one as a function of overvoltage. As expected, an increase as a function of overvoltage is observed. The probability of crosstalk, as well as the coincidental combination of hits and DCR here included, indeed increases with overvoltage. A slight increase is also visible when the sensors are operated at higher temperatures as the DCR contamination increases.

6.6.2 Spatial Resolution

The spatial resolution of DESY dSiPM in MIP detection can be estimated by investigating the spatial residuals described by Equation 6.1, as described in Section 6.5.3. An example of spatial residual distribution is shown in Figure 6.9. In this example, the correction described in Section 3.5.4 has been applied to compensate for time-dependent residual fluctuations. The distribution shows a characteristic shape with few entries around zero due to the non-sensitive region between the SPADs visible in Figure 4.9. The sum of the signal $S(\Delta x)$ and background $B(\Delta x)$ described by Equations 6.2 and 6.3 is fitted to the data (red line). The standard deviation of the fitted signal contribution (green line) is measured to be 19.2 µm in the example shown. The main source of uncertainty in the described procedure is a signal component not modeled in the fitted function due to events with cluster sizes larger than one. To include this effect, the Root Mean Square (RMS) of the entire residual distribution can be used to define an upper limit in the definition of the spatial resolution. By subtracting the spatial

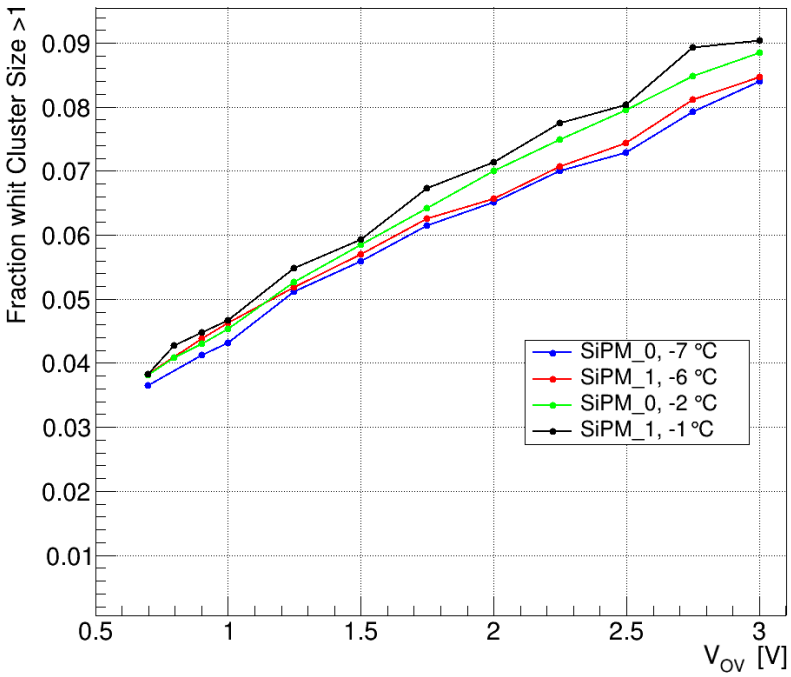

Figure 6.8: Fraction of events with cluster size greater than one for two different dSiPM as a function of overvoltage, for different T_{Chip}.

resolution of the telescope (estimated to be 3.5 µm in the example shown) from the two values indicated, an estimate of the spatial resolution of the dSiPM can be obtained as described in section 2.5.1. This is found to be in the range of 18.9 µm to 20.6 µm. The values are in agreement with what is expected for a binary sensor with a cluster size of one: $pixel_{pitch}/\sqrt{12}$ i.e. 69.6 µm/$\sqrt{12}$ = 20.1 µm. Variations smaller than 15 % are measured between the smallest and the highest overvoltage value. These variations can be attributed to the increased DCR effects that cause a deterioration of the spatial residuals.

6.6.3 Time Resolution

As described in Section 6.5.3, the time resolution of the dSiPM can be extracted from the time residuals described by Equation 6.4. In [107] an in-depth study of the time resolution of the DESY dSiPM is presented and a model is defined to describe the time residuals. Figure 6.10 shows an example of Δt: the time residuals between two dSiPMs. The time residuals are characterized by three components: a Gaussian peak, an exponential tail, and a flat background.

The Gaussian peak (or fast component) contains the 85 % of the entries and characterizes the hits reconstructed in the central region of the SPADs. In this region, the time resolution of the individual dSiPM is measured, using the method described in Section 2.5.2, to be: 50 ps in the example shown.

On the other hand, the exponential component characterizes hits involving the peripheral regions of the SPAD in either of the two dSiPMs. This component (also called slow component) is due to MIP

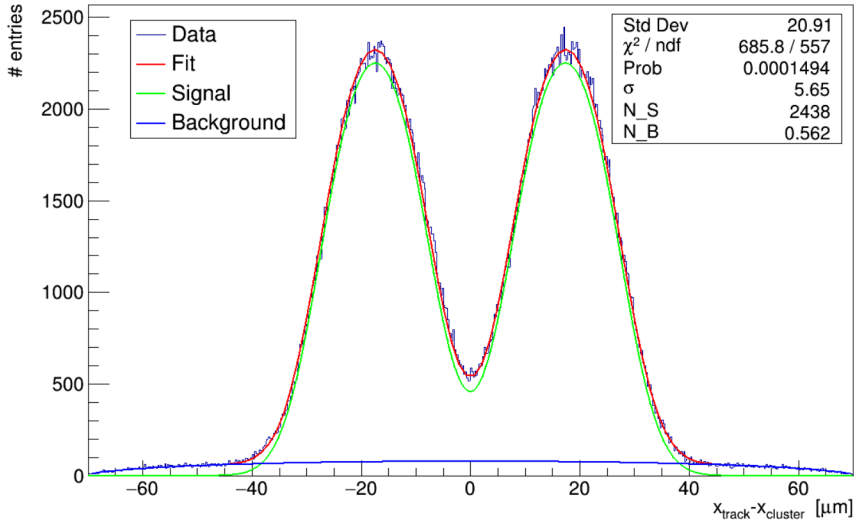

Figure 6.9: Spatial residuals Δx, measured at an overvoltage of 2 V and a T_{Chip} of -2 °C. The sum of $S(\Delta x)$ and $B(\Delta x)$ component is fitted (red line). The signal (in green) and background (in blue) components are also shown.

interactions in lower electric field regions of the SPADs, resulting in a slower time response of the sensor in the nanosecond regime.

The last component, flat background, is instead due to the presence of DCR. As described in Section 4.2.2. The first event in a frame defines the time stamp of the dSiPM quadrant. This means that if a DCR event occurs before a signal event in the same quadrant where the MIP interaction takes place, the timestamp of the event will be defined by the DCR event, resulting in a randomly distributed entry in the time residual, visible in the example as a constant flat component.

In [107, 108] the slow time response of the dSiPM is correlated with the position of the particle interaction within the SPADs. Figure 6.11 shows the results of this study. The image shows the position of the reconstructed tracks for events in the tails of the time residuals. It can be seen that these are mostly due to interactions in the edge regions of the SPAD, confirming the hypothesis that the time resolution of the SPADs in MIP detection deteriorates in the peripheral regions. Time resolution is studied for different temperatures and overvoltage. No particular variations are observed, and the average temporal resolution (fast component) is measured to be 46 ± 5 ps.

6.6.4 Efficiency

The efficiency described by Equation 6.5 is measured as a function of the in-pixel position. The in-pixel position corresponds to the intercept of the track reconstructed on the DUT. All pixels in the selected ROI within the trigger acceptance are overlaid to obtain sufficient statistics (excluding masked pixels and their neighbors). Figure 6.12 shows an example of an in-pixel efficiency map. By comparing the figure with Figure 4.9, where the pixel structure is shown, it is evident that the efficiency is maximal when the track intercepts the center of the SPAD and minimal in the inefficient

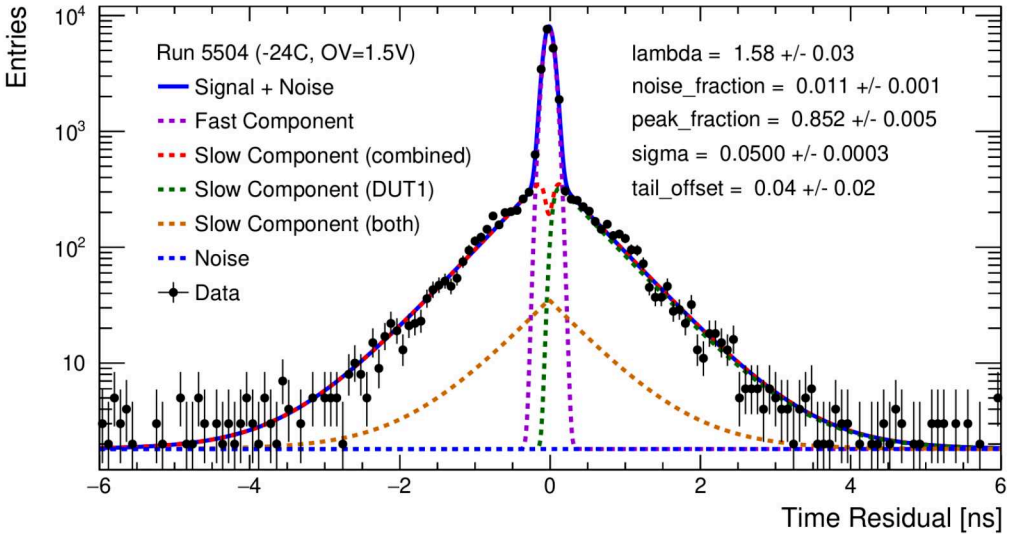

Figure 6.10: Distribution of the time residual Δt between two dSiPMs. Measured at an overvoltage of 1.5 V and T_{Chip} of $-7\,°C$ and $-6\,°C$. All the time resolution components are shown, as well as the key parameter of the fit. From [107].

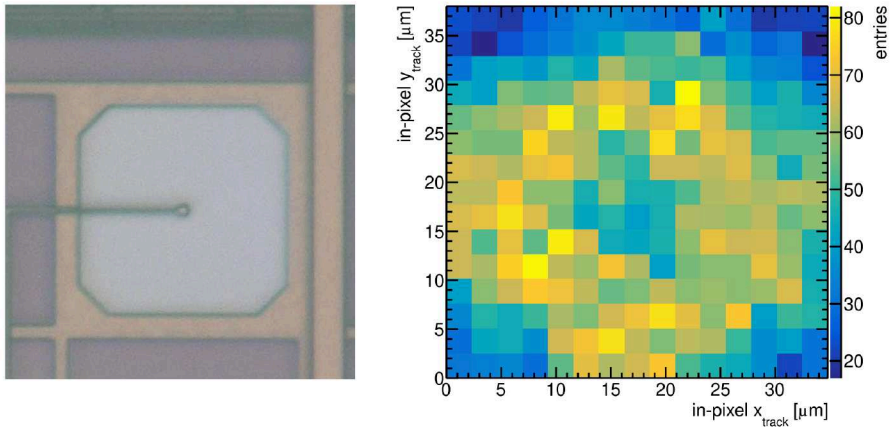

Figure 6.11: Microscope picture of a SPAD (left). In-SPAD hitmap of MIP events with cut on time residual tails (right). Adapted From [108].

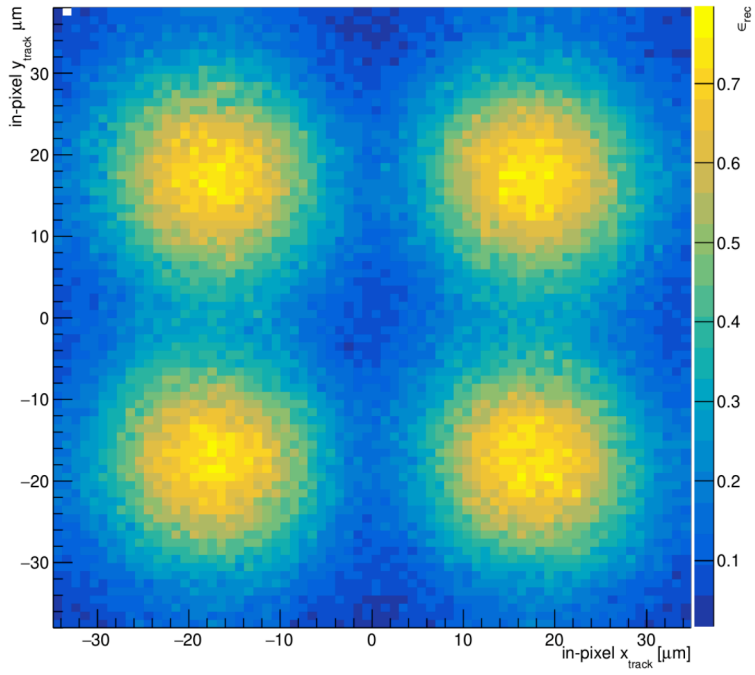

Figure 6.12: In-pixel hit detection efficiency measured at an overvoltage of 2 V and a T_{Chip} of −2 °C.

regions between SPADs. Note that the resolution of the in-pixel hitmap is also determined by the tracking uncertainty.

The integrated and corrected efficiency described by the Equation 6.6 is measured on two dSiPMs as a function of overvoltage for different temperatures. The results of this measurement are shown in Figure 6.13. Only statistical uncertainties are reported. all measurements are in agreement within 0.5 %. A slight increase in efficiency as a function of the overvoltage is observed, reaching a value of ∼31 % at 3 V overvoltage. The measured efficiency values are compatible with the nominal sensor fill-factor of 30 %. This confirms that the SPAD efficiency in MIP detection is significantly higher than the photon detection efficiency as anticipated in Section 6.5.3.

Although these results are in line with expectations, an efficiency value limited to ∼30 % is generally too low for the sensor to be used in the 4D-Tracking contexts. Possible approaches to increase the efficiency of the sensor while preserving spatial and time resolution are presented in the next chapter.

6.7 Summary of Results

The MIP detection performance of the DESY dSiPM is studied and described in this chapter. Characterizations are carried out at the DESY II test-beam facility with a 4 GeV electron beam.

The DESY dSiPM prototype is integrated into the test-beam setup and investigated as a direct particle detector using beam telescopes for track reconstruction.

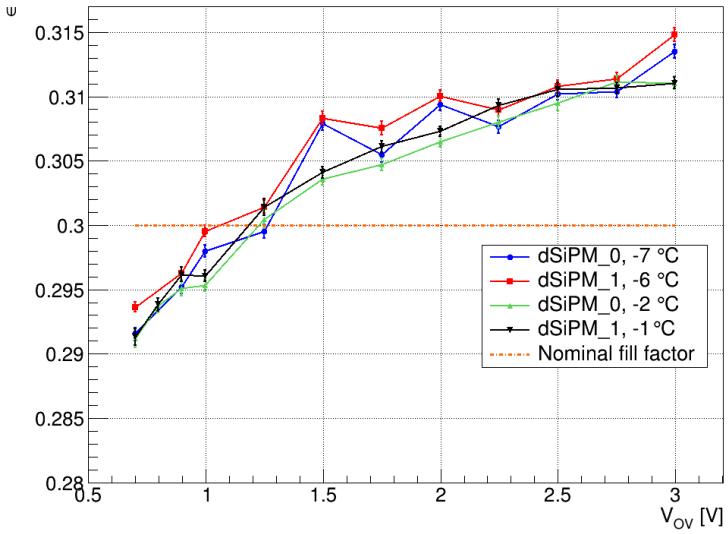

Figure 6.13: MIP detection efficiency of two dSiPM after DCR contamination correction for two different T_{Chip} settings. The expectation from the nominal fill-factor is included as a dashed horizontal line.

The Corryvreckan software is used for event reconstruction and data analysis. The framework was also extended in the context of this work to allow the study of sensors with atypical pixel structures such as that of DESY dSiPM.

Performance in MIP detection of bare DESY dSiPM samples are evaluated. The dimension of the cluster of MIP events is measured to be mainly unitary, the spatial resolution of the sensor of the order of 20 µm compatible with the binary resolution of the sensor, the temporal resolution of the order of 50 ps in most of the active area, and the efficiency of about 30 %. None of the measures show particular variations in the overvoltage and temperatures studied.

The main limitations in using monolithic dSiPMs as MIP detectors, as shown in this chapter, are the low efficiency limited by the fill-factor and the high DCR typical of the technology. The next chapter will describe some possible strategies to address these limitations.

CHAPTER 7

dSiPM coupled with Thin LYSO

To overcome some of the intrinsic limitations of Digital Silicon PhotoMultipliers (dSiPMs) in direct Minimum Ionising Particles (MIP) detection described in Chapter 6, this chapter introduces a detector concept that combines the dSiPM with a thin radiator. Section 7.1 discusses the advantages of this configuration while also exploring some potential applications. Section 7.2 provides an introduction to the detection mechanisms of MIP using radiators, describing the scintillation process and the Cerenkov effect. Section 7.3 presents the results of Geant4 simulations, performed as a preparatory study for coupling of dSiPM prototypes with thin Cerium-doped Lutetium Yttrium OxyorthoSilicate (LYSO(Ce)) radiators described in Section 7.4. The characterizations of dSiPM with thin Lutetium Yttrium OxyorthoSilicates (LYSOs), using a radioactive source, are then described. Finally, Section 7.5 reports test-beams results of dSiPM+LYSOs prototypes, showing their improvements and limitations compared with the results in MIP detection obtained with the bare prototype (i.e. without radiator coupling) described in Chapter 6. Parts of the presented results are published in [111].

7.1 Overcome SiPM Intrinsic Limits in MIP Detection

One of the main drawbacks in direct MIP detection using Silicon PhotoMultipliers (SiPMs) is the limited efficiency due to the fill-factor. The trench and avalanche containment regions between Single-Photon Avalanche Diodes (SPADs), as well as the additional space used by in-pixel electronics in monolithic SiPMs, are inefficient areas. DESY dSiPM also suffers from this inherent limitation as described in Section 6.6.4, where the efficiency in MIP detection is measured to be compatible with the sensor's fill-factor of $\sim$30 %. The use of advanced technologies such as BackSide Illumination (BSI) with charge focusing [84] may be a possible solution to this problem. Another method to improve efficiency is using thin radiators, as shown in this chapter.

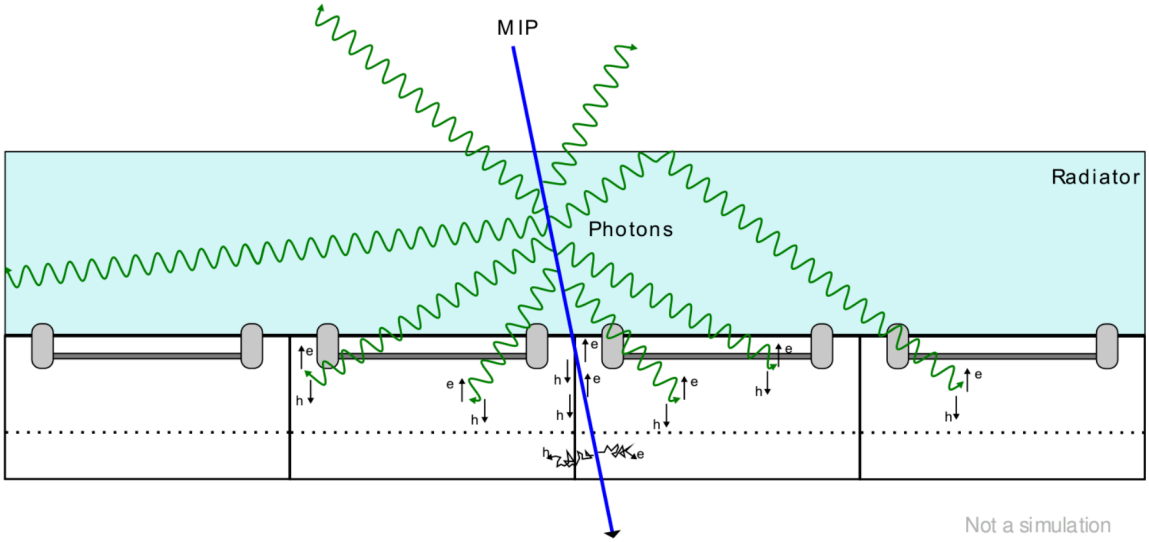

Figure 7.1: MIP detection using a SPAD array coupled to a radiator. The sketch is not to scale.

7.1.1 A new Detector Concept: Coupling with Thin Radiator

Radiators can be used to improve the efficiency of SiPMs in MIP detection. Particles crossing the radiator release energy, and Cerenkov or scintillation light can be produced (as described in Section 7.2). The emitted photons can reach the SiPM and eventually generate a SPAD discharge. Figure 7.1 schematically represents the process described: the MIP interacts in an inefficient area of a SPAD array but the photons produced by the radiator reach adjacent SPADs and interact in active areas of the sensor.

The use of radiators coupled to SiPM in MIP detection is a well-known detection technique [39]. Usually, in this context, centimeter-scale radiators are used to maximize the number of photons produced by improving efficiency and time resolution in MIP detection. If radiator coupling is to be used in 4D-tracking of MIP, the spatial performance of the sensor must also be preserved. Using dSiPMs with full hit-map readout, coupling with radiators can result in better spatial performance if the radiator is thin. The sketch in Figure 7.2 shows that, considering only geometrical aspects, the thinner the radiator, the smaller the region where most photons hit the sensor. It is then reasonable to deduce that the thinner the radiator, the better the spatial performance of the SiPM. On the other hand, radiators that are too thin would not produce enough photons to guarantee an accurate detection. The geometry and performance of the radiator, as well as properties of the SiPM in photon detection, are all aspects that determine the spatial and time resolution of the SiPM+thin-radiator detector concept.

7.1.2 Multipurpose Detector for Single Photons and MIPs

The possibility of improving efficiency in MIP detection using SiPMs coupled with thin radiators has already been demonstrated. In [112–114], it has been proven that protective resins used for the packaging of analog SiPMs have a positive influence on the efficiency of the sensors while used in

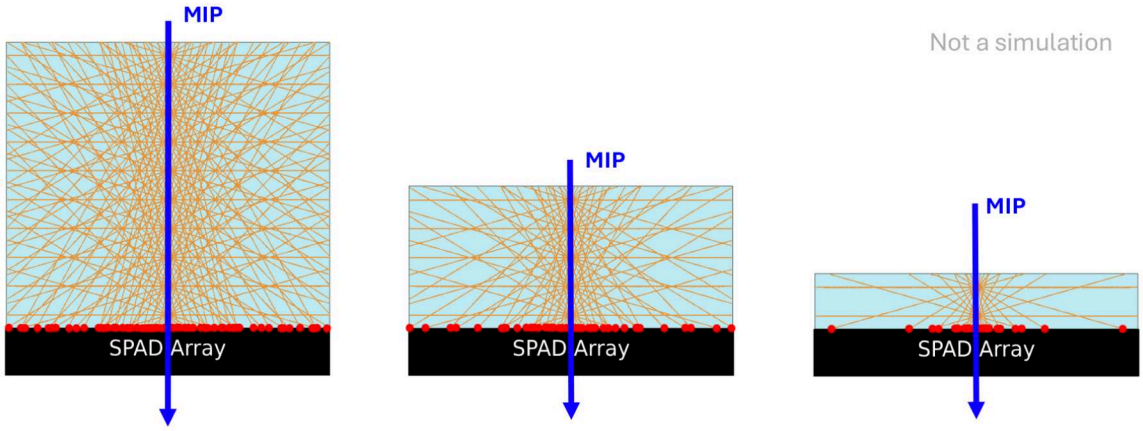

Figure 7.2: Impact of the thickness of the radiator (in light blue) on the size of the cluster of hits (red dots) on the SPAD array. A constant isotropic light emission is shown within the radiator crossed by the MIP. The sketch is not to scale.

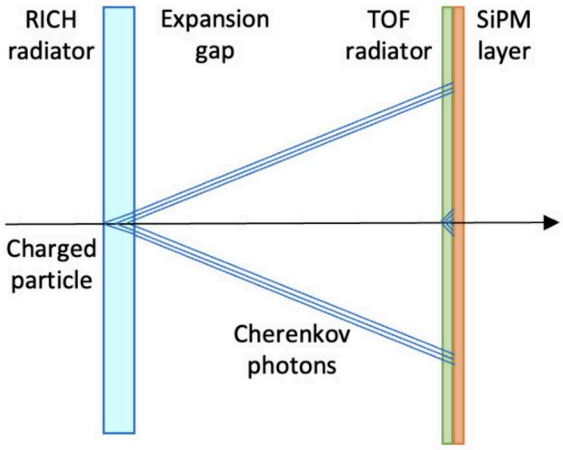

Figure 7.3: The image from [116] shows a schematic representation of a SiPM-based multipurpose detector system. A single SiPM detector layer is used for the simultaneous detection of photons produced by two different radiators in order to perform combined TOF and RICH measurements.

MIP detection. The studies are carried out in the context of the ALICE experiment upgrade ALICE 3 [115] described in Section 1.3. Among other proposals, the experiment suggests the use of analog or dSiPMs as a multi-purpose detector for a combined Ring Imaging CHerenkov (RICH) and Time Of Flight (TOF) measurement. The concept illustrated in [116] and shown in Figure 7.3, involves the use of a large area SiPM detector capable of detecting photons produced by a RICH-radiator (away from the sensors) and those produced by a TOF-radiator in close proximity of the SiPMs. The results shown in the next sections of this chapter are also valuable for evaluating possible applications of dSiPMs in this context.

7.2 Radiators for MIP detection

In the detection of MIP with radiators, two primary mechanisms are commonly exploited for light generation, namely the scintillation process and the Cherenkov effect.

7.2.1 The Scintillation Process

The scintillation process is a luminescence phenomenon (emission of light with a spectrum characteristic of the material) originating from the absorption of ionizing radiation [40]. Scintillating materials are traditionally classified according to their chemical composition into organic and inorganic. In organic materials, luminescence is produced through the transition of free valence electrons into molecular orbits.

Scintillation in Inorganic Crystals

Inorganic scintillators are usually crystals whose scintillation properties are due to transitions within the lattice band-gap. Luminescent centers are present in the crystal with an energy level distance smaller than the crystal band-gap and have a photon transition in the visible wavelength range. Luminescent centers can be intrinsic or added by doping. Figure 7.4 from [40] shows a simplified version of the scintillation process near a luminescent center. When an ionizing particle interacts with the scintillator, electron-hole (e-h) pairs are created. The electrons (holes) produced are called *hot* (*deep*) because they are far from their band energies. The hot electrons interact through inelastic scattering generating additional e-h pairs until the energy is below the ionization energy. The deep holes via Auger processes also create additional e-h pairs. A large number of electrons (holes) are thus created in the conduction (valence) bands on a time scale of 10^{-16} to 10^{-14} s. e-h thermalize by scattering with phonons, lattice vibrations, moving to lower energy values on a time scale of 10^{-12} s. At this point the electrons (holes) are located to the bottom (top) of the conduction (valence) band. Here electrons and holes are trapped (by defect, impurities, etc.). Depending on the specific trap mechanism, the excited states can persist for a relatively long time before recombination occurs (10^{-10} to 10^{-8} s). Finally e-h recombine; if the recombination is radiative, scintillation light is produced.

Scintillators Timing

The properties of the emitted light pulse shape determine the intrinsic time resolution of scintillators. A detailed discussion of this phenomenon is beyond the scope of this work and can be found in [117]. Several time constants govern the pulse shape of the emitted light and can be expressed as a sum of exponential terms. It is common to classify scintillators based on two time constants: τ_r and τ_d, which represent the rise time and decay time, respectively. These are key pulse shape characteristics and determine the scintillator's timing performance. Another important parameter that affects the time resolution of the scintillator is the light yield, i.e., the number of photons produced per MeV of deposited energy. Some scintillators have a prompt photon emission with a few ten picoseconds timing jitter and are suitable for high-speed applications where precise timing is critical. In contrast, others have a much slower timing but are, for example, better suited for applications prioritizing high light yield and energy resolution over timing precision.

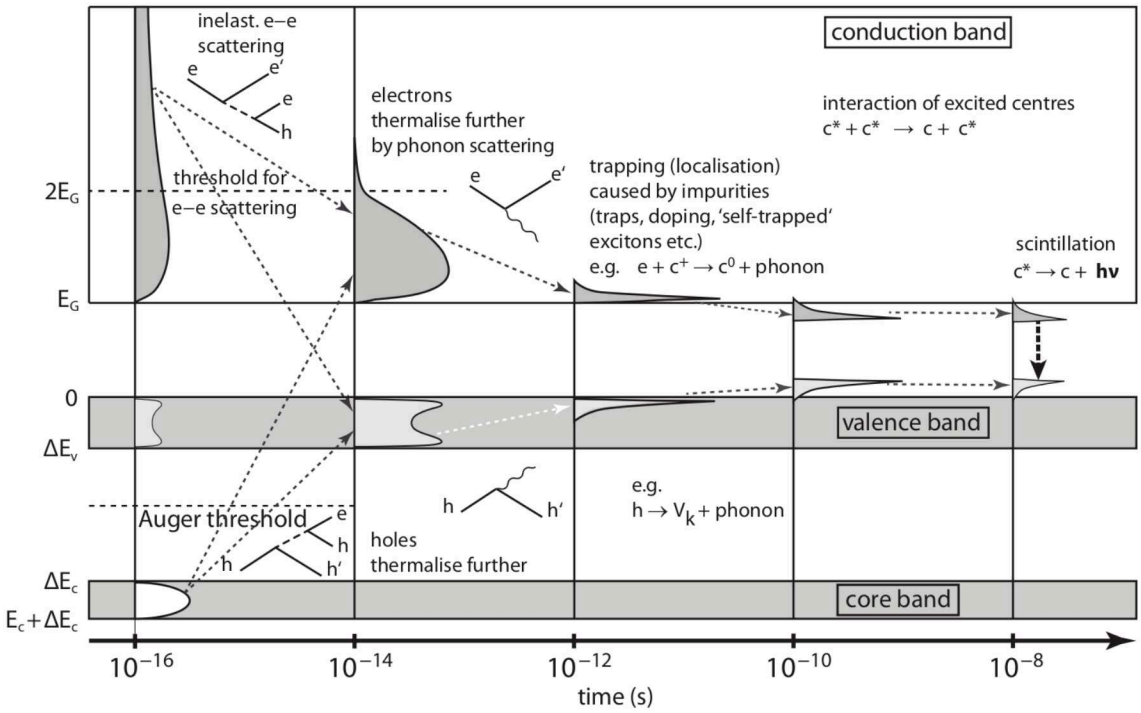

Figure 7.4: Scintillation process evolution in inorganic crystals. From [40].

Table 7.1: Properties of scintillation crystals. Adapted from [40].

Material	ρ (g/cm^3)	X_0 (cm)	λ_{max} (nm)	**Photons** (per MeV)	τ_{dec} (ns)
NaI(Tl)	3.67	2.59	410	43 000	245
CsI(Tl)	4.51	1.86	550	52 000	1220
CeF_3	6.16	1.77	340	4 500	25
GSO	6.71	1.38	430	8 000	56
BGO	7.13	1.12	480	8 200	300
LYSO(Ce)	7.10	1.14	402	32 000	41
LSO(Ce)	7.40	1.14	420	27 000	41
$PbWO_4$	8.30	0.89	425	130	30

Example of Inorganic Crystal Scintillators

Table 7.1 compares properties of scintillation crystals commonly used in particle detection and medical imaging. The tables report the radiation length (X_0), peak emission wavelength (λ_{max}), photon yield, and decay time constant (τ_{dec}). Shorter X_0 indicates materials better suited for compact detectors, while faster decay times are ideal for high-speed applications. Materials with high photon yields give a better energy resolution, while others like LYSO(Ce) balance fast response with yield. Each material has a unique combination of properties that determine its optimal use case.

7.2.2 The Cerenkov Effect

Cherenkov radiation is a prompt light production process [118]. It occurs when a particle passes through a dielectric with a velocity higher than the speed of light in the medium. This generates a perturbation in the electromagnetic field of the material that propagates in the form of Cherenkov light. Photons are produced if the particle velocity v exceeds the velocity v_{thr} which is the speed of light in the medium expressed as:

$$v_{thr} = \frac{c}{n}, \tag{7.1}$$

with c the speed of light and n the refractive index of the medium.

The number of photons emitted by Cherenkov radiation in a radiator can be estimated using the formula from [48]:

$$\frac{d^2N}{dxd\lambda} = \frac{2\pi\alpha z^2}{\lambda^2}\left(1 - \frac{1}{\beta^2 n^2(\lambda)}\right), \tag{7.2}$$

where $\frac{d^2N}{dxd\lambda}$ represents the number of photons emitted per unit length dx and per unit wavelength interval $d\lambda$, α is the fine-structure constant ($\approx 1/137$), z is the charge of the particle in units of elementary charge, λ is the wavelength of the emitted photon, β is the velocity of the charged particle relative to the speed of light ($\beta = v/c$), and $n(\lambda)$ is the refractive index of the medium at wavelength λ.

The total number of photons N_{ph} emitted by a charged particle traversing a Cherenkov radiator is given by integrating the above formula over the range $[\lambda_{min}, \lambda_{max}]$ of wavelengths and the path length L:

$$N_{\text{ph}} = \int_{\lambda_{min}}^{\lambda_{max}} \frac{d^2N}{dxd\lambda}\, d\lambda\, L, \tag{7.3}$$

Cherenkov photons, in contrast to scintillation, are not emitted isotropically but along a cone around the particle's axis of motion, with an aperture θ_c defined by:

$$\cos\theta_c = \frac{c}{nv}. \tag{7.4}$$

The light yield of Cherenkov radiators is usually much lower than that of scintillators; however, the almost-prompt emission makes Cherenkov radiators particularly suitable for fast-timing applications.

7.3 Geant4 Simulation

To verify the feasibility and to estimate the performance of the DESY dSiPM coupled with thin radiators, a simulation of the detector response is performed using the Geometry and Tracking Geant4 toolkit [119, 120]. The software package is designed to simulate the passage of particles through matter, encompassing all aspects of the simulation process: geometry, materials, particle tracking, and physics interactions. It provides tools for event generation, detector responses, data storage, and visualization.

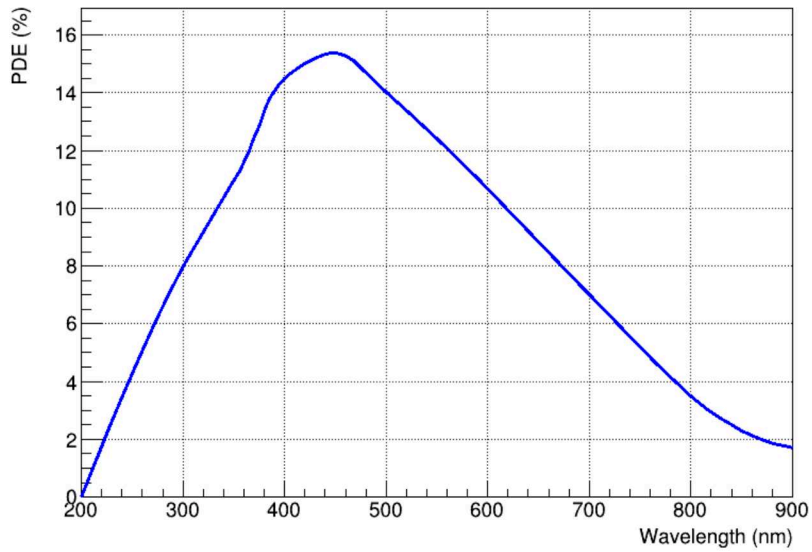

Figure 7.5: PDE simulated for DESY dSiPM. It should be noted that the reported values are not the result of a measurement but are based on scarce information available from the manufacturer. Effective dSiPM PDE may be significantly different.

7.3.1 Simulation Model

The goal of the simulation is to provide approximate estimates of the number of photons produced by the radiator and detected by the dSiPM as well as their spatial distribution. The work is carried out as a proof-of-concept and is to be considered preparatory to the coupling with thin radiators. A series of simplifications are made and only the spatial and efficiency performance are investigated.

The DESY dSiPM is modeled as an array of 32×32 blocks with the same effective pixel size. A radiator is then coupled to the sensor; this has configurable thickness and material and covers the entire sensor area. A third material, again of configurable thickness, can be interposed between the sensor and the radiator to simulate adhesives in the case of solid radiators coupling (LYSO crystals for example).

4 GeV electrons are generated perpendicular to the sensor coupled with the radiator (to emulate the typical DESY II test-beam situation). The interaction position can be constant or randomly distributed on the sensor surface. The electron deposits energy in the radiator, scintillation/Cherenkov photons are then produced and propagated according to the physics and radiator properties simulated. The response of the sensor is not simulated but is based on probabilistic considerations: photons reaching the sensor surface are classified as either detected or not by their wavelength λ and the Photon Detection Efficiency (PDE) spectrum in Figure 7.5. For example, considering the figure, only 15.4 % of photons with $\lambda = 450\,\text{nm}$ reaching the sensor are classified as detected. Incidence position of the electron, energy deposited in the radiator, number and position of photons reaching the sensor, and photons classified as detected are exported for each simulated event for subsequent analysis.

Table 7.2: Main properties of simulated materials. More details in [121]

LYSO Crystal	
Composition	Lu:2, Y:1, Si:1, O:5
Density	7.1 g/cm^3
Refractive Index	1.82
Scintillation Yield	33200 photons/MeV
Absorption Length (Photon Energy)	438 mm (1.0 eV) - 1.0 mm (4.08 eV)
Epoxy-Glue (for LYSO coupling)	
Composition	C:12, H:14, O:2, N:4
Density	1.15 g/cm^3
Refractive Index	1.5338
Epoxy Resin (radiator)	
Composition	C:27, H:32, O:4, N:2
Density	1.2 g/cm^3
Refractive Index	1.6

Several materials have been investigated as possible radiators to be coupled to the DESY dSiPM. The simulation results of two examples are illustrated and compared in the next section: an epoxy resin (Cherenkov radiator) and a LYSO crystal (scintillator) coupled using an epoxy glue. Generic materials properties are used for the simulation and are listed in Table 7.2. All the details on the materials as well as the Geant4 code used for the simulation can be found in [121].

7.3.2 Simulation Results

Geant4 Visualization

Figure 7.6 shows an event display from Geant4. On the left (right) the dSiPM, in brown, coupled with epoxy-resin (LYSO) radiator in Table 7.2 is simulated. In the example shown, the thickness of the radiator is 1 mm. In the case of the LYSO, a layer of 20 µm of epoxy glue (see Table 7.2) is interposed between the LYSO and the dSiPM. In both events, the incident particle (4 GeV electron) hits the sensor in the center. It's evident that the LYSO produces a considerable number of photons (in green) compared to the epoxy-resin. Furthermore, while the photon emission in LYSO is isotropic, in the epoxy resin the Cherenkov photons are emitted at the typical angle described by equation 7.4.

Produced and Detected Photons

The photons produced by the radiators cover a large range of wavelengths and have different emission spectra. In particular, the Cherenkov photons produced by the epoxy radiator are distributed according to the Equation 7.2 with higher emission for short wavelengths. The LYSO, on the other hand, has an emission spectrum that peaks in blue light and a number of photons emitted orders of magnitude

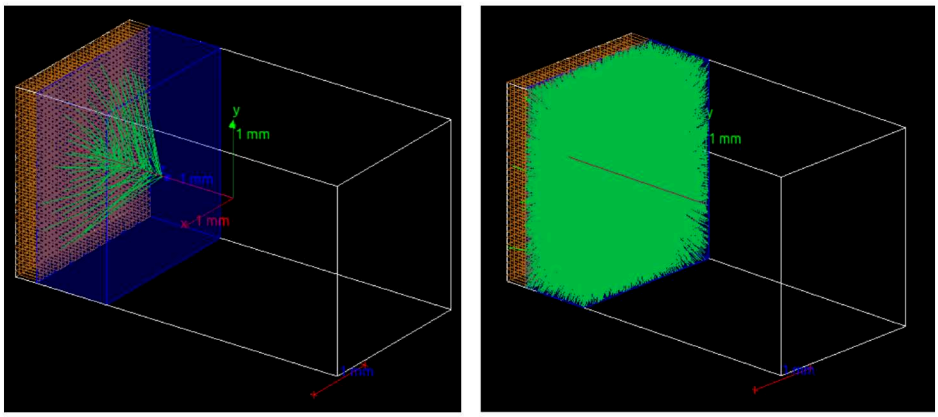

Figure 7.6: Single event display in Geant4. On the left, dSiPM (in brown) is coupled to epoxy-resin radiator (in blue). On the right, dSiPM (in brown) is coupled to LYSO radiator(in blue). Generated photons are indicated by green lines.

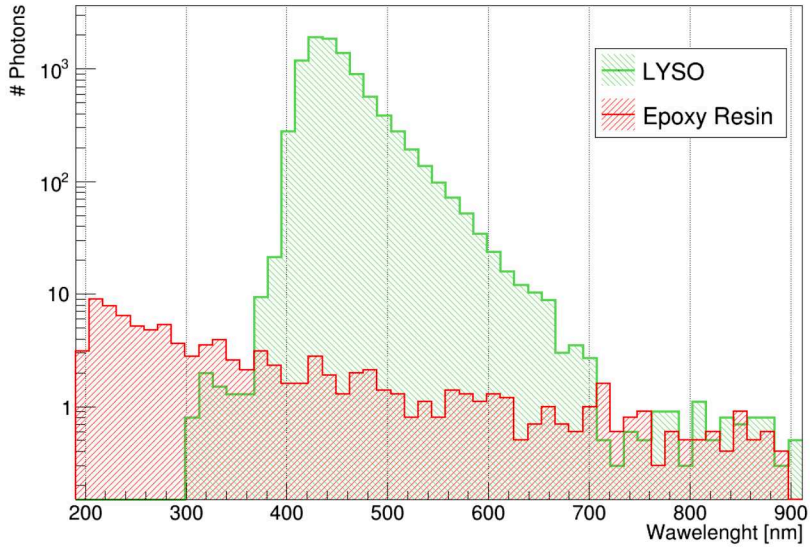

Figure 7.7: Average number of photons emitted per event as a function of wavelength by the radiators shown in Figure 7.6

higher. Figure 7.7 shows the number of photons produced in the wavelength range of interest obtained by averaging the simulation results of different events such as those shown in Figure 7.6.

Not all the photons produced reach the dSiPM and of these only a portion are detected in agreement with the PDE spectrum in Figure 7.5. It can be seen that the LYSO emission spectrum peaks at the wavelengths where the dSiPM is most sensitive, while the epoxy produces only a few photons in the most relevant regions. The number of photons detected for the events in Figure 7.6 is shown in Figure 7.8. These are the photons that passed the probability cut determined by the PDE and would, therefore, generate a discharge in the pixel. In the example shown, it can be seen that few photons are detected if the epoxy-radiator is used, whereas a large cluster of hits is visible if the LYSO-radiator is

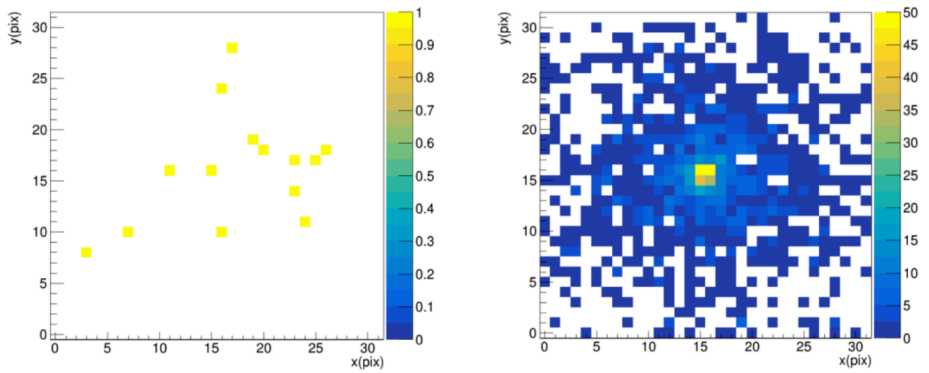

Figure 7.8: Number of photons detected by the dSiPM for the events in Figure 7.6. dSiPM+epoxy-radiator on the left, dSiPM+LYSO-radiator on the right.

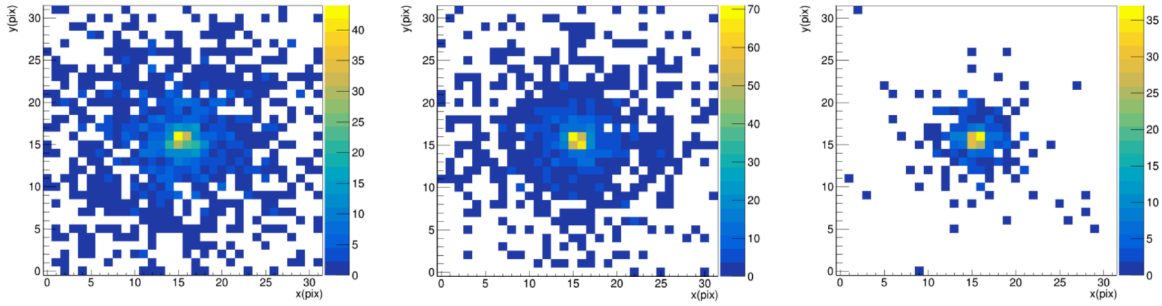

Figure 7.9: Simulated hitmaps of dSiPM coupled with LYSOs of three different thicknesses: from left 1 000 µm, 500 µm and 200 µm.

used. In both cases, the detection efficiency of the MIP (on sensor level) is measured to be close to 100 % with at least one hit due to the light produced by the radiator.

Effect of Thickness and Spatial Resolution Estimation

In order to preserve the intrinsic spatial resolution of the dSiPM as much as possible (see Figure 7.2), different radiator thicknesses are tested. Thinning the epoxy-resin leads to a considerable reduction in the detection efficiency. Simulations, therefore, show that this material is not well-suited due to the reduced number of photons produced and the low PDE of the sensor. LYSO, on the other hand, shows encouraging results and an improvement in spatial performance by using thinner crystals. Figure 7.9 shows an example of how the thickness of the LYSO affects the hitmap and the cluster size.

By repeating the simulation of events with incident electrons over the entire sensor area, it is also possible to estimate the spatial resolution of the dSiPM with thin LYSO coupling. The cluster center of the simulated events is calculated as the average position of the firing pixels (each pixel has a unit weight to simulate the binary response of the sensor). Spatial residuals are calculated as the distance between the known incident particle position and the cluster center. In order not to suffer from edge effects, only hits in an area of 1×1 mm from the center of the sensor are considered for this study. An example of spatial residuals for two of the simulated LYSO thicknesses is shown in Figure 7.10.

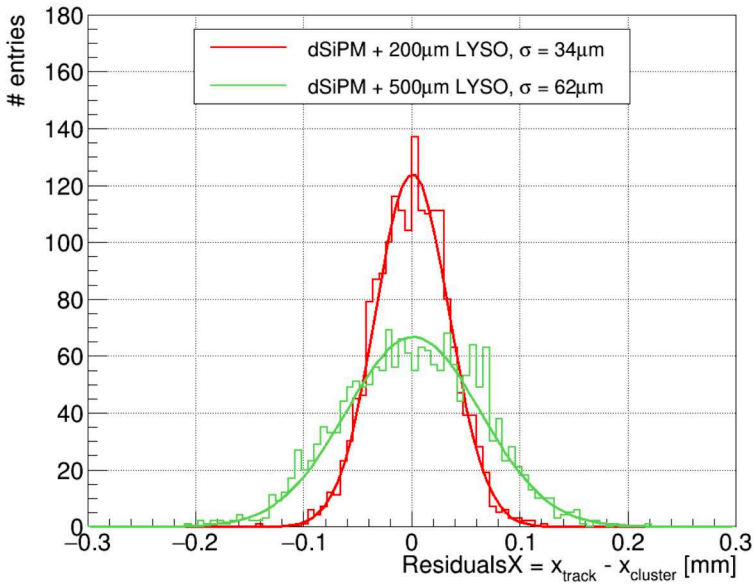

Figure 7.10: Simulated spatial residuals for dSiPM coupled with 500 µm (in green) and 200 µm (in blue) thick LYSO crystals.

The standard deviation σ of the Gaussian fit on the spatial residuals is a good estimate of the spatial resolution of the sensor.

The results of these simulations indicate that coupling with thin LYSOs is a good strategy to improve efficiency while preserving good spatial resolution of the DESY dSiPM. The choice of LYSO as the material to be used in the studies is also related to the availability of the material in the desired size and thickness.

7.4 DESY dSiPM and Thin LYSO Coupling

Following the encouraging simulation results, the DESY dSiPM sensors are coupled with thin LYSO crystals, and their performance is tested after the coupling process. LYSO(Ce)s crystals from OST photonics [122] in various sizes and thicknesses are used. The available properties of the crystals used are given in Table 7.3.

LYSO gluing is carried out using the low-viscosity epoxy-adhesive Polytec EP 601-LV [123] whose mechanical and optical properties are well suited for the purpose. The coupling took place in a clean room by placing a small drop of adhesive on the dSiPM surface and then placing on top the LYSO crystal by applying a small pressure, allowing the glue to extrude from the sides. The glue is then cured according to the manufacturer's instructions (the properties of the glue ensure the perfect functioning of any wire bonds partially encapsulated during the procedure). The uniformity of the glue and the absence of air bubbles are then verified. The thickness of the glue layer is measured to be less than 20 µm in the samples coupled. Figure 7.11 shows three crystals coupled to dSiPMs. In the example

Table 7.3: Main properties of the LYSO coupled to DESY dSiPM. From [122]

OST Photonics LYSO(Ce) Properties	
Density	7.4 g/cm^3
Radiation Length	1.10 cm
Effective Atomic Number	66
Decay Constant	40-44 ns
Light Yield (Relative to BGO=100%)	190
Refractive Index	1.82
Wavelength of Max Emission	420 nm
Melting Point	2050 °C

shown, crystals of $2.5 \times 2.5\,\mathrm{mm}^2$, 100, 200 and 500 µm thick, are coupled to fully cover the main sensor array.

7.4.1 Laboratory characterization with Sr-90

After the coupling procedure with the radiators, Dark Count Rate (DCR) and Current-Voltage (IV) are measured to verify that sensor functionalities have not been compromised. Having ascertained the functionality of the sensors, the prototypes shown in Figure 7.11 are used to detect electrons produced by a Sr-90 source. This measurement serves as partial validation of the simulation and is preparatory to test-beam studies of the sensors. The sensors are operated at a constant temperature of ~25 °C in the laboratory under dark conditions and exposed to the radioactive source. No trigger system is used, and random frames are saved for several hours. Analyzing frames with more than ten firing pixels excludes most DCR events and selects events whose origin is probably scintillation from MIP. A qualitative analysis of the hitmaps obtained confirmed the predictions described in Section 7.3.2: the thinner the radiator, the greater the confinement of hits on the sensor and the smaller the cluster size. Figure 7.12 shows examples of hitmaps obtained with the described procedure: clusters of hits are identifiable, and their spatial properties depend on the thickness of the radiator used.

7.5 Test-Beam Characterization

New test-beam campaigns were carried out to quantitatively characterize the properties of dSiPM coupled with LYSOs. The results presented here are obtained using setups and analysis chains similar to those used for the bare prototypes described in Chapter 6. Also in this campaigns, two Device Under Tests (DUTs) are tested simultaneously, alternating prototypes with different LYSO thicknesses. The next sections summarizes the spatial and timing performances obtained.

7.5.1 Clustering and Cluster Size

Simulations and laboratory measurements suggest large cluster sizes for MIP events detected using dSiPM+LYSO samples. The clustering algorithm used for these measurements only considers non-split

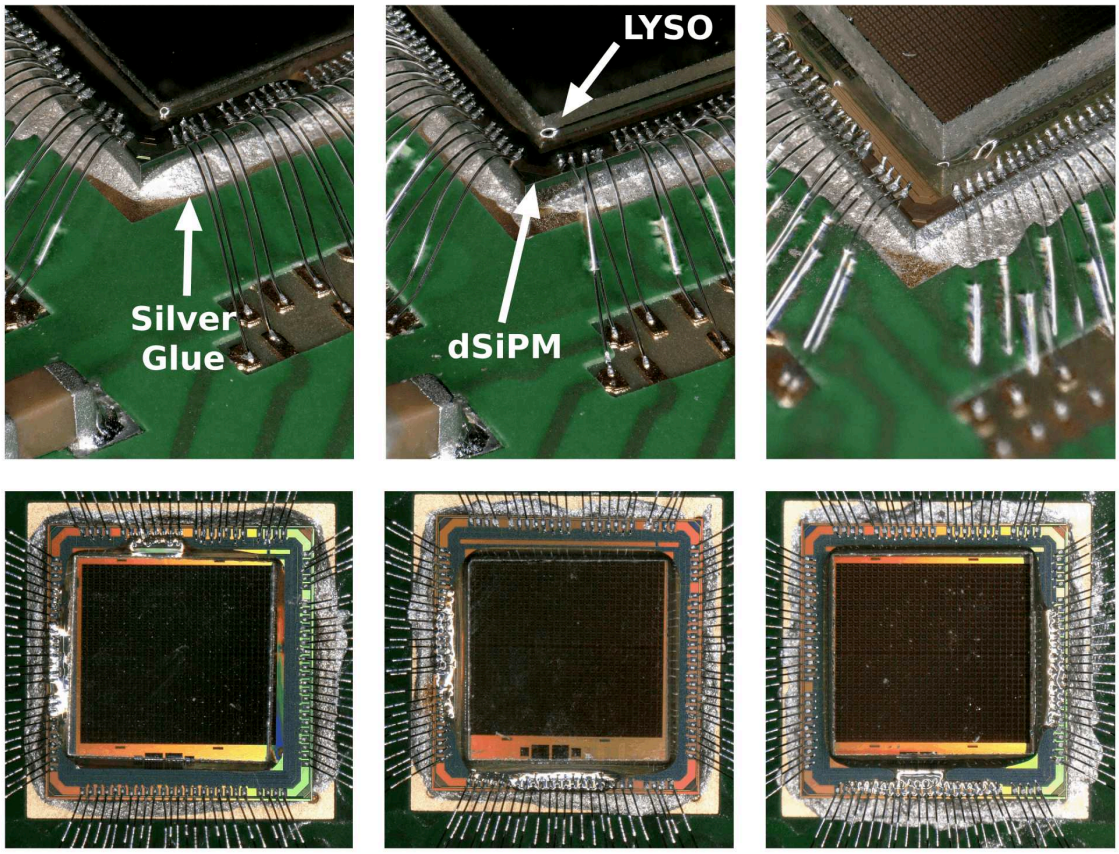

Figure 7.11: Microscope pictures of DESY dSiPM coupled with 100 µm (left), 200 µm (center) and 500 µm (right) thick LYSO crystals. Side and top view. The dSiPMs are glued with silver glue on a Printed Circuit Board (PCB) and wire-bonded before the LYSO coupling.

clusters (touching pixels). The cluster coordinate is defined as the centroid of the cluster's pixels based on their spatial coordinates. The cluster detection time is defined as the time stamp of the pixel closest to the center of the cluster. Similar to what is described in Section 6.6.1, the cluster size is measured on DUT clusters associated with reconstructed tracks. In contrast to bare prototypes, where the cluster size is mainly one, in prototypes with LYSOs the cluster size is considerably larger. Figure 7.13(a) shows an example of associated cluster size normalized to the number of entries for the three different LYSO thicknesses tested. It can be seen that the thicker the radiator, the larger the associated cluster size is as expected from the simulations. The average cluster size as a function of overvoltage is studied and shown in Figure 7.13(b). Here, an increase in cluster size as a function of overvoltage is observed in all sensors studied. This is mainly attributable to an increase in PDE as a function of overvoltage, which results in more photons being detected in the peripheral regions of the cluster[1]. The increase in DCR as a function of overvoltage also contributes marginally to this observable. The clustering algorithm used for this analysis excludes clusters with sizes smaller than three. This is verified to have no effect on the other observable described in the following sections. A cut-off on small clusters

[1] Where there is lower photon density

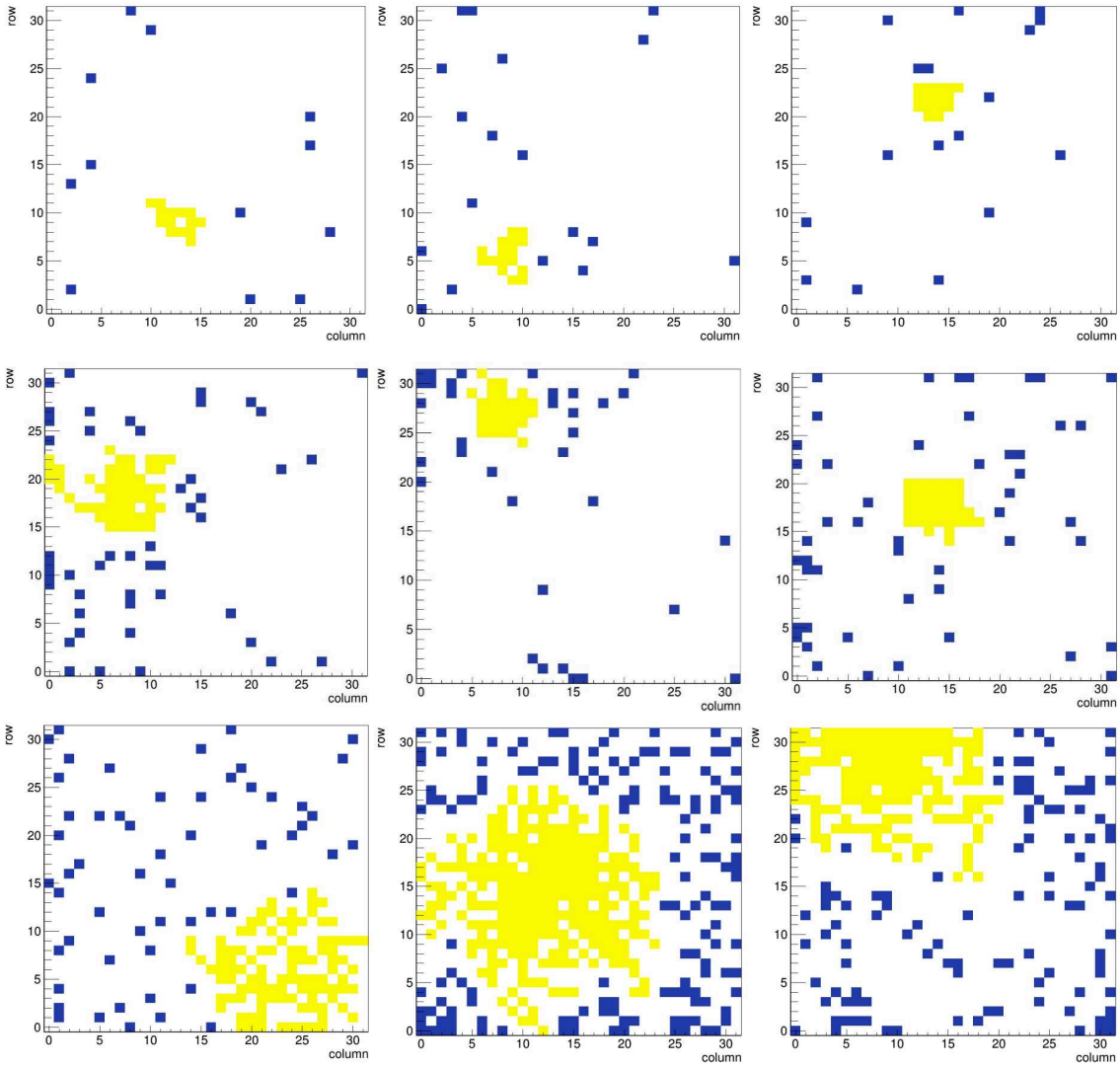

Figure 7.12: Examples of Sr-90 events hitmaps. DESY dSiPM coupled with 100 µm (top), 200 µm (center) and 500 µm (bottom) thick LYSO crystals. The biggest non-split cluster is marked in yellow.

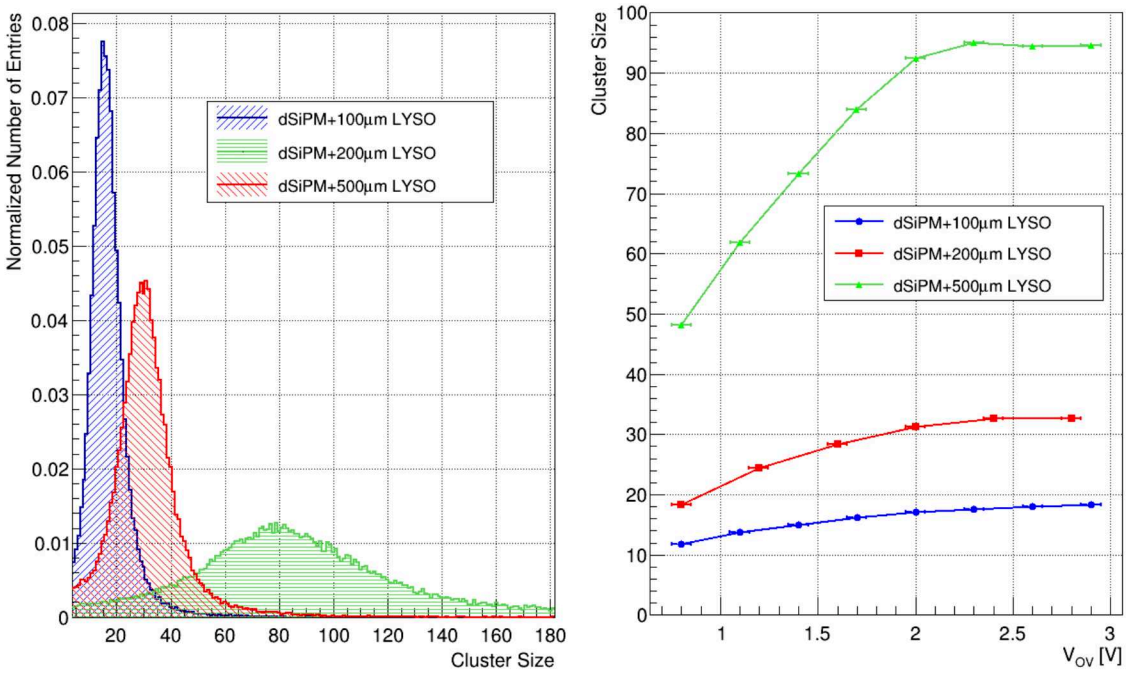

(a) (b)

Figure 7.13: Example of MIP associated events cluster size distribution for dSiPM+LYSOs operated at ~2 V overvoltage (a). Mean cluster size as a function of the overvoltage (b). Sensors operated in test-beam at ~0 °C. The dSiPMs are coupled with 100 µm (blue), 200 µm (red) and 500 µm (green) LYSO crystals.

can be seen as strong DCR suppression. The larger cluster size of MIP events, using LYSO coupling, allows to distinguish them from DCR events (with cluster size mainly one) that are then excluded from the analysis. The results shown in this and the following sections only consider events whose center of the associated cluster is far from the edges of the sensor[2], in order to avoid edge effects.

7.5.2 Spatial Resolution

The spatial resolution is calculated from the spatial residuals described by the equation 6.1. Unlike bare dSiPM, the spatial residuals of the samples coupled with LYSO are almost Gaussian as shown in the example in Figure 7.14(a). The standard deviation extracted from the Gaussian fit of the residuals is used to estimate the spatial resolution of the sensors as described in Section 2.5.1. Comparing Figure 7.14(a) with Figure 7.10, a qualitative agreement is observed, with the measured standard deviation σ slightly higher than the simulated value. The width as a function of overvoltage is shown for the three LYSO thicknesses tested in Figure 7.14(b). The spatial resolution is best for the sample coupled to the thinnest radiator and reaches a value of ~32 µm in this case. It should be noted that the spatial resolution is degraded compared to the bare dSiPM case where the spatial resolution is measured to be ~20 µm.

[2] Cluster with the center in a ring of eight pixels from the sensor edge are excluded

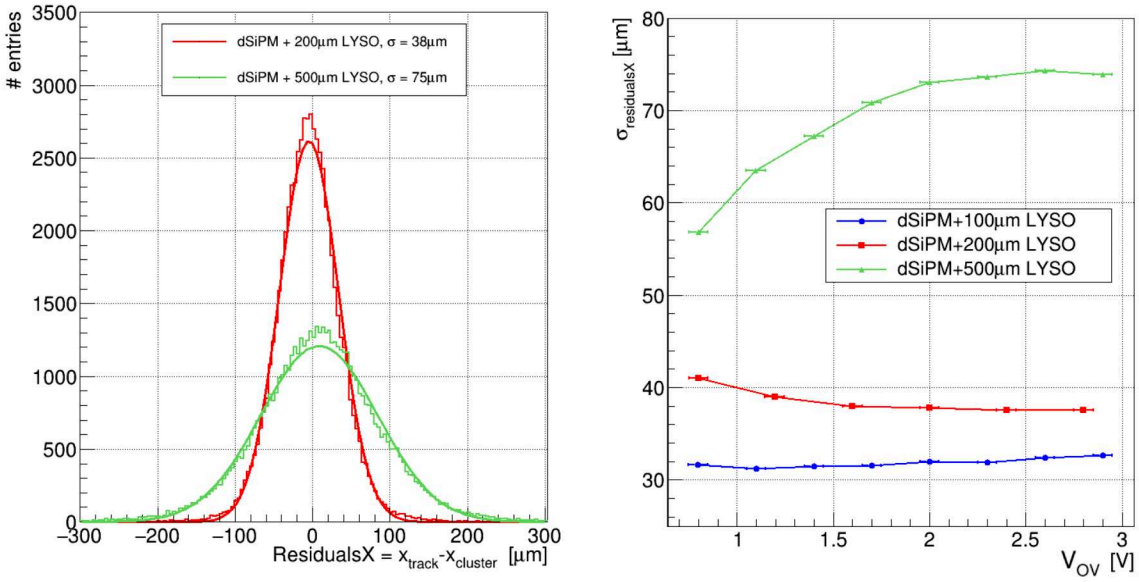

(a) (b)

Figure 7.14: Example of spatial residuals in X at ~2 V overvoltage (a). Width of spatial residuals in X as a function of the overvoltage (b). Sensors operated in test-beam at ~0 °C. The dSiPMs are coupled with 100 µm (blue), 200 µm (red) and 500 µm (green) LYSO crystals.

7.5.3 Efficiency

The main improvement obtained with dSiPM+LYSOs compared to MIP detection with bare dSiPMs is observed when analyzing the efficiency in MIP detection. This, defined by equation 6.5, is measured as a function of the hit position within the pixel similarly to what is described in Section 6.6.4. An example of an in-pixel efficiency map is shown in Figure 6.12, similar efficiency values are measured for all dSiPMs coupled with LYSOs at all tested overvoltages. Comparing Figure 7.15 with Figure 6.12 shows how the use of a radiator makes the sensor fully efficient and also the interaction of MIP in non-active regions of the pixel results in an indirect MIP detection (due to scintillation light). Efficiencies higher than 99 % are measured in all samples (i.e. all LYSOs thicknesses) and for all overvoltage tested.

7.5.4 Time Resolution

The time resolution is measured for samples coupled with LYSOs in a similar way as described in Section 6.6.3. Time residuals obtained as the difference of the timestamps of the associated clusters in the two DUTs are used to estimate the timing performance of the dSiPM+LYSO system. An example of time residuals is shown in Figure 7.16. As for the bare dSiPM case, also here the time residuals are characterized by a fast Gaussian core, in the tens of picoseconds regime, and slower tails, in the nanosecond regime. However, the nature of the events in the tails is different here as most of the events with slower time response come from MIP interactions happening in inactive regions of one of the two sensors. In this case, MIP detection is indirect and relies on scintillation light only. The asymmetry in

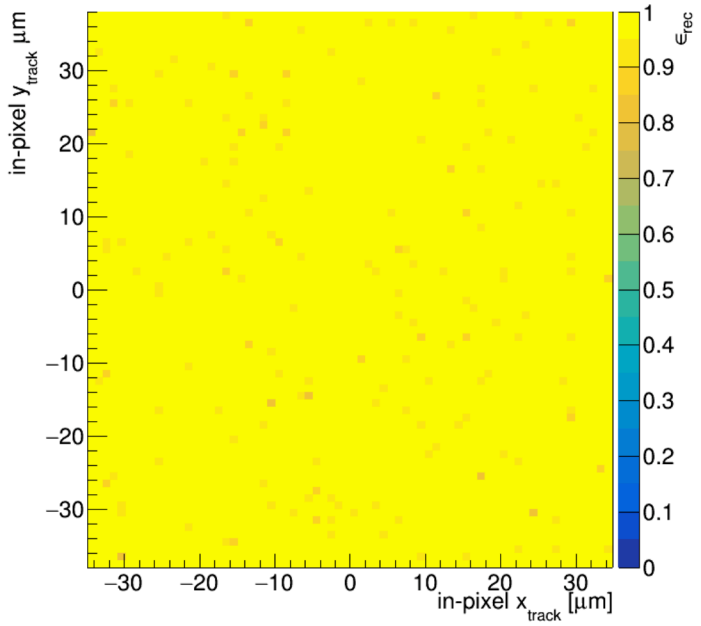

Figure 7.15: In-pixel hit detection efficiency measured at an overvoltage of 2 V and a temperature of ~0 °C for the dSiPM coupled with 200 µm LYSO crystal.

the tails of the example shown is due to the different time response of the two DUTs[3]. Decisive in this context are, therefore, the timing properties of the scintillator as well as the ability of the sensor to detect the few prompt photons. A radiator with a faster time response[4] or a sensor with a higher fill-factor (i.e. higer PDE) would lead to better time resolutions when this detector concept is used.

7.5.5 Independent LYSO Characterization Using Commercial SiPMs

To demonstrate that a higher fill-factor leads to better time resolutions, a test-beam is performed using commercial analogue SiPMs AFBR-S4N44P014M [124] coupled with LYSO crystals of the same type and size as those used with DESY dSiPMs. The SiPM used has a considerably higher PDE than DESY dSiPM, and is well suited to detecting the few prompt photons emitted by the scintillation of the LYSO. As a time reference and trigger, a SiPM is coupled with a smaller, thicker scintillator so that only events in the central region of the DUT are selected, as shown in Figure 7.17.

Analog waveforms are stored with an oscilloscope and analyzed. Reference and DUT Time Of Arrival (TOA) are defined with a fixed threshold on the waveform and then subtracted to define time residuals. An example of time residuals is shown in Figure 7.18(a). It can be seen that most events are confined to a single fast Gaussian peak. The sigma extracted from the Gaussian fit of the time residuals can be used as the upper limit of the time resolution of the DUT (SiPM+LYSO). It should be noted that this also includes the time resolution contribution of the trigger. The sigma of the fit as a function of bias and LYSO thickness is shown in Figure 7.18(b). Thicker radiators correspond to better time resolutions

[3] dSiPM coupled with 500 µm LYSO crystal has a better time resolution than dSiPM coupled with 100 µm LYSO

[4] Higher number of prompt photons with respect to the delayed ones

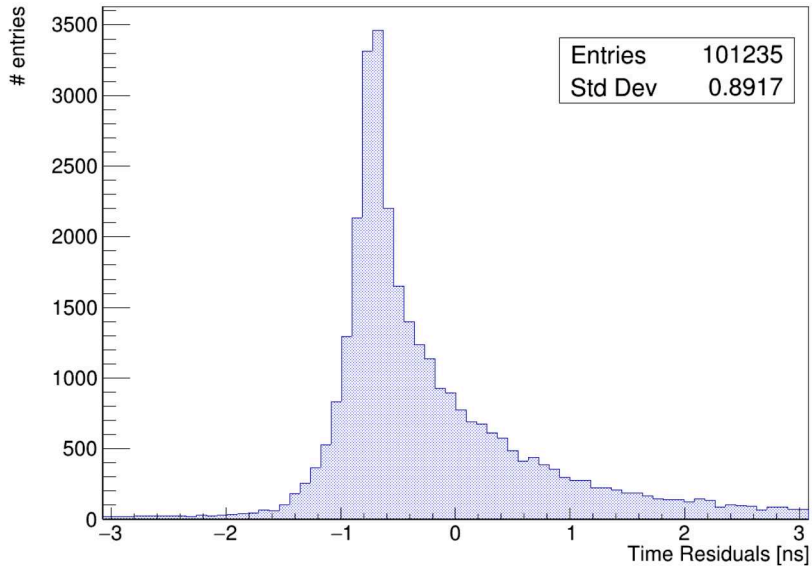

Figure 7.16: Example of time residuals obtained obtained with dSiPM coupled with 100 µm LYSO and dSiPM coupled with 500 µm LYSO. Measured at an overvoltage of 2 V and a temperature of ~0 °C

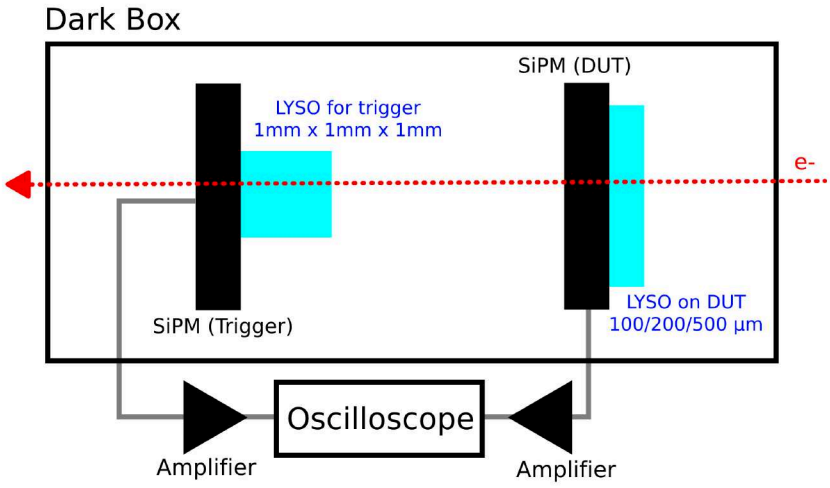

Figure 7.17: Setup used with analog SiPM to characterize LYSO crystal timing performances. The DUT is coupled with different crystal thicknesses. A second SiPM with thicker and smaller crystal is used to select a Region Of Interest (ROI) trigger and as time reference.

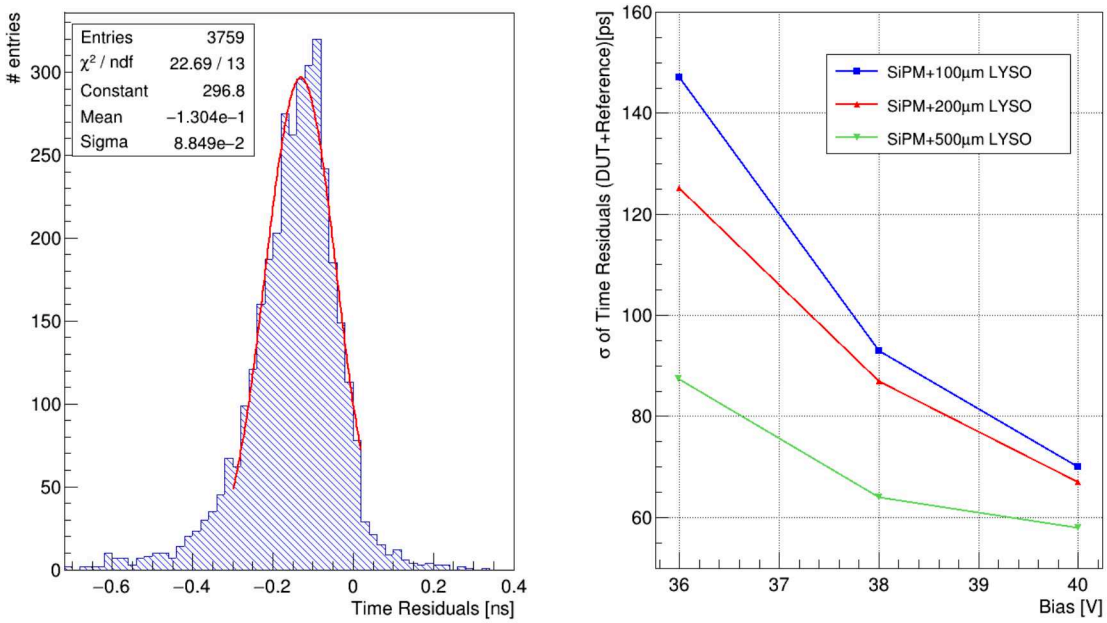

(a) (b)

Figure 7.18: Time residuals example obtained using SiPM coupled with 200 µm LYSO with 38 V bias (a). Time residuals as function of the bias for SiPM coupled with 100 µm (blue), 200 µm (red) and 500 µm (green) LYSO crystals.

(higher number of prompt photons emitted). Higher bias also results in better time resolutions because higher bias means higher PDE and, thus, a higher probability of detecting fast photons as well as better intrinsic time response of the sensor (higher gain).

These measurements suggest that the use of technologies in dSiPM that guarantee higher PDE (such as the use of microlenses or BSI) can bring the dSiPM+thin radiator concept to time resolutions on the order of a few tens of picoseconds. This, combined with full-efficiency and good spatial resolutions showed in the previous sections would make the technology a possible candidate for future 4D-tracking applications.

7.6 Summary of Results

In this chapter, the use of dSiPM coupled with thin radiators are presented as a novel detector-concept to overcome the limitations in efficiency and DCR in using dSiPM as a MIP detector, and opening the possibility of using this technology for future applications in 4D-tracking.

The feasibility of the study is evaluated through Geant4 simulations. The outcome of the simulations guided the choice of the type and geometric characteristics of the radiator to be coupled to the DESY dSiPM: LYSO(Ce) crystals with thicknesses in the range 100 to 500 µm.

The performance of the assemblies is therefore studied in laboratory and test-beam campaigns. The cluster size of MIP events is significantly increased compared to detection with bare dSiPM. This

allows a clear distinction of MIP and DCR events, removing noise contamination in MIP detection. Spatial resolution is slightly degraded compared to bare dSiPM approach reaching values of $\sim 32\,\mu m$ when using the thinnest radiators. Efficiencies in MIP detection greater than 99 % are measured with all samples and under all temperature and overvoltage conditions tested. The timing resolution is measured to be on the order of 1 ns using dSiPM + LYSO(Ce) approach, limited by radiator properties and PDE.

An independent characterization of the timing properties of the scintillators used showed that the use of SiPMs with higher PDE allow to achieve time resolutions of less than 100 ps using this detector-concept.

These results show that the dSiPM technology combined with thin radiators represents an interesting detector-concept in the context of Research and Development (R&D) for future 4D-Trackers.

Part II

Studies on Monolithic Active Pixel Sensors Prototypes

CHAPTER 8

MAPS in a 65 nm CMOS Imaging Technology

Complementary Metal-Oxide-Semiconductor (CMOS) Monolithic Active Pixel Sensors (MAPS) represent an essential research and development topic for future High-Energy Physics (HEP) experiments as introduced in Section 1.5. This chapter describes MAPS sensors, developed with a 65 nm technology, studied in this thesis. Sections 8.1 and 8.2 introduce MAPS and the different layouts investigated. Section 8.3 describes the research and development activities at DESY, the context in which this work is developed. Section 8.4, then, gives details of the investigated MAPS prototypes whose experimental results will be presented in Chapter 9.

8.1 Monolithic Active Pixel Sensors

MAPS were developed in the early 90s for the detection of visible light by exploiting CMOS technology. These sensors showed numerous advantages over traditional imaging devices, including improvements in functionality, power consumption, radiation resistance, speed, and ease of use [125, 126]. The high integration density and flexibility of the circuits prompted the use of MAPS in various fields, including HEP experiments for vertexing and tracking systems. Thanks to the possibility of integrating the particle detector and readout electronics on a single silicon chip, the complexity of tracking systems has been drastically reduced and the amount of material budget minimized, allowing for high accuracy in tracking and vertexing applications. One of the first successful demonstrations of MAPS in HEP came with the STAR experiment, using MIMOSA28 sensors [127, 128]. Subsequently, the ALICE experiment further developed this technology with the use of ALICE PIxel DEtector (ALPIDE) sensors in its Inner Tracking System 2 (ITS2) [129], produced using a 180 nm CMOS Imaging Process [130]. A sketch of the ALPIDE pixel is shown as an example of MAPS design in Figure 8.1. The type of MAPS of interest in this work is characterized by a small collection electrode with an input capacitance of a few femtofarads that guarantees a high signal-to-noise ratio and low power consumption. The presence of a deep p-well allows PMOS transistor to be produced on a p-type epitaxial-layer without affecting the charge collection. CMOS circuitry can be incorporated at the pixel level, allowing the implementation of elaborate readout architectures.

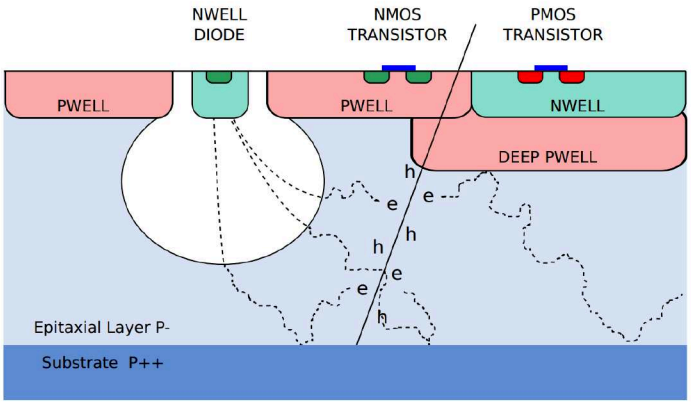

Figure 8.1: Schematic of an ALPIDE pixel with the deep p-well feature from [131].

8.2 MAPS Layouts

For the next generation of MAPS, several modifications to the layout are currently under investigation. The goal is to improve performance in terms of efficiency, spatial resolution, and time resolution by exploring the possibilities offered by current CMOS technologies and the sensor layout improvements already investigated in [132, 133]. In the *standard* MAPS layout, similar to ALPIDE, Figure 8.2(a), the pn-junction is located around the small collection electrode, resulting in a limited depleted region that assumes a bulb-like shape. Under these conditions, a significant fraction of the charge carriers generated by Minimum Ionising Particles (MIP) in the sensor move by diffusion, leading to a slower signal response due to the diffusion-dominated charge collection.

To address the slow response of the standard layout, a modified layout known as the $n - blanket$, Figure 8.2(b), introduces an additional n-doped layer beneath the deep p-well, which houses the electronics. This modification enlarges the depleted volume, allowing a greater portion of the sensor to collect charges by drift, thus significantly speeding up the sensor's response to particle detection. However, in this design, a minimum in the electric field can occur at the edges and corners of the pixel, slowing down charge collection in these regions and potentially reducing efficiency.

To mitigate this effect, another layout, called $n - Gap$, Figure 8.2(c), introduces a gap in the n-doped layer beneath the deep p-well at the pixel edges. This generates a lateral electric field at the boundaries of the pixels, helping to push the charges toward the collection electrode more efficiently. While this layout offers the fastest charge collection, it also reduces charge sharing between adjacent pixels, which deteriorates the spatial resolution.

8.3 MAPS R&D Activities at DESY

The Deutsches Elektronen SYnchrotron (DESY) is currently involved in Research and Development (R&D) activities aimed at developing the next generation of silicon detectors for vertexing and tracking, to which this work contributes. Among these activities, the TowArds Next GEneRation sIlicoN detectors (TANGERINE) project [134–136] aims to investigate the potential of novel technologies

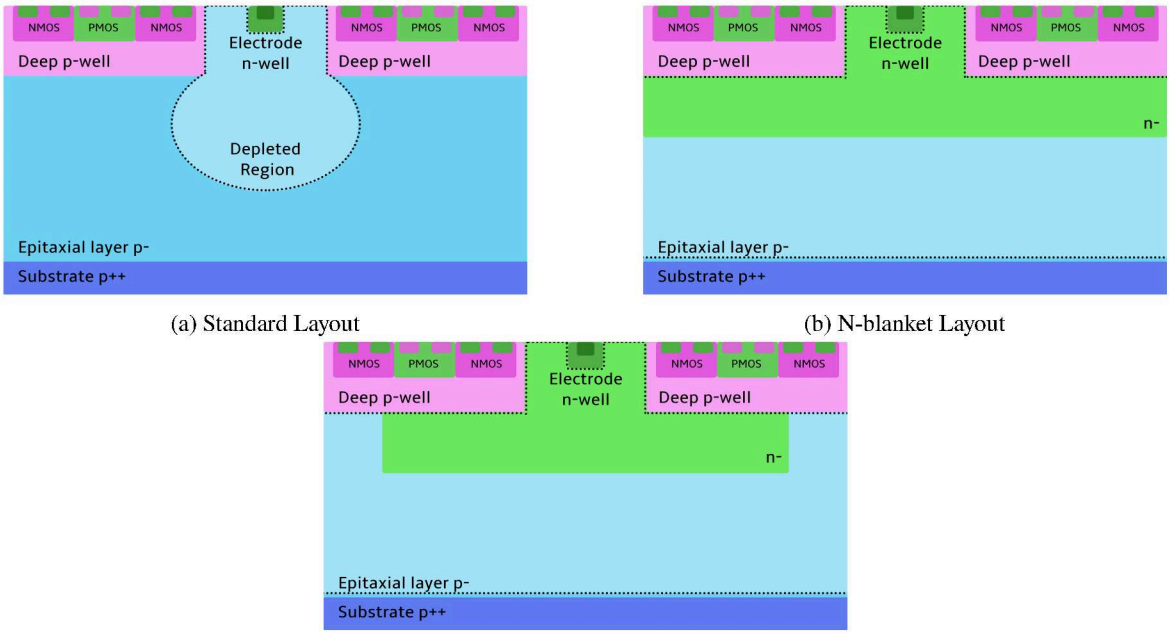

(a) Standard Layout

(b) N-blanket Layout

(c) N-Gap Layout

Figure 8.2: Sketch of the three different pixel layouts of MAPS investigated. The depleted region is marked with a dotted line.

Table 8.1: Requirements for future lepton colliders vertex detectors.

Property	**Requirements**
Material budget	O(50 µm of Si)
Single-point resolution	≤ 3 µm
Time resolution	~ ps - ns
Granularity	≤ 25 µm x 25 µm
Radiation tolerance	$O(1 \times 10^{11}\ n_{eq}/cm^2)$

towards the development of high precision silicon-detectors for future experiments. Within Work Package 1 (WP1) of the project, the MAPS technology developed in a 65 nm CMOS node (see next section) is chosen as potentially capable of meeting the requirements of future lepton-collider vertex detectors summarized in Table 8.1. Prototypes are designed and tested to understand better and exploit the potential of this technology. A technology-independent simulation approach was also developed and successfully tested on data [137, 138]. This helps to reduce production iteration while minimizing development time and costs. Some of the project outcomes are presented in [139] others discussed in this work in the following sections and in Chapter 9.

These activities were carried out in close collaboration with the European Organization for Nuclear Research (CERN) EP Strategic R&D Programme [140] Work Package 1.2, and with the A Large Ion Collider Experiment (ALICE) ITS3 Upgrade project [141]. In the coming years, DESY's involvement

in blue-sky R&D in the field of solid-state detectors will continue as part of the international DRD3 collaboration [142] currently forming.

8.4 Multi-Project Production using a 65 nm CMOS Imaging Process

A 65 nm CMOS Image Sensor Process [130] is chosen by the TANGERINE project for the production of prototypes. This is currently the most advanced CMOS node used for monolithic sensors in HEP applications. Compared to previous technologies (such as the 180 nm technology used by ALICE ITS2 [28]), the 65 nm technology offers a higher logic density that allows a reduction in pixel size and power consumption for the same CMOS logic. The technology comes with a thinner epitaxial layer[1] compared to the larger node technologies, which, although it allows the sensor thickness to be reduced by decreasing the material budget, results in smaller signals that require lower electronic noise and amplification to be detected.

Production involving several institutes are organized by CERN to allow different projects to share the production costs. The first submission is called Multi-Layer Reticle 1 (MLR1) [140] and includes test structures from several institutes and collaborations: ALICE, CPPM, DESY, IPHC, NIKHEF, STFC, and Yonsei University. The different masks designed by the respective institutes are assembled into a common reticle shown in Figure 8.3. All the designs in this production represent test structures used to evaluate the performance of the analog and digital components designed, as well as to compare the properties of the different layouts described in Section 8.2. Some modifications to the process have been developed in collaboration with the foundry [143] to enable the production of the structures described in Section 8.2.

Some of the implemented test structures are tested as part of this work and are described in the following.

8.4.1 DESY Chip V1 Prototype

The DESY Chip V1 prototype, fully developed at DESY, is designed to evaluate the performance of a newly-designed fast Charge Sensitive Amplifier (CSA) with Krummenacher type feedback [144] designed for Time Over Threshold (TOT) measurements.

The chip, shown in Figure 8.4, includes two distinct test structures. In the first test structure, located in the upper left-hand corner, are two CSAs with feedback capacitance of 1.5 fF and 2 fF, respectively, whose performance can be tested by pulse injection. The second test structure, in the bottom right corner of the figure, contains a 2×2 pixel matrix with analog readout. Each pixel has a pitch of 16.3 µm and incorporates a CSA with 2 fF Krummenacher feedback, as well as an additional operational amplifier. Most of the electronics in this prototype are located outside the pixel. The analog signal of each pixel can be directly sampled with an oscilloscope.

The main objective of the chip is the characterization of the electrical performance of the CSA and the evaluation of its response to MIP signal in the pixel array. The amplifiers provide nominal gains of 107 µV/e and 80 µV/e, depending on the variant used [145].

[1] Order of 10 µm

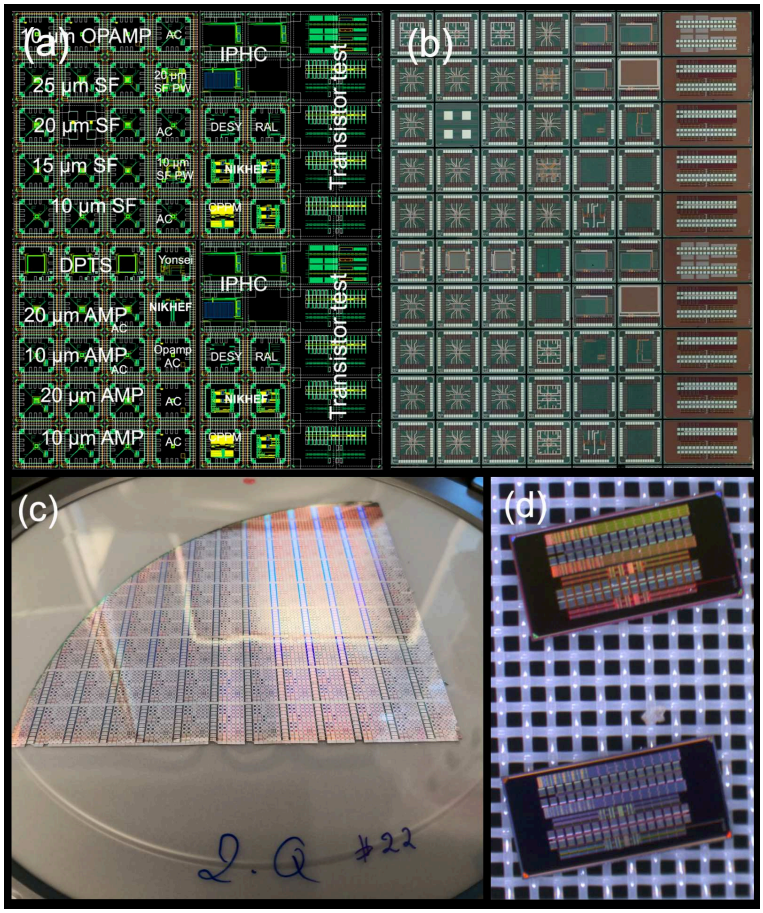

Figure 8.3: MLR1 in 65 nm CMOS technology: reticle layout (a), a picture of one reticle on the wafer (b), which contains 70 test chips with dimensions of either 1.5 mm x 1.5 mm or 3 mm x 1.5 mm (55 unique designs, with 15 chips repeated), a diced quarter wafer mounted on tape (c), and transistor test chips housed in a gel pack (d). Adapted from [143].

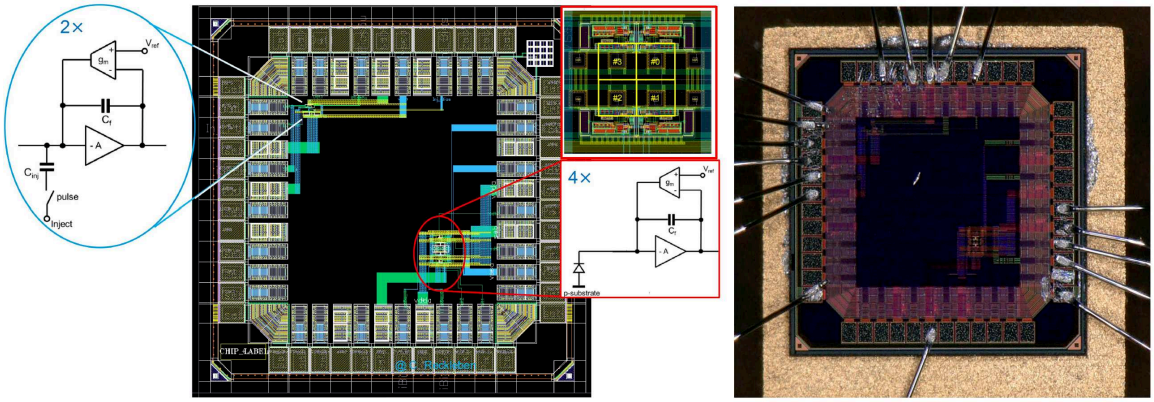

Figure 8.4: Layout of the DESY chip V1 prototype from MLR1 production (left). Microscope picture of a bonded sample (right). From [145]

Table 8.2: Details of APTS chips layouts and pitches studied ad DESY with the Caribou DAQ system. All samples have DC-coupling and a source follower for analog readout.

Chip ID	Pixel Pitch (µm)	Layout
17	15x15	Standard
27	15x15	N-gap
19	25x25	Standard
24	25x25	N-blanket
29	25x25	N-gap

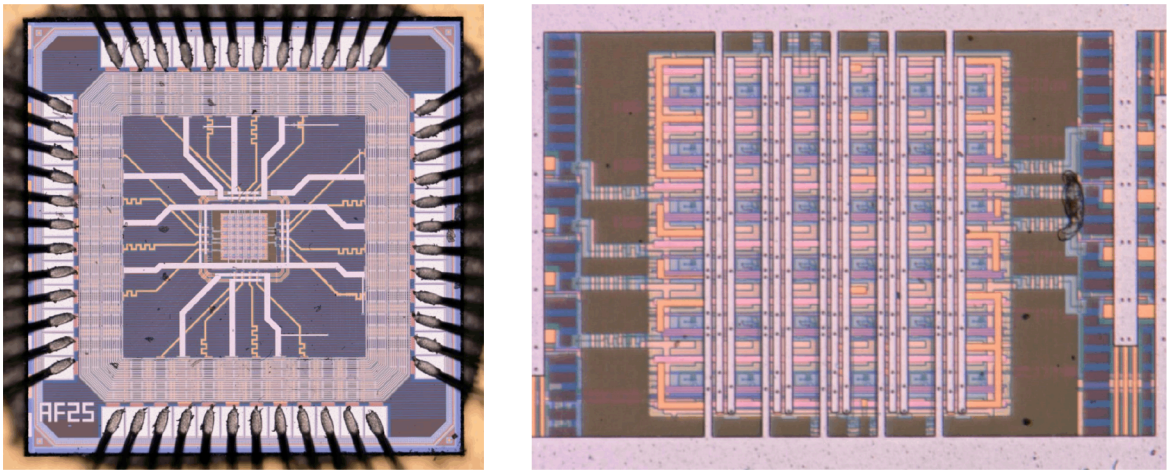

Figure 8.5: Microscope picture of a bonded APTS prototype from MLR1 production (left). Zoomed version showing the pixel matrix (right).

8.4.2 The Analogue Pixel Test Structure Prototype

The Analog Pixel Test Structure (APTS) is a prototype chip designed at CERN and is part of the MLR1 production. The APTS chip is available in variants with different pixel sizes, geometries, and layouts, including versions with pixel pitches of 10, 15, 20, and 25 µm. The chip has dimensions of 1.5×1.5 mm^2 and contains an array of 6×6 pixels, of which only the central 16 pixels (arranged in a 4×4 array) are active and read, while the outer pixels act as compensation elements to reduce electric field distortions. Each active pixel has an individually buffered analog output, which is connected to output pads to allow full access to the analog signal [146].

Results of extensive characterizations of these structures can be found in [147]. At DESY, some prototypes are independently characterized using the Caribou Data AcQuisition (DAQ) system described in Section 3.4.1. Caribou provides the necessary current and voltage sources, as well as the physical interface to the chip. It also integrates two 8-channel Analog to Digital Converters (ADCs) that sample the analog signals of all pixels at a rate of 65 MS/s. The chip versions studied at DESY have the pixels DC-coupled to the front-end electronics where a basic source follower structure offers their analog readout. The pitches and layouts characterized are summarized in Table 8.2. The Picture of a bonded chip is shoved in Figure 8.5.

In Section 9.3 and 9.4, some of the characterizations and calibration performed on APTS prototypes in the context of this work are presented. These studies are to be considered complementary to what is already published in [137–139].

CHAPTER 9

Laboratory & Test-Beam Characterization of MAPS Prototypes

This chapter reports on the laboratory and test-beam characterization of the Monolithic Active Pixel Sensors (MAPS) prototypes introduced in Chapter 8. Section 9.1 describes the laboratory studies on the DESY Chip V1, followed by the discussion in Section 9.2 of the outcomes of the test-beam campaigns at MAinzer MIkrotron (MAMI) Facility [148]. Section 9.3 reports the optimizations and characterizations carried out on the Analog Pixel Test Structure (APTS), including the determination of the gain curve and charge calibrations. Section 9.4 describes the measurements and performance of some APTS prototypes in Minimum Ionising Particles (MIP) detection.

9.1 DESY Chip V1 Laboratory Studies

Characterizations of the prototypes described in Section 8.4.1 are carried out in the laboratory to verify the performance of the Charge Sensitive Amplifier (CSA) and evaluate sensor response in particle detection. Measurements are made on the test structure with pixels using an ^{55}Fe source. The decay of ^{55}Fe emits monochromatic X-ray with energies of 5.9 keV, K-alpha emission, and 6.5 keV, K-beta emission. These X-rays, if absorbed in the silicon, generate ~1600 and ~1800 electron-hole (e-h) pairs, respectively [149]. Knowing the initial charge, and assuming that all generated charge carriers are collected, the measurement of the amplified signal allows the determination of the gain of the CSA.

The sensor operational parameters are summarized in Table 9.1. The amplified signals are sampled with a high-bandwidth oscilloscope (4 GHz, 10 Gs/s per channel).

Figure 9.1 shows an example of a single-pixel response of the DESY Chip V1 to the ^{55}Fe X-rays. Examples of waveforms are shown in the figure together with the amplitude distribution of the signals. A clear peak is visible in the amplitude distribution, corresponding to the K-alpha emission peak. The

Table 9.1: Details of operational parameters for amplifiers and source-followers in the DESY Chip V1 studies.

Description	**Value**
Supply voltage for amplifiers and source-follower (VDD)	1.25 V
P-well and substrate bias (SUB & PSUB)	−1.25 V
Bias for Amplifiers (VB5U)	0.95 V
Bias for last source-follower stage (VB80U)	2.22 V

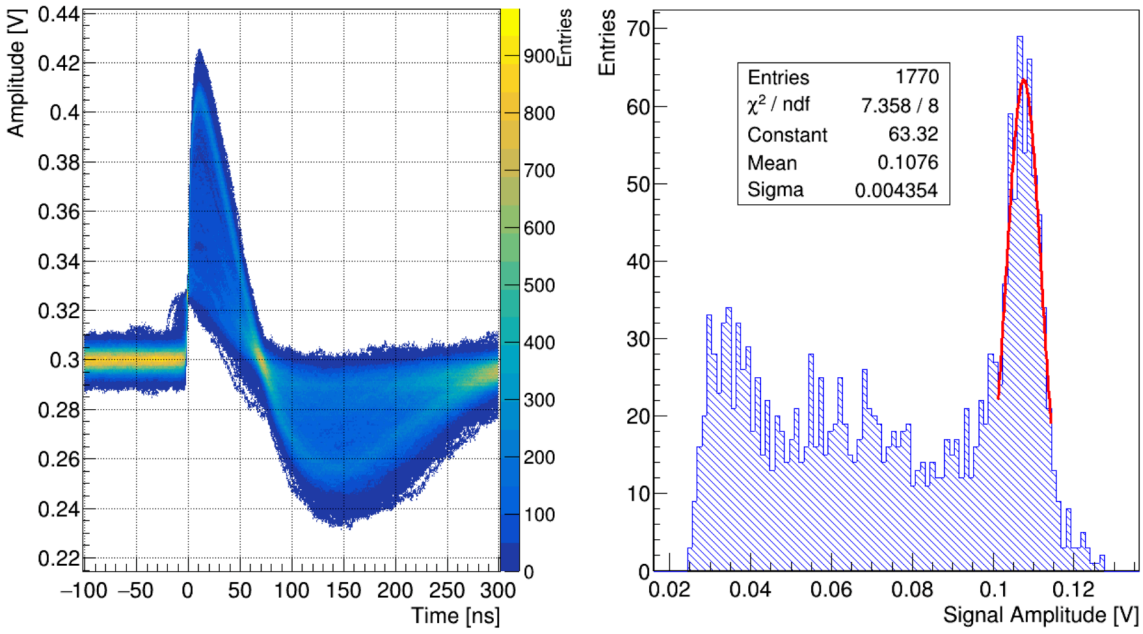

(a) (b)

Figure 9.1: Example of ^{55}Fe waveforms (a). Amplitude of ^{55}Fe events (b), the K-alpha peak is fitted with a Gaussian and results of the fit are reported. Pixel 00 of DESY Chip V1 sample 4 is here shown.

K-beta peak is not visible due to low statistics and noise. Signals with smaller amplitudes (i.e. the left tail of the spectrum) are attributed to Compton scattering or partial charge collection.

The measurements confirm the sensor's sensitivity to ionizing particles, and the measured amplitude is in line with the results of simulations performed by chip designers [145]. A detailed study of the sensor's performance is carried out in test-beam campaigns and presented in the following sections.

9.2 Test-Beam in MAMI

Test-beam campaigns on the prototype DESY Chip V1 have been carried out at CERN and DESY II test-beam facilities with observed trigger rates of ~ 0.001 Hz at DESY and ~ 0.01 Hz at CERN. The low rate is due to the small size of the active area caused by: the number of pixels (four), pixel pitch (only 16.3 µm), and a design issue in the sensing volume that was later identified. For an in-depth

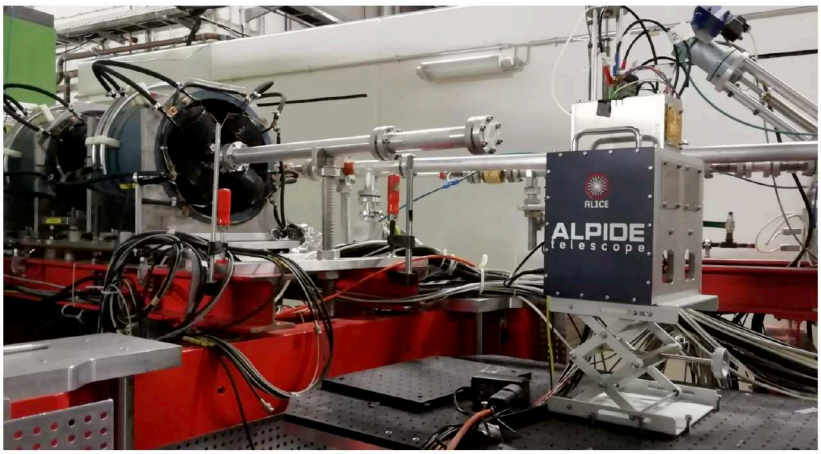

Figure 9.2: Test-beam setup in MAMI facility. The DESY Chip V1 is placed within an ALPIDE-based telescope and exposed to a 855 MeV electron beam.

characterization of the CSA response in MIP detection, further measurement campaigns are carried out at the MAMI facility [148]. The facility provides an electron beam with an energy of 855 MeV and high beam currents on a mm-scale spot size. During data taking, beam current was limited to protect the instrumentation used from damage, guaranteeing a trigger rate of approximately 1 Hz on the studied sensor.

The test-beam setup in MAMI facility is shown in Figure 9.2. Within this work, the effects on the MIP signals waveforms of certain bias parameters are studied. Further analyses based on the reconstruction of particle tracks are carried out using the frameworks described in Chapter 3. A beam-telescope[1] is used for particle tracking in order to evaluate the sensor performance in MIP detection. Results of these studies are reported in [135, 136].

9.2.1 Waveform Analysis

More than 500 k waveforms have been recorded and analyzed using the high-rate beam in MAMI. For these measurements trigger on Device Under Test (DUT) waveforms is used. The p-well and substrate bias (SUB & PSUB) and the bias for amplifiers (VB5U) are scanned in the range 1.25 to 2.2 V and 0.65 to 1.4 V respectively. The other main operational parameters used are those shown in Table 9.1. The observables investigated by analyzing the waveforms are illustrated in Figure 9.3. Definition and results of the measurements performed are summarized here:

- The signal baseline is defined as the mean value of the waveform in the region immediately before the signal (grey in the figure). The measured value is different for each pixel, as well as dependent on VB5U. Baseline values are measured in the range 150 to 350 mV.

[1] ALPIDE-based telescope kindly provided by the ALICE ITS3 group

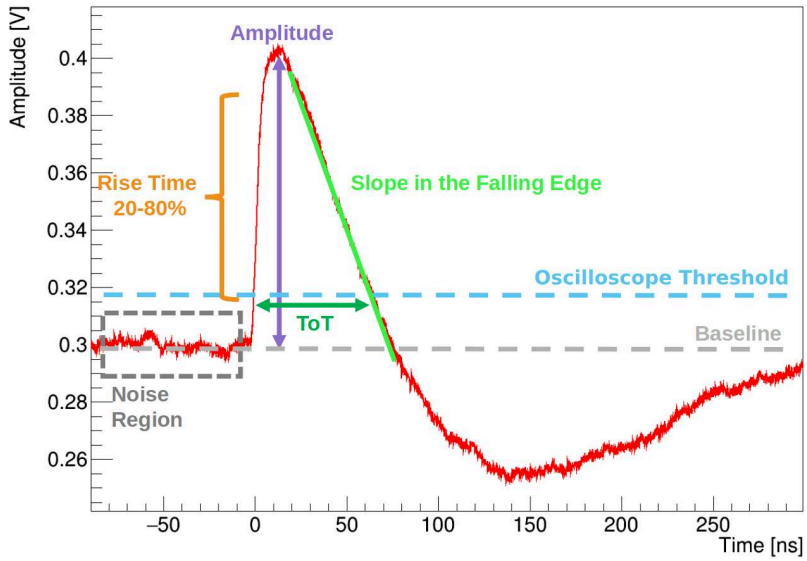

Figure 9.3: Example of waveform recorded in MAMI facility with DESY Chip V1. Investigated quantities are shown.

- The signal amplitude is defined as the difference between the maximum amplitude of the waveform and the baseline. The mean values measured show a slight decrease as VB5U increases. The mean amplitude of the MIP signals is measured in the range 40 to 90 mV.
- The signal rise-time is measured between 20 and 80 % of the amplitude. The rise-time decreases with increasing absolute p-well and substrate bias. Signal rise-time is measured in the range 4 to 9 ns.
- The Time Over Threshold (TOT) is measured as the time for which the signal remains above the defined scope threshold. The value decreases as VBU5 increases. Average TOT values are measured to be in the range 30 to 120 ns.
- The slope of the falling edge is measured using linear fit after the signal peak. the slope is measured in the range -0.2 to -1 mV/ns. and decreases as VBU5 increases.

Most of the measurements are in line with the simulations and characterizations performed by the chip designers [145]. However, deviations from expectations are observed. A pronounced undershoot following the signal characterizes pulses, as visible in the examples in Figure 9.1(a) and 9.3. Furthermore, a TOT non-linearity is found, as shown in Figure 9.4 where the amplitude of the signals is correlated to the TOT measured on the waveform. Here, the small slope for TOT values <50 ns is not desired and makes the sensor less accurate in charge measurements in this region, which also comprises the expected signal from MIP. The outcomes of the measurements performed in the context of this work served as input for the designers to improve CSA performance. The source of the issues are identified and solved. A new version of the CSA with a different type of capacitance in the feedback circuit is included in prototypes under characterization at the time of writing, and optimized operational parameters have been adopted [145].

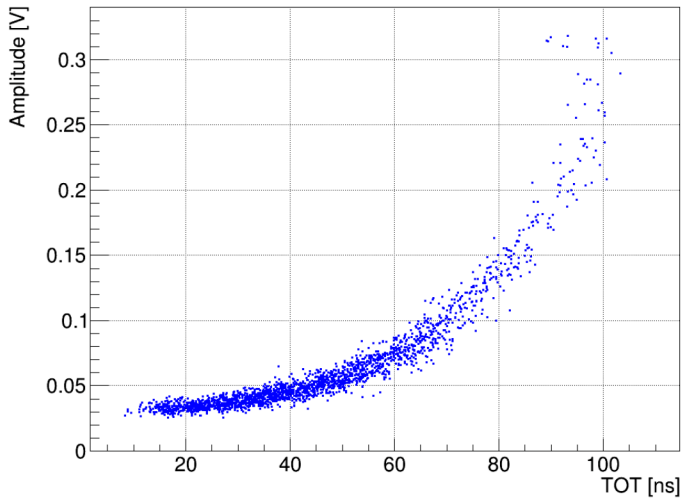

Figure 9.4: Amplitude of pulses as a function of TOT measured on DESY Chip V1 at MAMI facility. Sensor operated using values in Table 9.1 and a threshold of ~27 mV.

9.3 APTS Laboratory Studies

The characterization of APTS prototypes at DESY is performed using the Caribou Data AcQuisition (DAQ) system described in Section 3.4.1. Biasing and configuration procedures have been developed to properly operate the APTS with the setup, according to the chip specifications. The signals from the 16 pixels are amplified by an additional amplifier on the chip-board and then digitalized by the 12-bit Analog to Digital Converter (ADC) on the CarBoard with at 65 MS/s. The waveforms are then stored for the analysis. Different trigger logics are implemented in the DAQ firmware to allow internal triggers on signals above a configurable threshold or to accept external triggers with configurable latency.

The main objective of the characterization shown in this section is to find the best working point of the chips and correct for gain differences between the 16 pixels. The measurements are preliminary to test-beam studies where the sensor performance in MIP detection is tested. All the measurements presented here are complementary to what is shown in [139].

9.3.1 Charge Injection & Parameters Optimization

A pulsing circuit is implemented in the pixel design and allows charge injection into the first amplification stage via a capacitor with a nominal capacitance of 242 aF. The injected charge can be tuned by changing the voltage charging the capacitor.

The APTS operation parameters are optimized, starting from the nominal values provided by the chip designers, using a charge injection circuit. Optimal parameter values are chosen, in the characterizations described here, considering the Signal-to-Noise ratio (S/N) of the pulses of all 16 pixels and the objective of the characterizations. S/N is defined on the waveforms as the ratio of the signal amplitude and the standard deviation of the baseline in the noise region defined as shown in

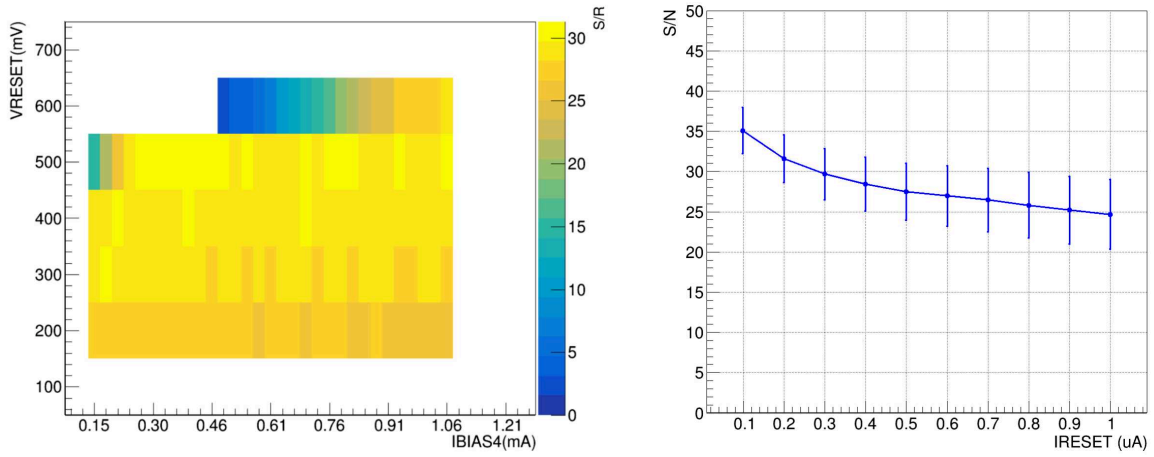

(a) (b)

Figure 9.5: S/N of APTS-24 prototype as a function of reset voltage $VRESET$ and the source follower NMOS current mirror bias $IBIAS4$ (a). Signal-to-noise as a function of the reset current $IRESET$ scan on APTS-17.

Table 9.2: Bias parameters used for APTS with source follower tested at DESY.

Parameter	**description**	**APTS 25 μm**	**APTS 15 μm**
IBIASN	Source drain follower NMOS current	20 µA	20 µA
IBIASP	Source drain follower PMOS current	2 µA	2 µA
VRESET	Reset voltage	500 mV	300 mV
IRESET	Reset bias	1 µA	0.1 µA
IBIAS3	Source follower PMOS current	200 µA	200 µA
IBIAS4	Source follower NMOS current	545 µA	365 µA

Figure 9.3. Figure 9.5(a) shows an example of a scan performed on the prototype APTS-24 (name according to Table 8.2) in the ranges provided by the designers for the parameter $VRESET$ and $IBIAS4$, respectively the reset voltage and the source follower NMOS current mirror bias of the chip. The optimal operation values are chosen from those with the highest S/N. Another example is shown in Figure 9.5(b) where the reset current $IRESET$ is scanned on the prototype APTS-17. Here smaller reset currents improve the S/N, however it results in a longer reset time, i.e. a longer recovery time of the pixels. This example shows how parameter optimization can be done considering the requirements of the specific application. The operation parameters used for the APTS studies shown in this work are summarized in Table 9.2. In order not to influence in the comparison of the different layouts studied, the same parameters are used for sensors with the same pixel-pitch. The same parameters are used for the studies presented in [139].

9.3.2 Gain Characterization

Charge injection is also used to characterize amplifier gain non-linearity and correct pixel-to-pixel variations. A gain curve is obtained for each pixel, sensor and p-well/p-sub bias. This is then applied

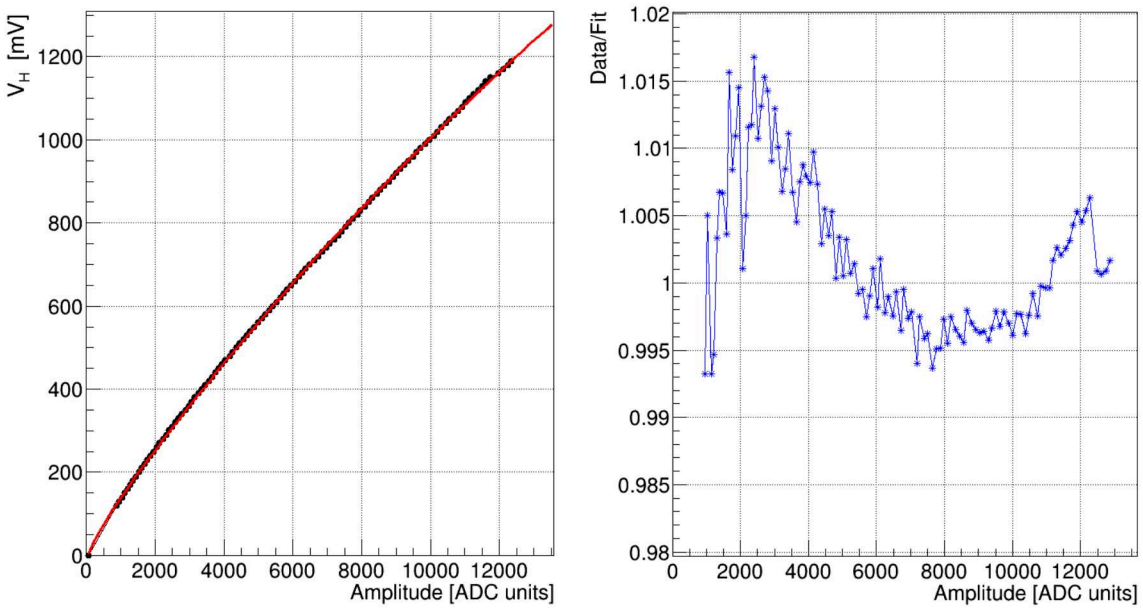

(a) (b)

Figure 9.6: Example of gain curve with fit (a). Data/Fit ratio (b). In the example pixel 00 of APTS-19 operated at 1.2 V p-well/p-sub bias is shown.

to subsequent prototypes characterizations. To obtain the gain curve, the charge injection capacitor is charged with a bias V_H and then discharged into the corresponding pixel. The injection is repeated 500 times and the average of the amplitudes of the signal waveforms, measured in ADC units, is obtained for values of V_H in the range 0 to 1 200 mV in steps of 10 mV. The gain curve is then defined as in the example shown in Figure 9.6(a) where the correlation between injected charge in V_H units and the average signal amplitude is shown. The gain curve is fitted with the empirical function:

$$V_H = (p_0(x - x_0) + p_1|x - x_0|^{0.5}) \times (p_2 x + p_3), \tag{9.1}$$

where x is the average waveform amplitude. Points within six σ from the Gaussian noise mean are excluded from the fit since the amplitude measurement in this region is subject to fluctuations (visible as a gap in the data point shown in Figure 9.6(a)). x_0 is the average amplitude of the noise in ADC unit, point fixed for $y = 0$. An example of a fit is shown in red in Figure 9.6(a). Figure 9.6(b) shows the data/fit ratio demostrating that all data points have a discrepancy of less than 2 % from the fit. Similar results to those shown in Figure 9.6 are obtained for all the pixels, sensors and p-well/p-sub bias studied.

9.3.3 Charge Calibration Using Fe-55 Source

The gain curves described in the previous section allow the correction of non-uniformity in sensor response. However, this does not provide an absolute calibration factor and is not sufficient to

determine the collected charge in electron units, which is useful when comparing measurements performed on prototypes with simulations.

The emission of X-rays from ^{55}Fe decay described in 9.1 is used for the absolute calibration of the APTS prototypes. The sensors are exposed to the source and high-static measurements are acquired in self-trigger mode for different p-weel/p-sub bias values on all prototypes available at DESY. The emission spectrum is then populated for each pixel with the amplitudes of all signals recorded in ADC units. Examples of emission spectra are shown in Figure 9.7(a), 9.7(b) and 9.7(c) for standard, n-blanket and n-gap layouts of APTS with 25 µm pitch, respectively. The K-alpha peaks are then fitted with a Gaussian function. Figure 9.7(d) shows the K-alpha peak position as a function of p-weel/p-sub bias for the examples shown.

In all examples in Figure 9.7, it is possible to identify both characteristic peaks. By comparing the different layouts it can be observed that the amplitude increases with the applied bias, effect that is more pronounced in the N-blanket and N-gap layouts. This can be attributed to the change of sensor capacitance, which results in a different amplifier response. Also notable is the difference in the left-tail of the spectrum in the different layouts. Those are mainly due to charge sharing: only if the entire energy of the X-ray is collected by the analyzed pixel the histogram is populated at the peaks-position. Events with charge sharing, typical of the standard layout, populate the left-part of the histogram.

Knowing the initial charge generated by the total absorption of ^{55}Fe X-rays, it is possible to calibrate the gain curves described in the previous section and obtain a conversion function between waveform amplitude in ADC units and collected charge in electron units as shown in the example in Figure 9.8. The calibrations thus obtained are used in the test-beam data analysis described in [137–139] as well as the results shown in the next section.

9.4 APTS Test-Beam Studies on a 15 µm Prototype

Several test-beam campaigns are carried out on calibrated APTS prototypes at DESY II test-beam facility [58]. The objective of the measurements is to evaluate the performance of the prototypes in MIP detection, compare the differences between different implemented layouts, and verify the predictions of the simulations. Results of extensive studies performed on prototypes with 25 µm are reported in [139]. This section presents complementary results of test-beam data analysis performed on the prototype with standard layout and 15 µm pitch (APTS-17 in Table 8.2).

9.4.1 Test-Beam Setup and Data Analysis

The test-beam setup of APTS studies uses the hardware and frameworks described in Chapter 3. The configuration used is comparable to that schematized in Figure 6.2 with the APTS in the DUT role. A photograph of the test-beam setup used for the measurements presented here is shown in Figure 9.9. EUDET-type telescope (described in Section 3.2) is used for particle track reconstruction with the DUT positioned in the center of the six planes of the telescope. The Telepix dectector [109] is used to define a trigger acceptance region (as described in Section 6.2.1) and is positioned as the last plane. The Trigger Logic Unit (TLU) (described in Section 3.4.2) and EUDAQ2 (presented in Section 3.4.3)

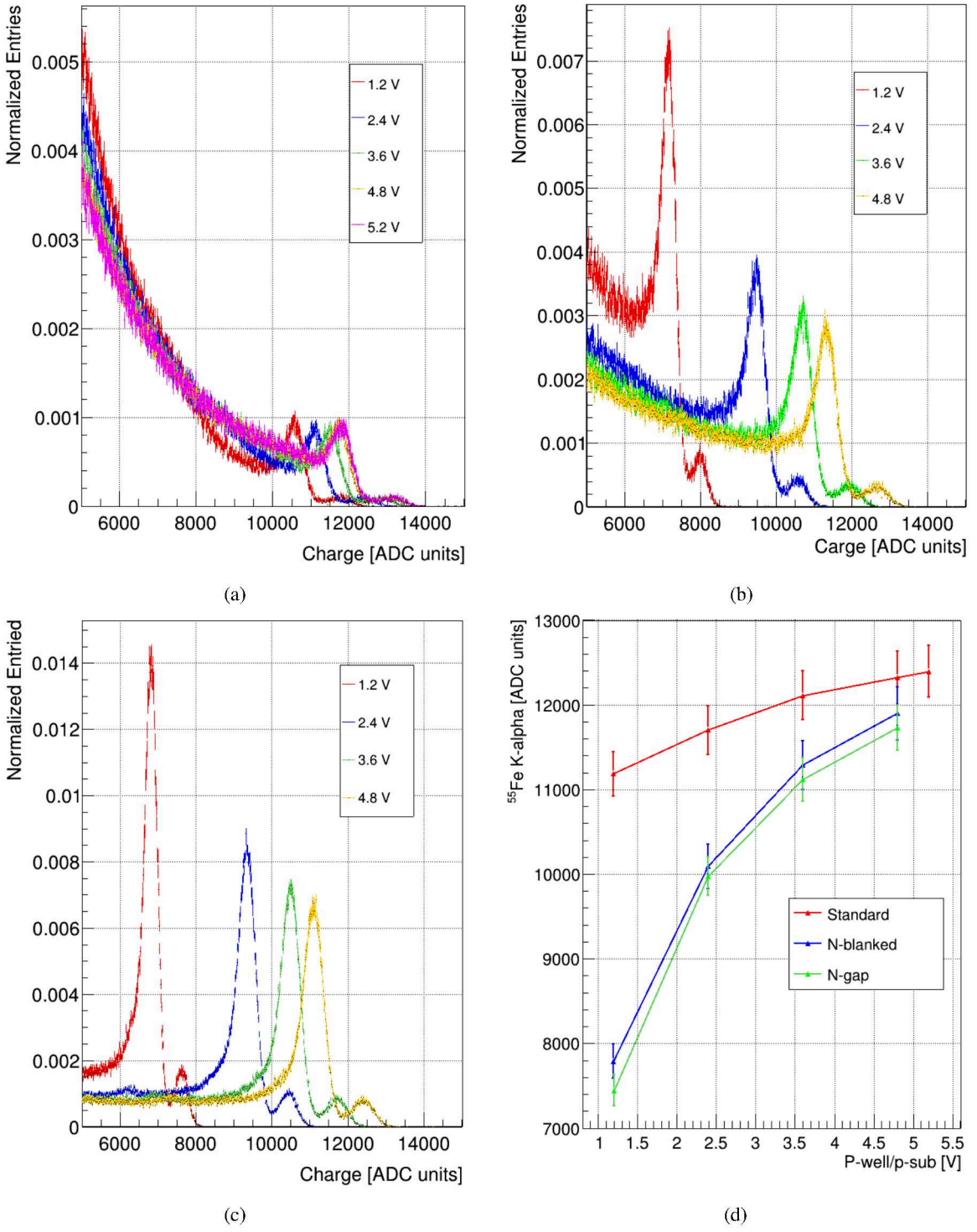

Figure 9.7: ^{55}Fe emission spectrum obtained on APTS with 25 µm pitch for different p-well/p-sub bias with standard (a), n-blanked (b) and n-gap (c) layout. Comparison of the position of K-alpha peak in ADC units for all bias and layout tested (d). All measurements refers to pixel 00 of the analysed samples.

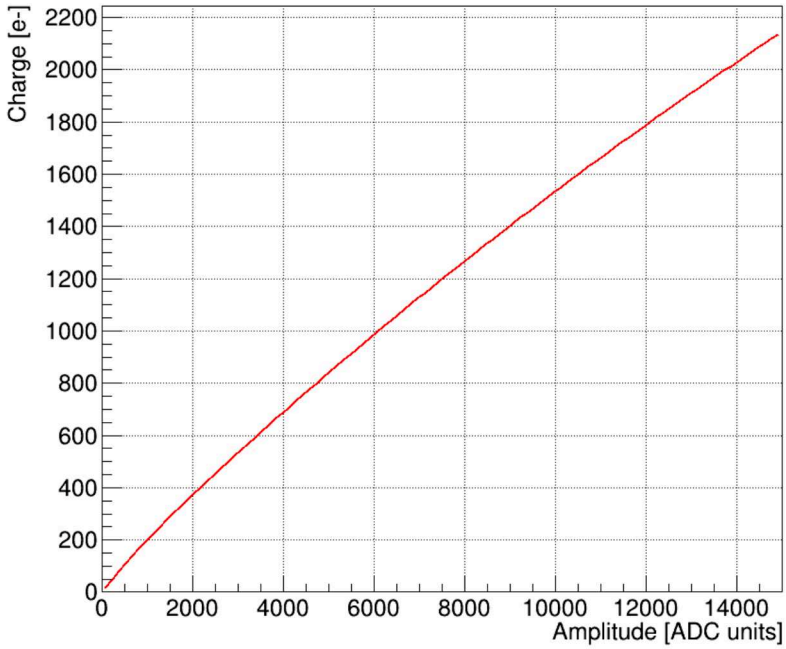

Figure 9.8: Example of calibration curve for pixel 00 of APTS-19 operated at 1.2 V p-well/p-sub bias.

are used to handle triggers, device synchronization, and data acquisition. A 4 GeV/c electron beam is used for the reported measurements.

For each accepted trigger, the 16 pixels waveforms are sampled using the Caribou DAQ system (described in Section 3.4.1). Corryvreckan is used for the data analysis, performed following the steps described in Section 3.5. Tracks are reconstructed using the General Broken Lines (GBL) track model. The calibration curve described in Section 9.3.3 is applied to convert the amplitude of the waveforms to charge, i.e. electrons units.

9.4.2 Clustering, Cluster Size and Cluster Charge

Clustering procedure described in Section 3.5.2 is used. The clustering algorithm uses the full analog waveform information (*[ClusteringAnalog]* module in Corryvreckan) and implements a configurable threshold on the DUT hits; only pixels with a charge higher than the selected threshold are used in the definition of the clusters. The cluster center is defined as the charge-weighted center-of-gravity. Clusters in the DUT are associated with the tracks if the nearest pixel in the cluster is within 30 µm from the interpolated track intercept. In this analysis, only events with interpolated tracks within the area of the central four pixels of the array are analyzed to avoid edge effects, similarly to what is done in [147].

The cluster size is dependent on the charge-sharing properties of the sensor. The layout of the APTS-17 is such that some areas of the sensor are non-depleted[2], in these areas the movement of charges is

[2] Details in Section 8.2, standard-layout

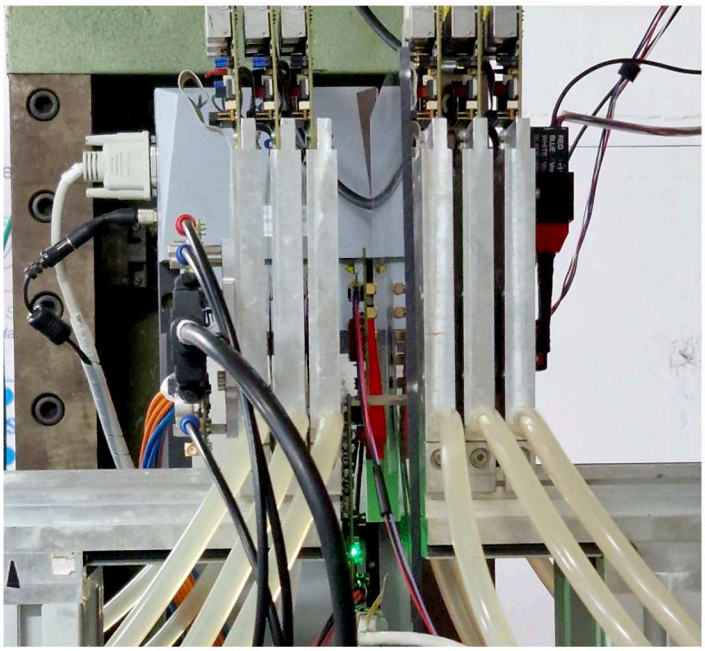

Figure 9.9: Test-beam setup in DESY II test-beam facility used for APTS prototypes testing.

dominated by diffusion, resulting in a wider charge distribution and charge sharing between adjacent pixels. Figure 9.10(a) shows the mean associated cluster size as a function of the threshold for the two values of p-well and p-sub bias studied on the APTS-17. The figure shows that the mean cluster size is strongly dependent on the threshold used. For low threshold values, the average cluster size increases as small signals are included. For high thresholds, on the other hand, the average cluster size decreases. A difference between the two investigated biases is visible in the mean cluster size: the cluster size is larger for the smaller bias. Smaller bias results in lower depleted volume and thus a larger diffusion region, and more charge sharing. An example of cluster size distribution for a threshold of 120 e- is shown in Figure 9.10(b), here an important contribution due to charge sharing is visible as clusters with size larger than one in both bias shown.

Cluster Charge is defined as the sum of the charge of all pixels in the cluster. An example of cluster charge distribution for APTS-17 in MIP detection is shown in Figure 9.11. In the example shown a threshold of 120 e- is used and a Landau function convolved with a Gaussian is fitted to the data. A Most Probable Value (MPV) of 543 e- is extracted from the Fit. Considering the discussion in Section 2.4.1, this value can be used to estimate an active sensor thickness of about 9 µm that is compatible with the expectation: the Complementary Metal-Oxide-Semiconductor (CMOS) process used [130] offers an active thickness of $\sim$ 10 µm.

9.4.3 Efficiency

MIP detection efficiency is defined as the ratio of the number of tracks associated with clusters on the DUT to the number of total tracks reconstructed in the DUT acceptance area. Similar to the results shown in the previous section, only tracks interpolated in the four central pixels of the matrix

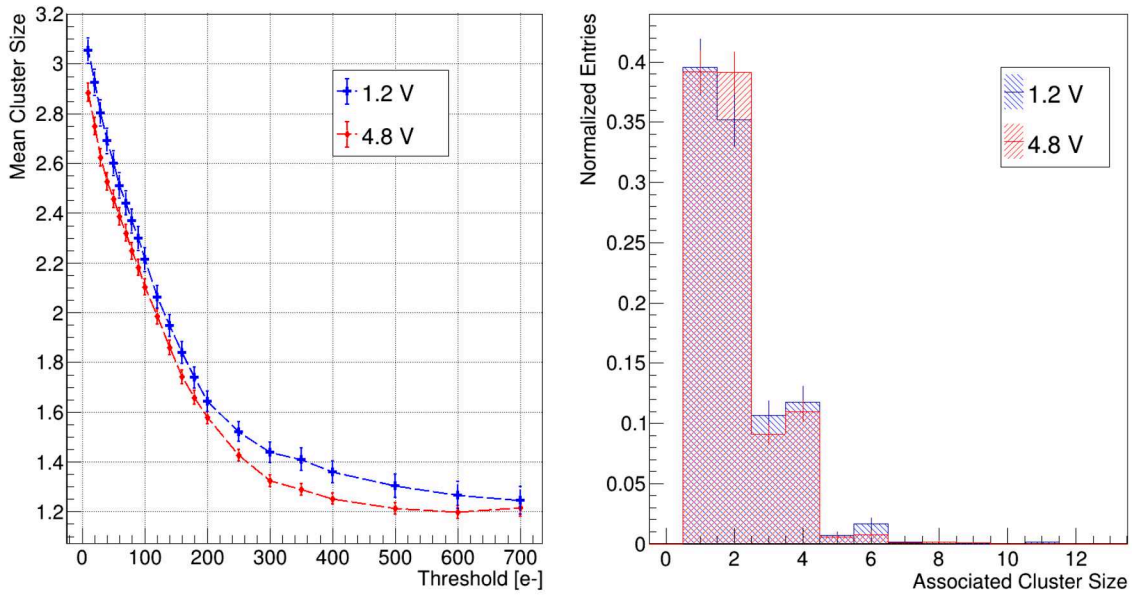

(a) (b)

Figure 9.10: Mean cluster size in MIP detection as a function of the threshold for APTS-17 sample (a). Example of cluster size distribution for 120 e- threshold. The two p-well and p-sub biases used are shown with different colors.

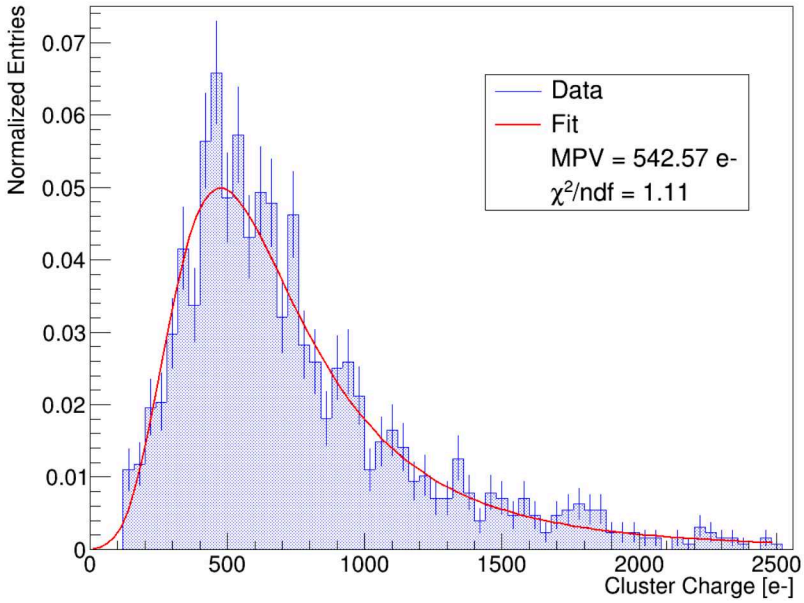

Figure 9.11: Example of cluster charge distribution fitted with a Landau function convoluted with a Gaussian. Measured using a 120 e- threshold at 4.8 V p-well and p-sub bias.

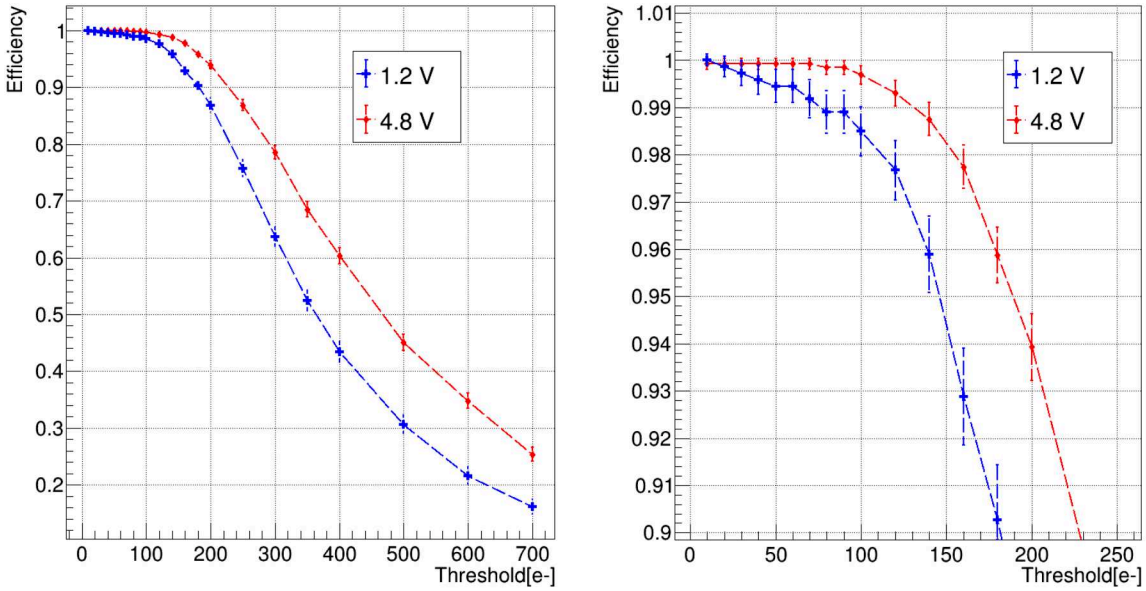

(a) (b)

Figure 9.12: Efficiency in MIP detection as function of threshold for APTS-17 sample (a). Zoom on the lower thresholds (b). The two p-well and p-sub biases used are shown with different colors.

of APTS-17 are considered for the efficiency study. The efficiency is measured as a function of the applied threshold; the results are shown in Figure 9.12. An important dependence between sensor p-well/p-sub bias and efficiency can be observed, with higher efficiency values for the higher bias studied. The efficiency exceeds the value of 99 % for threshold of ~130 e- and ~70 e- for biases of 4.8 V and 1.2 V, respectively. This shows that for the standard layout and small pixel pitch (15 µm in the sensor analyzed here) the applied bias has an important effect on efficiency. Higher biases result in a stronger electric field and a larger fraction of depleted volume, leading to faster charge collection, reducing the probability of recombination, and increasing the total collected charge as discussed in [139].

For very low thresholds the efficiency is measured to be of the 100 %, however, it is important to note that the choice of the optimal threshold must also be made considering noise contamination. Fake-hit-rate is studied on test-beam data for the optimal choice of operational threshold. The fake-hit-rate is defined as the number of hits on the DUT in the absence of a particle interaction (i.e., no associated tracks). Figure 9.13 shows The measured fake-hit-rate as a function of threshold in pixel units normalized to the number of analyzed events. It can be seen that for low thresholds, the fake hit rate increases drastically; however, for threshold values larger than 50 e- a noise contamination of less than 10×10^{-4} Hits/event is measured. The measurements show that the sensor has a window of operability as an MIP detector with efficiencies above 99 % and low noise contamination for threshold ranges of 50 to 70 e- and 50 to 130 e- for p-well/p-sub bias values of 1.2 V and 4.8 V, respectively.

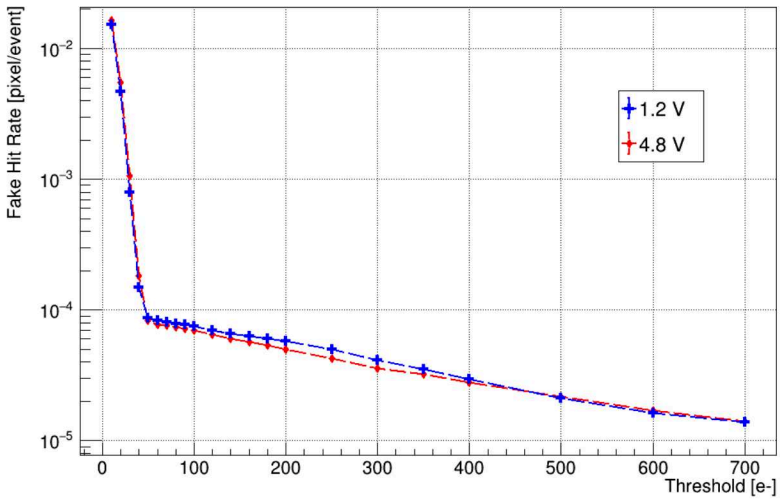

Figure 9.13: Normalized fake-hit-rate in MIP detection as function of threshold for APTS-17 sample. The two p-well and p-sub biases used are shown with different colors.

9.4.4 Spatial Resolution

The spatial resolution of a pixel detector can be measured by analyzing spatial residual as described in Section 2.5.1. The standard deviation of the spatial residuals σ_{meas} measured with APTS-17 for the x-coordinate is shown in Figure 9.14. σ_{meas} can be expressed as the quadratic sum of the contributions σ_{track} and σ_{APTS}, the spatial resolution of the reconstructed track and the intrinsic spatial resolution of the DUT (APTS-17), respectively:

$$\sigma^2_{meas} = \sigma^2_{track} + \sigma^2_{APTS}. \tag{9.2}$$

The resolution σ_{track} can be estimated by using the GBL formalism and the tool described in Section 3.3. For the estimation of σ_{track} the amount of material budget of the entire setup must be known. Although the chip thickness is known, the gluing procedure of the sensor to the Printed Circuit Board (PCB) resulted in uncertainty on the effective thickness of the adhesive used, which is part of the DUT material budget. The track resolution σ_{track} can, therefore, be estimated to be in the range of 1.9 to 4.5 µm[3].

Assuming for σ_{track} the mean value in the estimated range of 3.2 µm Figure 9.14 shows the σ_{APTS} in x as a function of threshold measured on APTS-17. DUT spatial resolutions smaller than 3.5 µm are measured for low thresholds. These values are well below the binary spatial resolution expected for a sensor with the same pixel-pith and cluster size equal to one, on the order of 4.3 µm, demonstrating how charge sharing, typical of MAPS with a standard layout, is beneficial in terms of spatial resolution.

[3] Adhesive layer thickness, and therefore material budget and track resolution, is measured using a 3D microscope scan. The measurement is subject to significant uncertainty that results in the indicated range. Estimation of the σ_{track} is also carried out using the method described in [150], resulting in a spatial resolution of the order of 4 µm

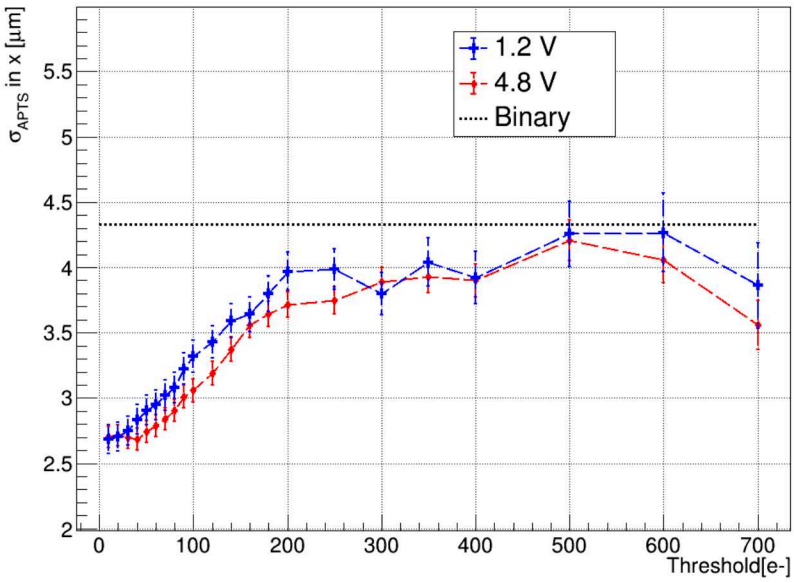

Figure 9.14: σ_{APTS} as a function of the threshold for APTS-17 sample assuming a σ_{track} of 3.2 µm. The two p-well and p-sub biases used are shown with different colors. The binary spatial resolution expected for a sensor with the same pixel-pith and cluster size equal to one is also reported.

9.5 Summary of Results

In this chapter, results of laboratory calibrations and characterizations as well as test-beams measurements of MAPS prototypes developed using a 65 nm CMOS imaging process are presented.

One of the prototypes investigated is the DESY Chip V1, fully developed at DESY with the objective of verifying the characteristics of a newly designed fast CSA. Studies with ^{55}Fe and test-beam measurements confirm, through direct analysis of signal waveforms, the functionality of the integrated circuits, showing, however, a pronounced post-signal undershoot and some limitations in the CSA linearity. The outcome of the measurement performed in the context of this work informed further design optimization, leading to an updated version of the CSA design under study at the time of writing.

Several APTS prototypes, MAPS test structures developed at CERN by the ALICE ITS3 group, are also investigated as part of this work. The performance in MIP detection of a 15 µm APTS prototype is studied. Characterizations are carried out at DESY II test-beam facility. The studies demonstrated a total collected charge compatible with the nominal active thickness of the sensor, spatial resolution better than 3.5 µm, and efficiencies above 99 % with low noise contamination. This performance is achieved for threshold ranges of 50 to 70 e- and 50 to 130 e- for p-well/p-sub bias values of 1.2 V and 4.8 V, respectively, highlighting a robust window of operability of the sensor in MIP detection. The operation parameters of the sensor are optimized by maximizing the S/N of injected pulses, and the sensor is calibrated using ^{55}Fe source. Similar calibrations are performed on all prototypes available. These calibrations have been adopted, in addition to this work, by several studies carried out at DESY on the same APTS sensors.

These studies, developed in the broad context of Research and Development (R&D) of future vertex/tracker detectors, support MAPS as a key technology potentially capable of meeting the stringent requirements of future experiments.

CHAPTER 10

Summary and Prospect

The study of key technologies is of crucial importance for the development of the next generation of particle physics detectors, which require unprecedented performance to push the boundary of current knowledge of the world of particles and fundamental interactions. This thesis explored two technologies that are emerging in High-Energy Physics (HEP) applications: digital Silicon Photomultipliers (dSiPMs) and Monolithic Active Pixel Sensors (MAPS). Both are developed using commercial Complementary Metal-Oxide-Semiconductor (CMOS) imaging processes and take advantage of continuous technological advancements enhancing the synergy between research and industry. dSiPMs and MAPS performance and potential make these technologies excellent candidates for future experimental applications.

Digital Silicon Photomultiplier Technology

The first part of this thesis describes the dSiPM technology and reports the results of characterizations performed on the DESY dSiPM prototype, designed using a 150 nm CMOS technology. Comprehensive laboratory calibrations and characterizations validated the functionality of the sensor and integrated CMOS circuits. The digital nature of the prototype, and the test structures implemented in the chip periphery, allowed the characterizations of sensor performance to be extended beyond what is accessible in conventional analog Silicon PhotoMultiplier (SiPM).

Temperature-dependent optimal working points were identified through Current-Voltage (IV) curves, and the Dark Count Rate (DCR) of the studied prototypes is measured to be in the range 0.5 kHz to 3 MHz depending on operating temperature and overvoltage. The effect of pixel masking on the DCR and power consumption was evaluated, showing considerable improvements in sensor performance while masking only few noisy pixels. The crosstalk effect was studied and correlated with the position of individual noisy Single-Photon Avalanche Diode (SPAD). A picoseconds pulsed laser was used to characterize several components of the temporal resolution of the sensor. The intrinsic time resolution of SPAD/pixel reached values of 12 ps while the implemented Time to Digital Converter (TDC)

showed an effective resolution of 27 ps. The measurement of signal propagation delays showed the significance of this contribution in terms of temporal resolution in large sensors, evaluated in DESY dSiPM to be of the order of 80 ps. This contribution can be corrected in DESY dSiPM if the location of the firing pixel determining the time stamp is known.

One of the primary objectives of this work was to investigate the potential of dSiPM technology as a possible candidate for Minimum Ionising Particles (MIP) detection. The integration of SPAD in CMOS processes allows the combination of readout electronics with intrinsically fast and highly efficient sensors. This makes the dSiPM technology a possible candidate for future 4D-tracking applications where temporal resolutions of less than 100 ps and spatial resolutions on the order of 10 µm are required for each ionizing particle.

The DESY dSiPM was therefore investigated at the DESY II test-beam facility as a MIP detector showing a spatial resolution of about 20 µm, a temporal resolution of 50 ps, and an efficiency of about 30 %. Studies and simulations were carried out by coupling the DESY dSiPM with thin Cerium-doped Lutetium Yttrium OxyorthoSilicate (LYSO(Ce)) scintillators, allowing the efficiency in MIP detection to be increased to values above 99 % while also providing a clear separation between signal and noise events due to the large cluster size of signal events.

The use of thin radiators coupled to dSiPM defines an innovative detector-concept where MIPs are detected with excellent spatial and temporal resolutions through the detection of light produced in the radiators. This study showed the potential of this concept while also highlighting some challenges. The use of radiators, although beneficial in terms of efficiency and signal discrimination, resulted in a deterioration of the spatial and temporal performance of the sensor. It is shown that the use of sensors with higher Photon Detection Efficiency (PDE) can be beneficial in terms of temporal resolutions. Further improvements can also come from different sensor designs, the use of more appropriate radiators, and more advanced reconstruction techniques. Scalability of dSiPM-based sensors, integration into large detector systems, and their impact on overall experiments performance are other aspects that need further investigation.

This study shows the great potential of dSiPM in MIP detection emphasizing the need for further Research and Development (R&D) that can rely on ongoing innovations of the technology driven by research and industry.

Monolithic Active Pixel Sensor Technology

The second part of the thesis analyzed another key technology for future applications in HEP experiments: MAPS. Two different prototypes fabricated in a 65 nm CMOS imaging technology were investigated, DESY Chip V1 and Analog Pixel Test Structure (APTS).

DESY Chip V1 is a test prototype that allowed the characterization of a newly designed fast Charge Sensitive Amplifier (CSA), developed at DESY within the TowArds Next GEneRation sIlicoN detectors (TANGERINE) project. Studies in the laboratory with radioactive sources and at the MAinzer MIkrotron (MAMI) test-beam facility confirmed the functionality of the design. The studies identified a nonlinearity in the TOT response and an undershoot effect in the signal waveform,

providing important feedback to CSA designers. A new optimized version of the design is being characterized at the time of writing.

APTS, tested in collaboration with CERN and ALICE ITS3 group, is a test structure that provides an excellent tool for investigating MAPS technology and the effect in MIP detection performance of sensor pitch, layout, and readout electronics. In the context of this thesis, operation parameters were optimized and charge calibrations performed on the prototypes available at DESY. The calibrations were used in several laboratory and test-beam measurement campaigns and allow the correct interpretation of the results as well as comparison with simulations performed within the TANGERINE group. The performance in MIP detection of one of the APTS prototypes with standard layout and 15 µm pixel pitch was presented. The sensor showed excellent spatial resolutions measured to be less than 3.5 µm and detection efficiency higher than 99 % with low noise contamination in a wide threshold window.

The known excellent performance of MAPS in MIP detection is validated with sensors produced in smaller CMOS technology nodes, as the examples shown in this work. Further MAPS R&D is needed, however, to meet the stringent requirements of vertex/tracker detectors for future collider experiments. Ongoing studies aim to validate and enhance MAPS temporal performance. Additionally, sensors must be scaled in size for integration into large detector systems, while maintaining high spatial and temporal performance with a low material budget. Again, in this example, the synergy between scientific research and industry is confirmed as crucial, generating mutual benefits and accelerating technological advancement.

List of Figures

1.1 Standard Model of particle physics 4
1.2 CERN accelerator complex 6
1.3 LHC/HL-LHC Schedule 7
1.4 Pileup events in ATLAS 8

2.1 Band structure 16
2.2 Band structure of doped semiconductors 17
2.3 pn-juntion 18
2.4 Photon interactions significance 20
2.5 Photon absorption cross section in silicon 21
2.6 Photon absorption depth in silicon 22
2.7 Straggling functions 23
2.8 Gain layer 26
2.9 Detector readout chain 27
2.10 Detector segmentation 28

3.1 DESY II test-beam facility 32
3.2 Particle track reconstruction 34
3.3 Track resolution estimation 35
3.4 Caribou DAQ system 36
3.5 Trigger logic unit 37
3.6 EUDAQ2 framework 38
3.7 Time-dependent alignment correction 40

4.1 Analog SPAD structure 44
4.2 Analog SiPM structure 45
4.3 Digital SPAD structure 46
4.4 LIDAR image sensor 46
4.5 SPAD electric field simulation 48
4.6 Correlated noise in SiPM 49
4.7 ASIC design of DESY dSiPM 51
4.8 DESY dSiPM quadrant structure 51

4.9 DESY dSiPM pixel . . . 52
4.10 DESY dSiPM TDC . . . 53
4.11 DESY dSiPM validation logic . . . 54
4.12 DESY dSiPM test structures . . . 55

5.1 DAQ system heath source . . . 58
5.2 dSiPM laboratory measurements - Temperature diodes calibration results . . . 59
5.3 dSiPM laboratory measurements - Current-voltage curves . . . 60
5.4 dSiPM laboratory measurements - Breakdown evaluation . . . 61
5.5 dSiPM laboratory measurements - Pixel DCR . . . 62
5.6 dSiPM laboratory measurements - Dark event hitmap with mask . . . 62
5.7 dSiPM laboratory measurements - Pixels DCR . . . 63
5.8 dSiPM laboratory measurements - Effect of masks on DCR . . . 64
5.9 dSiPM laboratory measurements - Effect of masks on IV . . . 64
5.10 dSiPM laboratory measurements - Crosstalk probability . . . 66
5.11 dSiPM laboratory measurements - Crosstalk as a function of overvoltage . . . 67
5.12 dSiPM laboratory measurements - Crosstalk probability and light emission . . . 68
5.13 Laser setup for timing studies . . . 69
5.14 dSiPM laboratory measurements - Analog Signal of pixel/SPAD . . . 70
5.15 dSiPM laboratory measurements - Example of TOA distribution . . . 71
5.16 dSiPM laboratory measurements - TOA as a function of overvoltage . . . 71
5.17 dSiPM laboratory measurements - Pixel delays . . . 73

6.1 Interactions in a SPAD . . . 76
6.2 DESY dSiPM test-beam DAQ system . . . 77
6.3 Hitmap of telescope planes with trigger . . . 78
6.4 DESY dSiPM test-beam campaigns . . . 79
6.5 DESY dSiPM material budget . . . 80
6.6 Track resolution estimation . . . 82
6.7 Bare dSiPM test-beam results - Cluster size distribution for signal and background . . . 85
6.8 Bare dSiPM test-beam results - Fraction of events with cluster size greater than one . . . 86
6.9 Bare dSiPM test-beam results - Spatial residuals . . . 87
6.10 Bare dSiPM test-beam results - Time residuals . . . 88
6.11 Bare dSiPM test-beam results - In-SPAD hitmap of slow events . . . 88
6.12 Bare dSiPM test-beam results - In-pixel efficiency . . . 89
6.13 Bare dSiPM test-beam results - Efficiency as function of overvoltage . . . 90

7.1 MIP detection using SPADs coupled with a radiator . . . 92
7.2 Impact of radiator thickness . . . 93
7.3 SiPM-based multipurpose detector . . . 93
7.4 Scintillation process . . . 95
7.5 DESY dSiPM PDE simulated . . . 97
7.6 dSiPM Simulation results - Geant4 events display . . . 99
7.7 dSiPM Simulation results - Average number of photons emitted . . . 99
7.8 dSiPM Simulation results - Number of photons detected . . . 100

7.9 dSiPM Simulation results - Effect of LYSO thickness . . . 100
7.10 dSiPM Simulation results - Spatial residuals . . . 101
7.11 dSiPM+LYSO coupling . . . 103
7.12 dSiPM+LYSO laboratory measurements - Sr-90 events hitmap . . . 104
7.13 dSiPM+LYSO test-beam results - Cluster size . . . 105
7.14 dSiPM+LYSO test-beam results - Spatial residuals . . . 106
7.15 dSiPM+LYSO test-beam results - In-pixel efficiency . . . 107
7.16 dSiPM+LYSO test-beam results - Time residuals . . . 108
7.17 Analog SiPM test-beam setup . . . 108
7.18 Analog SiPM time residuals . . . 109

8.1 ALPIDE pixel schematic . . . 114
8.2 MAPS layouts . . . 115
8.3 MLR1 production . . . 117
8.4 DESY chip V1 . . . 117
8.5 APTS microscope picture . . . 118

9.1 DESY chip V1 laboratory measurements - ^{55}Fe waveforms . . . 122
9.2 MAMI test-beam setup . . . 123
9.3 DESY chip V1 test-beam results - Waveform . . . 124
9.4 DESY chip V1 test-beam results - Amplitude as a function of TOT . . . 125
9.5 APTS laboratory measurements - Signal-to-noise ratio optimization . . . 126
9.6 APTS laboratory measurements - Example of gain curve . . . 127
9.7 APTS laboratory measurements - Charge calibration using ^{55}Fe . . . 129
9.8 APTS laboratory measurements - Example of calibration curve . . . 130
9.9 APTS test-beam setup . . . 131
9.10 APTS test-beam results - Cluster size . . . 132
9.11 APTS test-beam results - Cluster charge distribution . . . 132
9.12 APTS test-beam results - Efficiency . . . 133
9.13 APTS test-beam results - Fake-hit-rate . . . 134
9.14 APTS test-beam results - Spatial resolution . . . 135

List of Tables

1.1 Future lepton colliders design parameters 12

2.1 Impact ionization phenomenological parameter 25

7.1 Scintillation crystals properties 95
7.2 Properties of simulated materials 98
7.3 OST LYSO(Ce) properties 102

8.1 Future vertex detector requirements 115
8.2 APTS chip investigated at DESY 118

9.1 DESY chip V1 operational parameters 122
9.2 APTS optimized parameters 126

Glossary

AAD Average Absolute Deviation. 80

ADC Analog to Digital Converter. 27, 36, 118, 125, 127–129

ALICE A Large Ion Collider Experiment. 6, 10, 11, 115, 116

ALPIDE ALICE PIxel DEtector. 10, 33, 113, 114

APD Avalanche PhotoDiode. 43, 45

APTS Analog Pixel Test Structure. iii, 2, 118, 119, 121, 125–135, 138, 139

ASIC Application Specific Integrated Circuit. 28, 35, 50, 51, 54

ATLAS A Toroidal LHC ApparatuS. 6–8

BSI BackSide Illumination. 45, 46, 91, 109

BSM Beyond Standard Model. 5, 6, 11

CCD Charge Coupled Device. 66, 67

CERN European Organization for Nuclear Research. 5, 115, 116, 118

CFD Constant Fraction Discrimination. 29, 70

CLIC Compact Linear Collider. 12

CMOS Complementary Metal-Oxide-Semiconductor. iii, 1, 2, 10, 13, 14, 28, 33, 45, 48, 50, 51, 57, 60, 73, 113–117, 131, 135, 137–139

CMS Compact Muon Solenoid. 6, 8, 9

CSA Charge Sensitive Amplifier. iii, 116, 121, 123, 124, 135, 138, 139

DAQ Data AcQuisition. 35, 36, 51–53, 57, 59, 76, 79, 118, 125, 130

DCR Dark Count Rate. 46, 48, 57–65, 72, 73, 79, 81, 83–87, 90, 102, 103, 105, 109, 110, 137

DESY Deutsches Elektronen SYnchrotron. 31, 43, 50, 114–116, 118

DLL Delay Locked Loop. 53

DNL Differential Non-Linearity. 72

dSiPM Digital Silicon PhotoMultiplier. iii, 1, 2, 14, 31, 43, 45, 49–53, 57–59, 61, 65, 67, 69, 72–83, 85–93, 96–110, 137, 138

DUT Device Under Test. 28–35, 37, 39, 69, 76, 77, 79–84, 87, 102, 103, 106–108, 123, 128, 130, 131, 133, 134

e-h electron-hole. 16, 19, 22–26, 44, 47, 49, 75, 83, 94, 121

ECFA European Committee for Future Accelerators. 13, 14

EPPSU European Particle Physics Strategy Update. 11, 13

EW ElectroWeak. 11, 12

FCC-ee Future Circular Collider electron-positron. 12

GBL General Broken Lines. 33–35, 39, 81, 82, 130, 134

HEP High-Energy Physics. iii, 1–3, 13–15, 28, 43, 75, 113, 116, 137, 138

HGTD High Granularity Timing Detector. 8

HL-LHC High-Luminosity LHC. 3, 7–11, 13, 14

ILC International Linear Collider. 12

IT Inner Tracker. 8, 9

ITk Inner Tracking system. 7, 8

ITS2 Inner Tracking System 2. 113, 116

IV Current-Voltage. 46, 47, 57–61, 63, 64, 73, 102, 137

LC Lepton Collider. 3, 5, 11–13

LEP Large Electron-Positron collider. 5

LGAD Low Gain Avalanche Diode. 8, 9, 11, 14

LHC Large Hadron Collider. 1, 3, 5–8

LHCb Large Hadron Collider beauty. 6, 9, 10

LIDAR LIght Detection And Ranging. 46

LYSO Lutetium Yttrium OxyorthoSilicate. 91, 97–109

LYSO(Ce) Cerium-doped Lutetium Yttrium OxyorthoSilicate. iii, 9, 91, 95, 101, 109, 110, 138

MAMI MAinzer MIkrotron. 121, 123–125, 138

MAPS Monolithic Active Pixel Sensors. iii, 1, 2, 10, 11, 13, 14, 31, 33, 113–115, 121, 134–139

MBI Material Budget Imaging. 79

MIP Minimum Ionising Particles. iii, 1, 2, 13, 20, 31, 75, 76, 78, 79, 81, 83–94, 100, 102, 105, 106, 109, 110, 114, 116, 121, 123–125, 128, 131–135, 138, 139

MPV Most Probable Value. 23, 131

MTD MIP Timing Detector. 9

NIR Near InfraRed. 22, 67

OT Outer Tracker. 9

PCB Printed Circuit Board. 80, 103, 134

PDE Photon Detection Efficiency. 14, 43, 47, 61, 70, 83, 97, 99, 100, 103, 107, 109, 110, 138

PET Positron Emission Tomography. 49

PID Particle IDentification. 10

PMTs PhotoMulTipliers. 37, 43, 44, 76

R&D Research and Development. 1, 2, 13, 14, 110, 114–116, 136, 138, 139

RICH Ring Imaging CHerenkov. 10, 93

RMS Root Mean Square. 85

ROI Region Of Interest. 81, 87, 108

S/N Signal-to-Noise ratio. 125, 126, 135

SCR Space Charge Region. 17

SiPM Silicon PhotoMultiplier. 9–11, 14, 43–50, 52, 57, 58, 61, 63, 67, 69, 75, 91–93, 107–110, 137

SM Standard Model. 1–6, 11

SPAD Single-Photon Avalanche Diode. 14, 43–52, 54, 55, 57, 59–61, 63, 65–76, 82–89, 91–93, 137, 138, 142

TANGERINE TowArds Next GEneRation sIlicoN detectors. 114, 116, 138, 139

TDC Time to Digital Converter. 30, 50–54, 72–74, 137

TLU Trigger Logic Unit. 36, 37, 75, 76, 81, 83, 128

TOA Time Of Arrival. 29, 30, 70–72, 107

TOF Time Of Flight. 10, 14, 93

TOT Time Over Threshold. 124, 125

Bibliography

[1] M. Thomson, *Modern Particle Physics*, Cambridge University Press, 2013, DOI: 10.1017/CBO9781139525367.

[2] Wikipedia contributors, *Standard Model of Elementary Particles*, Accessed: 2024-11-24, 2024, URL: https://en.wikipedia.org/wiki/File:Standard_Model_of_Elementary_Particles.svg.

[3] M. Blagojević and F. W. Hehl, *Gauge Theories of Gravitation*, 2022, URL: https://arxiv.org/abs/1210.3775.

[4] A. D. Sakharov, *Violation of CP Invariance, C asymmetry, and baryon asymmetry of the universe*, Pisma Zh. Eksp. Teor. Fiz. (1967), DOI: 10.1070/PU1991v034n05ABEH002497.

[5] E. Corbelli and P. Salucci, *The extended rotation curve and the dark matter halo of M33*, Monthly Notices of the Royal Astronomical Society (2000), DOI: 10.1046/j.1365-8711.2000.03075.x.

[6] N. Kaiser and G. Squires, *Mapping the Dark Matter with Weak Gravitational Lensing*, APJ (1993), DOI: 10.1086/172297.

[7] E. J. Copeland, M. Sami and S. Tsujikawa, *Dynamics of Dark Energy*, International Journal of Modern Physics D (2006), DOI: 10.1142/S021827180600942X.

[8] M. C. Gonzalez-Garcia and Y. Nir, *Neutrino masses and mixing: evidence and implications*, Rev. Mod. Phys. (2003), DOI: 10.1103/RevModPhys.75.345.

[9] M. Ibe, A. Kusenko and T. T. Yanagida, *Why three generations?*, Physics Letters B (2016), DOI: 10.1016/j.physletb.2016.05.025.

[10] P. Fayet and S. Ferrara, *Supersymmetry*, Physics Reports (1977), DOI: 10.1016/0370-1573(77)90066-7.

[11] P. Langacker, *Grand unified theories and proton decay*, Physics Reports (1981), DOI: 10.1016/0370-1573(81)90059-4.

[12] ATLAS Collaboration, *LHC Run-3 Starts*, Accessed: 2024-11-24, 2024, URL: https://atlas.cern/Updates/Press-Statement/LHC-Run3-Starts.

[13] R. Aßmann, M. Lamont and S. Myers, *A brief history of the LEP collider*, Nuclear Physics B - Proceedings Supplements (2002), DOI: 10.1016/S0920-5632(02)90005-8.

[14] ATLAS Collaboration, *The ATLAS Experiment at the CERN Large Hadron Collider*, JINST (2008), DOI: 10.1088/1748-0221/3/08/S08003.

[15] CMS Collaboration, *The CMS experiment at the CERN LHC*, JINST (2008), DOI: 10.1088/1748-0221/3/08/S08004.

[16] ATLAS Collaboration, *Observation of a new particle in the search for the Standard Model Higgs boson with the ATLAS detector at the LHC*, Physics Letters B (2012), DOI: 10.1016/j.physletb.2012.08.020.

[17] CMS Collaboration, *Observation of a new boson at a mass of 125 GeV with the CMS experiment at the LHC*, Physics Letters B (2012), DOI: 10.1016/j.physletb.2012.08.021.

[18] ALICE Collaboration, *The ALICE experiment at the CERN LHC*, JINST (2008), DOI: 10.1088/1748-0221/3/08/S08002.

[19] LHCb Collaboration, *The LHCb Detector at the LHC*, JINST (2008), DOI: 10.1088/1748-0221/3/08/S08005.

[20] M. Zinser, *The Large Hadron Collider Search for New Heavy Charged Bosons and Measurement of High-Mass Drell-Yan Production in Proton-Proton Collision*, Springer International Publishing, 2018, DOI: 10.1007/978-3-030-00650-1_4.

[21] HL-LHC Project Team, *High-Luminosity LHC Project Schedule*, Accessed: 2024-11-25, 2024, URL: https://project-hl-lhc-industry.web.cern.ch/content/project-schedule.

[22] O. Aberle et al., *High-Luminosity Large Hadron Collider (HL-LHC): Technical design report*, tech. rep., CERN, 2020, URL: https://cds.cern.ch/record/2749422.

[23] P. Vankov, *ATLAS Upgrade for the HL-LHC: meeting the challenges of a five-fold increase in collision rate*, EPJ Web of Conferences (2012), DOI: 10.1051/epjconf/20122812069.

[24] F. L. Manghi, *ATLAS upgrade for the HL-LHC*, Nucl. Instrum. Methods Phys. Res., Sect. A (2024), DOI: 10.1016/j.nima.2024.169917.

[25] M. Mannelli, "The CMS HL-LHC Phase II upgrade program: Overview and selected highlights", *The Future of the Large Hadron Collider*, 2023, DOI: 10.1142/9789811280184_0012.

[26] V. Denysenko, *Measurement of the Branching Fraction of the Decay $B^+ \to K^+\mu^+\mu^-$ at LHCb and Study on Mighty Tracker for Future LHCb Upgrade*, Zurich U., 2023, URL: https://cds.cern.ch/record/2894824.

[27] I. Sanna, *Novel silicon detectors in ALICE at the LHC: The ITS3 and ALICE 3 upgrades*, EPJ Web of Conferences (2024), DOI: 10.1051/epjconf/202429608002.

[28] M. Mager, *ALPIDE, the Monolithic Active Pixel Sensor for the ALICE ITS upgrade*, Nucl. Instrum. Methods Phys. Res., Sect. A (2016), DOI: 10.1016/j.nima.2015.09.057.

[29] M. Mager, *The future of bent MAPS, full-wafer (stitched) design: Status and challenges*, Nucl. Instrum. Methods Phys. Res., Sect. A (2024), DOI: 10.1016/j.nima.2024.169447.

[30] European Strategy Group,
Deliberation document on the 2020 Update of the European Strategy for Particle Physics, tech. rep., CERN, 2020, URL: https://cds.cern.ch/record/2720131.

[31] H. M. Gray, *Future colliders for the high-energy frontier*, Reviews in Physics (2021), DOI: 10.1016/j.revip.2021.100053.

[32] P. Bambade et al., *The International Linear Collider: A Global Project*, 2019, URL: https://arxiv.org/abs/1903.01629.

[33] P. N. Burrows et al., eds., *Updated Baseline for a Staged Compact Linear Collider*, CERN, 2016, DOI: 10.5170/CERN-2016-004.

[34] A. Abada et al., *FCC-ee: The Lepton Collider*,
The European Physical Journal Special Topics (2019),
DOI: 10.1140/epjst/e2019-900045-4.

[35] ECFA Detector R&D Roadmap Process Group,
The 2021 ECFA detector research and development roadmap, tech. rep., CERN, 2021,
URL: http://cds.cern.ch/record/2784893.

[36] W. Snoeys, *CMOS monolithic active pixel sensors for high energy physics*,
Nucl. Instrum. Methods Phys. Res., Sect. A (2014), URL:
https://www.sciencedirect.com/science/article/pii/S0168900214008596.

[37] D.-L. Pohl et al.,
Radiation hard pixel sensors using high-resistive wafers in a 150 nm CMOS processing line,
JINST (2017), DOI: 10.1088/1748-0221/12/06/P06020.

[38] N. Cartiglia et al., *4D tracking: present status and perspectives*,
Nucl. Instrum. Methods Phys. Res., Sect. A (2022), DOI: 10.1016/j.nima.2022.167228.

[39] S. Gundacker and A. Heering, *The silicon photomultiplier: fundamentals and applications of a modern solid-state photon detector*, Physics in Medicine & Biology (2020),
DOI: 10.1088/1361-6560/ab7b2d.

[40] H. Kolanoski and N. Wermes, *Particle Detectors: Fundamentals and Applications*,
Oxford University Press, 2020, DOI: 10.1093/oso/9780198858362.003.0001.

[41] S. M. Sze and K. K. Ng, *Physics of Semiconductor Devices*, John Wiley & Sons, 2006.

[42] S. Spannagel, *Test Beam Measurements for the Upgrade of the CMS Pixel Detector and Measurement of the Top Quark Mass from Differential Cross Sections*,
PhD thesis: Universität Hamburg, 2016, DOI: 10.3204/DESY-THESIS-2016-010.

[43] Wikipedia contributors, *Pn-junction-equilibrium-graphs*, Accessed: 2024-11-09, 2020,
URL: https://commons.wikimedia.org/w/index.php?title=File:Pn-junction-equilibrium-graphs.png&oldid=451423606.

[44] H. A. Bethe, *Zur Theorie des Durchgangs schneller Korpuskularstrahlen durch Materie*,
Annalen der Physik (1930), DOI: 10.1002/andp.19303970303.

[45] R. D. Evans, *The Atomic Nucleus*, McGraw-Hill, 1955.

[46] D. Durini and D. Arutinov, *High Performance Silicon Imaging (Second Edition)*, Woodhead Publishing, 2020, DOI: 10.1016/B978-0-08-102434-8.00002-7.

[47] C. Boit et al., *From IC Debug to Hardware Security Risk: The Power of Backside Access and Optical Interaction*, IEEE (2016), DOI: 10.1109/IPFA.2016.7564318.

[48] S. Navas et al., *Review of particle physics*, Phys. Rev. D (2024), DOI: 10.1103/PhysRevD.110.030001.

[49] H. Bichsel, *Straggling in thin silicon detectors*, Rev. Mod. Phys. (1988), DOI: 10.1103/RevModPhys.60.663.

[50] W. Maes, K. M. D. Meyer and R. V. Overstraeten, *Impact ionization in silicon: A review and update*, Solid-state Electronics (1990), URL: https://api.semanticscholar.org/CorpusID:15686146.

[51] D. Massey, J. David and G. Rees, *Temperature Dependence of Impact Ionization in Submicrometer Silicon Devices*, IEEE Transactions on Electron Devices (2006), DOI: 10.1109/TED.2006.881010.

[52] M. Ferrero, R. Arcidiacono, M. Mandurrino, V. Sola and N. Cartiglia, *An Introduction to Ultra-Fast Silicon Detectors*, Taylor & Francis, 2021, DOI: 10.1201/9781003131946.

[53] R. Van Overstraeten and H. De Man, *Measurement of the ionization rates in diffused silicon p-n junctions*, Solid-State Electronics (1970), DOI: 10.1016/0038-1101(70)90139-5.

[54] Y. Okuto and C. Crowell, *Threshold energy effect on avalanche breakdown voltage in semiconductor junctions*, Solid-State Electronics (1975), DOI: 10.1016/0038-1101(75)90099-4.

[55] M. Valdinoci et al., "Impact-ionization in silicon at large operating temperature", *1999 International Conference on Simulation of Semiconductor Processes and Devices. SISPAD'99 (IEEE Cat. No.99TH8387)*, 1999, DOI: 10.1109/SISPAD.1999.799251.

[56] D. Renker, *Geiger-mode avalanche photodiodes, history, properties and problems*, Nucl. Instrum. Methods Phys. Res., Sect. A (2006), DOI: 10.1016/j.nima.2006.05.060.

[57] N. Cartiglia et al., *The 4D pixel challenge*, JINST (2016), DOI: 10.1088/1748-0221/11/12/C12016.

[58] R. Diener et al., *The DESY II test beam facility*, Nucl. Instrum. Methods Phys. Res., Sect. A (2019), DOI: 10.1016/j.nima.2018.11.133.

[59] D. Dannheim et al., *Corryvreckan: a modular 4D track reconstruction and analysis software for test beam data*, 2021, DOI: 10.1088/1748-0221/16/03/P03008.

[60] H. Jansen et al., *Performance of the EUDET-type beam telescopes*, EPJ Techn Instrum (2016), DOI: 10.1140/epjti/s40485-016-0033-2.

[61] Y. Liu et al., *ADENIUM — A demonstrator for a next-generation beam telescope at DESY*, JINST (2023), DOI: 10.1088/1748-0221/18/06/P06025.

[62] J. Baudot et al., “First test results Of MIMOSA-26, a fast CMOS sensor with integrated zero suppression and digitized output”, *2009 IEEE Nuclear Science Symposium Conference Record (NSS/MIC)*, 2009, DOI: 10.1109/NSSMIC.2009.5402399.

[63] G. R. Lynch and O. I. Dahl, *Approximations to multiple Coulomb scattering*, Nucl. Instrum. Methods Phys. Res., Sect. B (1991), DOI: 10.1016/0168-583X(91)95671-Y.

[64] S. Spannagel and H. Jansen, *GBL Track Resolution Calculator v2.0*, 2016, DOI: 10.5281/zenodo.48795.

[65] T. Vanat, *Caribou — A versatile data acquisition system*, PoS (2020), DOI: 10.22323/1.370.0100.

[66] Caribou authors, *Caribou Project Documentation*, Accessed: 2024-12-28, URL: https://caribou-project.docs.cern.ch.

[67] Caribou Collaboration, *Peary: Caribou DAQ Framework*, Accessed: 2024-11-08, 2016, URL: https://gitlab.cern.ch/Caribou/peary.

[68] P. Baesso, D. Cussans and J. Goldstein, *The AIDA-2020 TLU: a flexible trigger logic unit for test beam facilities*, JINST (2019), DOI: 10.1088/1748-0221/14/09/p09019.

[69] Y. Liu et al., *EUDAQ2—A flexible data acquisition software framework for common test beams*, JINST (2019), DOI: 10.1088/1748-0221/14/10/p10033.

[70] C. authors, *Corryvreckan Project*, Accessed: 2024-11-08, 2023, URL: https://project-corryvreckan.web.cern.ch/project-corryvreckan.

[71] C. authors, *Corryvreckan - A Generic Reconstruction and Analysis Framework*, Accessed: 2024-11-08, 2023, URL: https://gitlab.cern.ch/corryvreckan/corryvreckan.

[72] R. Brun and F. Rademakers, *ROOT - An Object-Oriented Data Analysis Framework*, Accessed: 2024-11-08, 1997, URL: https://root.cern.

[73] F. Acerbi and S. Gundacker, *Understanding and simulating SiPMs*, Nucl. Instrum. Methods Phys. Res., Sect. A (2019), URL: https://www.sciencedirect.com/science/article/pii/S0168900218317704.

[74] S. Cova, M. Ghioni, A. Lacaita, C. Samori and F. Zappa, *Avalanche photodiodes and quenching circuits for single-photon detection*, Appl. Opt. (1996), URL: https://opg.optica.org/ao/abstract.cfm?URI=ao-35-12-1956.

[75] S. Vinogradov, *The Silicon Photomultiplier (SiPM): Concept and Design Development*, Accessed: 2024-12-04, 2015, URL: https://www.appec.org/news/the-silicon-photomultiplier-sipm-concept-and-design-development.

[76] A. Mathewson, R. Duane and G. Wrixon, “CMOS compatible avalanche photodiode (APD) arrays”, *Space Optics 1994: Earth Observation and Astronomy*, 1994, DOI: 10.1117/12.185271.

[77] S. Vinogradov and E. Popova, *Status and perspectives of solid state photon detectors*, Nucl. Instrum. Methods Phys. Res., Sect. A (2020), DOI: 10.1016/j.nima.2018.12.067.

[78] H. Finkelstein, M. J. Hsu, S. Zlatanovic and S. Esener, *Performance trade-offs in single-photon avalanche diode miniaturization*, Review of Scientific Instruments (2007), DOI: 10.1063/1.2796146.

[79] P. W. R. Connolly et al., *High concentration factor diffractive microlenses integrated with CMOS single-photon avalanche diode detector arrays for fill-factor improvement*, Appl. Opt. (2020), DOI: 10.1364/AO.388993.

[80] K. Zang et al., *Silicon single-photon avalanche diodes with nano-structured light trapping*, Nature Communications (2017), DOI: 10.1038/s41467-017-00733-y.

[81] M. Wojtkiewicz, B. Rae and R. K. Henderson, *Review of Back-Side Illuminated 3-D-Stacked SPADs for Time-of-Flight and Single-Photon Imaging*, IEEE Transactions on Electron Devices (2024), DOI: 10.1109/TED.2024.3389639.

[82] B. Swinnen et al., *3D integration by Cu-Cu thermo-compression bonding of extremely thinned bulk-Si die containing 10 µm pitch through-Si vias*, 2006 International Electron Devices Meeting (2006), URL: https://api.semanticscholar.org/CorpusID:37222897.

[83] B. Aull, *Geiger-Mode Avalanche Photodiode Arrays Integrated to All-Digital CMOS Circuits*, Sensors (2016), URL: https://www.mdpi.com/1424-8220/16/4/495.

[84] K. Morimoto et al., "3.2 Megapixel 3D-Stacked Charge Focusing SPAD for Low-Light Imaging and Depth Sensing", *2021 IEEE International Electron Devices Meeting (IEDM)*, 2021, DOI: 10.1109/IEDM19574.2021.9720605.

[85] R. Klanner, *Characterisation of SiPMs*, Nucl. Instrum. Methods Phys. Res., Sect. A (2019), DOI: 10.1016/j.nima.2018.11.083.

[86] W. Shockley and W. T. Read, *Statistics of the Recombinations of Holes and Electrons*, Phys. Rev. (1952), DOI: 10.1103/PhysRev.87.835.

[87] J. Frenkel, *On Pre-Breakdown Phenomena in Insulators and Electronic Semi-Conductors*, Phys. Rev. (1938), DOI: 10.1103/PhysRev.54.647.

[88] C. Piemonte and A. Gola, *Overview on the main parameters and technology of modern Silicon Photomultipliers*, Nucl. Instrum. Methods Phys. Res., Sect. A (2019), DOI: 10.1016/j.nima.2018.11.119.

[89] L. W. Davies and A. R. Storm, *Recombination Radiation from Silicon Under Strong-Field Conditions*, Phys. Rev. (1961), DOI: 10.1103/PhysRev.121.381.

[90] A. Lacaita, F. Zappa, S. Bigliardi and M. Manfredi, *On the bremsstrahlung origin of hot-carrier-induced photons in silicon devices*, IEEE Transactions on Electron Devices (1993), DOI: 10.1109/16.199363.

[91] C. Dietzinger et al., "Reduction of optical crosstalk in silicon photomultipliers", *Biosensing and Nanomedicine V*, 2012, DOI: 10.1117/12.930473.

[92] W.-S. Sul, C.-H. Lee and G.-S. Cho,
Influence of Guard-Ring Structure on the Dark Count Rates of Silicon Photomultipliers,
IEEE Electron Device Letters (2013), DOI: 10.1109/LED.2012.2236296.

[93] P. Lecoq and S. Gundacker, *SiPM applications in positron emission tomography: toward ultimate PET time-of-flight resolution*, Eur. Phys. J. Plus (2021),
URL: https://cds.cern.ch/record/2759050.

[94] I. Diehl et al.,
Monolithic MHz-frame rate digital SiPM-IC with sub-100 ps precision and 70 µm pixel pitch,
JINST (2024), DOI: 10.1088/1748-0221/19/01/P01020.

[95] I. Diehl, DESY, Private communication, 2024.

[96] F. King et al., *Test Beam Characterization of a Digital Silicon Photomultiplier*, 2024,
URL: https://arxiv.org/abs/2412.06687.

[97] Jenoptik Optical Systems GmbH, *Jenoptik Thermographic Camera Solutions*,
Accessed: 2024-11-30, 2024, URL: https://www.jenoptik.com/products/cameras-and-imaging-modules/thermographic-camera.

[98] Angelantoni Test Technologies Srl, *DY200 - ACS Compact Climatic Chamber*,
Accessed: 2024-11-30, 2024, URL: https://acs.angelantoni.com/en/news/dy200_acs-compact-climatic-chamber.

[99] Tektronix, *2400 Standard Series SourceMeter Instruments*, Accessed: 2024-11-30, 2024,
URL: https://www.tek.com/en/products/keithley/source-measure-units/2400-standard-series-sourcemeter.

[100] N. Dinu, A. Nagai and A. Para, *Breakdown voltage and triggering probability of SiPM from IV curves at different temperatures*, Nucl. Instrum. Methods Phys. Res., Sect. A (2017),
DOI: 10.1016/j.nima.2016.05.110.

[101] Z. Liu et al.,
In-depth study of single photon time resolution for the Philips digital silicon photomultiplier,
JINST (2016), DOI: 10.1088/1748-0221/11/06/P06006.

[102] E. Engelmann, E. Popova and S. Vinogradov, *Spatially resolved dark count rate of SiPMs*,
The European Physical Journal C (2018), DOI: 10.1140/epjc/s10052-018-6454-0.

[103] Jenoptik AG, *Jenoptik - Optical Technologies, Systems, and Solutions*, Accessed: 2024-12-04,
URL: https://www.jenoptik.com/.

[104] Optophase, *ALS Laser Systems*, Accessed: 2024-11-30, 2024,
URL: http://www.optophase.com/als_laser.html.

[105] Teledyne LeCroy, *WaveRunner 6 Zi Series Oscilloscopes Datasheet*, Accessed: 2024-11-30, 2015, URL:
https://cdn.teledynelecroy.com/files/pdf/waverunner-6zi-datasheet.pdf.

[106] I. Tektronix, *Model 3390 50 MHz Arbitrary Waveform/Function Generator*, 2024,
URL: https://www.tek.com/de/products/arbitrary-waveform-generators/model-3390.

[107] S. Lachnit, *Time Resolution of a Fully-Integrated Digital Silicon Photo-Multiplier*, MA thesis: University of Hamburg, 2024, DOI: 10.3204/PUBDB-2024-00529.

[108] I. Diehl et al., *The DESY digital silicon photomultiplier: Device characteristics and first test-beam results*, Nucl. Instrum. Methods Phys. Res., Sect. A (2024), DOI: 10.1016/j.nima.2024.169321.

[109] H. Augustin et al., *TelePix – A fast region of interest trigger and timing layer for the EUDET Telescopes*, Nucl. Instrum. Methods Phys. Res., Sect. A (2023), DOI: 10.1016/j.nima.2022.167947.

[110] J.-H. Arling and I.-M. Gregor, *Material budget imaging with multi-GeV electrons - calibration and applications for 2D material scanning*, Journal of Physics: Conference Series (2022), DOI: 10.1088/1742-6596/2374/1/012007.

[111] I. Diehl et al., *4D-tracking with digital SiPMs*, Nucl. Instrum. Methods Phys. Res., Sect. A (2024), DOI: 10.1016/j.nima.2024.169985.

[112] F. Carnesecchi et al., *Direct detection of charged particles with SiPMs*, JINST (2022), DOI: 10.1088/1748-0221/17/06/P06007.

[113] Carnesecchi, F. et al., *Understanding the direct detection of charged particles with SiPMs*, Eur. Phys. J. Plus (2023), DOI: 10.1140/epjp/s13360-023-03923-4.

[114] Carnesecchi, F. et al., *Measurements of the Cherenkov effect in direct detection of charged particles with SiPMs*, Eur. Phys. J. Plus (2023), DOI: 10.1140/epjp/s13360-023-04397-0.

[115] ALICE Collaboration, *Letter of intent for ALICE 3: A next-generation heavy-ion experiment at the LHC*, 2022, URL: https://arxiv.org/abs/2211.02491.

[116] N. Nicassio et al., "A combined SiPM-based TOF+RICH detector for future high-energy physics experiments", *2023 9th International Workshop on Advances in Sensors and Interfaces (IWASI)*, 2023, DOI: 10.1109/IWASI58316.2023.10164558.

[117] P. Lecoq, A. N. Annenkov, A. Gektin, M. Korzhik and C. Pédrini, *Inorganic Scintillators for Detector Systems: Physical Principles and Crystal Engineering; 1st ed.* Springer, 2006, URL: https://cds.cern.ch/record/976470.

[118] P. Cerenkov, "Visible luminescence of pure liquids under the influence of γ-radiation", *Dokl. Akad. Nauk SSSR*, 1934, DOI: 10.3367/UFNr.0093.196710n.0385.

[119] S. Agostinelli et al., *Geant4—a simulation toolkit*, Nucl. Instrum. Methods Phys. Res., Sect. A (2003), DOI: 10.1016/S0168-9002(03)01368-8.

[120] J. Allison et al., *Geant4 developments and applications*, IEEE Transactions on Nuclear Science (2006), DOI: 10.1109/TNS.2006.869826.

[121] G. Vignola, *G4_dSiPM*, Accessed: 2024-10-01, 2024, URL: https://github.com/gianpierovignola/G4_dSiPM.git.

[122] OST Photonics, *LYSO(Ce) Scintillation Crystal*, Accessed: 2024-10-08, 2024, URL: https://www.ost-photonics.com/products/scintillation-crystal/scintillation-crystal-material/lysoce-2/.

[123] Polytec PT, *Polytec EP 601 LV Datasheet*, Accessed: 2024-10-08, 2024, URL: https://www.polytecstore.fr/polytec_images/documents/FT_PT/ep/polytec-ep-601-lv_en.pdf.

[124] Broadcom Inc., *AFBR-S4N44P014M: High Performance SiPM, NUV-MT*, Accessed: 2024-10-08, URL: https://www.broadcom.com/products/optical-sensors/silicon-photomultiplier-sipm/high-performance-sipm-nuv-mt/afbr-s4n44p014m.

[125] B. Dierickx, G. Meynants and D. Scheffer, "Near 100% fill factor CMOS active pixels", *Proc. IEEE CCD & AIS workshop*, 1997.

[126] B. Pain, S. K. Mendis, R. C. Schober, R. H. Nixon and E. R. Fossum, "Low-power low-noise analog circuits for on-focal-plane signal processing of infrared sensors", *Infrared Detectors and Instrumentation*, 1993.

[127] I. Valin et al., *A reticle size CMOS pixel sensor dedicated to the STAR HFT*, JINST (2012), DOI: 10.1088/1748-0221/7/01/C01102.

[128] G. Contin et al., *The STAR MAPS-based PiXeL detector*, Nucl. Instrum. Methods Phys. Res., Sect. A (2018), DOI: 10.1016/j.nima.2018.03.003.

[129] G. Aglieri Rinella, *The ALPIDE pixel sensor chip for the upgrade of the ALICE Inner Tracking System*, Nucl. Instrum. Methods Phys. Res., Sect. A (2017), DOI: 10.1016/j.nima.2016.05.016.

[130] Tower Semiconductor, *CMOS Image Sensor Technology*, Accessed: 2024-10-15, 2024, URL: https://towersemi.com/technology/cmos_image_sensor/.

[131] B. Abelev on behalf of The ALICE Collaboration, *Technical Design Report for the Upgrade of the ALICE Inner Tracking System*, Journal of Physics G: Nuclear and Particle Physics (2014), DOI: 10.1088/0954-3899/41/8/087002.

[132] W. Snoeys et al., *A process modification for CMOS monolithic active pixel sensors for enhanced depletion, timing performance and radiation tolerance*, Nucl. Instrum. Methods Phys. Res., Sect. A (2017), DOI: 10.1016/j.nima.2017.07.046.

[133] M. Munker et al., *Simulations of CMOS pixel sensors with a small collection electrode, improved for a faster charge collection and increased radiation tolerance*, JINST (2019), DOI: 10.1088/1748-0221/14/05/C05013.

[134] A. Simancas et al., *Developing a Monolithic Silicon Sensor in a 65nm CMOS Imaging Technology for Future Lepton Collider Vertex Detectors*, IEEE (2022), DOI: 10.1109/NSS/MIC44845.2022.10398964.

[135] A. Chauhan et al., *Towards a new generation of Monolithic Active Pixel Sensors*, Nucl. Instrum. Methods Phys. Res., Sect. A (2023), DOI: 10.1016/j.nima.2022.167821.

[136] H. Wennlöf et al.,
The Tangerine project: Development of high-resolution 65 nm silicon MAPS,
Nucl. Instrum. Methods Phys. Res., Sect. A (2022), DOI: 10.1016/j.nima.2022.167025.

[137] A. Simancas et al.,
Simulations and performance studies of a MAPS in 65 nm CMOS imaging technology,
Nucl. Instrum. Methods Phys. Res., Sect. A (2024), DOI: 10.1016/j.nima.2024.169414.

[138] H. Wennlöf et al., *Simulating Monolithic Active Pixel Sensors: A Technology-Independent Approach Using Generic Doping Profiles*, 2024, DOI: 10.48550/arXiv.2408.00027.

[139] A. Simancas,
TCAD Simulations and Test Beam Characterization of MAPS for Future Lepton Colliders,
PhD Thesis: University of Bonn, 2024.

[140] G. Aglieri et al.,
Strategic R&D Programme on Technologies for Future Experiments - Annual Report 2020,
tech. rep., CERN, 2020, URL: https://cds.cern.ch/record/2764386.

[141] M. Buckland,
Development of the ITS3: A bent-silicon vertex detector for ALICE in the LHC Run 4,
Nucl. Instrum. Methods Phys. Res., Sect. A (2022), DOI: 10.1016/j.nima.2022.166875.

[142] N. Cartiglia et al., *DRD3 - Solid State Detectors - Research Proposal*, tech. rep., CERN, 2024, URL: https://cds.cern.ch/record/2901958.

[143] W. Snoeys et al., "Optimization of a 65 nm CMOS imaging process for monolithic CMOS sensors for high energy physics", *Proceedings of 10th International Workshop on Semiconductor Pixel Detectors for Particles and Imaging — PoS(Pixel2022)*, 2023, DOI: 10.22323/1.420.0083.

[144] F. Krummenacher, *Pixel detectors with local intelligence: an IC designer point of view*,
Nucl. Instrum. Methods Phys. Res., Sect. A (1991),
DOI: 10.1016/0168-9002(91)90152-G.

[145] C. Reckleben, DESY, Private communication, 2024.

[146] W. Deng et al., *Design of an analog monolithic pixel sensor prototype in TPSCo 65 nm CMOS imaging technology*, JINST (2023), DOI: 10.1088/1748-0221/18/01/C01065.

[147] G. A. Rinella et al., *Characterisation of analogue Monolithic Active Pixel Sensor test structures implemented in a 65 nm CMOS imaging process*, 2024,
DOI: 10.48550/arXiv.2403.08952.

[148] T. Walcher, *The Mainz microtron facility MAMI*,
Progress in Particle and Nuclear Physics (1990), DOI: 10.1016/0146-6410(90)90016-W.

[149] I. V. Kotov, H. Neal and P. O'Connor,
"Pair creation energy and Fano factor of silicon measured at 185 K using Fe55 x-rays",
High Energy, Optical, and Infrared Detectors for Astronomy VIII, 2018,
DOI: 10.1117/12.2310131.

[150] M. Antonello et al.,
Precision determination of the track-position resolution of beam telescopes, 2024,
URL: https://arxiv.org/abs/2408.17215.

Acknowledgments

The conclusion of this journey represents not only the achievement of a small personal milestone but also gave me the opportunity to reflect on all the people who made this accomplishment possible, and whom I wish to thank here.

Thank you Simon for everything you taught me, for your open door, for supporting and guiding me, and for being the kind of supervisor every student hopes for.

Thank you Ingrid for making the DESY ATLAS group my second family, for your thoughtful guidance, dedication, and for all the opportunities for growth you've given me.

Thank you Finn for your precious hints, for patiently guiding me, for all the time you dedicated to me, and for resisting my constant siege.

Thank you Inge for the enjoyable days spent in the lab, sharing all the small successes (and failures) of the dSiPM. My thanks also go to Christian, Tomas, Eric, Dennis, Stefano, and Karsten for all the support. I learned so much from each of you and greatly appreciated your help.

Thank you *Tangerines* - you are all wonderful people! Thank you for the Wednesday discussions, for inspiring me, and for the enjoyable moments during trips and evenings together. A special thank you to Adry, Larissa, Manuel, Naomi, and Sara, who shared with me the joys and anxieties of the PhD journey, intense gossip sessions, fantastic food, and so much more.

Thank you to my amazing office mates Alberto, Naomi, and Stephan for enduring my picoseconds discussions and for the, at times, very expansive conversations.

Thank you to all the people and colleagues I met in meetings, workshops, conferences, and retreats. Thank you to all past colleagues and supervisors who continue to support me. Thank you to everyone who contributed to my professional and personal growth during these wonderful years of study.

Last but not least, I want to thank my lifelong friends and my family. Grazie *Casalinesi* e amici di studio diventati amici di vita, per le piacevoli distrazioni e i momenti insieme sempre piú rari e preziosi. Grazie ai miei genitori, a mio fratello Gabriele, e mia sorella Cinzia per avermi reso quello che sono, e per il vostro supporto incondizionato. Infine grazie Marika, la mia roccia, il mio punto di riferimento, grazie per aver reso la mia vita a colori.